Terrestrial Radio Wave Propagation at Millimeter-Wave Frequencies

Hao Xu

Dissertation submitted to the Faculty of the
Virginia Polytechnic Institute and State University
in partial fulfillment of the requirements for the degree of

Doctor of Philosophy
in
Electrical and Computer Engineering

Theodore S. Rappaport, Chair
Gary S. Brown
David A. de Wolf
Werner E. Kohler
Tim Pratt
Brian Woerner

May 1, 2000
Blacksburg, Virginia

Keywords: wireless communications, radio wave propagation, channel models, channel measurements, millimeter-wave, 38 GHz, 60 GHz, broadband wireless, LMDS, BMS, NGI.

Terrestrial Radio Wave Propagation at Millimeter-Wave Frequencies

by

Hao Xu

Committee Chairman: Theodore S. Rappaport

Bradley Department of Electrical Engineering

Abstract

This research focuses on radio wave propagation at millimeter-wave frequencies. A measurement based channel characterization approach is taken in the investigation.

First, measurement techniques are analyzed. Three types of measurement systems are designed, and implemented in measurement campaigns: a narrowband measurement system, a wideband measurement system based on Vector Network Analyzer, and sliding correlator systems at 5.8 GHz, 38 GHz and 60 GHz. The performances of these measurement systems are carefully compared both analytically and experimentally.

Next, radio wave propagation research is performed at 38 GHz for Local Multipoint Distribution Services (LMDS). Wideband measurements are taken on three cross-campus links at Virginia Tech. The goal is to determine weather effects on the wideband channel properties. The measurement results include multipath dispersion, short-term variation and signal attenuation under different weather conditions. A design technique is developed to estimate multipath characteristics based on antenna patterns and site-specific information.

Finally, indoor propagation channels at 60 GHz are studied for Next Generation Internet (NGI) applications. The research mainly focuses on the characterization of space-time channel structure. Multipath components are resolved both in time of arrival (TOA) and angle of arrival (AOA). Results show an excellent correlation between the propagation environments and the channel multipath structure.

The measurement results and models provide not only guidelines for wireless system design and installation, but also great insights in millimeter-wave propagation.

Acknowledgments

First of all, I would like to express my sincere appreciation to my advisor, Professor Theodore S. Rappaport, for his invaluable inspiration, encouragement and support throughout my doctoral study. I am also grateful for all my committee members for their insightful technical guidance and warm-hearted relationship. Also, acknowledgment is due to MPRG faculty and staff for providing all their assistance. I consider myself fortunate to be able to work in such a supporting environment.

A measurement campaign is never a solo task. I would like to acknowledge Dr. James Schaffner from HRL laboratories for working with me closely on the propagation research. Special thanks are due to Dr. Robert Boyle, Ray Lovestead, and Yi-Ju Ou for their help in the 38 GHz measurement campaign, and Vikas Kukshya, Agnes Tan, Benjamin Henty, and Jason Aron for their help in the 60 GHz measurement campaign. I wish to express my appreciation to Professor David A. de Wolf for his technical input in the theoretical rain scattering calculation. I am very grateful to my colleagues and friends Gregory Durgin, Keith Blankenship, Paolo Cardieri, Neal Patwari, and Roger Skidmore for always being there to help. Also, I would like to thank many other friends at MPRG who made my PhD study an enjoyable experience.

No words can express my deep appreciation and gratitude to my parents and relatives in China for their love, encouragement, and understanding throughout the years, especially during the last 11 years of my study overseas. I would also take this opportunity to thank my MS advisor Professor M. Kolomeitseva and other professors in Russia for their support.

Finally, it is my pleasure to acknowledge the financial supports from HRL Laboratories, Hughes Network Systems and MPRG, without which this PhD work would be impossible.

Contents

1 Introduction **1**

1.1 Trends Towards Millimeter-Waves 1

1.2 Advantages of Millimeter-Wave Systems 2

1.3 Proposed Millimeter-Wave Applications 3

1.3.1 LMDS/LMCS 4

1.3.2 WLAN 7

1.3.3 Mobile Applications 8

1.4 Challenges in Millimeter-Wave Propagation 9

1.5 Organization of the Report 10

2 Propagation and Reception Fundamentals **12**

2.1 System Coverage 13

2.1.1 Path Loss Models 13

2.1.2 Link Budget 15

2.2 Multipath Propagation 16

2.2.1 Space-Time Channel Models 16

2.2.2 Receiver Bandwidth Consideration 18

2.2.3 Antenna Beamwidth Consideration 22

2.3 Summary 23

3 Channel Measurement Techniques and Measurement System Design 25

3.1 Narrowband Techniques 26

3.1.1 Principle of Operation 26

3.1.2 Implementations of Narrowband Measurement Systems 27

3.2 Direct RF Pulse System 29

3.3 VNA Measurement System 32

3.3.1 Principle of Operation 32

3.3.2 Implementation of VNA Measurement Systems 34

3.4 SCS Measurement System 36

3.4.1 Correlation Method 36

3.4.2 Properties of PN Sequence 37

3.4.3 Mathematical Models of SCS Channel Sounding 38

3.4.4 Implementation of SCS 42

3.4.5 Analysis of the Time Measurement Accuracy 44

3.5 Measurements Comparing VNA and SCS 45

3.5.1 System Settings 46

3.5.2 Measurement Results 47

3.5.3 Summary of the Comparison Measurements 49

3.6 SCS at 38 GHz and 60 GHz 50

3.6.1 System Hardware 50
3.6.2 Choice of Parameters 52
3.6.3 Antennas 54
3.6.4 Free Space Calibration 54
3.7 Summary 57

4 Terrestrial Millimeter-Wave Propagation 58

4.1 General Considerations 59
4.1.1 Microwave LOS Links 59
4.1.2 Specifics for Millimeter-Wave LOS Links 60
4.2 Diffraction: Fresnel Zone Clearance 61
4.2.1 Diffraction Loss vs. Frequency 63
4.2.2 Fresnel Zone Clearance 63
4.3 Refraction: Effects of Refractive Index Change 65
4.3.1 Multipath due to Refractive Index Change 66
4.4 Reflection: Effects of Rough Surface 68
4.4.1 Reflection: Snell's Law 68
4.4.2 Rayleigh Criterion 69
4.4.3 Scattering Loss Factor 71
4.4.4 Reflection Measurement Results 72
4.5 Scattering: Radar Cross Section 74
4.6 Scattering: Effects of Vegetation 75
4.6.1 Vegetation Scattering Measurement Results 76

4.7 Scattering: Effects of Rain 77
  4.7.1 The aR^b Rain Attenuation Model 78
  4.7.2 Crane's Rain Attenuation Model 79
  4.7.3 Rain Attenuation Measurement Results 80
4.8 Other Outdoor Propagation Measurement Results 82
  4.8.1 LMDS Applications 82
  4.8.2 Street-Level-Propagation 85
4.9 Outdoor Propagation Study at 60 GHz 86
4.10 Literature Survey on Indoor Propagation Measurements 86
  4.10.1 Narrowband Measurement Results 86
  4.10.2 Wideband Measurement Results 92
  4.10.3 AOA Measurements 95
  4.10.4 Spatial Diversity 95
  4.10.5 Coherent Bandwidth 96
  4.10.6 Human Induced Variation 96
4.11 Research Directions 98

5 Wideband Point-to-Point Radio Wave Propagation Study at 38 GHz 100

5.1 Introduction 101
5.2 Measurement Setup 101
  5.2.1 Measurement System 101
  5.2.2 Measurement Sites 102
5.3 Measurement Results 108

5.3.1 Multipath Statistics. 109

5.3.2 Short-term Variation. 111

5.3.3 Rain Attenuation. 114

5.3.4 Hail Attenuation. 117

5.3.5 Other Attenuation Measurements. 118

5.4 Theoretical Study of Short-term Signal Variation During Rain 119

5.4.1 Introduction 119

5.4.2 Signal Analysis 120

5.4.3 Variations in Attenuation γ 120

5.4.4 Signal Analysis (Contd.) 123

5.5 Summary 124

6 A Novel Prediction Technique for Wideband Point-to-Point/Multipoint Millimeter-wave Channel 127

6.1 Introduction 128

6.2 3D Geometry of a Point-to-Point Link 129

6.3 Relative Power Zone 130

6.4 Excess Delay Zone 131

6.5 Application Examples 133

6.5.1 Estimate Worst Case Multipath Based on a Site Map 133

6.5.2 Clearance Criterion for Given Multipath Requirements 134

6.6 Comments Regarding the Model 136

6.7 Summary 137

7 Spatial and Temporal Characteristics of 60 GHz Indoor Channels 139

7.1 Introduction . . . 140

7.2 Measurement Setup . . . 141

7.2.1 Methods to Separate Multipath Components . . . 141

7.2.2 Measurement Procedure . . . 142

7.2.3 Antenna Patterns . . . 144

7.2.4 Site Description . . . 144

7.3 Relating Multipath Structure to Propagation Environments . . . 146

7.3.1 Power Angle Profiles . . . 146

7.4 Statistical Parameters of the Channel . . . 152

7.4.1 Definition of the Statistical Parameters . . . 152

7.4.2 Results of Measured Statistical Parameters . . . 154

7.4.3 AOA Statistics . . . 155

7.4.4 TOA Statistics . . . 159

7.4.5 Received Signal Power . . . 160

7.5 Summary . . . 164

8 Summary and Future Research Directions 165

8.1 Summary of Results . . . 165

8.2 Related Publications by the Author . . . 168

8.3 Future Research Directions . . . 168

8.4 Conclusions . . . 170

A Measurement Results from VNA and SCS Comparison 171

A.1 Measurement Site Information 171

A.2 Measurement Results 173

B Analysis on Time Measurement Accuracy for the SCS 178

B.1 Introduction 178

B.2 Influence on the Synchronization Pulses 179

B.3 Influence on Excess Delay Measurements 180

B.4 Influence on the Absolute Propagation Time Measurements 181

C Canonical Antenna Patterns for Relative Power Zone Derivation 185

D Site Photos and Maps for 60 GHz Measurement Campaign 187

E Abbreviations and Acronyms 200

List of Figures

1 LMDS system configuration. 5

2 Wireless distribution methods of broadband services. 6

3 Application scenario for WLAN. 8

4 Application scenario for Intelligent Transport Systems [1]. 9

5 Path loss scatter plot for the residential measurement data at 5.85 GHz [2]. 14

6 Fundamental propagation mechanisms. 16

7 AOA model. 18

8 Wideband and narrowband channel models 19

9 Spatial resolution of the receiver antenna. 22

10 Block diagram of the CW measurement system at 5.85 GHz [3]. 28

11 Five seconds of CW power data taken in a local area [3]. 29

12 Principle of operation of a direct RF pulse system. 30

13 The duality of channel characterization in the frequency domain and the time domain. 33

14 Block-diagram of VNA channel sounding system. 34

15 M-sequence PN code and its autocorrelation. 37

16 Mathematical models of SCS channel sounding. 39

17 Block diagram of the SCS hardware configured at 5.85 GHz with a clock rate of 100 MHz and a slip rate of 10,000. 43

18 Shift of the recorded PDP due to the frequency offset. 45

19 The combined system for SCS and VNA comparison. 46

20 Site-by-site comparison for location B1 in the lawn: "o" denotes the peaks of multipath components recorded from SCS, and "*" denotes the peaks of multipath components recorded from VNA. 48

21 Site-by-site comparison for location B1 in the conference room. 48

22 Site-by-site comparison for location B2 in the hallway. 49

23 Block-diagram of the 38 GHz channel sounder. 51

24 Characterization of the system speed. 54

25 The transmitter horn antenna. 55

26 The receiver dish antenna. 55

27 Geometry of the free space calibration. 56

28 Scenario for the free space calibration. 57

29 Knife-edge diffraction 62

30 Knife-edge diffraction gain as a function of Fresnel diffraction parameter v. 63

31 Knife-edge diffraction gain as a function of frequency: $d_1 = d_2$=500m, h=1m. 64

32 Fresnel zone boundaries. 65

33 Wave bending caused by the refraction index change. 66

34 Multipath propagation caused by the refraction index change [4]. 67

35 Geometry of the specular reflection over a smooth surface 69

36 Rough surface scattering: with the increase of surface roughness, specular reflected field decreases and diffuse scattered field increases [5] 70

37 Derivation of Rayleigh criterion [6] 71

38 Model of transport theory [7] 75

39 Passive repeater measurements [8]. 91

40 Weather monitoring system on rooftop of GBJ Student Center. 103

41 Geometry of the Slusher-Whittemore link: 605 m unobstructed LOS (L1). (a) top view. (b) side view. 104

42 View from transmitter on L1. 105

43 Geometry of the McBryde - Student Center link: 265 m obstructed link (L2,L3). (a) top view. (b) side view. 106

44 View from receiver on L2 and L3. 107

45 Typical PDP under rainy conditions: May 3, 265 m unobstructed LOS link, average rain rate of 45.72 mm/hr. 108

46 Comparison of PDPs: 605 m unobstructed LOS. Note: no multipath was measured under clear conditions. 110

47 a) Received power PDF over 2-3 minute interval: June 2, 265 m partially obstructed link, R=122 mm/hr. b) Rician K factor vs. rain rate 113

48 Received signal power during rain: June 2^{nd}, 265 m partially obstructed LOS. Each point represents a wideband power measurement taken every 0.02 s. 115

49 Measured rain attenuation in excess of free space path loss and comparison to the Crane model: a) 605 m unobstructed LOS; b) 265m partially obstructed, and obstructed links. 116

50 Hail attenuation measurements on May 1: average excess attenuation of 25.7 dB over the 605 m path, signal variation of 7 dB 117

51 Typical PDP during hailstorm: average received signal power is 27.6 dB lower than the LOS power during clear weather. 118

52 Patches of rain across the LOS 122

53 General form $C(z)$ 122

54 $10\log_{10}(P_{rms}/P_c)$ as function of rain rate 124

55 Geometry of a point-to-point link with an arbitrary scatter in 3D. 129

56 The relative power contour plot in azimuth for horn and parabolic antennas, for any D, (all contour units in dB relative to LOS power). 132

57 The excess delay contour plot in azimuth for D=1000 m (all contour units in ns). . . 133

58 Example of application of power zone and delay zone on site map. 134

59 Automated track system [9]. 142

60 Track and spin measurement procedure. 143

61 Receiver and transmitter antenna patterns used in the measurement campaign. . . . 145

62 AOA measurements for propagation within a room (location 4), relative power levels given in polar plots and peak multipath power (P) given in text. Rays are shown only for locations 4.2 and 4.4 in the figure, similar procedure can be performed for all the locations. 147

63 AOA measurements for propagation along a hallway (location 2), relative power levels given in polar plots and peak multipath power (P) given in text. 148

64 AOA measurements for propagation into rooms (locations 5 and 6), relative power levels given in polar plots and peak multipath power (P) given in text. 149

65 Scatter plot of the measured path loss values 163

66 Measurement locations in the lawn. 172

67 Measurement locations in the conference room. 172

68 Measurement locations in the hallway. 173

69 Influence of the frequency offset on (a) time between sync pulses, (b) time between actual alignments of PNs, and (c) absolute propagation time. 182

70 Theoretical power patterns for horn and dish antennas: azimuth. 186

71 Location 1 – hallway on the third floor of NEB building. 188

72 Location 2 – hallway on the second floor of Whittemore building. 189

73 Location 3 – conference room in NEB. 190

74 Location 4 – classroom in Whittemore. 191

75 Location 5 – from hallway into Lab 2 in NEB, and location 6 – from Lab 2 to Lab 3 in NEB. 192

76 Location 8 – outdoor near NEB building. 193

77 Location 1.2 – hallway on the third floor of NEB building, near the transmitter. . . 194

78 Location 1.4 – hallway on the third floor of NEB building, open area near elevator. . 195

79 Location 1.7 – hallway on the third floor of NEB building, far from transmitter. . . . 195

80 Location 2 – hallway on second floor of Whittemore Hall. 196

81 Location 3.1 – conference room 460 in NEB building. 196

82 Location 4 – measurements in classroom 277 in Whittemore Hall. 197

83 Location 5.1 – measurements within the lab. 197

84 Location 5.3 – hallway to room measurements through a glass door. 198

85 Location 6: measurements from room to room through a wall 198

86 Location 7 – outdoor measurments in a parking lot. 199

87 Location 8: outdoor measurements near a stone wall of NEB building. 199

List of Tables

1 System Settings of the SCS and VNAS. 47

2 Maximum Path Length to Avoid Refracted Multipath [4] (for New Jersey climate region) 68

3 Reflection Loss Measurement Results from [10] 73

4 Experimental Setup for LMDS Measurements. 82

5 Summary of Measured Path Loss Exponent Results 88

6 Summary of Penetration Loss Results 89

6 Summary of Penetration Loss Results - Continued 90

7 Measured Delay Spreads for Different Types of Antennas [11] 92

8 Measured Delay Spreads for Different Polarization of Antennas [12] 94

9 Summary of Multipath Occurrence and Maximum Observed Multipath (MP) Level (w.r.t. LOS). The Maximum MP Signals Were Delayed by 10 to 30 ns from LOS. . . 109

10 Mean Excess Delay, RMS Delay Spread and Maximum Multipath (MP) Level (w.r.t. LOS) from PDPs Containing Multipath Components. 112

11 $10\log_{10}(P_{rms}/P_c)$ 120

12 Maximum Distances of Excess Delay Zone for Horn and Parabolic Antennas. 135

13 Maximum Distances of Relative Power Zone for Horn and Parabolic Antennas. . . . 135

14 Spin Measurements: Transmitter-Receiver Separations (TR) in m, Time Dispersion Parameters ($\bar{\tau}$ and σ_τ) in ns, Angular Dispersion Parameters (Λ and γ) are dimensionless, Maximum Fading Angle(θ_{max}) and AOA of Maximum Multipath ($maxAOA$) in Degree, Ratio of Maximum Multipath Power to Average Power ($\frac{Peak}{Avg}$) in dB, and Maximum Multipath Power (P_{max}) in dBm. 156

15 Track Measurement Results: TR Separations (TR) in m, Time Dispersion Parameters ($\bar{\tau}$ and σ_τ) in ns, Variations of Time Dispersion Parameters ($\delta\bar{\tau}$, $\triangle\bar{\tau}$, $\delta\sigma_\tau$ and $\triangle\sigma_\tau$) in ns, and Average Received Power (P_r) in dBm. 157

16 Measured Penetration Losses and Results from Literature. 162

17 Results for the Lawn. 174

18 Results for Conference Room. 175

18 Results for Conference Room (cont.). 176

19 Results for Hallway. 177

20 Time Measurement Error due to Specified RO Frequency Offsets and PN Frequency Settings. 184

Chapter 1

Introduction

1.1 Trends Towards Millimeter-Waves

The birth of wireless communications dates back to the nineteenth century, when H. R. Hertz, N. Tesla, G. Marconi, and other scientists experimented with the transmission and reception of electromagnetic waves [13]. Since Marconi patented his first wireless telegraph in 1897, wireless communication has evolved into one of the fastest growing industries of the 20^{th} century [14]. Today's wireless services include not only two-way voice communications, but also data and multimedia transmissions. The most distinct trends in the evolution of wireless communications are the search for better grades of service, higher system capacity, and higher frequency and bandwidth (higher data rates).

In the last 20 years, cellular and personal communications services (PCS) have grown into a global telecommunications service with over 300 million subscribers, 40% of the world's installed wired telephone base. Most of these services occupy low frequency bands such as 824 MHz - 894 MHz for cellular systems and 1.8 GHz - 2.0 GHz for PCS in the US. Targeted mainly for the low-data-rate voice transmission, the assigned channel bandwidth is relatively narrow: 30 kHz for the Advance Mobile Phone Systems (AMPS) and 200 kHz for the Global System for Mobile (GSM), for example.

The integration of the voice, video, data and other broadband services has created enormous growth potential for the wireless industry. The Internet and the desire for untethered communications has propelled numerous broadband wireless services. Emerging wireless systems include wireless data transmission, video distribution, wireless local area networks (WLAN), teleconferencing, last mile Internet access, wireless local loop telephony (WLL), intelligent transport systems (ITS), and telemedicine.

These wireless systems offer a number of advantages over their wired counterparts, including mobility of operation, and flexibility in installation and maintenance. The asynchronous transfer mode (ATM) technology, which is independent of the media of transport at the physical layer, allows the integration of wireless systems, satellite networks, fiber networks, cable networks and telephone networks into the Broadband Integrated Services Digital Network (B-ISDN) [15].

Unlike voice transmission, data and multimedia services require much higher bandwidth. The proposed data rate in wireless broadband systems is as much as 155 megabits per second (Mb/s)[1]. Future wireless communications systems will require even higher bandwidth to be able to provide *any service* at any time anywhere in the world. Due to the frequency congestion at lower frequencies and the high bandwidth requirement, microwave and millimeter-wave frequencies are the best candidates for these future wireless systems.

1.2 Advantages of Millimeter-Wave Systems

Millimeter-waves [1] possess unique advantages in indoor and short-range outdoor communications. These advantages are *large spectrum availability, high frequency reuse potential, and small antenna and equipment size* [1].

- Proposed broadband systems require up to hundreds of MHz of bandwidth to support high network capacity (see Section 1.3). Large bandwidth availability makes millimeter-wave frequencies uniquely preferable for broadband services. At 60 GHz, for example, as much as 5 GHz bandwidth (from 59 GHz to 64 GHz) is available as license free spectrum in the US [16].

---

[1] Millimeter-wave frequency ranges from 30 GHz to 300 GHz. This frequency range is also designated as extra high frequency (EHF).

- Millimeter-waves suffer high attenuation due to precipitation, gaseous absorption, and penetration loss through vegetation or walls. In particular, at 60 GHz, the oxygen absorption causes excess attenuation of 15 dB/km in addition to the free space path loss [17]. Due to the high propagation loss and high noise floor over a wide bandwidth, millimeter-wave systems will be used only for short range communications from a few meters up to few kilometers. The small cell size allows high frequency reuse potential and, thus, increased system capacity. For indoor applications, frequency reuse can be possible even between neighboring rooms because of the severe penetration loss through inner walls [18]. Finally, the large propagation loss at millimeter-wave frequencies can be also used to secure transmitted information in military or other security applications.

- At millimeter-wave frequencies, antenna size is greatly reduced. Highly directional antennas can be used to provide high power gain and to suppress multipath interference. Due to the small wavelength, a very small separation distance is required to implement spatial antenna diversity techniques to improve system performance.

- The size of radio-frequency components also reduces with the increase of frequency. Advances in radio-frequency (RF) integrated circuits (IC) technology are a driving force for millimeter-wave system development. Today's IC technology has pushed transistor operation speeds well above 10 GHz. Technological growth in Very High Speed Integrated Circuit (VHSIC) and Microwave and Millimeter-wave Monolithic ICs (MMICs) greatly improves the performance of millimeter-wave components, while reducing the size and cost [19].

In summary, the advantages of millimeter-wave systems coupled with the enabling technology makes the millimeter-wave frequency band the most attractive candidate for broadband wireless services with low-cost miniaturized equipment.

1.3 Proposed Millimeter-Wave Applications

The exploration of upper-microwave and millimeter-wave frequencies supports the development of applications with high data rate and high bandwidth requirements. With high available bandwidth, millimeter-wave applications are capable of integrating voice, data, multimedia and other information services. The proposed applications are multipoint distribution systems, WLAN, ITS, emergent *ad hoc* systems, Next Generation Internet (NGI), and other broadband applications [1].

Commercialization of millimeter-wave frequencies is initiated by governments throughout the world. In particular, the U.S. Federal Communications Commission (FCC) auctioned a large part of the millimeter-wave spectrum around 28 GHz for Local Multipoint Distribution Service (LMDS) in February 1998, and allocated 38.6 - 40 GHz band for fixed point-to-point/multipoint as well as mobile communications in 1999. The tentative date for the auction of the 38 GHz band is the forth quarter of 1999. As much as 5 GHz (59-64 GHz) of spectrum around 60 GHz is license-free and may potentially be used for indoor and short-range applications [16]. In Canada, 1 GHz RF spectrum in the 28 GHz band is allocated for Local Multipoint Communications Services (LMCS) in November, 1996 [20]. In Europe, the proposed broadband wireless services are High-Performance Radio LAN (HIPERLAN) at 5 GHz and 17 GHz [21, 22], Multichannel Multipoint Distribution Systems (MMDS) at 42 GHz [23], and Mobile Broadband Systems (MBS) at 40 GHz and 60 GHz [1, 22]. HIPERLAN is in the standardization phase in the European Telecommunications Standards Institute (ETSI), and MBS is still in the development phase [22]. This section reviews some of the most important applications.

1.3.1 LMDS/LMCS

The idea of using wireless point-to-point links to provide data transmission has been used at microwave frequencies. The frequency bands of 2 to 18 GHz are used to provide LOS microwave links. These microwave links have typical path length of tens of kilometers, and antenna tower heights of 50 to 100 m [24, 25]. Due to the huge available bandwidth, millimeter-wave frequencies are also proposed to provide point-to-point/multipoint links, such as LMDS. Unlike their microwave counterparts, millimeter-wave links have much shorter path lengths, typically up to few kilometers.

Typical LMDS systems have a configuration similar to cellular system as shown in Figure 1. Coverage area is divided into small cells with radii of up to few kilometers. Each cell contains a centrally located transmitter (hub) and multiple receivers or transceivers (subscribers). Point-to-point links are used to interconnect the cell with a central processing center and/or with other cells. For point-to-multipoint links within a cell, transmitter antennas are typically sector antennas, and receiver antennas are highly directional antennas. LMDS is capable of offering subscribers a variety of one- and two-way broadband services, such as video distribution, teleconferencing, WLL, high speed data transmission, and Internet access. LMDS offers a flexible, low-cost alternative to wired local exchange and cable television services [16].

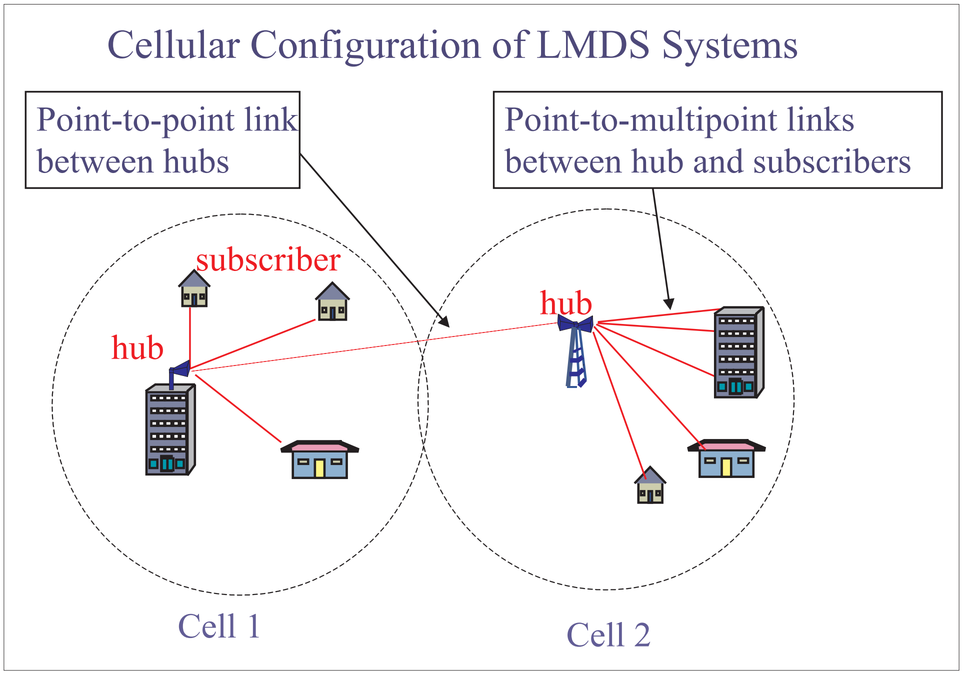

Figure 1: LMDS system configuration.

Millimeter-wave links can also be used to interconnect fiber or satellite networks to their end-users to provide video distribution and Internet access [26]. Figure 2 demonstrates possible configurations that will enable apartment dwellers to access broadband satellite or fiber networks using millimeter-wave links. Comparing with cable or fiber connections, millimeter-wave links offer easy installation, easy maintenance, and highly flexible reconfiguration.

Although LMDS was first proposed at 28 GHz, other millimeter-wave frequencies are also considered for point-to-point/multipoint links. In the US, the 38 GHz band is allocated both for millimeter-wave point-to-point/multipoint links and other mobile applications [16]. In Europe, the 38 GHz band (37-39.5 GHz) has been allocated for use in personal communications network (PCN) systems to interconnect base stations. These millimeter-wave links connect the base station controller and the individual cell base stations, or interconnect cell base stations. Typical length of these links is

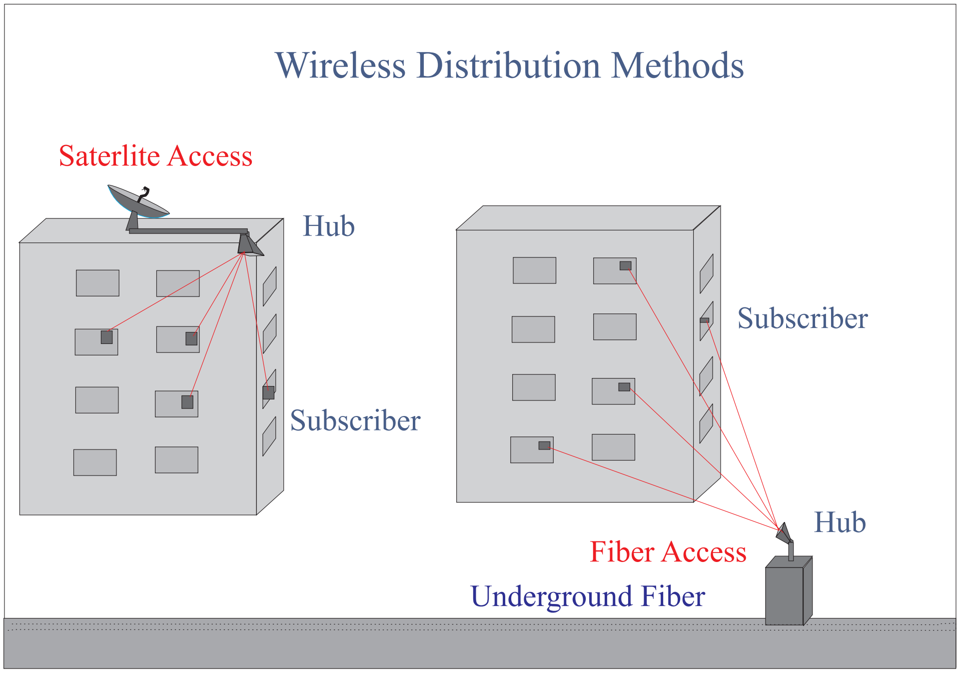

Figure 2: Wireless distribution methods of broadband services.

less than 10 km [23].

Current Service Providers and Supporting Technology

In terms of the national deployment of LMDS, Canada is a few years ahead of the US. In Canada, 28 GHz band was allocated for broadband wireless services in 1996, two years before the 28 GHz spectrum auction in the US. Industry Canada selected three companies, Cellular Vision Canada, MaxLink Communications and Rural Vision, to provide LMCS in Canada [20]. In the US, the top five LMDS license holders are WNP Communications, NEXTBAND Communications, Winstar, Baker Creek Communications and Cortelyou Communications Corp [16].

In Canada, Newbridge Networks (Ontario) provides the network technologies, including the multiservice switch and wireless transceivers, to interconnect end-users to the asynchronous-transfer-mode (ATM) backbone. In the US, Lucent Technologies offers network products such as the GlobeView 2000 broadband switch to support ATM networks with 5 to 20 Gb/s data capacity. Nortel supplies its Reunion point-to-multipoint radio-access system, which connects the users to a central base station. The base station connects to the network through fiber optic links (OC-3, 155.520 Mb/s). Private-branch exchanges (PBX) and computer networks are connected to the network using T1, T3 and Ethernet 10Base T connections. Bosch Telecom offers a system called SpectraPoint to provide two-way digital distribution of multimedia services for LMDS applications. Winstar is concentrating on providing high bandwidth voice and data into office buildings, especially video teleconferencing. Advanced Radio Telecom Corporation (ART) is partnered with Lucent Technologies to provide networks with internet services. ART is currently operating an Internet Protocol (IP) ATM backbone network with 64 kb/s to 10 Mb/s data rates in Seattle, WA, Phoenix, AZ and Portland, OR [27]. Cellular Vision (New Jersey) is currently operating an analog broadcast video system in New York using the 28 GHz LMDS technology. Cellular Vision systems have a cell radius of 4.8 km, a bandwidth of 20 MHz for each channel, and a radiated power of 10 mW per channel.

1.3.2 WLAN

WLAN provides untethered Internet and data access. Today's WLAN deployments are mainly in microwave frequencies between 900 MHz and 5.8 GHz. In Europe, HIPERLAN has been proposed as an extension or replacement for fixed LANs. HIPERLAN supports indoor communications between computers, as well as real-time voice and image signals. It allows physical channel bit rates up to 23.5 Mb/s at 5 GHz and 17 GHz bands [22]. In the US, current WLANs are developed mainly in the license-free Industrial, Scientific, and Medical (ISM) bands and National Information Infrastructure (NII) band. The ISM bands occupy 902 MHz to 928 MHz, 2.4 GHz to 2.4835 GHz, and 5.725 GHz to 5.85 GHz. The NII band is allocated in the 5.15-5.35 GHz and 5.725-5.825 GHz range and was formed by the FCC in 1997 to initiate the formation of a nationwide "information superhighway", which interconnects computers, telecommunication networks, and other services and applications [28].

Millimeter-wave WLAN technology is mainly being developed in the 40 GHz and 60 GHz frequency bands [1, 18, 22]. Figure 3 demonstrates a scenario for a millimeter-wave WLAN. Frequency can be reused in adjacent rooms due to the high attenuation. Huge license-free bandwidth can support voice, data, and video at much higher speed than today's microwave WLAN.

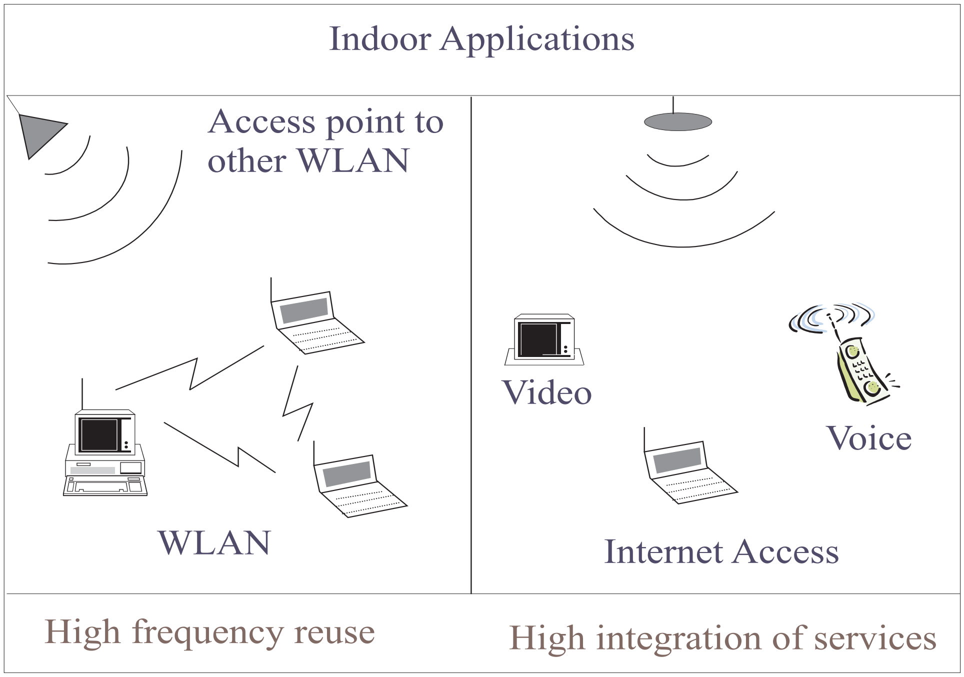

Figure 3: Application scenario for WLAN.

1.3.3 Mobile Applications

Due to the extremely high variability of the millimeter-wave channel, the majority of millimeter-wave applications are proposed for fixed LOS links such as LMDS. Some applications allow low degree of mobility such as WLAN, where a portable computer may be in very slow motion. Few applications are proposed for mobile applications, such as ITS. In such systems, millimeter-wave is used to interconnect vehicles and exchange information about road conditions, relative speed, relative distance, etc. Such information can also be gathered from an information center near the road as shown in Figure 4.

In Europe, services with both high data rate and mobility are supported by MBS. The objective of MBS is a mobile and wireless extension or replacement of fixed broadband integrated services digital network (B-ISDN) [22]. It has wide range of both indoor and outdoor, fixed and mobile applications including wireless access to banking, High Definition (HD) video phone, High Definition Television (HDTV) distribution, LAN interconnection, and interactive TV. MBS will occupy the 40 GHz and 60 GHz bands and it will support channel bit rates as high as 155 Mb/s [22].

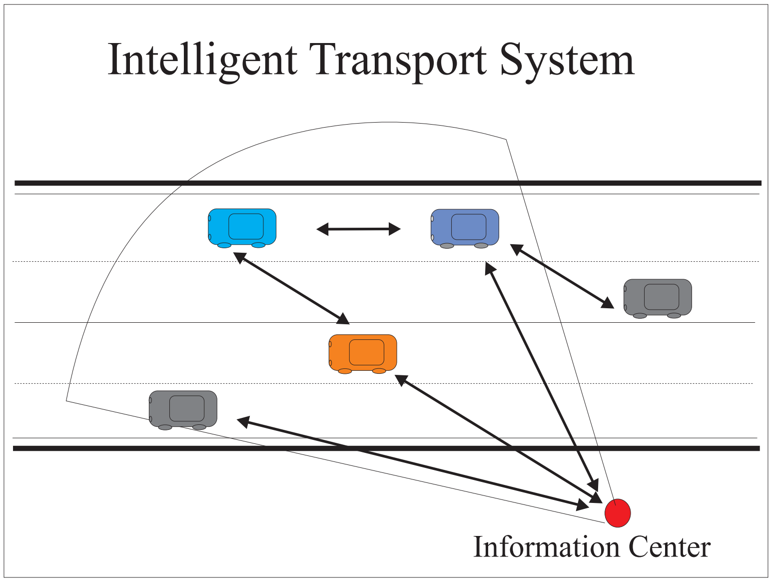

Figure 4: Application scenario for Intelligent Transport Systems [1].

1.4 Challenges in Millimeter-Wave Propagation

The millimeter-wave spectrum offers enormous application potential and will become the next frontier for terrestrial-based wireless communications. As with any engineering development, employment of millimeter-wave frequencies also has great technical challenges. One fundamental challenge is the characterization of the radio wave propagation channel at these frequencies.

Due to the small wavelength at millimeter-wave frequencies, the propagation channel may be extremely time varying and unpredictable. At 60 GHz, for example, the wavelength is only 5 mm, and the phase of an electromagnetic wave shifts 180 degrees for every 2.5 mm in propagation distance. Furthermore, most reflective surfaces appear rough with respect to this wavelength, and the incident wave will be scattered both in specular and non-specular directions, resulting in both coherent and incoherent field components. Compared to the small wavelength, vegetation leaves will be large random scatterers, causing attenuation, depolarization and beam-broadening. Finally, the wideband millimeter-wave channel is subject to change under different weather conditions. Atmospheric effects, such as rain, hail and media inhomogeneity will cause excess attenuation, beam bending, depolarization and multipath propagation. These effects must be studied quantitatively for reliable system design.

1.5 Organization of the Report

Although a lot of research has been undertaken at lower frequencies such as UHF and microwave frequencies [14, 29, 30], much less research has been performed to investigate the millimeter-wave propagation channel. This research focuses on terrestrial millimeter-wave radio channel characterization. Both experimental and theoretical approaches were taken to measure and model the millimeter-wave channel. Research was performed at 38 GHz for LMDS applications and at 60 GHz for indoor applications. A wideband measurement system was built to operate in the 38 GHz and 60 GHz bands. The system was used to measure 38 GHz channels under different weather conditions in a campus environment. The measurement results include excess attenuation, channel time dispersion and short-term signal variation during different weather events from the measurements. A new design technique was developed to estimate wideband channel characteristics based on site-specific information. The research at 60 GHz mainly focused on the space-time characteristics. Results include power delay profiles and power angle profiles of the multipath channels. The organization of the dissertation is as follows.

Chapter 2 introduces fundamental concepts of radio wave propagation and various channel models. Effects of the receiver bandwidth and the antenna beamwidth on the received signal characteristics are also discussed.

Chapter 3 presents a thorough technical review of various measurement techniques. Narrowband techniques and three wideband measurement techniques are analyzed. Mathematical models and operation principles for these techniques are reviewed, and implementation issues are discussed with hardware design examples. A measurement campaign was performed to compare two most commonly used wideband techniques: the time domain technique using a sliding correlator system (SCS) and the frequency domain technique using a vector network analyzer (VNA). Also included is a time measurement error analysis for the SCS. The theoretical results are verified by the measurements. Finally, the 38 GHz and 60 GHz wideband channel sounding systems are described.

Chapter 4 includes a overview of the main propagation considerations for terrestrial millimeter-wave applications. Fundamental propagation mechanisms such as diffraction, refraction, reflection and scattering are discussed. Special emphasis has been placed on the rough surface scattering and the random media scattering due to the vegetation and rain. A detailed literature survey on millimeter-wave propagation is performed for both outdoor and indoor environments.

Chapter 5 describes results of an extensive measurement campaign performed at 38 GHz using three cross-campus radio links from April to August 1998 at Virginia Tech. A total of 73,963 power delay profiles (PDPs) were recorded during different weather events such as clear sky, rain, and hailstorm. The measurement results include wideband channel PDPs, short-term signal variation during rain, change of the coherent and incoherent fields as a function of rain rate, and attenuation due to rain, hail, glass and vegetation.

Chapter 6 presents a novel design technique developed to estimate channel multipath characteristics based on antenna patterns and site-specific information. New metrics such as *relative power zones* and *excess delay zones* are defined and contour plots are developed to determine potential reflectors from an area site map.

Chapter 7 presents the results of a propagation study at 60 GHz. Measurements were performed at 6 indoor locations and 2 outdoor locations. Multipath components were resolved in time delay by a sliding correlator and in space by sweeping a directional antenna in azimuth. The multipath structure was carefully analyzed in each location. Results show excellent correlation between the propagation environment and the channel multipath structure.

Finally, Chapter 8 summarizes the results and defines future research directions.

Chapter 2

Propagation and Reception Fundamentals

This chapter introduces fundamental concepts of radio wave propagation and reception. In any wireless system, the received signal must exceed the receiver noise floor by a minimum signal-to-noise ratio (SNR) in order for the receiver to correctly detect the transmitted information [31, 32]. Issues concerning received signal power and system coverage are discussed in Section 2.1. Furthermore, in wideband wireless systems, multipath dispersion may cause intersymbol interference (ISI) and increase bit-error-rate (BER) [33]. Multipath channel models and effects of receiver bandwidth on the received signals are described in Section 2.2. Finally, for systems deploying narrowbeam antennas, such as LMDS, spatial channel information is extremely important. Spatial channel models and effects of antenna beamwidth on the received signals are discussed in Section 2.2.

The concepts and models presented in this chapter are essential for channel measurements and modeling that will be presented in Chapters 4 through 7 of this work.

2.1 System Coverage

2.1.1 Path Loss Models

Free Space Path Loss Model

Channel induced attenuation is characterized by *path loss*, which is the difference of transmitted power and received power expressed in dB calibrating out system gains and antenna gains. The power attenuation in free space is given by Friis free space path loss [14]

$$PL_{fs}(d) = 20\log(4\pi d/\lambda) \tag{2.1}$$

where d is the transmitter-receiver (TR) separation and λ is the wavelength.

This model is valid only for the distances that are in the far-field, or *Fraunhofer region* of the transmitter antenna. The far-field is the region that satisfies the following relationships [34]

$$\begin{aligned} d &\gg D && (2.2)\\ d &\gg \lambda && (2.3)\\ d &> d_f && (2.4)\\ d_f &= \frac{2D^2}{\lambda} && (2.5) \end{aligned}$$

where D is the largest dimension of the antenna, λ is the wavelength, and d_f is Fraunhofer distance.

Path Loss Exponent Model

Most often, a close distance d_0 is used as a reference distance for path loss models, where d_0 is larger than d_f, and smaller than practical transmitter and receiver separation distance. Typical d_0 values are 1 m for indoor systems, 100 m or 1 km for outdoor environments [14].

Path loss over distance $d > d_0$ can be described by the path loss exponent model as following:

$$\overline{PL}(d)[\mathrm{dB}] = PL_{fs}(d_0)[dB] + 10n\log_{10}(\frac{d}{d_0}) \tag{2.6}$$

where $\overline{PL}(d)$ is the average path loss value at a TR separation of d, $PL(d_0)$ is the free space path loss at the reference distance d_0, and n is the *path loss exponent* that characterizes how fast is the path loss increases with the increase of TR separation. For free space propagation, n equals 2. Obstructions between the transmitter and receiver, and multipath propagation change the n value [2]. One example of the measured path loss exponent is presented in Figure 5. In path loss exponent model, only one parameter n is used to characterize the channel. Although it provides a simple tool for path loss estimates, it normally results in large variance of the prediction error between the predicted path loss and actual measurement results.

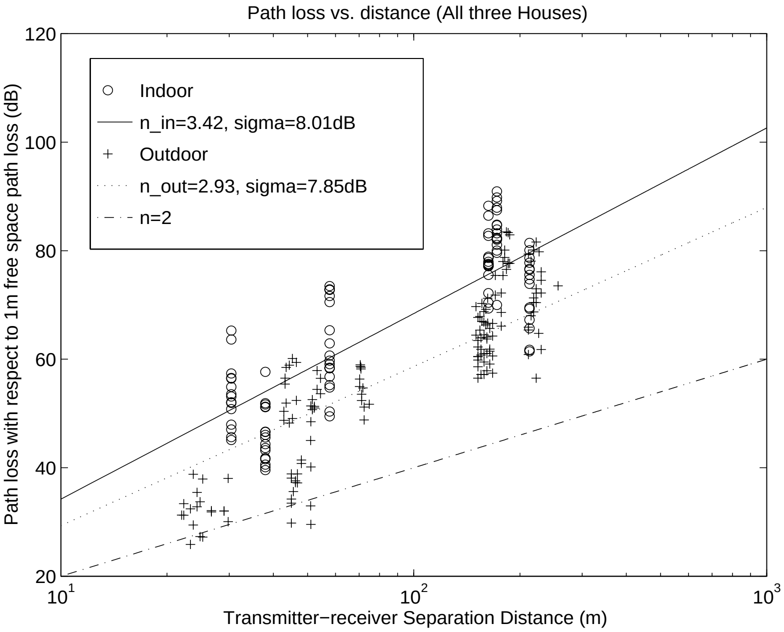

Figure 5: Path loss scatter plot for the residential measurement data at 5.85 GHz [2].

Partition Based Path Loss Model

It is found that path loss is highly correlated with the total number and types of obstructions between the transmitter and the receiver [2, 35, 36]. Partition based path loss models take into account site-specific information in propagation prediction. This model estimates the total path loss as the sum of the free space path loss and the penetration loss caused by each of the obstructions as follows:

$$\overline{PL}(d)[\mathrm{dB}] = PL(d_0)[\mathrm{dB}] + 20\log_{10}\frac{d}{d_0} - \sum_{i=1}^{N} X_i[\mathrm{dB}] \tag{2.7}$$

where X_i is the attenuation value of the ith obstruction between the transmitter and the receiver. For outdoor propagation environments, the obstructions can be exterior walls, trees, or terrain. For indoor propagation environments, the obstructions can be interior walls and furniture. Results from [2] show that the partition based path loss model effectively reduces the standard deviation of the prediction error as compared to the path loss exponent model.

2.1.2 Link Budget

The received signal power, P_r, is given by

$$P_r[\mathrm{dBm}] = P_t[\mathrm{dBm}] + G_t[\mathrm{dB}] + G_r[\mathrm{dB}] - PL(d)[\mathrm{dB}] \tag{2.8}$$

where P_t is the transmitted power, G_t and G_r are transmitter and receiver gains, respectively, d is the TR separation, and PL(d) is the path loss evaluated by (2.1) for free space, (2.6) or (2.7) for other environments.

As mentioned in the beginning of this chapter, the received signal power must exceed the receiver noise floor by a minimum SNR for signal detection. SNR is defined as the ratio of the received signal power, P_r, and noise power, P_N, in linear scale, or difference of P_r and P_N in dB.

$$\mathrm{SNR}[\mathrm{dB}] \quad = \quad P_r[\mathrm{dB}] - P_N[\mathrm{dB}] \tag{2.9}$$

Noise power of the receiver is determined by effective receiver noise temperature and receiver bandwidth as [31, 32]:

$$P_N[\mathrm{dB}] = 10\log_{10} k + 10\log_{10} T + 10\log_{10} B \tag{2.10}$$

where k is Boltzmann constant, which equals 1.38×10^{-23} J/K, T is the effective noise temperature of the receiver system in K, and B is the receiver bandwidth in Hz.

At millimeter-wave frequencies, the system coverage area is much reduced compared with systems at microwave frequencies, if transmitted power and required SNR are assumed to be equal. This is due to several reasons. Equations (2.8) shows that as the carrier frequency increases, the free space path loss increases and the received signal power decreases. Furthermore, measurements showed high penetration loss through glass, walls, vegetation and other obstacles at millimeter-wave frequencies [10, 37, 38, 39, 40]. As a result, the coverage area of millimeter-wave systems is mainly constrained to the area with LOS clearance to the receiver. Also, millimeter-waves suffer high attenuation due to precipitation such as rain and hail, so a link budget margin is required to guarantee system coverage under severe weather conditions. Finally, due to the wide bandwidth used in millimeter-wave systems, the receiver noise power is increased. The reduction of received signal power and increase of receiver noise power lead to a limited coverage area for millimeter-wave systems. Typical millimeter-wave systems have distances less than a few kilometers.

2.2 Multipath Propagation

2.2.1 Space-Time Channel Models

In a typical propagation environment, the EM waves traverse different paths from the transmitter antenna to the receiver antenna as the results of scattering, reflection, or diffraction. Figure 6 shows the basic propagation mechanisms that cause multipath propagation. Detailed discussions of reflection, scattering and diffraction are presented in Chapter 4.

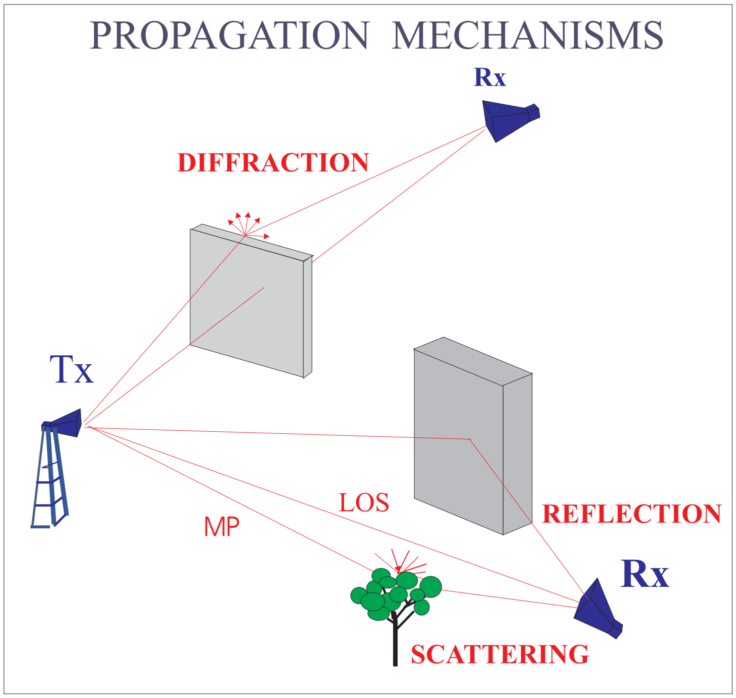

Figure 6: Fundamental propagation mechanisms.

At any point in space, the total electro-magnetic (EM) field is the superposition of LOS component and other multipath components. Each multipath component can be characterized by its amplitude, phase, time of arrival (TOA), and angle of arrival (AOA). These EM waves excite the receiver antenna, and produce the complex voltage of the received signal [34]. The received signal power and envelope (amplitude) depend on not only the exciting EM waves, but also the receiver time resolution (bandwidth), and the antenna spatial resolution (beamwidth).

As a starting point, we assume that the system has infinite resolutions in both time and space (AOA). When the system has an infinite time resolution, i.e. an infinitely wide bandwidth, the RF channel can be modeled as a linear filter with a complex baseband channel impulse response, h_b, as following [14, 41, 42, 43]:

$$h_b(\tau) = \sum_{i=0}^{N-1} a_i \exp(-j\psi_i)\delta(\tau - \tau_i) \tag{2.11}$$

where τ is the delay time variable, N is the number of the multipath components, a_i, ψ_i and τ_i are the amplitude, phase and TOA of the i_{th} multipath component, respectively, and the $\delta()$ denotes *delta* function.

When the receiver antenna has an infinite spatial resolution, i.e. infinitely narrow beamwidth, the space-time channel model has the following form:

$$h_b(\tau, \theta, \phi) = \sum_{i=0}^{N-1} a_i \exp(-j\psi_i)\delta(\tau - \tau_i)\delta(\theta - \theta_i)\delta(\phi - \phi_i) \tag{2.12}$$

where ϕ and θ are the azimuthal and elevational AOAs, as shown in Figure 7. This space-time channel model fully describes the stationary channel response. In a time varying channel, parameters $h_b, a_i, \psi_i, \tau_i, \theta_i, \phi_i$ can be time dependent variables [44].

Practical systems have finite receiver bandwidths and antenna beamwidths; therefore, the received signal is a phasor summation of multipath components that arrive within the receiver pulse duration and the receiver antenna beamwidth.

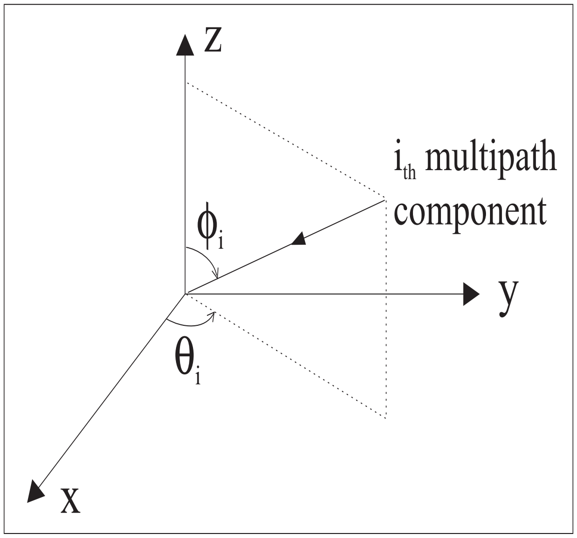

Figure 7: AOA model.

2.2.2 Receiver Bandwidth Consideration

Wideband Systems

In practice, a system is considered wideband [1] if the transmitted signal has a pulse duration less than the relative delay between any two multipath components. In other words, the receiver has a bandwidth wide enough to distinguish each multipath component by its delay. The received signal would be a sequence of multipath components spaced by their TOA. The impulse response of the channel consists of discrete impulses of multipath components as shown in (2.11) and Figure 8.

In wideband systems, the multipath delay times are larger than the pulse duration. Therefore, when data are transmitted, delayed multipath components of one information bit may arrive at the time slots of later information bits, which gives rise to ISI. On the other hand, in a small local area (on the order of 10 squared wavelength), although the phase of each multipath component may change rapidly, the power or envelope of each multipath component does not change significantly. Therefore, in wideband systems, system performance is mainly determined by multipath time

---

[1] It must be mentioned that terminology "wideband" is defined differently in RF circuit design or antenna design, where wideband or narrowband is determined based on the ratio of signal bandwidth with respect to the carrier frequency. For example, a system with a 2 GHz RF bandwidth centered at 60 GHz, operating in a channel with a minimum relative delay larger than 1 ns, will be wideband by the propagation definition, since it can resolve 1 ns of time delay. But it will be narrowband in antenna design terminology, because the bandwidth represents only 3% of the carrier frequency.

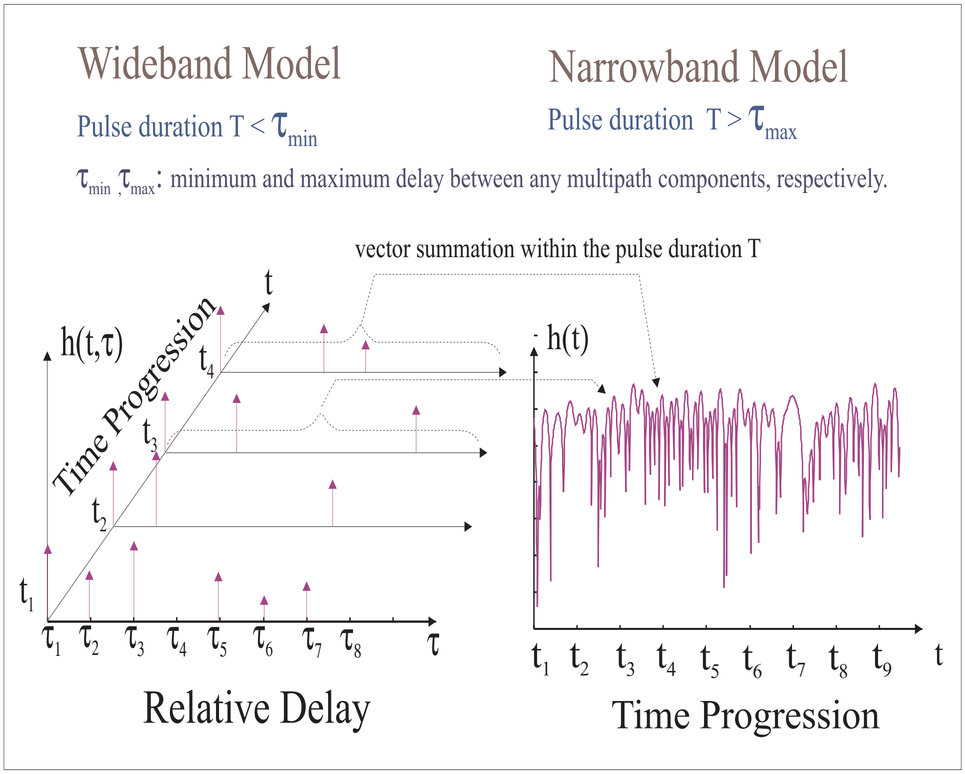

Figure 8: Wideband and narrowband channel models

dispersion.

Wideband Channel Characterization

The wideband RF channel can be described by *power delay profiles* (PDPs), which are plots of relative received power as a function of excess delay with respect to a fixed time delay reference [14]. For the channel impulse response model given in (2.11), the PDP is given by

$$|h_b(\tau)|^2 = \sum_{i=0}^{N-1} |a_i|^2 \delta(\tau - \tau_i) = \sum_{i=0}^{N-1} P_i \delta(\tau - \tau_i) \tag{2.13}$$

where P_i is the power of the ith multipath component.

Most often, parameters such as the total number of multipath components, mean excess delay, root-mean-square (rms) delay spread, and coherent bandwidth are used to describe channel time dispersion [14, 45].

Mean excess delay is the first moment of the PDP and it is defined as

$$\overline{\tau} = \frac{\sum\limits_{k=1}^{N} a_k^2 \tau_k}{\sum\limits_{k=1}^{N} a_k^2} = \frac{\sum\limits_{k=1}^{N} P(\tau_k)\tau_k}{\sum\limits_{k=1}^{N} P(\tau_k)} \tag{2.14}$$

where a_k, τ_k, and $P(\tau_k)$ are the amplitude, delay and power of the kth multipath component, respectively.

The *rms delay spread* is the square root of the second central moment of the power delay profile and is defined as

$$\sigma_\tau = \sqrt{\overline{\tau^2} - \overline{\tau}^2} \tag{2.15}$$

where

$$\overline{\tau^2} = \frac{\sum\limits_{k=1}^{N} a_k^2 \tau_k^2}{\sum\limits_{k=1}^{N} a_k^2} = \frac{\sum\limits_{k=1}^{N} P(\tau_k)\tau_k^2}{\sum\limits_{k=1}^{N} P(\tau_k)} \tag{2.16}$$

Both the delay values and power values in (2.14) to (2.16) are measured relative to the first detectable signal at the receiver.

Coherent bandwidth is a statistical measure of the range of frequencies over which the channel responses have approximately equal gain and linear phase, i.e. the channel responses are correlated [14]. Corelation bandwidth can be measured indirectly from wideband time measurements by taking the Fourier Transform of the average PDP [46], or it can be measured directly from frequency sweeping measurements using VNA. Lee has shown that, as a rule of thumb, the correlation bandwidth with correlation level of 0.9 is related to RMS delay spread by [30]

$$B_c \approx \frac{1}{50\sigma_\tau} \tag{2.17}$$

Narrowband Systems

In narrowband communications systems, the pulse duration is large relative to the channel time delay spread. The received signal is the vector summation of all the multipath components. The narrowband channel model can be achieved by assigning delays to zero in the channel wideband impulse response, resulting in the following

$$h_b(t) = \sum_{i=0}^{N-1} a_i(t) \exp\left[-j\psi_i(t)\right] \tag{2.18}$$

The time variable is added to account for the channel time variations due to the transmitter/receiver motion, or any other changes in the channel.

When adding the multipath components, the enhancement or reduction in the amplitude of the resulting received signal depends on the phase differences of the multipath components. Due to the rapid phase change of each multipath component along the wave propagation path, multipath components interfere with each other constructively and destructively along the receiver path in space. Received signal power not only experience large-scale attenuation due to the increase of distance, but also undergoes rapid fluctuation in a small local area, i.e. *small-scale fading* [47, 48]. Note that small scale fading is the result of the vector summation of the multipath components. Therefore, if the bandwidth of a system is wide enough to resolve each multipath component, the system does not undergo small scale fading. Practical wideband systems have finite bandwidths, and the signal pulse may still contain several multipath components. In this case, the small scale fading behavior of the wideband pulse is determined by the multipath components that arrive within the pulse duration [49].

Narrowband Channel Characterization

In a narrowband system, the received signal power may change rapidly due to small scale fading. Therefore, the received signal power is of major concern.

The distributions of the received signal envelope in small scale fading channels are described by *probability density functions* (PDFs) such as Rician distribution, Rayleigh distribution and TIP (Two-Wave with Incoherent Power) distribution [49, 50, 51]. In [47], Clark proposed a classical model for small-scale fading signal. The received signal is modeled as the vector summation of *coherent field* and *incoherent field* components. The incoherent fields are the results of diffuse scattering, and their phase terms are completely random. The coherent fields are the field components that have constant phase terms, such as the LOS field component and specular reflected field components. When the received signal consists of numerous incoherent field components and none of them has a dominant power, the signal envelope follows the Rayleigh distribution [6, 14, 17, 51]. When received signal is the sum of a strong coherent field component and numerous small incoherent field components, the signal envelope obeys the Rician distribution [50, 52, 53]. The class of PDFs is extended by Durgin to TIP, which describes the envelope of the received signal, consisting of two coherent waves and numerous incoherent waves [49].

Besides signal PDFs, parameters such as average received power, fading depth, level-crossing rate and fade duration are used to describe the power level and rate of change of the received signal [47, 54].

2.2.3 Antenna Beamwidth Consideration

Similar to the fact that a wideband receiver separates multipath components by their TOAs, a narrowbeam antenna allows spatial separation of multipath components by their AOAs. As shown in Figure 9, when the antenna beamwidth increases, the received signal is the vector summation of the multipath components that arrive within the antenna beamwidth.

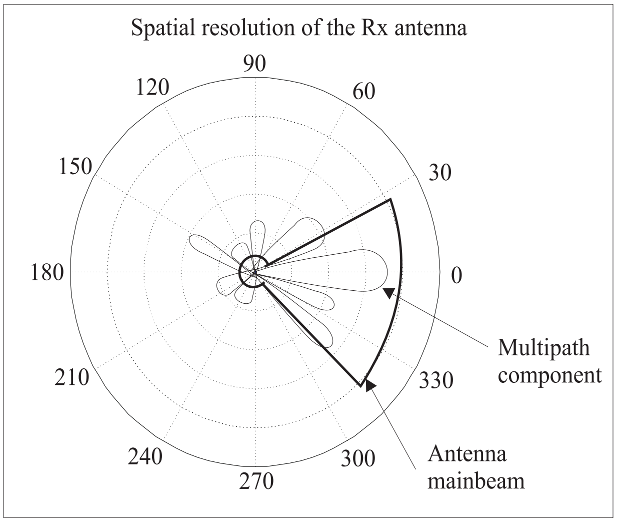

Figure 9: Spatial resolution of the receiver antenna.

For typical terrestial propagation, radio waves arrive at the receiver from azimuthal directions about the horizon [48]. Channel AOA information can be characterized by the angular distribution of the multipath power, $p(\theta)$, where θ is the azimuthal angle in the range of $[0,2\pi]$.

Similar to rms delay spread, angular dispersion is characterized by *rms angular spread*, σ_θ, as following [55]:

$$\sigma_\theta = \sqrt{\overline{\theta^2} - \overline{\theta}^2} \tag{2.19}$$

where

$$\overline{\theta} = \frac{\sum\limits_{k=1}^{N} a_k^2 \theta_k}{\sum\limits_{k=1}^{N} a_k^2} = \frac{\sum\limits_{k=1}^{N} P(\theta_k)\theta_k}{\sum\limits_{k=1}^{N} P(\theta_k)} \tag{2.20}$$

$$\overline{\theta^2} = \frac{\sum\limits_{k=1}^{N} a_k^2 \theta_k^2}{\sum\limits_{k=1}^{N} a_k^2} = \frac{\sum\limits_{k=1}^{N} P(\theta_k)\theta_k^2}{\sum\limits_{k=1}^{N} P(\theta_k)} \tag{2.21}$$

where $a_k, \theta_k, P(\theta_k)$ are amplitude, AOA and power of the kth multipath component, respectively.

An alternative angular spread definition is proposed in [56]. Angular spread, Λ, is defined as following

$$\Lambda = \sqrt{1 - \frac{|F_1|^2}{|F_0|^2}} \tag{2.22}$$

$$F_n = \int\limits_0^{2\pi} p(\theta) \exp(jn\theta) d\theta \tag{2.23}$$

where F_n is the nth complex Fourier coefficient of $p(\theta)$. By this definition, angular spread ranges from 0 to 1, where 0 denotes the extreme case of single multipath component from a single direction, and 1 denotes no clear bias in the angular distribution of the received power [56].

2.3 Summary

This chapter reviews the fundamentals of RF channel characterization. Mathematical models for path loss, multipath time dispersion and angular dispersion are presented. Key channel characterization parameters, including path loss exponent, rms delay spread and angular spread, are defined. The frequency domain (time domain) filtering effects of the receiver bandwidth (signal pulse width), and the spatial filtering effects of antenna beamwidth on the received signal are discussed in detail.

The models and concepts presented in this chapter are essential for the material presented in Chapters 4 through 7 of this work.

Chapter 3

Channel Measurement Techniques and Measurement System Design

Channel measurements are perhaps the most direct method to study radio wave propagation, achieve statistical models and verify propagation theory. Different measurement techniques have been developed to study different aspects of the RF channel. These techniques are generally classified as narrowband techniques and wideband techniques, depending on the bandwidth of the probing signal and the delay spread of the channel. Wideband channel sounding techniques resolve each multipath component and provide time dispersion information of the channel. There are three types of commonly used wideband channel sounding systems: the *direct RF pulse system*, the *vector network analyzer (VNA) measurement system*, and the *spread spectrum sliding correlator system (SCS)*.

This chapter presents a detailed analysis of various measurement techniques. The principle of operation is explained with mathematical models, and implementation issues are discussed with hardware design examples. One narrowband technique and three wideband techniques are discussed in Sections 3.1 through 3.4. A measurement campaign was performed to compare the frequency-domain technique using a VNA and the time-domain technique using a SCS. The results are presented in Section 3.5. An error analysis on the time measurements of a SCS due to the clock frequency offset is presented in Appendix B. Finally, a 38 GHz channel sounding system used in this research is described in Section 3.6.

3.1 Narrowband Techniques

3.1.1 Principle of Operation

Narrowband techniques are used to measure path loss, narrowband fading and channel Doppler spread. The main advantages of the narrowband measurement technique are its simplicity and high sampling rate as compared to wideband measurement systems.

In narrowband techniques, a continuous wave (CW) signal with known power is transmitted. Received signal power is measured over space or time. In mobile applications, small-scale signal fading is studied by moving the transmitter or receiver in a *small local area* (a few square wavelengths) and recording the received power continuously. Path loss is studied by measuring the average received power over a large number of local areas, where the local areas span several decades of distance from the transmitter [14, 54]. In fixed point-to-point/multipoint applications, the average received power and signal variation is studied over *short-term time intervals*, where the channel variation is stationary. For example, in Chapter 5, the short-term signal variation during rain is analyzed over 2-3 minute intervals of constant rain rates.

Narrowband techniques have certain advantages for channel Doppler measurements. Motion of the transmitter, receiver, or objects in the channel cause received signal variation in the time domain and Doppler frequency shift in the frequency domain. Channel variation is studied by sampling the received signal power at a rate at least twice as high as the maximum Doppler frequency. A narrowband measurement system samples the channel at a single frequency; therefore, its sampling rate can be much higher than the sampling rate of a wideband measurement system. As shown in Sections 3.3 and 3.4, the sampling rate of a wideband system is limited due to the long sweep time over a wide bandwidth for a VNA system, or long repetition time between two consecutive correlation peaks for a SCS system.

The disadvantage of the narrowband technique is that the received signal represents only the envelope of the vector summation of the multipath components; no direct quantitative multipath information is available. When a high bandwidth signal is used, wideband measurement techniques must be employed to estimate the channel time dispersion.

3.1.2 Implementations of Narrowband Measurement Systems

In this section, narrowband signal power measurements and hardware design issues are discussed based on a measurement campaign performed at 5.8 GHz for path loss and building penetration loss measurements [2, 3, 57, 58, 59].

The CW measurement system diagram is presented in Figure 10. The transmitter consists of a synthesized sweeper, an amplifier, and a discone antenna. Since the measurements were made with transmitter height of 5.5m, the setup required a 6m coaxial cable to connect the ground-based signal generator with the mast-mounted antenna. These long coaxial cables have significant loss at 5.85 GHz . Measurements show that losses in the 6m coaxial cables used in this experiment campaign range from 7 to 9 dB . In order to achieve the maximum transmitted power, the amplifier was placed on the top of the mast and connected to the antenna via a short cable with negligible loss. This allows as much as 30 dBm of power to be sent directly into the transmitter antenna, which is the maximum output power of the amplifier.

The received signal is passed through two stages of filtering and amplification separated by a step attenuator. A five pole interdigital BPF and a Mini-circuit ZVE-8G amplifier are used in the first stage. They are attached to the top of the mast to filter and preamplify the signal in order to reduce the noise figure and overcome the loss in the long connection cable. The band pass filter was used as a precaution to keep out-of-band signals from penetrating the amplifier. The attenuator has an attenuation ranging from 0 dB to 70 dB in 10 dB steps. It is used between the amplifiers to assure the appropriate signal power levels at the input and the output of the amplifiers. The two stages of amplification are designed to reduce the influence of high detector noise figure induced by the spectrum analyzer, which is 32 dB .

In order to record the signal strength over a period of time, the spectrum analyzer is set to zero span mode and the voltages of the Y-axis, which are proportional to the signal power, are saved through a GPIB board into a laptop computer for later analysis. Figure 11 shows five seconds of

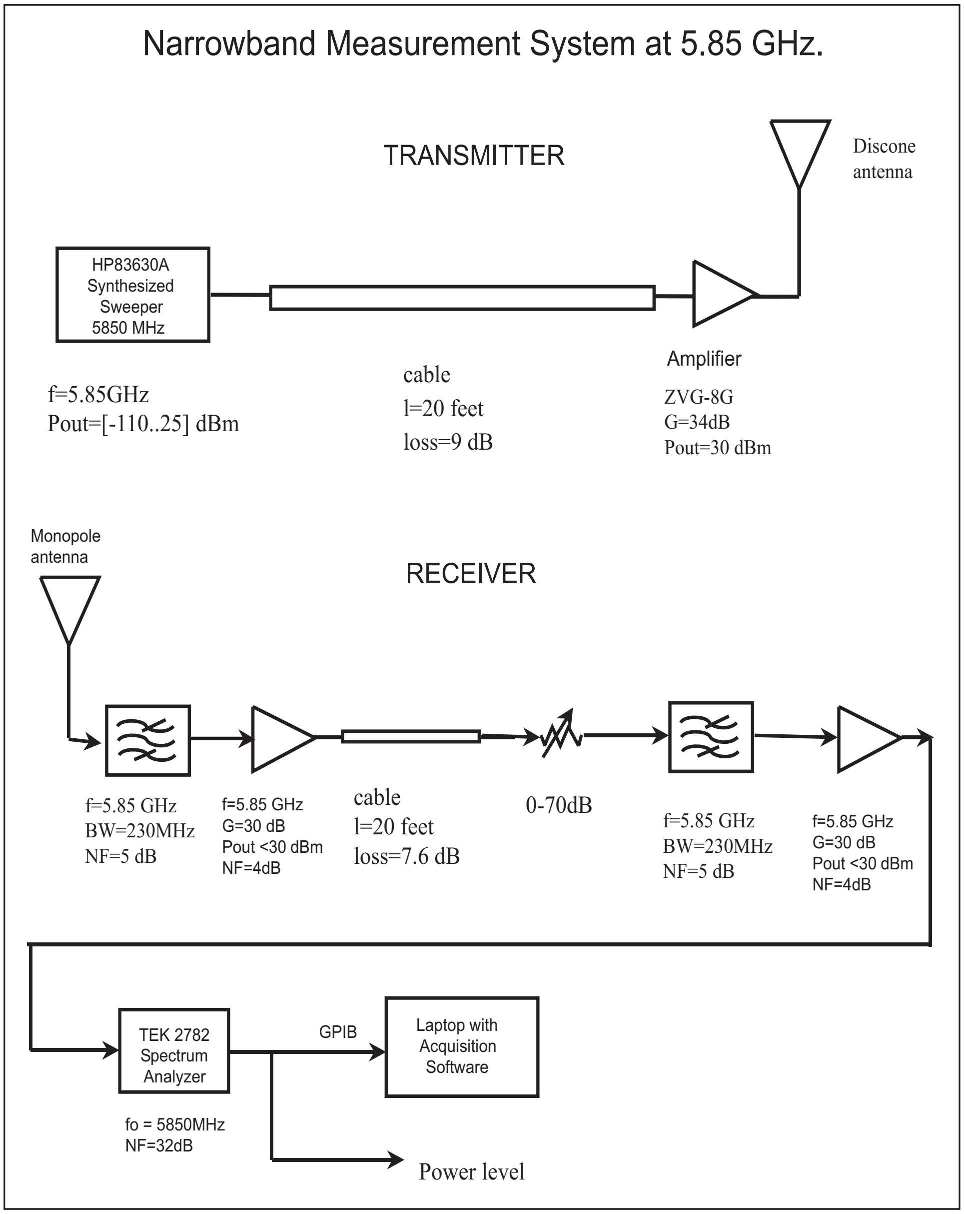

Figure 10: Block diagram of the CW measurement system at 5.85 GHz [3].

CW power data taken as the receiver is moved around in a local area. The linear average of the received power is used for the path loss calculation.

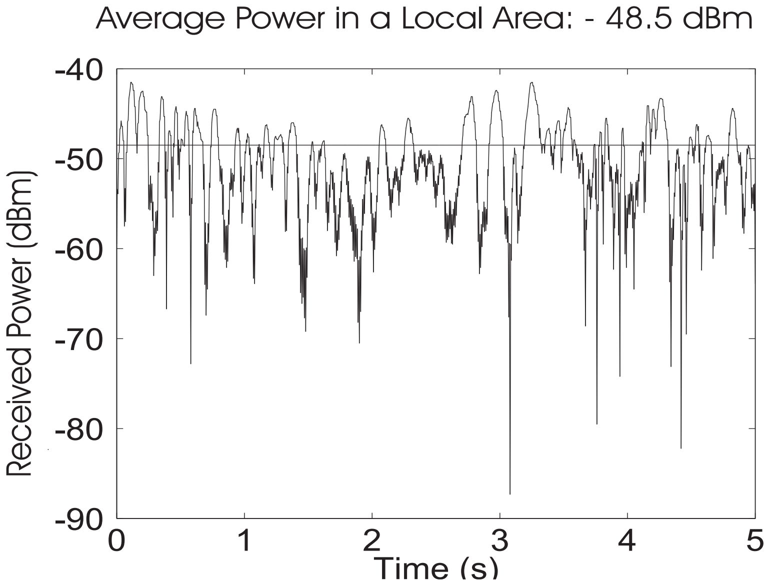

Figure 11: Five seconds of CW power data taken in a local area [3].

3.2 Direct RF Pulse System

In direct RF pulse systems, a probing RF pulse with very short duration T_c is transmitted periodically with a period of T_p. The operation of the direct pulse system is shown in Figure 12.

As shown in Section 2.2, the RF channel can be modeled as a linear system with a baseband impulse response, $h_b(t)$ [1]. The received baseband signal, $y(t)$, is related to the transmitted baseband signal, $x(t)$, by

$$y(t) = h_b(t) * x(t) = \int_{-\infty}^{\infty} h_b(\eta) x(t-\eta)\, d\eta \tag{3.25}$$

where * denotes convolution of two functions.

---

[1] The bandpass impulse response, $h(t)$, is related to the baseband impulse response, $h_b(t)$, as [31]

$$h(t) = 2\mathrm{Re}\{h_b(t)\exp(j\omega t)\} \tag{3.24}$$

where $\mathrm{Re}(x)$ denotes the real part of x, and ω is the carrier frequency.

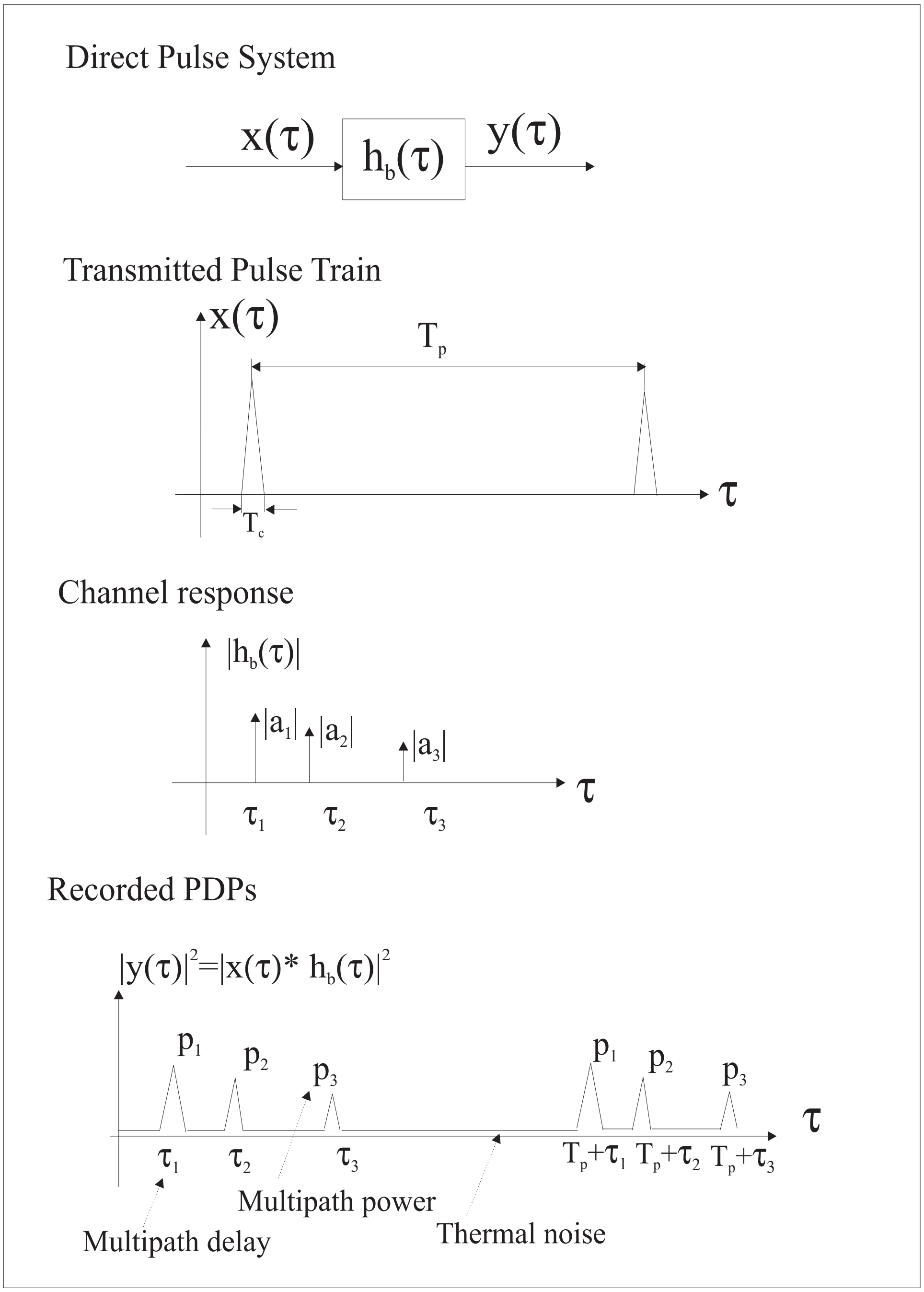

Figure 12: Principle of operation of a direct RF pulse system.

Recall from (2.11) that h_b is given as :

$$h_b(\tau) = \sum_{i=0}^{N-1} a_i \exp(-j\psi_i)\delta(\tau - \tau_i)$$

Substituting (2.11) into (3.25), we can express $y(t)$ as:

$$y(t) = \sum_{i=0}^{N-1} a_i \exp(-j\psi_i)x(\tau - \tau_i) \tag{3.26}$$

If the pulse duration is much shorter than the multipath delay in the channel, then the received signal power is given by

$$|y(t)|^2 = \sum_{i=0}^{N-1} |a_i|^2 |x(\tau - \tau_i)|^2 = \sum_{i=0}^{N-1} P_i \; |x(\tau - \tau_i)|^2 \tag{3.27}$$

where P_i is the power of each multipath component.

In the recorded PDP, each pulse corresponds to a multipath component of the channel, with the same relative delay and power proportional to the multipath power. Furthermore, in order for the direct RF pulse system to correctly measure each multipath component, the following conditions must be satisfied:

- In order to distinguish each multipath component, the pulse duration T_c must be less than the minimum relative delay between any two multipath components. Recorded multipath pulses will overlap if they arrive at relative delays less than T_c. This pulse duration determines the measurement system *time resolution.*
- The period T_p must exceed the maximum delay of any multipath. This period T_p determines the maximum measurable range without ambiguity, or *unambiguous range* of the measurement system.
- Since the transmitted pulse has a constant amplitude and duration, its effect can be calibrated out. Then the recorded $y(t)$ and $|y(t)|^2$ provide accurate estimates of the channel impulse response and PDP, respectively.

The advantage of the direct pulse system is its simple realization and quick determination of the PDP. The disadvantage is that, due to the short pulse duration (wide bandwidth), a wideband receiver is necessary. Since only wideband filters are used in the transmitter and receiver, this system suffers from interference and noise, which limits its dynamic range. Also, the pulse system triggers the oscilloscope on the first arriving signal. If the LOS signal is not higher than the threshold, the system will trigger on the next multipath component that exceeds the threshold and cause measurement error [14]. Therefore, VNA or SCS channel sounding methods are more frequently used for wideband measurements.

3.3 VNA Measurement System

3.3.1 Principle of Operation

Because of the dual relationship between the time and frequency domain representations, the multipath channel can also be fully described by the complex frequency response, $H(f)$, which is the Fourier transform of the bandpass channel impulse response $h(t)$ [60]. The complex frequency response can be measured by comparing the transmitted signal, $X(\omega)$, and the received signal, $Y(\omega)$, in the frequency domain as

$$H(\omega) = \frac{Y(\omega)}{X(\omega)} \tag{3.28}$$

In a VNA channel sounding system, a synthesized frequency sweeper is used to sweep through a chosen RF bandwidth of B_{sw} with a frequency step of Δf. The channel complex frequency response is achieve by comparing $Y(\omega)$ and $X(\omega)$ over bandwidth B_{sw}. Based on the Fourier analysis, the finite sweeping bandwidth B_{sw} in the passband corresponds to a pulse with a duration of $2/B_{sw}$, and the discrete frequency spacing Δf corresponds to a repetitive signal with a period of $1/\Delta f$ in the time domain. Thus, the frequency domain measurements are equivalent to time domain measurements using a periodic pulse train with $T_c = 2/B_{sw}$ and $T_p = 1/\Delta f$. Figure 13 shows graphically the dual nature of the frequency and time domain techniques.

Although the VNA measurement system is the frequency-domain dual of the direct RF pulse system, it has several advantages. The VNA system measures the channel response at one tone at a time; therefore, narrowband filters, which tune in step with the transmitted tones, can be used to reject out-of-band interference and noise, and effectively increase the receiver dynamic range.

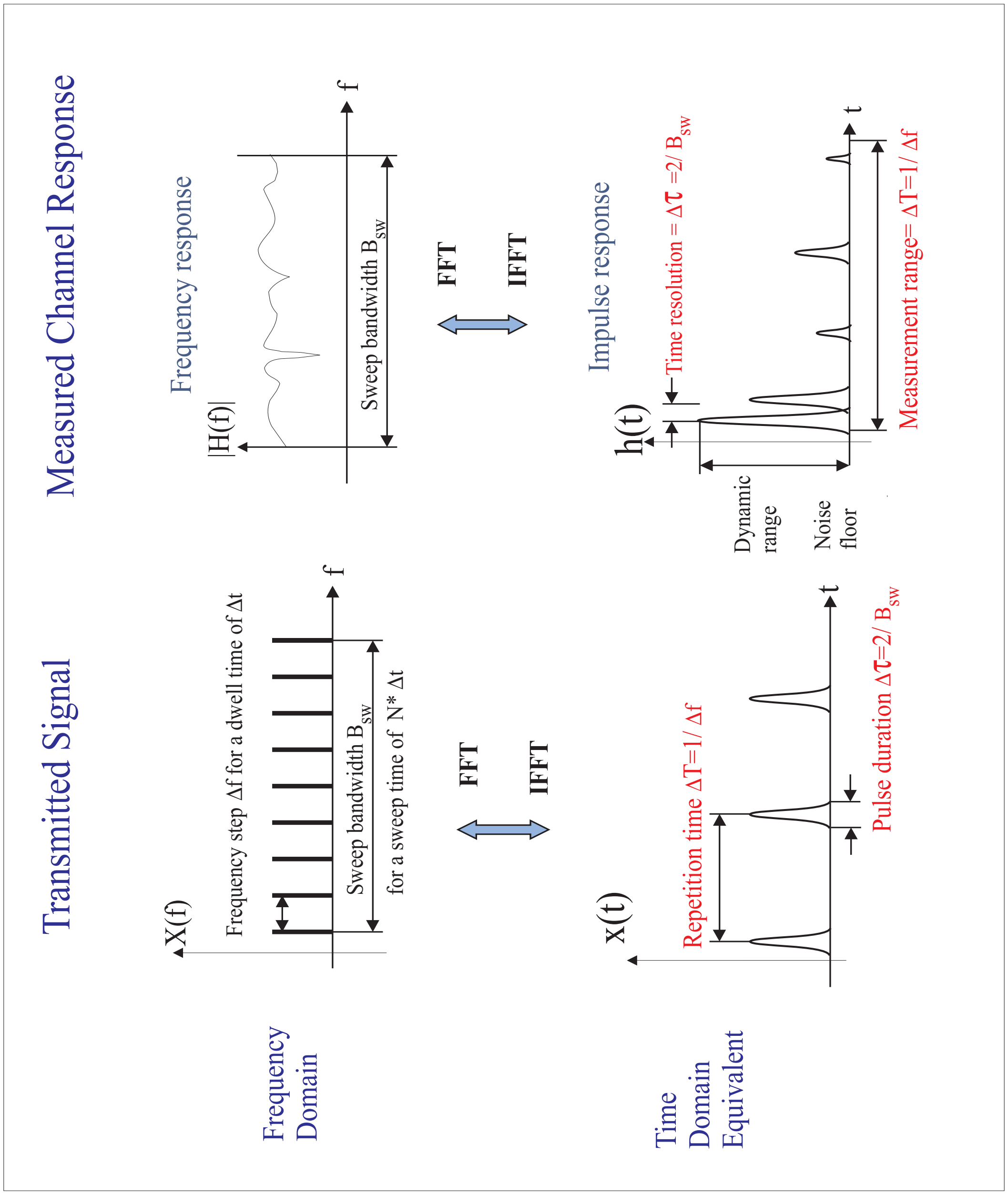

Figure 13: The duality of channel characterization in the frequency domain and the time domain.

Furthermore, the VNA provides the frequency domain and time domain channel responses with both amplitude and phase. The disadvantage of the VNA is that it requires the channel be linear time-invariant during the complete frequency sweep. VNA sweeps the channel at discrete frequency tones to achieve frequency response over the bandwidth B_{sw}. This decomposition is valid only for a time-invariant channel. Also, the necessity of phase measurements and synchronized sweeping requires hardware connection between the transmitter and receiver, which limits the VNA to short-range outdoor and, mainly, indoor operation. For long-range outdoor measurements, the SCS can be used.

3.3.2 Implementation of VNA Measurement Systems

Figure 14 presents the diagram of a VNA channel sounding system. This system was used in the measurement campaign for the performance comparison with the SCS [61].

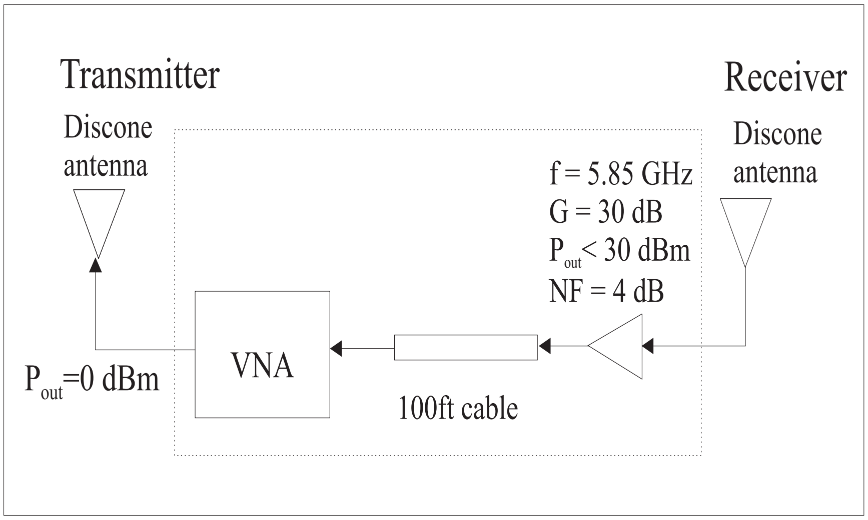

Figure 14: Block-diagram of VNA channel sounding system.

As shown in Figure 14, a 100-foot Heliax coaxial cable was used to connect the transmitter and the receiver for the phase measurements. A 30 dB gain amplifier was included at the receiver to overcome the loss in the cable. Calibration standards are used to effectively bring the source RF port of the VNA up to the transmitting antenna input connector and the receive RF port of the VNA to the receiving antenna output connector. Then the measured complex transmission coefficient includes only the effects of the RF channel and the antenna gains. The antenna gain can be then measured and calibrated out.

Parameters of the VNA must be chosen based on the measurement requirements. These parameters are sweep bandwidth, step size, and sweep time.

- The sweep bandwidth, B_{sw}, is chosen based on the desired measurement time resolution Δt by

  $$B_{sw} = 2/\Delta t \tag{3.29}$$

  For example, to measure the channel impulse response with a resolution of 10 ns , B_{sw} should be approximately 200 MHz .

- Frequency step, Δf, determines the unambiguous period of the measurement without aliasing by

  $$T_p = 1/\Delta f \tag{3.30}$$

  For example, if the channel maximum delay is less than 1 ms, then the maximum frequency step is 1 kHz in order to capture all the multipath components within the unambiguous range. Also, the frequency step is related to the sweep bandwidth and the total number of data points, N, by

  $$\Delta f = B_{sw}/N \tag{3.31}$$

  For a given B_{sw}, a smaller step size results in a larger unambiguous range, but more data points and more measurement time.

- The sweep time needs to be chosen such that the channel remains time-invariant during the entire sweep. For example, the Anritsu 37369A VNA used for the measurements in [61] takes approximately one second to step through 1200 frequencies, which requires the channel be stationary for one second. The sweep time of the VNA is related to the sweeping bandwidth, number of data points and the calibration methods. There is a basic tradeoff among measurement resolution, ambiguous range and measurement speed. Better resolution or longer unambiguous range results in longer sweep time.

3.4 SCS Measurement System

3.4.1 Correlation Method

In a SCS channel sounding system, a correlation method is used for system identification. Spectrum analysis shows that for stochastic processes, the Power Spectrum Density (PSD) of the output signal, $S_{yy}(\omega)$, is related to the PSD of the input signal, $S_{xx}(\omega)$, by the frequency response of the linear system, $H(\omega)$, as following

$$S_{yy}(\omega) = |H(\omega)|^2 S_{xx}(\omega) \tag{3.32}$$

Furthermore, the relationship between the cross-power spectrum, $S_{xy}(\omega)$, and $S_{xx}(\omega)$ is given by [62]

$$S_{xy}(\omega) = H^*(\omega) S_{xx}(\omega) \tag{3.33}$$

where $H^*(\omega)$ is the complex conjugate of the system frequency response.

By definition, the PSD of a stochastic process, $S_{xx}(\omega)$, is the Fourier transform of its autocorrelation function, $R_{xx}(t)$; and the cross-power spectrum of two signal, $S_{xy}(\omega)$, is the Fourier transform of their cross-correlation $R_{xy}(t)$. Therefore, the inverse Fourier transform of (3.33) leads to the following

$$R_{xy}(\tau) = R_{xx}(\tau) * h^*(-\tau) \tag{3.34}$$

If the input of the system is a white-noise process, $w(t)$, with autocorrelation of

$$R_{ww} = \delta(t) \tag{3.35}$$

then the output is

$$R_{yw}(\tau) = R_{wy}(-\tau) = \delta(t) * h^*(\tau) = h^*(\tau) \tag{3.36}$$

For real processes, $h^*(t) = h(t)$, and system impulse response can be estimated by the cross-correlation of the input white noise signal with the output signal.

3.4.2 Properties of PN Sequence

In a practical spread spectrum system, the white noise signal is approximated by a pseudo-noise (PN) sequence. A PN sequence is a deterministic sequence of -1 and 1 with noise-like autocorrelation properties. One of the most widely used PN sequences is the maximum-length shift-register sequence (or *m-sequence* for short), which can be produced using cascaded shift-register stages with linear feedback loops [63]. When k stages of shift-registers are used, the m-sequence code length is given by $N = 2^k - 1$.

Let $n(t)$ represents a periodic PN signal made of a m-sequence with a code length of N and chip duration of T_c. The period of $n(t)$ is $T_p = NT_c$. The PN sequence $n(t)$ and its autocorrelation is presented in Figure 15.

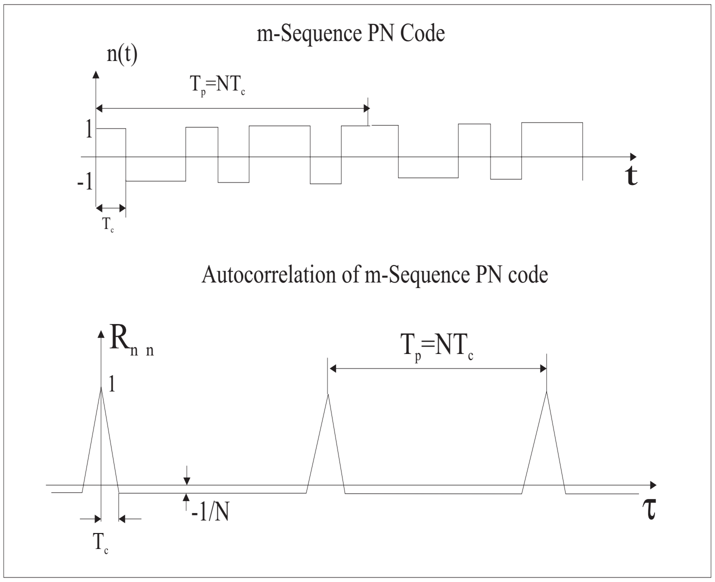

Figure 15: M-sequence PN code and its autocorrelation.

The autocorrelation of the PN sequence is a periodic pulse train with a period of T_p and pulse duration of $2T_c$. In each period, the autocorrelation of $n(t)$ is given by [64]

$$R_{nn}(\tau) = \begin{cases} 1 - \frac{1+1/N}{T_c}\tau & \text{for} \quad 0 \leq \tau < T_c \\ -1/N & \text{for} \quad T_c \leq \tau < T_p - T_c \\ 1 + \frac{1+1/N}{T_c}(\tau - T_p) & \text{for} \quad T_b - T_c \leq \tau < T_p \end{cases} \tag{3.37}$$

3.4.3 Mathematical Models of SCS Channel Sounding

A baseband model for the SCS is demonstrated in Figure 16 [45, 64]. A known transmitter PN sequence, $n_t(t)$, is sent through the channel with a baseband channel impulse response of $h_b(t)$. The received signal $y(t)$ is multiplied with the receiver PN sequence and then integrated over a period of T. The power of $z(t)$ is recorded as the measured PDP of the channel. In a SCS, the receiver PN sequence has a different clock rate from the transmitter clock rate. As a starting point, we first study the case where both PN sequences have the same clock rates.

Correlation method with the same PN clock rates

The received signal y(t) is given by the convolution of h_b and n_t:

$$y(t) = h_b(t) * n_t(t) = \int_{-\infty}^{\infty} h_b(\zeta) n_t(t - \zeta)\, d\zeta \tag{3.38}$$

At the receiver, correlation of $y(t)$ and the receiver PN sequence $n_r(t-\tau)$ is performed by multiplication (a mixer) and integration (a narrowband filter). This correlation is calculated for any delay values, τ, between the received signal y(t) and the receiver PN sequence. The resulting signal $z(t)$ is given by

$$z(\tau) = \frac{1}{T}\int_{0}^{T} y(t) n_r(t - \tau)\, dt \tag{3.39}$$

Substituting (3.38) into (3.39), we can express the received signal $z(\tau)$ as

$$z(\tau) \quad = \quad \frac{1}{T}\int_{0}^{T} \left\{ \int_{-\infty}^{\infty} h_b(\zeta) n_t(t - \zeta) d\zeta \right\} n_r(t - \tau)\, dt \tag{3.40}$$

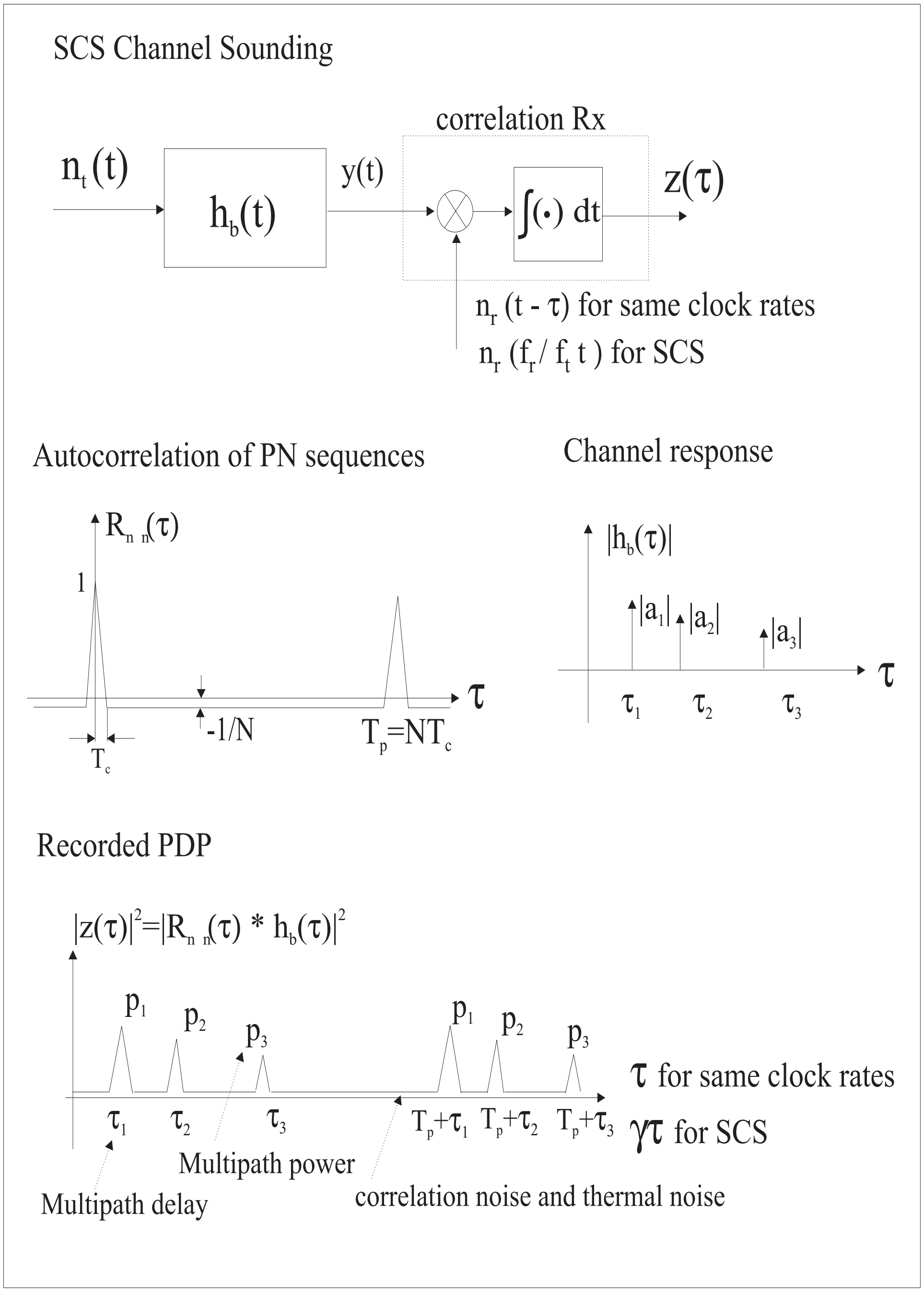

Figure 16: Mathematical models of SCS channel sounding.

$$= \int_{-\infty}^{\infty} h_b(\zeta) \left\{ \frac{1}{T} \int_{0}^{T} n_t(t-\zeta) n_r(t-\tau) dt \right\} d\zeta \tag{3.41}$$

$$= \int_{-\infty}^{\infty} h_b(\zeta) R_{tr}(\tau-\zeta)\, d\zeta \tag{3.42}$$

$$= h_b(\tau) * R_{tr}(\tau) \tag{3.43}$$

where R_{tr} represents the correlation [2] of the transmitter and receiver PN sequences, given by

$$R_{tr}(\tau-\zeta) = \frac{1}{T} \int_{0}^{T} n_t(t-\zeta) n_r(t-\tau)\, dt \tag{3.44}$$

When the transmitter and receiver PN sequences are identical and have the same clock speed, this correlation is the autocorrelation of a PN sequence given by (3.37).

Applying the channel impulse response model from (2.11) to (3.43), we will have the output signal as follows

$$z(\tau) = h_b(\tau) * R_{tr}(\tau) \tag{3.45}$$

$$= \sum_{i=0}^{N-1} a_i \exp(-j\psi_i) \delta(\tau-\tau_i) * R_{tr}(\tau) \tag{3.46}$$

$$= \sum_{i=0}^{N-1} a_i \exp(-j\psi_i) R_{tr}(\tau-\tau_i) \tag{3.47}$$

The power of the output signal is given by

$$|z(\tau)|^2 = \sum_{i=0}^{N-1} |a_i|^2 R_{tr}^2(\tau-\tau_i) \tag{3.48}$$

$$|z(\tau)|^2 = \sum_{i=0}^{N-1} P_i R_{tr}^2(\tau-\tau_i) \tag{3.49}$$

Figure 16 and (3.49) clearly show the similarity between the direct RF pulse channel sounding technique and the SCS technique. The output signal of a SCS is a periodic pulse train with the period of T_p and pulse width of $2T_c$. Each pulse records the delay and power of a multipath component of the channel. Similar to the direct pulse system, the following conditions must be satisfied for the SCS operation:

---

[2] In general, correlation of two functions x(t) and y(t) is given by $R_{xy}(t_1,t_2) = \frac{1}{T}\int_0^T x(t_1)y^*(t_2)\, dt$, where $y^*(t)$ is the complex conjugate of $y(t)$. Since n_t and n_r are both real functions, their complex conjugates are the same as the functions.

- The chip duration T_c determines the measurement system time resolution. It must be less than the relative delay between two multipath components in order to distinguish them.
- The period T_p must exceed the maximum delay of any multipath. This period T_p determines unambiguous range of the SCS. For example, the measurement system used in this research uses PN code generated from 11 stage shift-registers. The maximum code length is $2^{11} - 1 = 2047$. With a chip duration of 10 ns , this results in a period of $T_p = 20.47\mu s$ and an unambiguous range of 6.14 km. This is much larger than typical multipath pathlength.
- In practical systems, the PN sequence does not have a unit amplitude. Consequently, the recorded signal, $|z(\tau)|^2$, is weighted by the power of the correlation peak. This value can be estimated in the *back-to-back calibration*, where the transmitter and receiver are connected through a coaxial cable with known loss and delay. By comparing the transmitted and recorded signal power, the pulse amplitude, as well as other system losses can be calibrated out.

Sliding Correlation

The above discussion is based on the assumption that the receiver PN sequence can be shifted by any delay of τ relative to the transmitter PN sequence. This is possible when the correlation is performed by digital signal processing (DSP). Alternatively, in a sliding correlator system, the shift of n_t relative to n_r is accomplished by using slightly different clock rates for these two PN sequences [45]. The transmitter has a PN clock rate of f_t and the receiver has a slower clock rate of f_r. This slight difference in the chip rates $f_s = f_t - f_r$, i.e. the *frequency offset*, results in the “sliding” of one sequence with respect to the other. For the sliding correlation, the receiver PN sequence can be represented as [64]

$$n_r(t) = n_r(\frac{f_t - f_s}{f_t}t) \tag{3.50}$$

The output signal of the SCS $z_{scs}(\tau)$ is given by

$$\begin{aligned} z_{scs}(t) &= \frac{1}{T}\int_0^T y(t)\, n_r(\frac{f_t - f_s}{f_t}t)\, dt && (3.51) \\ &= \frac{1}{T}\int_0^T \{h_b(t) * n_t(t)\}\;\; n_r(\frac{f_t - f_s}{f_t}t)\, dt && (3.52) \end{aligned}$$

$$= \frac{1}{T}\int_0^T \left\{ \int_{-\infty}^{\infty} h_b(\zeta) n_t(t-\zeta)\,d\zeta \right\} n_r(\frac{f_t - f_s}{f_t}t)\,dt \tag{3.53}$$

$$= \int_{-\infty}^{\infty} h_b(\zeta) \left\{ \frac{1}{T}\int_0^T n_t(t-\zeta)\,n_r(\frac{f_t - f_s}{f_t}t)\,dt \right\} d\zeta \tag{3.54}$$

$$\approx \int_{-\infty}^{\infty} h_b(\zeta) R_{tr}(\frac{f_s}{f_t}t - \zeta)\,d\zeta \tag{3.55}$$

$$= \int_{-\infty}^{\infty} \left\{ \sum_{i=0}^{N-1} a_i \exp(-j\psi_i)\delta(\tau - \tau_i) \right\} R_{tr}(\frac{f_s}{f_t}t - \zeta)\,d\zeta \tag{3.56}$$

$$= \sum_{i=0}^{N-1} a_i \exp(-j\psi_i) R_{tr}(\frac{f_s}{f_t}t - \tau_i) \tag{3.57}$$

Note that the transition from (3.54) to (3.55) is approximate. The frequency offset must be small enough in order not to destroy the cross-correlation properties of $n_t(t)$ and $n_r(t)$ [45, 65]. The ratio between the f_t and f_s is defined as the *slip rate*, $\gamma = f_t/f_s$. The higher the slip rate, the lower the frequency offset. Typical values of sliding factor range from 1000 to 10,000 [45].

The recorded PDP from the SCS has the following form

$$|z_{scs}(t)|^2 = \sum_{i=0}^{N-1} P_i R_{tr}^2(\frac{f_s}{f_t}t - \tau_i) \tag{3.58}$$

Note that (3.58) is very similar to (3.27) for direct pulse measurements, and to (3.49) for correlation measurements with identical clock rates. The only difference is the time dependence. The SCS scales time by the slip rate γ. If the absolute propagation time of a multipath component is τ, then a correlation peak will occur at the observation time t, where

$$\frac{f_s}{f_t}t - \tau = 0 \tag{3.59}$$

$$t = \tau\gamma \tag{3.60}$$

As shown in Figure 16, for SCS, the observation time is scaled by γ according to (3.60).

3.4.4 Implementation of SCS

Figure 17 presents block diagrams of the transmitter and receiver of a SCS channel sounding system [61, 66, 67]. This system was used in the wideband channel measurement campaign at 5.85 GHz [61].

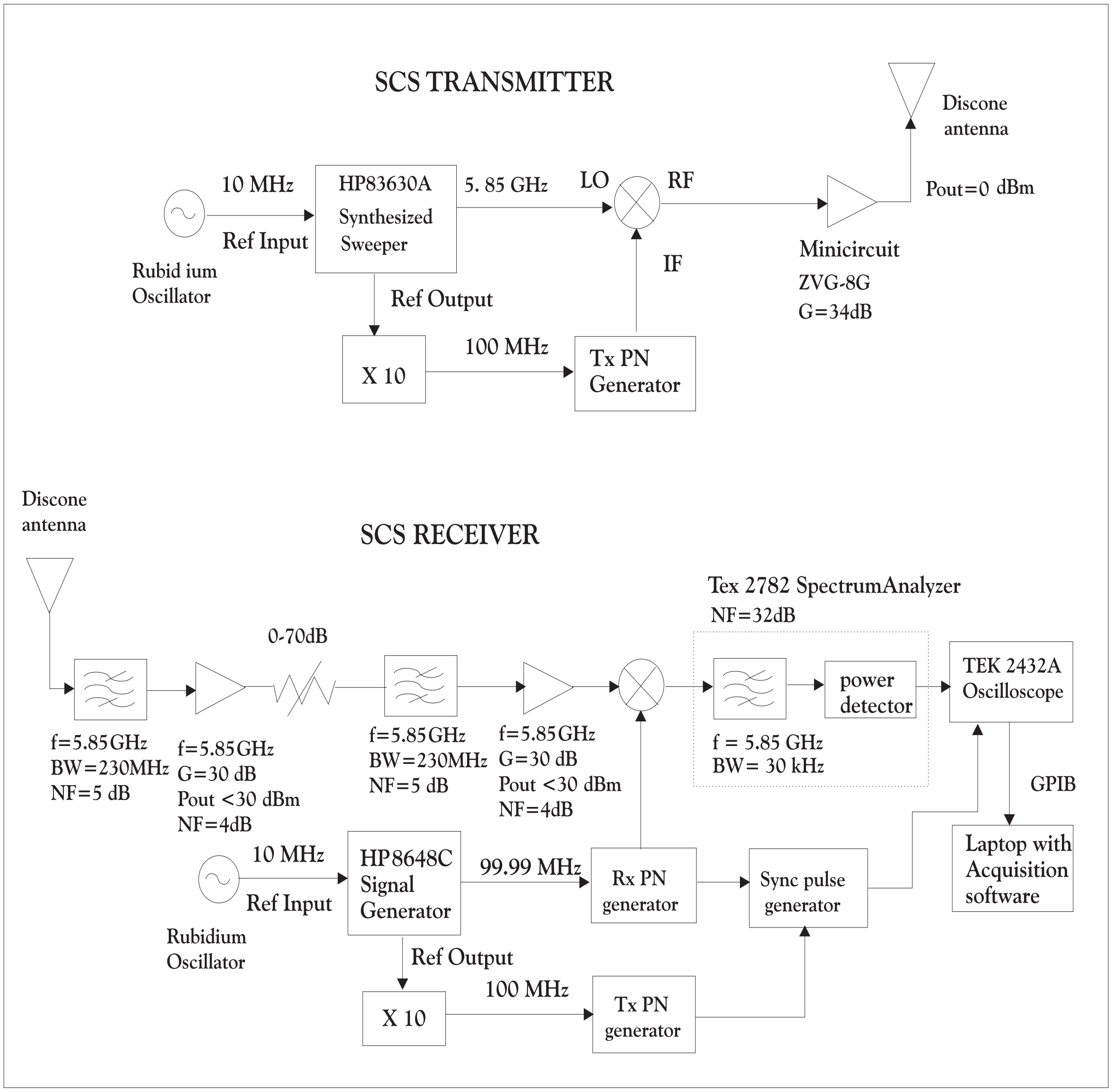

Figure 17: Block diagram of the SCS hardware configured at 5.85 GHz with a clock rate of 100 MHz and a slip rate of 10,000.

The PN sequence is up-converted by the mixer to the desired carrier frequency of 5.85 GHz . A 34 dB gain power amplifier is used to overcome the path loss in the channel. Rubidium clocks are used in the transmitter and receiver to provide precise frequency standards for PN generators and the frequency synthesizers.

At the receiver, two stages of filtering and amplifications are performed in order to reject out-of-band spurious signals and to achieve high dynamic range. An attenuator serves as a gain control to manually adjust the received signal power level. The correlation between the received signal and the receiver PN sequence is performed by a mixer followed by a narrowband RF filter. A spectrum analyzer set in the zero-span mode serves as both a down-converter and an envelope detector. The oscilloscope displays the video output of the spectrum analyzer, which is proportional to the received signal power in dB. The purpose of using an oscilloscope is to provide triggering and different time and power scales to view the recorded channel response. The displayed data are saved into a laptop computer through a GPIB board for further processing. Careful calibration procedures are performed to establish the exact relationship between the recorded voltage and time with the actual multipath power and delay.

3.4.5 Analysis of the Time Measurement Accuracy

One major advantage of the SCS over VNA is that the SCS can operate without a hardwire connection between the transmitter and receiver. However, this separation requires transmitter and receiver PN generators to be referenced to different frequency oscillators. The accuracy of the rubidium oscillators directly determines the time measurement accuracy of the SCS. Before each measurement campaign, the rubidium oscillators must be adjusted to be as close in frequency as possible. Even so, when they are separated, the frequencies will inevitably drift slowly apart. This frequency offset results in a continuous time axis shift in the measured multipath, as shown in Figure 18. By calibrating the SCS system before and after a set of channel sounding measurements, this drift can be accounted for and removed from the results. A detailed analysis of the effect of the oscillator frequency offset can be found in the Appendix B.

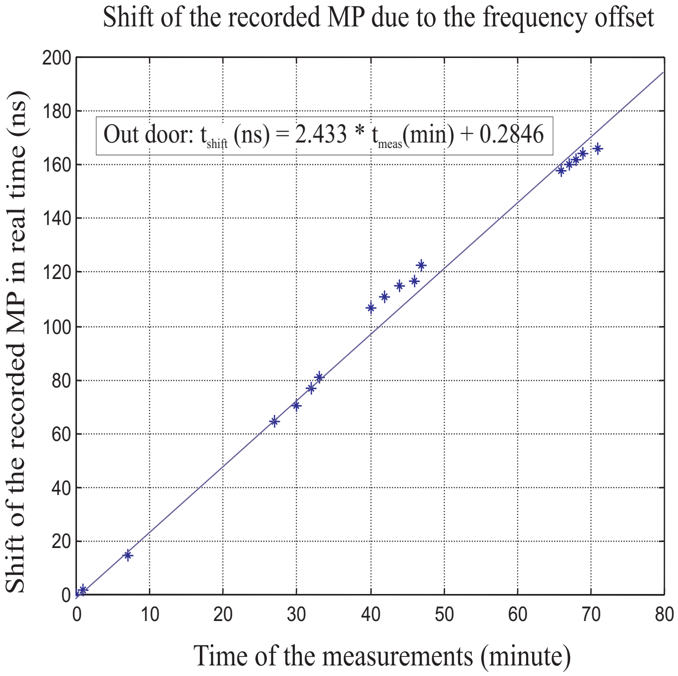

Figure 18: Shift of the recorded PDP due to the frequency offset.

3.5 Measurements Comparing VNA and SCS

To date, wideband channel measurement campaigns that have been reported use time domain measurement techniques [10, 41, 45, 46, 68, 69, 70, 71, 72, 73] or frequency domain techniques [11, 12, 18, 43]. Fourier transform theory guarantees that these two techniques should produce identical results, but there has been little literature on research to carefully compare these two measurement techniques. This section presents a direct comparison of frequency domain channel sounding using VNA and time domain channel sounding using SCS at 5.85 GHz.

A measurement campaign was designed to compare the performance of the two systems in identical environments. The measurements were performed at HRL Laboratories at Malibu, CA in August 1997. The system hardware is presented in Figure 19. Two synchronized electronic switches allowed the antennas to be time shared between the VNA and the SCS so that comparative measurements could be made rapidly for minimum channel variations.

Two indoor sites and one outdoor site were used to measure delay spread and path loss of the multipath channels. Comparison of results demonstrated the duality between both measurement

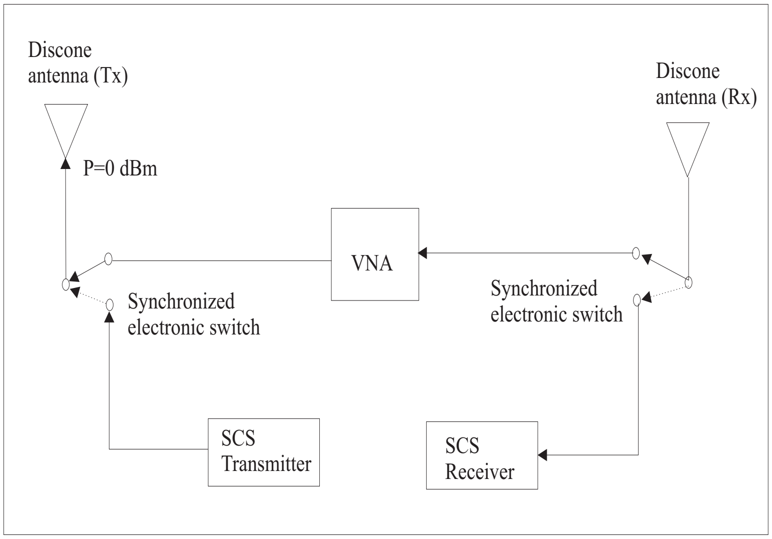

Figure 19: The combined system for SCS and VNA comparison.

techniques. The ultimate choice of measurement technique will depend on the measurement requirements and the propagation environments.

3.5.1 System Settings

The measurement parameters for both systems were chosen to be as close as possible. The parameters used in the measurement campaign for both methods are listed in Table 1.

As shown in Table 1, both systems have a center frequency of 5.85 GHz . The sweep bandwidth of the VNA is chosen 230 MHz , which is the same as the bandwidth of bandpass filters in the SCS. This results in 10 ns and 8.7 ns time resolution of these systems. An average of eight wave forms are taken to reduce the noise and possible channel transient caused by the moving objects. In Table 1, the 35 dB is the display dynamic range of the SCS, which is determined by the correlation noise of the PN sequences. The detectable signal dynamic range is close to 65 dB due to the adjustable gain control by the step attenuator in the receiver. Note that the VNA has a slower measurement speed than the SCS due to the frequency sweep. The number of data points of VNA is chosen to be half of the number of SCS to increase the measurement speed of VNA. The display ranges of the SCS and VNA are determined by the time scale of the oscilloscope and VNA, respectively. A 600

Table 1: System Settings of the SCS and VNAS.

	SCS	VNA
center frequency	5.85 GHz	5.85 GHz
passband bandwidth	200 MHz	230 MHz
resolution	10 ns	8.7 ns
averaging	8 times	8 times
dynamic range	35 dB	80 dB
measurement speed	1.6 s/PDP	4 s/PDP
number of samples	1024	401
display range	600 m	552 m

m distance corresponds to a 2000 ns of delay. For short-distance outdoor and indoor environments, this is much larger than the maximum excess delays typically measured, which are from 10 to several hundred ns [14].

3.5.2 Measurement Results

Three typical sites at HRL Laboratories were chosen for the outdoor and indoor measurements. The outdoor site was a lawn of approximately 35 × 35 m, the two indoor sites included an 8 × 10 m conference room, and a 3 × 50 m hallway. Care was taken to ensure that there were no people walking around during the measurement to achieve a static channel. Detailed site information is presented in Appendix A.

The data profiles were compared on a location-by-location basis in terms of amplitudes and arrival times of individual multipath components by overlaying the averaged PDPs from the VNA and the SCS at each receiver location. Examples of the combined PDPs are presented in Figure 20 for the lawn, Figure 21 for conference room, and Figure 22 for the hallway. As shown in the plot legend, the calculated results include the number of multipath peaks, N_{mp}, mean excess delay, τ, and RMS delay spread, σ_τ, for each PDP. Also listed are the power in the first received pulse, P_{max}, and the maximum excess delay, ΔT, for a threshold value of 15 dB .

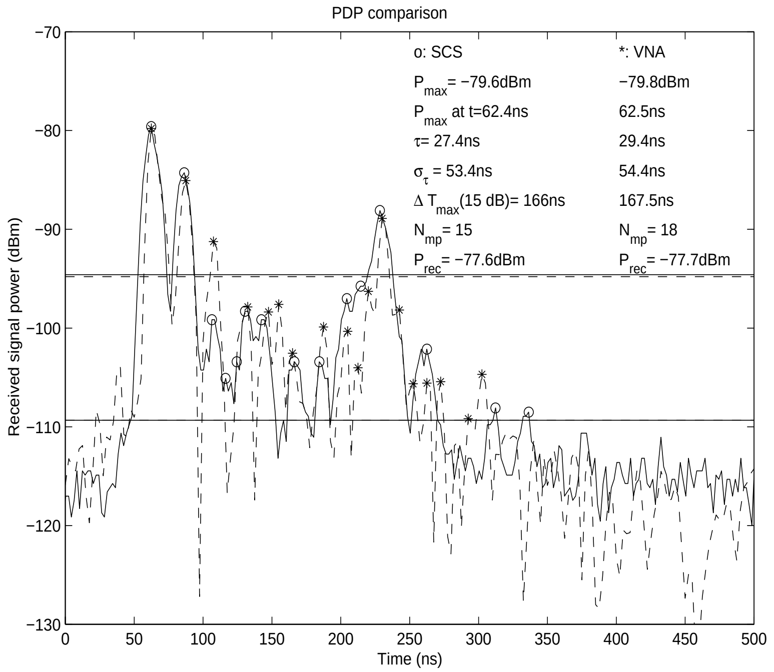

Figure 20: Site-by-site comparison for location B1 in the lawn: "o" denotes the peaks of multipath components recorded from SCS, and "*" denotes the peaks of multipath components recorded from VNA.

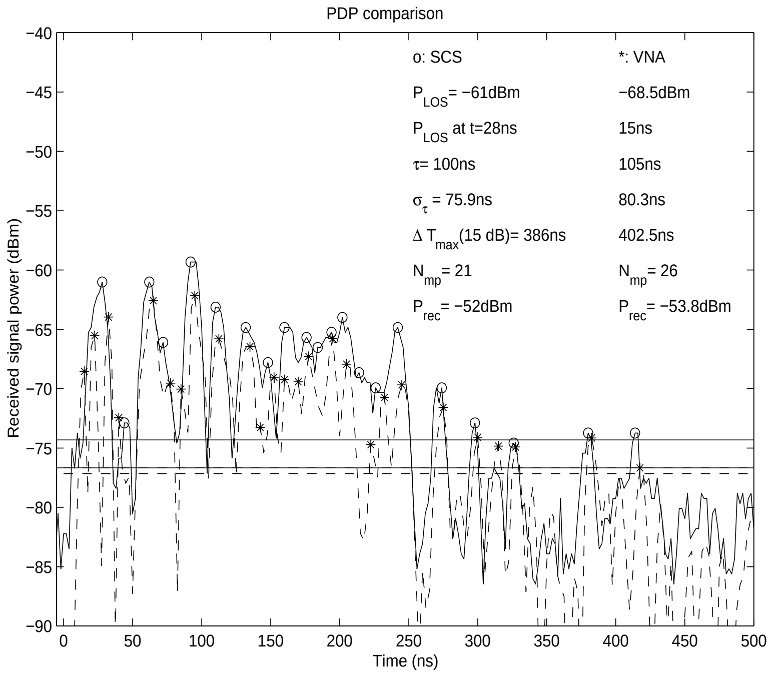

Figure 21: Site-by-site comparison for location B1 in the conference room.

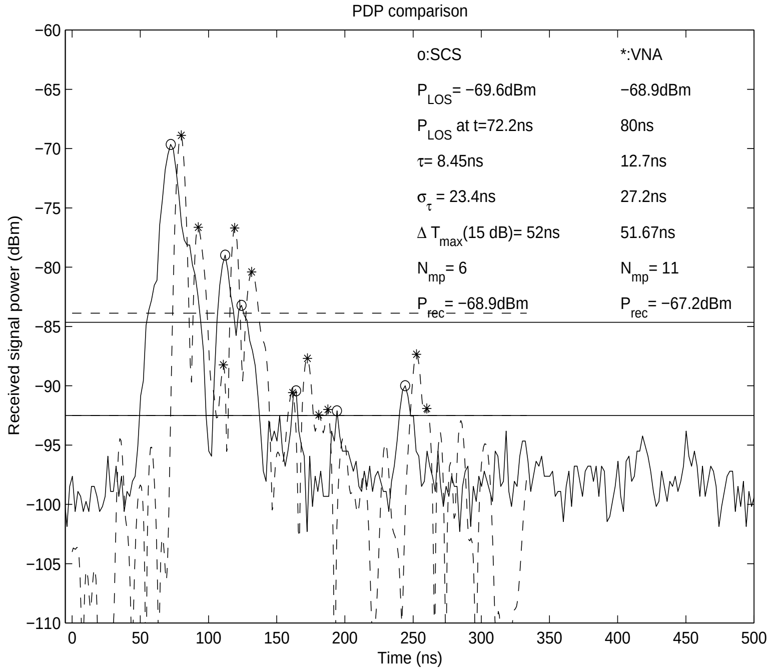

Figure 22: Site-by-site comparison for location B2 in the hallway.

Detailed measurement results are presented in Appendix A. In general, the results from the two measurement methods track very well. For the outdoor measurements, two systems produced nearly identical results in Figure 20. For the indoor measurements, VNA produced a slightly higher number of multipath components. Some of the differences, especially at the lower signal levels can be attributed to the windowing done by the VNA during the calculation of the Inverse Discrete Fourier Transform (IDFT). The frequency window had a nearly ideal bandpass response so that the calculated impulse in the time domain showed sidelobes. This can be seen, for instance, in Figure 20, where the VNA results show pre-first-pulse sidelobes. Using a filter with a slower frequency roll-off would reduce the sidelobe levels, but would also increase the width of the multipath pulses and reduce the resolution.

3.5.3 Summary of the Comparison Measurements

The similarity of the PDPs from the two systems and the close values of the measured channel parameters verify the dual relationship of the frequency and time domain measurement techniques. Since either method gives the same RF channel characterization, the choice of system will depend upon the particular environment to be measured.

The VNA has more flexibility in the choice of the center frequency, sweep bandwidth (measurement resolution) than the SCS. Also, it provides both amplitude and phase information of the channel response. However, the phase measurement requires a cable connection between the transmitter and the receiver, so the VNA is preferred for indoor and short distance outdoor channel sounding. In addition, due to the relatively longer sweep time, the VNA system is constrained to channels that are relatively more stationary than those that can be measured with the SCS system.

The SCS provides the amplitudes and arrival times of the multipath components. Since the measurements are performed in the time domain, phase information is not required for the PDP measurements. The transmitter and receiver do not need to be connected by a cable. However, care must be taken to ensure the time measurement accuracy. Appendix B presents a detailed analysis of the effects of the clock frequency offsets on the measurement accuracy. Results show that not only high precision frequency standards, such as rubidium oscillators, must be used to provide clock reference, but also a calibration procedure is required to account for the time-shift due to the frequency offset of the clocks. With these precautions, the SCS can operate in an untethered mode, which is preferable for long-distance or mobile operations. Finally, SCS typically operates at a higher speed than VNA; therefore, it has a weaker requirement for the channel stationarity. Section 3.6 will show how to chose system settings in SCS to achieve high measurement speed, which is required for the millimeter-wave channel sounding.

3.6 SCS at 38 GHz and 60 GHz

3.6.1 System Hardware

For millimeter-wave propagation study, HRL laboratories and MPRG researchers upgraded the 5.85 GHz SCS presented in Figure 17, to operate at 38 GHz and 60 GHz . This section presents the 38 GHz SCS hardware. The block-diagram of the system is presented in Figure 23.

The basic operation of the SCS is the same as the 5.85 GHz system. The intermediate frequency (IF) is chosen to be 5.4 GHz in order to have a radio frequency (RF) as close to 38 GHz as

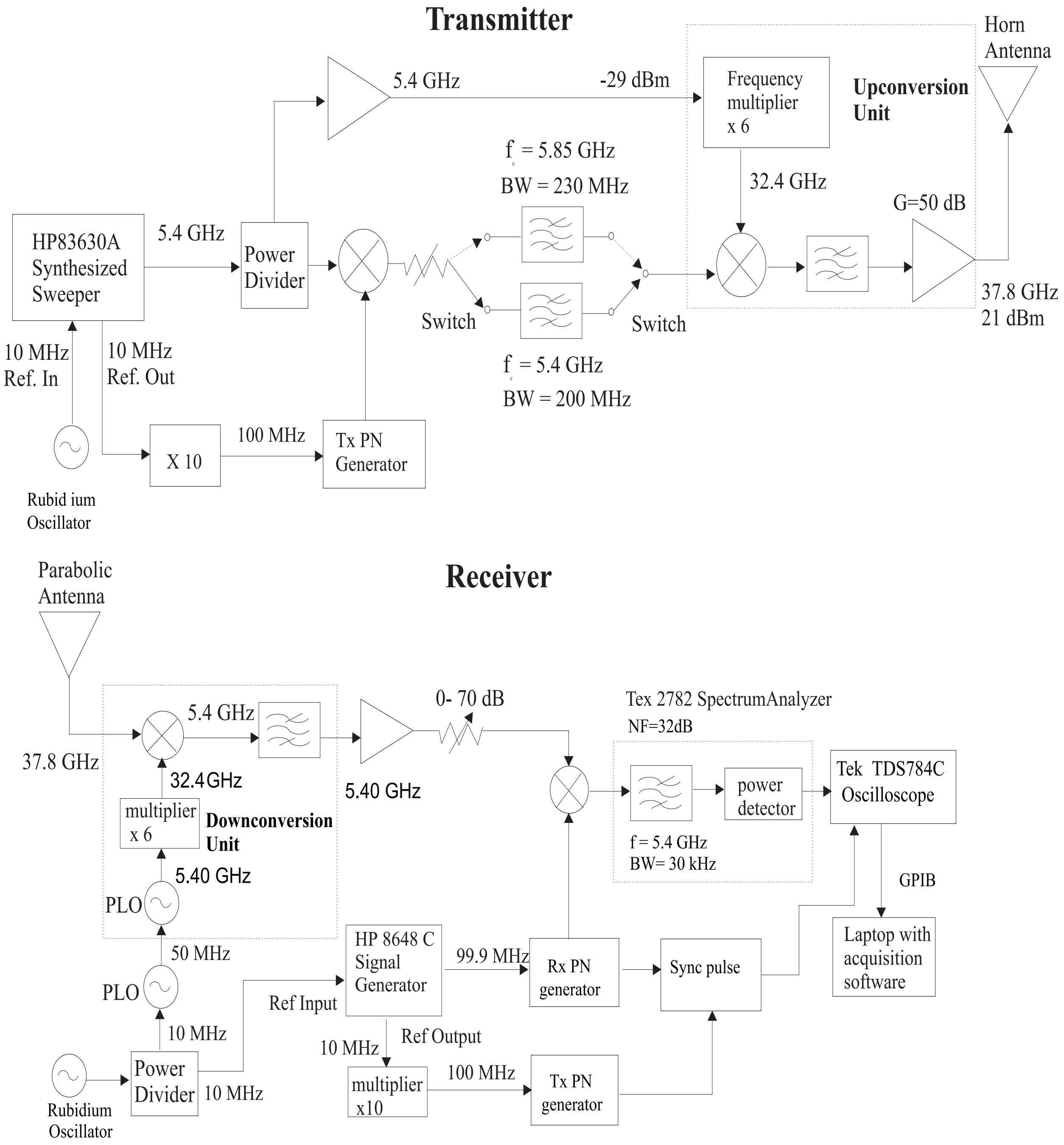

Figure 23: Block-diagram of the 38 GHz channel sounder.

possible. This IF frequency is multiplied by six times to provide a local oscillator (LO) frequency for the mixer. The resulting RF signal is 37.8 GHz . This signal is filtered and amplified before it is sent to the transmitter antenna. The IF signal is filtered by a 200 MHz bandpass filter to attenuate out-of-band noise prior to the upconversion to 37.8 GHz . The maximum allowable input power into the upconversion unit is -29 dB m. The overall gain of the conversion unit is 50 dB . Hence the maximum transmitted power is 21 dBm , which was the transmitted signal power in the measurement campaign presented in Chapter 5. An electronic switch allows the IF to switch between 5.85 GHz and 5.4 GHz .

In the receiver, the downconversion unit is used to downconvert the RF signal from 37.8 GHz to 5.4 GHz . A filter is built into the unit to reject image signals and out-of-band noise. The IF signal is then amplified and mixed with the receiver PN sequence. The correlation and data recording system is identical to the 5.85 GHz SCS described in Section 3.4.4.

3.6.2 Choice of Parameters

The millimeter-wave channel is extremely time-varying due to the short wave length and atmospheric effects. In order to measure outdoor millimeter-wave channels and study weather effects, the measurement system speed is critical. Parameters of the sliding correlator system are chosen in order to optimize both the system performance and the measurement speed.

Tradeoffs among the frequency offset, measurement speed and dynamic range

The minimum time between two successive measurements is determined by the time interval between two consecutive correlations of the transmitter and receiver PN sequences. This time difference is given by

$$T_p = NT_c\gamma = NT_c\frac{f_c}{f_t - f_r} = \frac{N}{f_t - f_r} \tag{3.61}$$

where f_t is the transmitter PN chip rate, f_r is the receiver PN chip rate, and N is the PN sequence length. In the MPRG SCS, PN code length $N = 2047$. f_t is chosen maximum available value of

100 MHz to provide best time resolution. From (3.61), the choice of f_r, or frequency offset $f_t - f_r$ determines T_p.

The f_r and f_t must be close enough to preserve proper correlation properties of the PN sequences and maintain the system dynamic range. With larger frequency offset, fewer PN chips will be aligned at the peak correlation time, and the correlation peak reduces and the correlation noise increases. When f_r is 99.99 MHz , the measurement speed is 0.2 s per PDP, the system dynamic range is measured to be 35 dB . When f_r is 99.9 MHz , the measurement speed is 0.02 s per PDP, and the system dynamic range reduces to 25 dB .

As will be shown in Chapter 5, weather events can change dramatically within a minute. In order to characterize the effect of weather on the millimeter-wave propagation, the frequency offset of the SCS was chosen at 100 KHz to achieve a fast measurement speed while maintaining reasonable dynamic range.

Oscilloscope configuration for fast acquisition

The measurement speed is also dependent on the acquisition and recording speeds of the oscilloscope. The Tektronix TDS784C oscilloscope is set to a fast frame mode, which records the input signal continuously for a chosen number of PDPs. A signal flow plot with required time at each stage is summarized in Figure 24.

For the measurement campaign presented in Chapter 5, we chose a record of 10 successive PDPs for each fast frame file. Each PDP records the channel impulse response over 0.02 s. Therefore, it takes the oscilloscope $0.02 \times 10 = 0.2$ s to accomplish each fast frame acquisition.

Each fast frame record is transferred through a GPIB interface to the laptop computer and saved on the hard disk. The transfer time and the scope reset time is approximately 0.55 s for each fast frame file. Therefore, the time required for one fast frame acquisition into the PC is $0.2 + 0.55 = 0.75$ s.

In order to capture the channel dynamics, 20 fast frame files were taken for each data acquisition. Thus, the time required to take one data acquisition is $0.75 * 20 = 15$ s. Finally, it takes 32 s for the PC to save one data acquisition (20 fast frame files) to the hard drive. Considering the scope reset, file transfer and saving time, the measurement system is capable of capturing 200 PDPs every 47

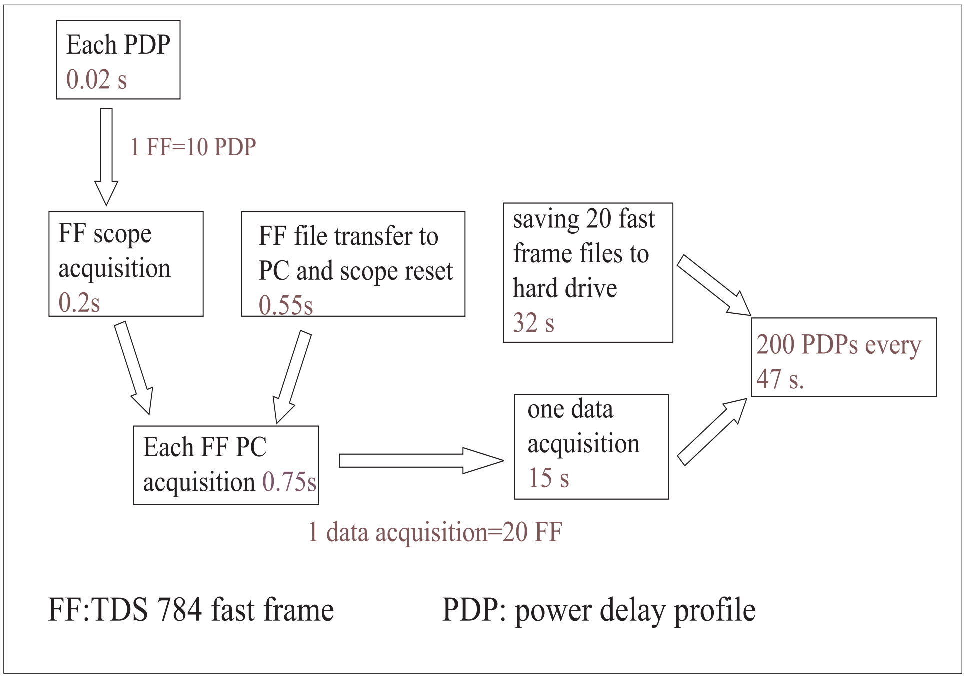

Figure 24: Characterization of the system speed.

seconds.

3.6.3 Antennas

Antennas are selected to represent antenna systems proposed for emerging millimeter-wave point-to-multipoint links. As shown in Figure 25, the transmitting (hub) antenna is a horn with a maximum gain of 19 dB and half power beamwidths of 45^0 and 6.5^0 in azimuth and elevation, respectively. The receiver (subscriber) antenna is a parabolic reflector with a maximum gain of 39 dB and half power beamwidths of 1.5^0 in both azimuth and elevation. Both antennas are vertically polarized.

3.6.4 Free Space Calibration

Free space calibration is performed to verify the hardware system performance. The free space path loss is calculated theoretically and compared with the measurement results.

The transmitter and receiver are separated by a distance larger than the Fraunhofer distance so

Figure 25: The transmitter horn antenna.

Figure 26: The receiver dish antenna.

that they are both in the far fields. Also, the Fresnel zone radius is calculated to ensure both LOS and first Fresnel zone clearance. The T-R separation is chosen to be 30.5 m (100 ft) and 45.7 m (150 ft) for the calibration. The Fresnel radii for these two distances are both less than 1 m.

Antenna heights are chosen so that no significant ground reflected wave will be received. Figure 27 shows the antenna separation and the antenna 3 dB beamwidths patterns. Most of the transmitted energy will be concentrated in the region enclosed by the 3 dB pattern of the antennas. Basic geometric calculation shows that with these antenna patterns, the points where the 3 dB power beams intersect are 0.32 m from the LOS direct path. For the calibration, the antenna heights were chosen to be 1.5 m, which is much higher than 0.32 m.

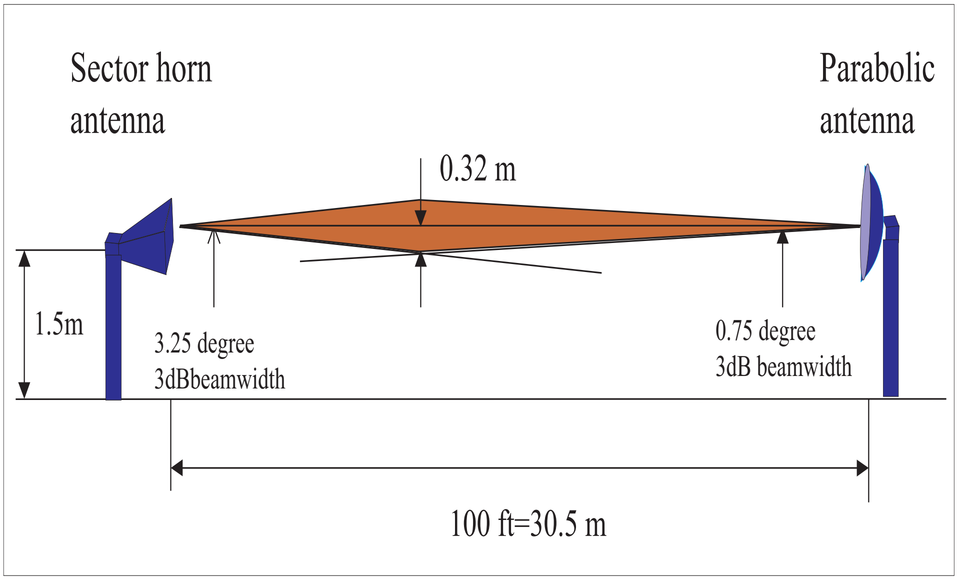

Figure 27: Geometry of the free space calibration.

The scenario for the free space calibration at a 100-foot separation is shown in Figure 28.

The free space path loss based on the Friis equation (2.1) is 93.7 dB and 97.2 dB for 100 ft and 150 ft separation distances, respectively. The measured values are 94.7 dB and 98.5 dB. The differences between the theoretical and measured values are less than 1.3 dB , which verifies the proper operation of the system.

Figure 28: Scenario for the free space calibration.

3.7 Summary

This chapter discusses different measurement techniques. Theoretical backgrounds of narrowband techniques and three different wideband techniques are presented. Implementation issues of each techniques are analyzed with the hardware design examples and measurement results. SCS and VNA measurement systems are analyzed in detail, and their performances are compared experimentally for identical propagation environments at 5.85 GHz . Finally, a millimeter-wave SCS measurement system is described. This system is instrumental for the 38 GHz measurement campaign presented in Chapter 5 and the 60 GHz measurement campaign presented in Chapter 7. The hardware implementations and measurement examples present practical values for any measurement system design and channel measurements .

Chapter 4

Terrestrial Millimeter-Wave Propagation

The radio frequency (RF) channel is relatively well understood for narrow band systems at cellular and PCS bands [14, 29, 30]. However, much less research is available for millimeter-wave propagation. Wireless communication systems at millimeter-wave frequencies are not common, and will feature high carrier frequency and high data rates. The dominant propagation mechanisms are quite different from those at UHF or microwave frequencies. In order to provide the same system performance as fiber or cable systems, quantitative knowledge of the millimeter-wave channel is crucial.

The following sections present a detailed discussion and literature search on the fundamental propagation mechanisms in millimeter-wave channels. Some research results at microwave frequencies are also included for comparison purposes. Due to the significant difference in propagation environments and system requirements, outdoor and indoor channel characterizations are treated separately.

The first part focuses on considerations for outdoor propagation channels including LOS clearance, diffraction, refraction, reflection, and scattering due to vegetation and rain. The second part presents indoor propagation considerations including path loss exponent, penetration loss, signal PDFs, multipath propagation, effects of antennas, and human induced variations. Some of the results such as penetration loss and reflection measurements provide insights into the interplay between outdoor and indoor channel characterizations. For different environments, the main propagation considerations are pointed out, and important measurement results and models are highlighted.

The main purpose of this chapter is to clearly identify the present state of millimeter-wave propagation research, which will help define the need for new research directions.

4.1 General Considerations

Due to the high penetration loss through buildings, vegetation, and other obstacles, millimeter-wave systems are deployed mainly under LOS conditions in outdoor environments. One major application for outdoor millimeter-wave systems is fixed point-to-point/multipoint communications. Historically, fixed *microwave* LOS radio links have been used to provide broadband communications at frequency bands ranging from 2 GHz to 18 GHz [24]. This section first briefly summarizes the main considerations for point-to-point propagation at microwave frequencies, and then emphasizes the specifics of millimeter-wave LOS links.

4.1.1 Microwave LOS Links

Typical microwave links use antennas with beamwidths of about 1 degree, have path lengths on the order of tens of kilometers, and have antenna tower heights of 50 to 100 meters [24]. A number of researchers have investigated microwave LOS links, and design rules have been established [4, 25, 74, 75].

The following items summarize the main *propagation effects* that need to be considered in the design of *microwave* radio links [76]:

- Effects of nearby objects
    - LOS and Fresnel zone clearances (see Section 4.2)
    - Diffraction due to obstruction of the path by terrain obstacles

  - Fading due to multipath from surface reflection
  - Attenuation and scattering due to vegetation
- Effects of atmosphere
  - Fading, beam spreading and variation of angle of arrival (AOA) due to changes in the refraction index (see Section 4.3)
  - Attenuation due to atmospheric gases
  - Attenuation and depolarization due to precipitation or hydrometeors in the atmosphere

4.1.2 Specifics for Millimeter-Wave LOS Links

Although results presented in Section 4.1.1 are obtained for microwave LOS links, they can be extended to millimeter-wave links. The following items summarize the differences of the microwave and millimeter-wave propagation channels.

- Millimeter-waves suffer higher attenuation and diffraction loss due to wall, or other terrain obstacles (see Sections 4.2 and 4.10.1).
- Millimeter-wave links are typically less than a few kilometers in length. Therefore, the effects of refractive index changes are not as significant as in microwave links, which have typical lengths of tens of kilometers [25] (see Section 4.3).
- At millimeter-wave frequencies, the wavelength is much smaller than, or comparable to typical building surface variations. Rough surface scattering needs to be considered (see Section 4.4).
- Foliage exhibits higher attenuation at millimeter-wave than at microwave frequencies [77] (see Section 4.6).
- Rain attenuation increases with frequency [78] (see Section 4.7).
- Millimeter-wave links can be employed in both rural and urban environments; therefore, they are subject to multipath due to the dense concentration of surrounding objects (see Section 4.8).

These propagation effects may result in serious *system performance degradation* including:

- Reduced system coverage (see Sections 2.1.2 and 4.8)
- Signal distortion due to frequency selective fading (multipath)
- Reduction in cross-polarization discrimination (XPD)[1] in multipath or precipitation conditions
- Increased time variation in the channel

4.2 Diffraction: Fresnel Zone Clearance

For point-to-point/multipoint links, not only LOS path clearance is required, but also *Fresnel zone clearance* is highly desirable in order to avoid diffraction loss. This section briefly reviews diffraction mechanisms with the example of *knife-edge diffraction.* The increase of diffraction loss with the increase of frequency is demonstrated, and the Fresnel zone clearance criterion is described.

Figure 29 shows a scenario of an obstructed transmitter-receiver path. Diffraction describes the phenomenon that radio waves propagate around obstacles into the shadowed region. In realistic system deployment, the obstructions can be buildings, hills and other terrain obstacles. As a starting point, the limiting case of propagation over a knife-edge is studied.

Diffraction can be explained by *Huygen's principle.* Huygen's principle states that each point on a wave front can be considered as the source of a secondary wavelet, and these wavelets combine to produce a new wavefront in the direction of propagation [79]. Diffraction is caused by the propagation of the secondary wavelets into the shadowed region. Consider the example in Figure 29, the field strength at any point in the shadowed region will be the vector sum of the fields generated by all the secondary Huygen's sources in the plane above the knife-edge. The electric field intensity,

---

[1] XPD is defined as the ratio of the co-polarized received power $P_{\|}$ to the cross-polarized received power $P_{\perp}$ expressed in dB.

$$XPD = 10 \log_{10} \frac{P_{\|}}{P_{\perp}} \tag{4.62}$$

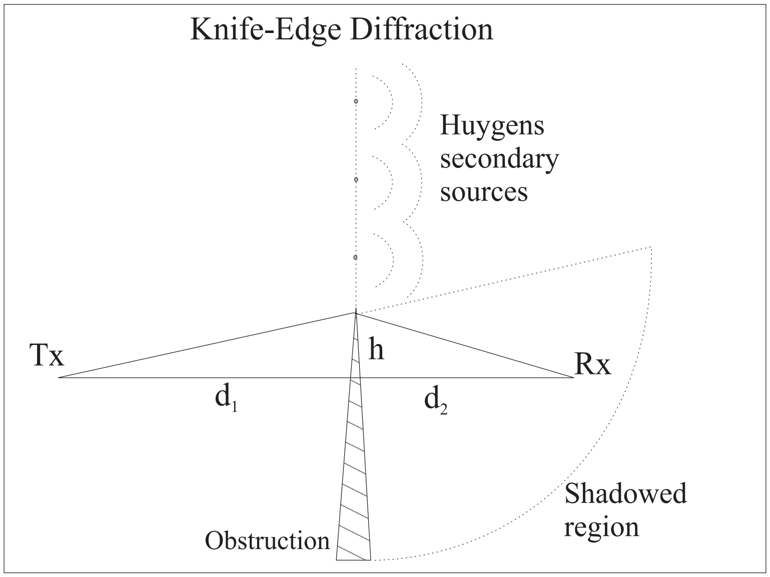

Figure 29: Knife-edge diffraction

E_d, of a knife-edge diffracted wave is given by [79]

$$\frac{E_d}{E_0} = F(v) = \frac{1+j}{2}\int_v^{\infty} \exp[(-j\pi t^2)/2]dt \tag{4.63}$$

$$v = h\sqrt{\frac{2(d_1+d_2)}{\lambda d_1 d2}} \tag{4.64}$$

where E_0 is the free space field strength in the absence of the knife edge, $F(v)$ is the complex Fresnel integral, and v is the *Fresnel-Kirchoff diffraction parameter*.

The diffraction gain due to the knife-edge as compared to the free space propagation is given by

$$G_d(\mathrm{dB}) = 20\log_{10}|F(v)| \tag{4.65}$$

The Fresnel integral can be evaluated using tables or graphs, and dependence of G_d on v is shown in Figure 30.

As shown in Figure 30, the diffraction loss increases with the increase of v. The dependence of v on the wavelength (frequency) and link geometry is given by (4.64).

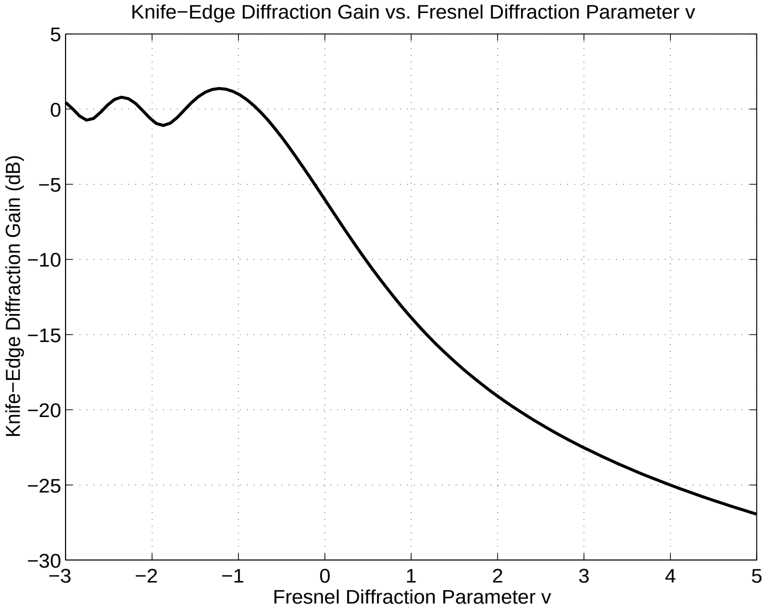

Figure 30: Knife-edge diffraction gain as a function of Fresnel diffraction parameter v.

4.2.1 Diffraction Loss vs. Frequency

As shown in (4.64), v increases with the decrease of λ or increase of frequency. Figure 31 shows an example of the dependence of diffraction gain on frequencies. In the example, d_1 and d_2 are chosen at 500m, and h is chosen as 1 m. Results show that a 1m obstruction causes 7 dB diffraction loss at 1 GHz , but 15.5 dB loss at 60 GHz .

4.2.2 Fresnel Zone Clearance

The dependence of diffraction loss on the link geometry is well explained by *Fresnel zones*. Consider the geometry shown in Figure 32, the LOS path length is $d_1 + d_2$, and a secondary wave has a path length of $d_3 + d_4$. Fresnel zones are defined as regions where the secondary waves have path lengths that are $n\lambda/2$ greater than the LOS path length. Therefore, for the nth Fresnel zone boundary

$$d_3 + d_4 = n\lambda/2 + d_1 + d_2 \tag{4.66}$$

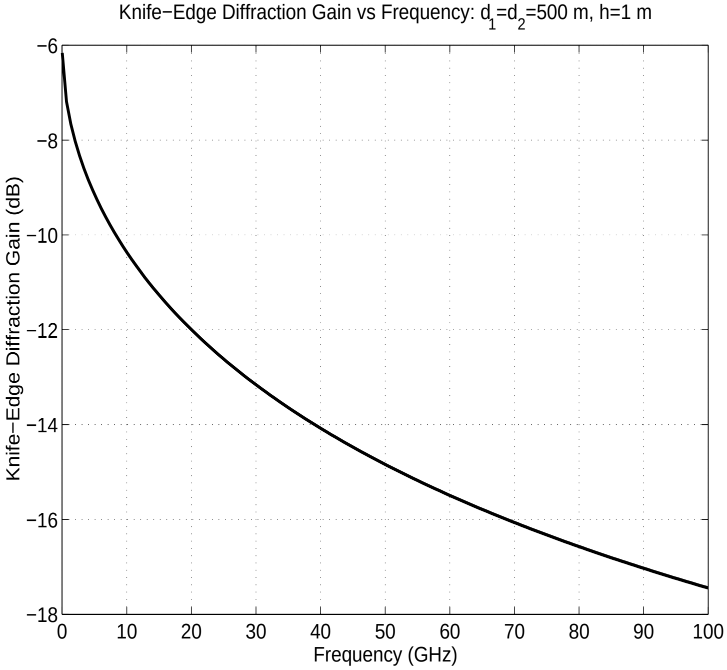

Figure 31: Knife-edge diffraction gain as a function of frequency: $d_1 = d_2$=500m, h=1m.

The points defined by (4.66) form an ellipsoid with the transmitter and receiver as focal points. The radius of the nth Fresnel zone on the vertical plane A is given as follows.

$$d_1^2 + r_n^2 = d_3^2 \tag{4.67}$$

$$d_2^2 + r_n^2 = d_4^2 \tag{4.68}$$

Under the assumption $d_1, d_2 \gg r_n$, we have

$$r_n = \sqrt{\frac{n\lambda d_1 d_2}{d_1 + d_2}} \tag{4.69}$$

In Figure 32, the concentric circles correspond to the Fresnel zone radii. Diffraction loss is caused by blockage of the Fresnel zones. As shown in Figure 30, the diffraction loss can be avoided if $v < -0.8$, which corresponds to 56% of the first Fresnel zone clearance. In point-to-point communications system design, in addition to LOS path clearance, 56% of the first Fresnel zone clearance is required to reduce the diffraction loss [17].

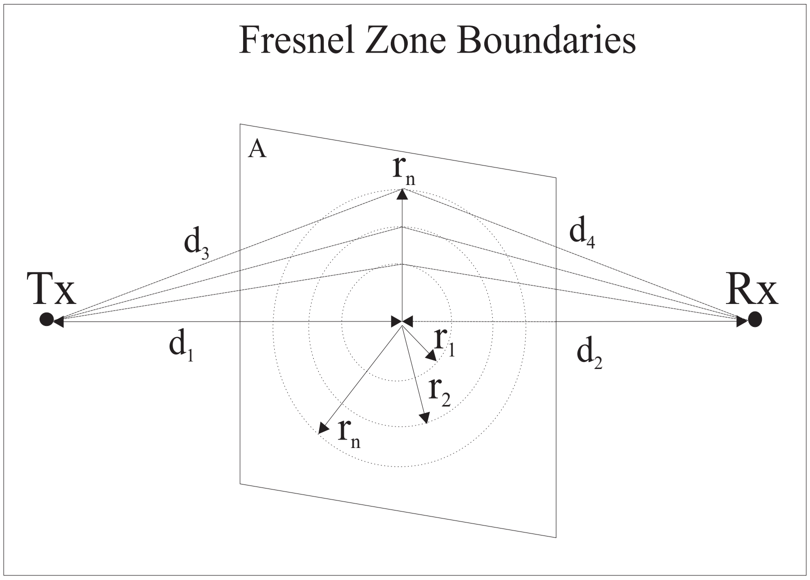

Figure 32: Fresnel zone boundaries.

4.3 Refraction: Effects of Refractive Index Change

Variations in the climatic conditions such as temperature, pressure and humidity cause changes in the refractive index of the air. The refractive index of air at sea level differs from unity by about $300 * 10^{-6}$, and decreases approximately exponentially with height [17, 75]. It is convenient to express refractivity in N units, where

$$N = (n - 1) * 10^6 \tag{4.70}$$

and n is the refractive index of the atmosphere

$$n \approx (1 + 300 \times 10^{-6}) \tag{4.71}$$

Refractive index is related to atmospheric conditions as follows [17]

$$N = \frac{77.6}{T}[P + \frac{4810e}{T}] \tag{4.72}$$

where P is total pressure in mb, e is water-vapor pressure in mb, and T is absolute temperature. With the increase of height, P, e, T and N decrease exponentially. Over the first kilometer of height above the ground, the refractive index N falls by 39 N-units in a standard atmosphere.

It has been shown in [81], that a constant gradient of the refractive index will result in a wave propagation path in the shape of an arc with a radius of R, where R is given by

$$\frac{1}{R} \approx - \bigtriangledown (n) = -\frac{dn}{dh} = -10^{-6}\frac{dN}{dn} \tag{4.73}$$

where h is the height above the ground, and $\bigtriangledown(\cdot)$ denotes the gradient operation. For example, for the standard atmosphere, the radius of the propagation path is $R_0 = 25,640$ km.

The effects of the refractive index change on the LOS propagation path are demonstrated in Figure 33, where R_e is the radius of earth. Depending on the sign of the gradient of the refractive index, the propagation path may bend towards or away from the earth.

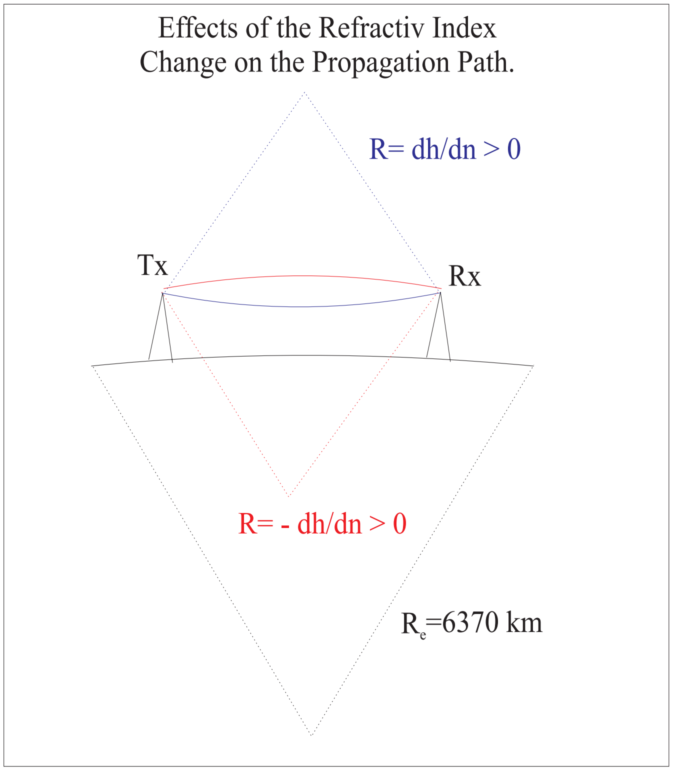

Figure 33: Wave bending caused by the refraction index change.

4.3.1 Multipath due to Refractive Index Change

Typical microwave links have antenna tower heights of 50 to 100 meters. Under normal conditions, these microwave links operate essentially error free, that is with BER less than 10^{-10} [24]. When the index of refraction of the atmosphere changes, eletromagnetic waves may arrive at receiver antenna along slightly different paths. In [4], transmission over LOS microwave radio is analyzed with the aid of a piece-wise linear approximation of the atmospheric indes of refraction. The model predicts that one, two or three discrete multipath components can be refracted to the receiver depending on the height of the refractive layer. Consequently, the signal suffers frequency selective fading [4, 24, 74].

The mechanism of the multipath propagation caused by the refraction index change in the atmosphere is depicted in Figure 34. In a standard atmosphere, the decrease of n with the height is very slow, resulting in a slight bending of the LOS ray towards the earth with a downward curvature, R_0. Under certain weather conditions, the meteorological effects can produce a refractive layer with negative gradients in the refractive index of the atmosphere [4]. As a results, several ray paths may exist between the transmitter and the receiver. The changes of the refractive index are small, so that only waves with small launching angles can be refracted to the receiver [4].

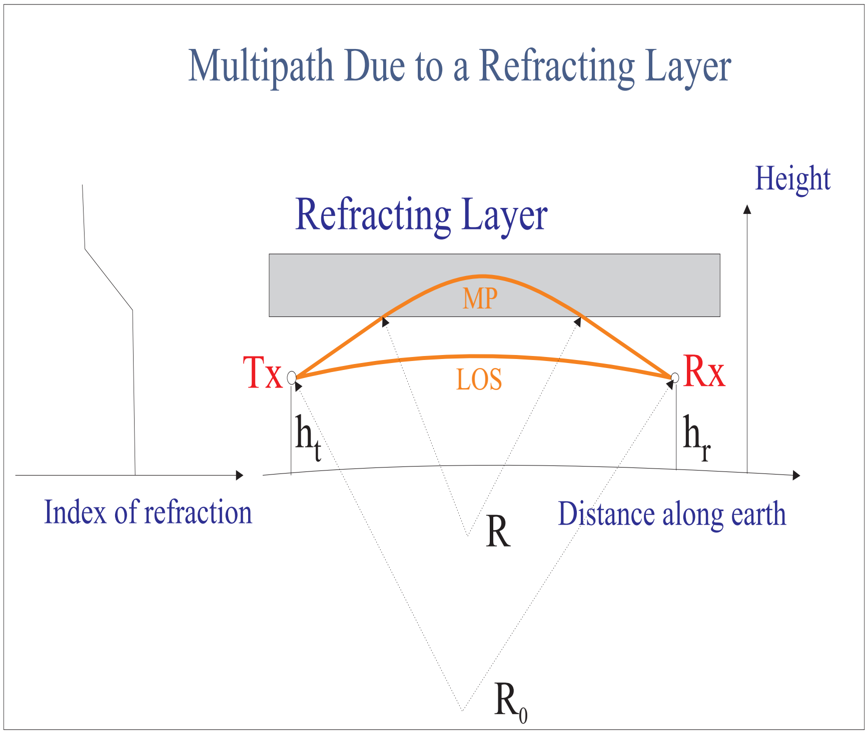

Figure 34: Multipath propagation caused by the refraction index change [4].

In [4], Ruthroff showed that, based on (4.73), if a maximum gradient of refractive index is given for a particular climate region, then a path length L_0 exists, such that for any distance less than L_0, there will be no deep fading. L_0 can be estimated from

$$L_0^3 = 9\lambda R^2 \frac{(1 - R/2R_0)^2}{(1 - R/R_0)^4} \tag{4.74}$$

Table 4.3.1 presents the path length L_0 estimated based on the measurement results from [74] for New Jersey region. Results show that for path length less than 3.8 km , refractive index change would not cause fading in the LOS links. As shown in Table 4.3.1, for typical short millimeter-wave links, the effects of refractive index changes are negligible.

Table 2: Maximum Path Length to Avoid Refracted Multipath [4] (for New Jersey climate region)

Frequency (GHz)	Wavelength (cm)	L_0 (km)
4	7.5	9.37
6	5.0	8.2
10	3.0	6.93
20	1.5	5.5
30	1.0	4.8
60	0.5	3.8

4.4 Reflection: Effects of Rough Surface

4.4.1 Reflection: Snell's Law

When an EM wave impinges on a surface with finite conductivity, part of the energy is reflected back and part of the energy is transmitted into the surface. When the reflecting surface is smooth, the reflected wave and transmitted wave are related to the incident wave by reflection coefficient and transmission coefficient given by Snell's law [82].

$$\theta_r = \theta_i \tag{4.75}$$

$$E_r = \Gamma E_i \tag{4.76}$$

$$\Gamma_{\parallel} = \frac{E_r}{E_i} = \frac{\eta_2 \cos\theta_t - \eta_1 \cos\theta_i}{\eta_2 \cos\theta_t + \eta_1 \cos\theta_i} \tag{4.77}$$

$$\Gamma_{\perp} \quad = \quad \frac{E_r}{E_i} = \frac{\eta_2 \cos\theta_i - \eta_1 \cos\theta_t}{\eta_2 \cos\theta_i + \eta_1 \cos\theta_t} \tag{4.78}$$

where θ_i is the angle of incidence, θ_r is the angle of reflection, E_i is the incident field intensity, E_r is the reflected field intensity, Γ is reflection coefficient, which equals $\Gamma_{\parallel}$ or $\Gamma_{\perp}$ for parallel or perpendicular polarization, respectively, η_i is the intrinsic impedance of the ith medium (i=1,2), and is given by $\sqrt{\mu_i/\epsilon_i}$. Geometry of specular reflection over a smooth surface is presented in Figure 35.

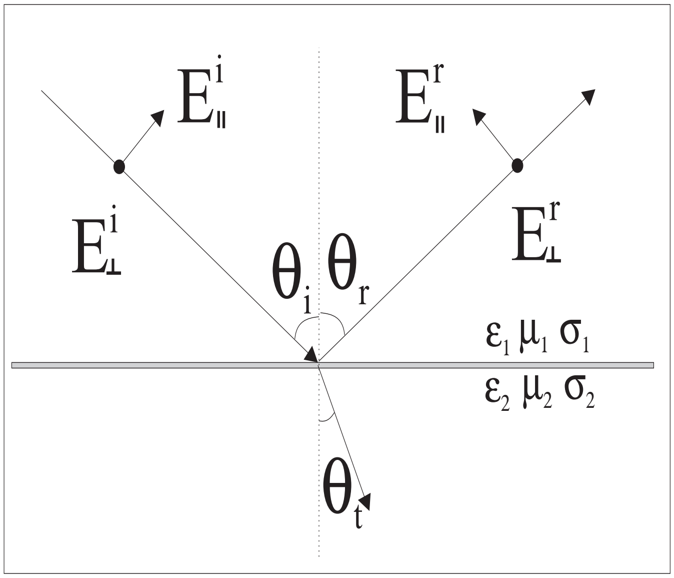

Figure 35: Geometry of the specular reflection over a smooth surface

Based on Snell's law, the angle of reflection equals the angle of incidence. This reflection is referred to as *specular reflection*. When the surface is rough, the incident wave is scattered into not only the specular direction, but also other directions. Figure 36 qualitatively shows the effect of surface roughness on the reflected wave. With increase of the surface roughness, the specular reflected field decreases and the incoherent scattered field increases.

4.4.2 Rayleigh Criterion

The most common criterion to describe surface roughness is the *Rayleigh criterion*. The basic principle of the Rayleigh criterion is presented in Figure 37.

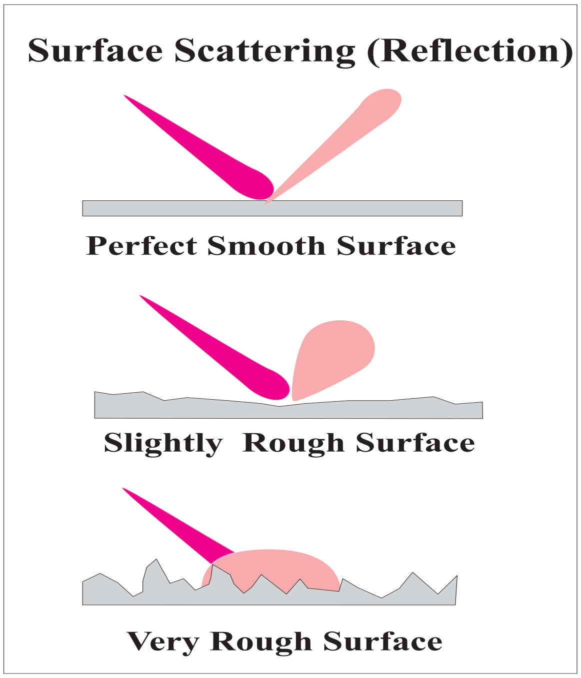

Figure 36: Rough surface scattering: with the increase of surface roughness, specular reflected field decreases and diffuse scattered field increases [5]

When two rays incident on a rough surface with an average height of irregularity, h, the path difference between the two reflected waves, Δr, is [6]

$$\Delta r = 2h\cos(\theta) \tag{4.79}$$

where

$$\theta = \theta_i = \theta_r \tag{4.80}$$

as shown in Figure 37.

This is easily seen by comparing ray 1 with the auxiliary ray 2', which is identical to ray 2 but shifted to the location of ray 1. The carrier phase difference of these two reflected waves is

$$\Delta\phi = \frac{2\pi}{\lambda}\Delta r = \frac{4\pi h}{\lambda}\cos(\theta) \tag{4.81}$$

Let us consider two extreme cases. First case is when the surface is smooth, h is zero, and the phase difference $\Delta\phi$ is zero. All the rays add up coherently, producing a strong reflected wave in the specular direction. Another extreme case is when $\Delta\phi = \pi$, the two reflected waves are out of phase and cancel each other. There is no reflected wave in the specular direction, and all

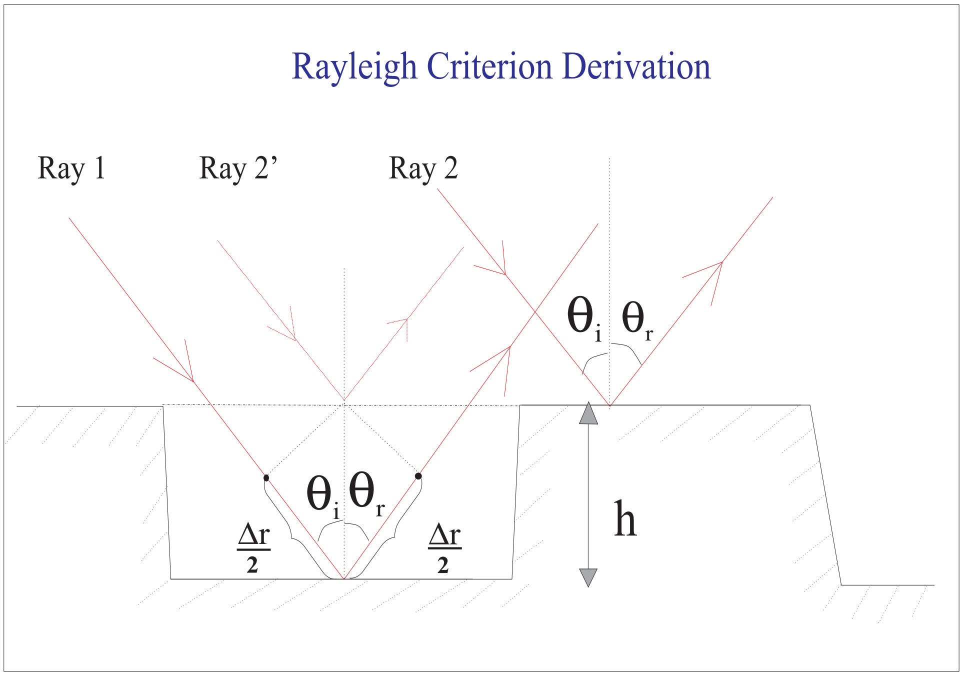

Figure 37: Derivation of Rayleigh criterion [6]

the incident energy is scattered into other directions. The Rayleigh criterion chooses the phase difference midway between these two extreme cases, i.e. $\Delta\phi = \pi/2$. When $\Delta\phi > \pi/2$, the surface needs to be treated as a rough surface. Most often, the Rayleigh criterion is expressed in terms of h. A surface is thus considered as a rough surface if

$$h > \frac{\lambda}{8\cos(\theta)} \tag{4.82}$$

Although the Rayleigh criterion is based on a simplified surface scattering scenario, it predicts the basic trends of rough surface scattering. Qualitatively, rough surface scattering is a function of incident angle, wavelength, and average height of the surface irregularity. *A given surface becomes rougher when the frequency increases or the incident angle decreases.*

4.4.3 Scattering Loss Factor

A simple treatment of the surface roughness was provided in [83] and [84], where a scattering loss factor, ρ_s, was used to account for the additional loss in the specular reflected wave due to the rough surface effects. In [83], Ament showed that if the surface heights are Gaussian distributed,

ρ_s can be expressed as

$$\rho_s = \exp\{-8(\frac{\pi\sigma_h \cos\theta_i}{\lambda})^2\} \tag{4.83}$$

where σ_h is the standard deviation of the surface height about the mean surface height in the first Fresnel zone of the illuminating antenna. This model was then modified in [84] to better fit the measurement data. The modified scattering loss factor is given by

$$\rho_s = \exp\{-8(\frac{\pi\sigma_h \cos\theta_i}{\lambda})^2\} I_0\{8(\frac{\pi\sigma_h \cos\theta_i}{\lambda})^2\} \tag{4.84}$$

where $I_0(\cdot)$ is the modified Bessel function of zero order. Measurements from [85] showed reasonable agreement with the modified model (4.84) for large exterior walls made of rough limestone.

Due to the random nature of the surface profiles, characterization of surface roughness is a complicated problem and still remains unsolved. Numerical methods are developed to solve rough surface problems [86, 87]. More rigorous theoretical approaches to the rough surface scattering problems can be found in [5, 6, 88, 89, 90, 91].

4.4.4 Reflection Measurement Results

At millimeter-wave frequencies, almost any surface appears rough except when the incident angle is close to 90 degree (i.e., grazing angle). Measurements of reflected and/or scattered signals were made for a variety of surfaces at normal incidence by Violette *et al* in [10]. The transmitter and receiver antennas were colocated and pointed at the building surfaces. In [10], reflection loss was measured as the difference (in dB) between the reflected power and the received signal power via free space LOS path with the same path length. Measurement results are summarized in Table 4.4.4.

Results from [10] show an apparent reduction of the reflected power with the increase of the frequency from 9.6 GHz to 28.8 GHz and 57.6 GHz . The high reflection loss at millimeter-wave frequencies is an expected result due to the rough surface scattering.

Langen *et al* presented reflection measurement results at 60 GHz in [92]. Reflection loss at various angles was measured using two horn antennas with a 3 dB beamwidth of 3°. Results showed that when the standard deviation of the surface height is equal to or greater than 0.3 mm, the rough surface structure has distinct influence on the reflection loss. In [92], the rough surface effect was modeled using (4.83).

Table 3: Reflection Loss Measurement Results from [10]

Surface	9.6 GHz	28.8 GHz	57.6 GHz	One-way pathlength (m)
Metal	0	-1	-1	50
Metal	2	-5	-7	41
Metal	-2	-3	-1	50
Metal	1	-8	-7	80
Metal	-6	1	-9	109
Average	-1	-3	-5	
Brick(solid)	-2	-7	-7	95
Brick(solid)	-6	-14	-8	47
Brick(windows,doorway)	-9	-14	-18	93
Brick(windows,doorway)	-12	-15	-15	135
Concrete(ribbed)	-6	-11	-19	64
Concrete(aggregate)	-12	-10	-20	75
Concrete(aggregate)	-6	-12	-17	75
Average	-8.5	-11.25	-15.25	

In [93], Seville *et al* presented results of building scattering measurements at an incident angle of 30°. CW measurements of specular and nonspecular reflections of a brick wall in a 2 story building was measured at 37.53 GHz. The transmitter antenna was located 30 m from the wall, and both copolar and crosspolar reflected waves were measured around an arc with radius of 30 m. Results show that the copolar reflection loss is 13.7 dB in the specular direction. Non-specular reflection was found to be significant; however, no quantitative measurement results were given. The contribution of cross-polar reflections is 10-25 dB lower than from co-polar reflections.

At grazing angles, however, the surface reflection is close to the smooth surface reflection independent of frequency. Measurements in [10] showed that, at very small grazing angles, the measured reflection coefficient approaches -1 even at millimeter-wave frequencies.

4.5 Scattering: Radar Cross Section

When the surfaces of a distant object are irregular or rough, the energy incident upon the object is scattered into different directions. Bistatic radar equation can be used to model the scattered energy from a target (scatterer) [94]. The target intersects part of the incident power and reradiates into different directions [95]. The power flux at the radar target due to the transmitted signal is given by

$$S_{target} = \frac{P_t G_t}{4\pi R_1^2} \tag{4.85}$$

where P_t is the transmitted power, G_t is the transmitter antenna gain, and R_1 is the distance from the transmitter to the target.

The power flux at the receiver antenna due to the reradiating of the target is given by

$$S_{receiver} = \frac{P_t G_t}{4\pi R_1^2} \frac{\sigma}{4\pi R_2^2} \tag{4.86}$$

where R_2 is the distance from the target to the receiver, and σ is the radar cross-section (RCS) of the target. RCS is used as a measure of the effective area as seen by the radar that intersects and reradiates the power. RCS has the units of area. The received signal power is given by

$$P_r = \frac{P_t G_t}{4\pi R_1^2} \frac{\sigma}{4\pi R_2^2} A_e \tag{4.87}$$

where A_e is the effective area of the receiver antenna, which is

$$A_e = \frac{G_r \lambda^2}{4\pi} \tag{4.88}$$

where G_r is the receiver gain. The received power can be expressed in terms of receiver gain by substituting (4.88) into (4.87) as follows:

$$P_r = \frac{P_t G_t G_r \lambda^2 \sigma}{(4\pi)^3 R_1^2 R_2^2} \tag{4.89}$$

Models based on the bistatic radar equation (4.89) have been used to estimate the received signal power due to scattering in urban mobile communications [14, 71, 96]. Typical radar frequencies range from 220 MHz to 35 GHz [95]. Potential millimeter-wave radar applications include high-resolution radar, cloud-physics radar, interference-free radar, and missile guidance. However, millimeter-wave radar is not widely used due to the cost of components, high attenuation due to water and oxygen, small antenna aperture size to collect the scattered energy, and possible effects of high doppler shifts [95].

4.6 Scattering: Effects of Vegetation

At millimeter-wave frequencies, the dimensions of tree leaves are larger or comparable to the wavelength. Therefore, vegetation can be modeled as a random medium of discrete, lossy scatterers [7, 77]. Propagation of millimeter-waves through vegetation is characterized by attenuation, beam broadening and depolarization.

A theory for millimeter-wave propagation in woods and forests was developed in [77]. Radio wave propagation in vegetation was modeled by using a *theory of radiative energy transfer (transport theory).* In transport theory, the scattering media is characterized by the absorption cross section per unit volume, σ_a, the scatter cross section per unit volume, σ_s, and the power scatter function, $p(\hat{S}, \hat{S}')$, where unit vectors $\hat{S}$ and $\hat{S}'$ indicate the scatter direction and the incident direction, respectively. The model for transport theory is shown in Figure 38.

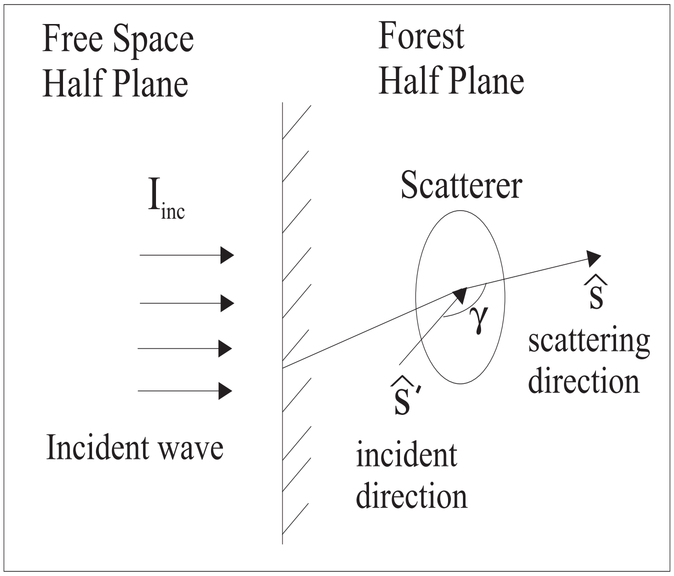

Figure 38: Model of transport theory [7]

It is assumed that the scattering surfaces of the vegetation are randomly oriented, and much larger than the wavelength. Therefore, *" the scatter function is isotropic in the sense that it depends only on the angle* $\gamma = \cos^{-1}(\hat{S} \cdot \hat{S}')$*"*, and it should *"consist of a strong narrow forward lobe and an isotropic background"* [77]. Under the further assumption that the forward lobe has a Gaussian profile, the scatter function p has the form of

$$p(\gamma) = \alpha(\frac{2}{\Delta\gamma})^2 \exp\{-(\gamma/\Delta\gamma)^2\} + (1-\alpha) \tag{4.90}$$

$$\gamma = \cos^{-1}(\hat{S} \cdot \hat{S}') \tag{4.91}$$

where $\Delta\gamma$ is the beamwidth of the forward lobe and α is the ratio of the forward scattered power to the total scattered power. The vegetation scattering problem is then treated as a plane wave impinges upon an infinite forest half space with constant parameters $\sigma_a, \sigma_s, \Delta\gamma$ and α. The detailed solution of the problem can be found in [97], and here only the qualitative results are given.

The total field intensity, I_{total}, in the forest half plane consists of reduced incident intensity, I_{ri}, and the diffuse intensity, I_d. The diffuse intensity can be further split into forward scattered field intensity, I_{fs}, and backward scattered field intensity, I_{bs}.

$$I_{total} = I_{ri} + I_d = I_{ri} + I_{fs} + I_{bs} \tag{4.92}$$

The coherent field component, I_{ri}, dominates at short distances and decreases exponentially due to the absorption and scattering. The incoherent field component, I_d, increases linearly at short distances, and then decreases exponentially at large distances. The forward scattered field I_{fs} is dominant at the intermediate distances. The backward scattered field I_{bs} has the smallest magnitude and attenuation rate, and it dominates at large distances.

4.6.1 Vegetation Scattering Measurement Results

A comprehensive measurement campaign on microwave/millimeter-wave propagation in woods and forests was performed by Schwering *et al.* at 9.6, 28.8, and 57.6 GHz [77]. The main focus of the research was to study beam broadening and depolarization effects of the vegetation at different ranges (vegetation depth) and frequencies. A regularly planted, well-groomed stand of trees of equal height (a pecan orchard) was measured under both winter and summer conditions. CW measurements were taken over path lengths of 0.1 to 0.9 km with 1 to 35 trees on the path.

The experimental investigation of range dependence showed that attenuation due to vegetation increases rapidly at small vegetation depth, but the attenuation increases much more slowly at larger vegetation depth. The transition of attenuation rates occurs at the vegetation depth of 3-4 trees. Just after the change of attenuation rate, significant beam broadening and depolarization occurs. Measurements for frequency dependence showed a much higher loss at the two millimeter-wave frequencies than at 9.6 GHz in the canopy region. The loss at 28.8 GHz and 57.6 GHz is almost the same.

The measurement results are well explained by transport theory. The theory confirms the transition from a high attenuation rate at small vegetation depth into a much reduced attenuation rate at large vegetation depth. At short distances, the coherent field I_{ri} decreases rapidly, while at larger distances, the diffuse scattered field I_{bs} decreases much more slowly. Furthermore, the substantial beam broadening at the transition region is also explained by the interplay of the coherent and the incoherent field components.

Other measurement campaigns are reported in [37, 38, 93, 98]. In [93], propagation through sycamore and lime trees of vegetation depths of 0 to 46 m is studied at 38 GHz . Measurement results also show the decrease of attenuation rate with the increase of vegetation depth, and a transition from the dominant coherent field at small vegetation depth into the dominant incoherent field at large vegetation depth. Furthermore, measurements show that the back-scattered field has a higher value with greater fluctuation at the tree trunk level than at the canopy level. Measurements from [37, 38, 98] show that attenuation caused by vegetation is one of the main limiting factors in LMDS coverage. The depolarization caused by vegetation and other signal scatterers was found to be much greater than rain-induced depolarization [98].

4.7 Scattering: Effects of Rain

Effects of rain on radio wave propagation have been studied extensively for attenuation and depolarization, both theoretically and experimentally. This section briefly addresses some of the most important rain attenuation models presented by Olsen [99] and Crane [78], and measurement results summarized by Lin [100]. More rigorous theoretical treatments of rain scattering can be found in [101, 102, 103, 104]. Rain effects on satellite-to-ground propagation can be found in [105, 106, 107].

Throughout this work, rain attenuation (in dB) is defined as the reduction of the received signal power due to the rain as compared to the received signal power under clear weather conditions. It does not include the free space path loss.

4.7.1 The aR^b Rain Attenuation Model

Rain can be modeled as a random medium of sparsely distributed scatterers [99]. Rain attenuation is caused by both absorption and scattering of the rain drops. The average rain attenuation, A_R, in addition to the free space path loss is given as follows [99]

$$A_R = \frac{20k\mathrm{Im}(n)}{\ln(10)} \quad \mathrm{dB/km} \tag{4.93}$$

where k is the wave number, which equals $2\pi/\lambda$, and $\mathrm{Im}(\cdot)$ denotes imaginary part. The bulk refractive index, n, for the random medium of rain is given by

$$n = 1 - j\frac{2\pi}{k^3}\int_0^\infty S(0,D)N(D)dD \tag{4.94}$$

where $S(0,D)$ is the forward scattering amplitude, D is the rain drop diameter, and N(D) is the drop size distribution. Substituting (4.94) into (4.93), A_R is expressed as

$$A_R = 4.343\int_0^\infty Q_t(D)N(D)dD \quad \mathrm{dB/km} \tag{4.95}$$

where $Q_t(D)$ is the extinction cross section, given by

$$Q_t(D) = \frac{4\pi}{k^2}\mathrm{Re}[S(0,D)] \quad m^2 \tag{4.96}$$

where $\mathrm{Re}(\cdot)$ denotes real part.

The forward scattering amplitude of a spherical particle can be approximated by a series summation under low frequency assumptions [99, 108],

$$S(0,D) = jx^3(M_1 + M_2x^2 + M_3x^3 + M_4x^4 + M_5x^5 ...) \tag{4.97}$$

where x is the size parameter $x = \pi D/\lambda$, and coefficients M_i are functions of the refractive index of the water.

Marshall and Palmer first proposed the drop size distribution in the following form

$$N(D) = N_0 \exp\{-\Lambda D\} \tag{4.98}$$

$$\Lambda = \alpha R^{-\beta} \tag{4.99}$$

where N_0, α, β are constants, which are obtained through measurements.

Detailed theoretical and numerical analysis of rain attenuation is presented in [99] by applying Mie scattering calculation and different dropsize distributions. General rain attenuation is derived theoretically and simplified by an exponential relationship as

$$A_R = aR^b \quad \text{dB/km} \tag{4.100}$$

where a and b are functions of frequency and rain temperature. The resulting set of values for a and b is presented in both tabular and graphical form for the frequency range of 1 to 1000 GHz [99].

4.7.2 Crane's Rain Attenuation Model

Rain attenuation has been studied extensively by Crane [78]. Crane's rain attenuation model takes into account the variation of rain rates along a horizontal path. A path-averaged rain rate is calculated based on the point rain rate (rain rate measured at a single location). Measurement results from [109, 110, 111] were analyzed for path lengths of 5, 10, and 22.5 km. Results show that the average rain rate is related to the point rain rate by

$$\overline{R} = f_1(d)R^{1+f_2(d)} \tag{4.101}$$

where d is the path length, and $f_1(d)$ and $f_2(d)$ are empirically derived functions.

A theoretical prediction model was proposed by Crane based on the aR^b rain attenuation model and (4.101). The model is summarized in Equations (4.102) to (4.105) [78, 112].

$$\begin{aligned} A_R &= aR^b[\frac{e^{ubd}-1}{ub}] && (\text{ for } 0 \le d \le D_0) && (4.102)\\ &= aR^b[\frac{e^{ubD_0}-1}{ub} - \frac{B^b e^{cbD_0}}{cb} + \frac{B^b e^{cbd}}{cb}] && (\text{ for } D_0 \le d \le 22.5 \text{ km}) && (4.103) \end{aligned}$$

where

$$\begin{aligned} D_0 &= 3.8 - 0.6\ln(R)[\text{km}]; && B = 2.3R^{-0.17} && (4.104)\\ c &= 0.026 - 0.03\ln(R); && u = \ln[Be^{cD_0}]/D_0; && (4.105) \end{aligned}$$

and A_R is the rain attenuation in dB, R is point rain rate in mm/hr, and d is path distance in km. Multipliers a and b are rain attenuation coefficients, which are functions of frequency and polarization.

For paths longer than 22.5 km, the attenuation A_R is calculated for a 22.5 km path, and the resulting rain attenuation is multiplied by a factor of $(d/22.5)$. All the parameters are well tabulated for different *global rain climate zones.* The global geographic regions are divided into rain climate zones based on the rain rate statistics collected over several years. Point rain rate vs. time distribution has been tabulated for each rain climate region [78].

Example of Crane Model Calculation

In Virginia, for example, the rain rate climate region is D2 [78]. For vertical polarization, the coefficients a and b are 0.281 and 0.943 at 38 GHz , respectively. From the point rain rate vs. time distribution table, the rain rate is 49.0 mm/hr for 0.01% of a year for which this rain rate is exceeded. For this rain rate,

$$B = 2.3R^{-1.7} = 1.187 \tag{4.106}$$

$$c = 0.026 - 0.03 \ln R = -0.0908 \tag{4.107}$$

$$D_0 = 3.8 - 0.6 \ln R = 1.465 \text{ km} \tag{4.108}$$

For the 38 GHz point-to-point measurements presented in Chapter 5, the path lengths, d, are 206 m and 605 m. The predicted rain attenuation for measurements in Chapter 5, using the Crane model, is $A_R = aR^b[\frac{e^{ubD_0}-1}{ub}] = 2.3$ dB for the 206 m path, and 6.7 dB for the 605 m path at a rain rate of 49 mm/hr .

4.7.3 Rain Attenuation Measurement Results

Many experiments have been performed to characterize rain attenuation [78, 100]. In [100], 31 sets of experimental data collected by different authors were summarized and the statistical behavior of rain attenuation was investigated. Each of these measurement sets was performed over a period of 6 months or longer. From these measurements, 6 sets were performed over earth-space paths at

16, 19 and 30 GHz . The other 25 sets were performed over terrestrial paths ranging from 0.61 km to 80 km at frequencies from 11 to 100 GHz .

The results show that the distribution of rain attenuation A_R in dB is approximately lognormal with a standard deviation σ_A ranging from 4.6 to 7.1 dB for earth-space paths, and from 3.3 to 8.6 dB for terrestrial paths. The distribution of the *rain fade duration* [2], τ_R, is also approximately lognormal with a standard deviation σ_τ ranging from 4.4 to 7 dB for both earth-space and terrestrial paths.

The rain attenuation is a function of many random time-varying parameters of the medium. These parameters include the number of rain drops in the path, the raindrop shape, the drop size distribution, the spatial characteristics of the rain density along the path, the storm cell shapes and sizes, wind velocity, raindrop temperature, the presence of up or down drafts, and other effects [78, 100]. The lognormal distribution of the A_R is explained by the *central limit theorem*, assuming that the rain rate is affected by these factors in a multiplicative way. The central limit theorem states that if the random variables x_i are independent, then under general conditions, the PDF of their sum

$$x = \sum_{i=1}^{N} x_i \tag{4.109}$$

tends to a normal distribution as $n \to \infty$ [62]. If a random variable is the result of multiplication of other independent random variables

$$x = \prod_{i=1}^{N} x_i \tag{4.110}$$

then the logarithm of x is given by

$$10 \log_{10} x = \sum_{i=1}^{N} 10 \log_{10} x_i \tag{4.111}$$

or

$$x[\text{dB}] = \sum_{i=1}^{N} x_i[\text{dB}] \tag{4.112}$$

Applying the central limit theorem, the logarithmic value of x is normally distributed. This hypothesis explains the experimental results of lognormal distribution; however, there is no theoretical proof of how different factors affect the rain attenuation *multiplicatively.*

---

[2] Rain fade duration is defined as the time duration when the rain attenuation exceeds a certain threshold.

4.8 Other Outdoor Propagation Measurement Results

4.8.1 LMDS Applications

Millimeter-wave channel for LMDS applications are studied experimentally in [37, 38, 98]. The detailed setup of these three measurement campaigns is summarized in Table 4.

Table 4: Experimental Setup for LMDS Measurements.

References	[98]	[37]	[38]
City	Northglenn, CO, San Jose, CA	Boulder, CO	Brighton Beach, NY
Environment	suburban	suburban	urban
f_c (GHz)	28.8, 30.3	28.8, 30.3	28
Bandwidth	CW, 500 MHz	CW, 500 MHz	CW
Range (km)	0.5, 1.0, 2.0	2-7	≤ 6
h_{TX}(m)	12.2, 24.4	16, 40	95
h_{RX}(m)	1-2 (above roof)	1 (above roof)	4, 7.3, 11.3
Antenna BW_{TX}(°)	90(azim.), 20(elev.)	26	omni
Antenna BW_{RX}(°)	2.5	5.5	12(azim), 10 (elev)
Polarization	V, H	V	V

In [98], Papazian *et. al.* presented both CW and wideband measurements for LMDS over 0.5-,1.0- and 2.0-km suburban cells with foliated trees in Northglenn, Colorado and in San Jose, California. CW measurements were performed at 28.8 GHz and wideband (500 MHz) measurements were performed at 30.3 GHz. The transmitting antenna was a vertical horn antenna with 90° and 20° beamwidths in azimuth and elevation, respectively, and the receiving antennas were two dish antennas with 2.5° beamwidth. One dish was vertical polarized and the other one was horizontally polarized. The transmitter had a fixed location and two different heights of 12.2 m (40 ft) and 24.4 m (80 ft). The receiver locations were randomly chosen at houses within a quadrant cell of radius less than 500 m. Receiver antenna heights were 1-2 meters above the house rooftop. The area coverage probability is computed as the ratio of the number of receiver locations with sufficient power level, to the total number of tested receiver locations.

Area coverage estimates were found to vary considerably with cell size, transmitter antenna height, and required minimum signal level. Results show that strong signals are received only through unobstructed LOS links. Under clear weather conditions, foliage attenuation is the major propagation impediment for LMDS services. Similar results were also observed in [37]. *Short-term variation* measurement results show that Rician distribution predicts deeper fades than the measured values under clear weather conditions [98]. *RMS Delay spread* of up to 3 ns was measured with a threshold of 20 dB below LOS component. These multipath components may be caused by surface reflection, or multiple scattering due to tree leaves or other objects. A *depolarization* study showed that vegetation induced depolarization is more severe than rain induced depolarization. Results from [113] and [114] showed that signal XPD during rain remained above 24 dB for rain attenuation up to 30 dB. Cross-polarization measurements within 0.5 km cells showed signal XPD of 14 dB at an attenuation of 30 dB, which is 10 dB lower than the XPD during rain [37]. This depolarization was caused by vegetation within the measurement cell.

In [37], Papazian *et al.* presented wideband measurements at 30.3 GHz for LMDS study in a suburban neighborhood in Boulder, Colorado. Transmitters were located at heights of 16 m and 40 m above ground in a 13-story apartment building. Receiver locations were chosen at one- and two-story single family homes and one- to three-story townhouses. At these locations, the receiver antenna was raised 1 m above the house roof height. For the transmitter antenna height of 40 m, the multipath rms delay spread was between 0.8 and 10 ns with a median value of 1 ns using a 10 dB threshold. For the antenna height of 16 m, rms delay spread varied mainly between 0.7 ns and 5.5 ns. The measured excess path loss relative to free space LOS ranged between -6 dB (i.e. the measured path loss is 6 dB less than the free space path loss) and 35 dB, and the medium value ranged between 15 dB and 18 dB for 45 receiver stations and two transmitter heights.

In [38], Seidel *et al.* performed narrowband measurements at 28 GHz in Brighton Beach, NY, to investigate path loss and the presence of specular reflections as a function of antenna height. The Cellular Vision (see Section 1.3.1) [3] broadcast signal was used as transmitted signal. In the measurement campaign, a standard horn antenna was used at the receiver. The transmitter was

---

[3] Cellular Vision systems have a cell radius of 4.8 km, a bandwidth of 20 MHz for each channel, and a radiated power of 10 mW per channel. In typical Cellular Vision systems, omnidirectional antennas are used at the transmitter and fixed-phased-array antennas are used at the receiver [115].

located on a 95 m tall apartment building, and 77 discrete receiver locations were chosen within a distance of 6 km from the transmitter. At each receiver location, the receiver antenna was rotated by 360 degree in azimuth at three different antenna heights of 4 meter, 7.3 meter and 11.3 meter above ground level. Angle-of-arrival measurements show detectable specular reflections at many locations. These specular reflections may potentially be used to reduce system coverage holes.

Passive Repeater Study

Passive repeaters are typically metallic, strong reflectors that can be used to redirect (reflect) micro- or millimeter-wave signals over or around obstructions. Passive repeaters are used at microwave frequencies to increase the received signal power level in obstructed regions and increase the system coverage area.

In [37], CW measurements at 28.8 GHz were performed for passive repeater study. The repeater loss is given by [116]

$$L_{pr}(\mathrm{dB}) = P_t + G_t + G_r + G_{pr} - P_r - L_{fs}(r_1) - L_{fs}(r_2) \tag{4.113}$$

where L_{pr} is the passive repeater loss, P_r is the received power, P_t is the transmitted power, G_t is the transmitter antenna gain, G_r is the receiver antenna gain, $L_{fs}(r_1)$ is the free space path loss, and G_{pr} is the repeater gain given by

$$G_{pr} = 20\log_{10}(4\pi A\cos\alpha/\lambda^2) \tag{4.114}$$

where A is the repeater area, α is the incident angle, and λ is the wavelength. Passive repeater gain is defined as the difference (in dB) of the power density at a distant point due to the passive repeater to the power density which would exist at the same point if the passive repeater were replaced by a matched, isotropic antenna of 100% ohmic efficiency and fed with RF power equal to that accepted by the passive repeater [116].

In [37], repeater loss of a 1.2 m^2 aluminum reflector was measured. Measurements showed 4-6 dB repeater loss and 16-24 dB XPD at incident angle of 1.5° to 54.5° at 28.8 GHz. The authors attribute the repeater loss to the scattering off the tripod, which supported the repeater, and the fact that the repeater surface was not perfectly flat.

4.8.2 Street-Level-Propagation

In [10], Violette *et. al.* presented measurement results on point-to-point transmission at street level. Both LOS and non-LOS propagation were studied using wideband and narrowband measurement systems operated in the upper microwave and millimeter-wave bands. Three measurement campaigns over a three-year period were reported. Two operating systems were used for these measurements. Using the first system, CW measurements were performed at 9.6, 28.8 and 57.6 GHz. Using the second system, CW measurements were performed at 11.4 and 28.8 GHz, and wideband measurements (with 1 GHz RF bandwidth) at 30.3 GHz.

Non-LOS measurements through buildings were performed by placing the antennas on opposite sides of the building and pointing them perpendicular to the building walls. The excess path loss (with respect to free space) through steel reinforced concrete or brick buildings was about 84 dB at 9.6 GHz and more than 100 dB at 28.8 and 57.6 GHz [10]. When both antennas were rotated in the elevation plane, the received signal power was maximized when both antennas were pointed towards the roof edges. This indicates the flat rooftop supported a diffraction mode that has a path loss lower than the penetration loss through the building.

Propagation through metalized glass exhibited 25 to 50 dB loss for each metalized layer, but small loss was measured through clear glass [10]. Reflection measurements were performed for a variety of building surfaces. The reflection measurement results are presented in Section 4.4.4.

Unlike LMDS, where the transmitter and receiver are located above the majority of obstacles, street-level propagation is much more confined by the surrounding objects. Multipath reflections due to ground, wall, signs, cars, or other flat surfaces, must be considered in channel characterization. Multipath signals were detected in the street-level propagation, even with narrow-beam antennas ($2-3°$) at heights of 2-3 m above street level [10]. Multipath caused by ground reflection resulted in fades in excess of 30 dB, and multipath delay of less than 1 ns. Reflections from building walls and other surfaces resulted in multipath components that were at least 15 dB below the LOS component and with delay time greater than 10 ns.

In [117], ray tracing techniques are used to predict wideband channel impulse response for street-level millimeter-wave propagation. Surface reflection is modeled using Snell's reflection coefficient with a roughness factor. Predicted results showed general agreement with measurement results in terms of average received power and delay spread. However, due to the lack of detailed site information, ray tracing only provided qualitative knowledge of the channel in [117].

4.9 Outdoor Propagation Study at 60 GHz

Path loss at 60 GHz was studied by Correia *et al* in [118, 119]. In [119], a path loss model was proposed for received signal power estimated on the basis of a path loss exponent model (2.6) as follows

$$PL(d)\ [\text{dBm}] = PL_{fs}(d_0)[\ \text{dB}] + 10n\log_{10}(\frac{d}{d_0}) + (A_R + A_O)[\ \text{dB/km}]\cdot d[\ \text{km}] \tag{4.115}$$

where A_R and A_O are attenuation coefficients due to rain and oxygen absorption, respectively, and the other parameters are defined in the path loss exponent model in (2.6). In [118], results from CW measurements along a street show that if the path loss exponent model (2.6) is used, the range for n is from 2.3 to 2.8 for $d \in$ [0,250] m, and from 7.0 to 7.5 for $d \in [1, 2]$ km. When model 4.115 is used to separate the effects of oxygen absorption, the n values is in the range from 2.0 to 2.5.

In [120], fading characteristics are studied along a canyon-like street at 60 GHz. The transmitter was fixed in the middle of the street at a height of 3 m above the ground. CW measurements were taken as the receiver was moved along the street. The transmitter antenna had a beamwidth of 25°, and the receiver antenna was an omnidirectional slot antenna. Results show that the small-scale fading was well described by the Rician distribution.

4.10 Literature Survey on Indoor Propagation Measurements

4.10.1 Narrowband Measurement Results

CW measurements were performed in [8, 70, 121, 122] to characterize a narrowband millimeter-wave channel. Main measurement results include path loss exponent, penetration loss through walls and other obstructions, and received signal PDF.

Path Loss Exponent

Path loss exponent measurement results are summarized in Table 4.10.1. In [121], Kalivas et al performed CW measurements on the third floor of an engineering building at Carleton University. The floor area was $30 \times 45m^2$. In [8], Kajiwara performed CW measurements at 94 GHz in a hall, room and corridor on an office building floor. The floor and walls were made of reinforced concrete and plaster boards, respectively. In [123], Bultitude et al performed wideband measurements at 40 GHz in two office buildings using a VNA system. The received signal power was measured as the sum of the power at each frequency component multiplied by a calibration factor. Scatter plots were developed for the TR separations of $d < 25m$, and $25m < d < 40m$.

Path loss exponent was found to be 1.2-1.8 for LOS, and 3-4 for non-LOS (NLOS) propagation [8, 121]. Note that in LOS propagation, the path loss exponent is less than the free space path loss exponent of 2, i.e. the received signal power is higher than the free space LOS power. This indicates that strong reflected waves are received along with the LOS component. As shown in [14], the spatial average received power is the sum of the power of individual multipath components. Therefore, the total received power is the sum of LOS power and the power of reflected waves. One prominent example is wave propagation in corridors or tunnels, where the wave guide effects of surrounding walls reduce the path loss exponent to be less than 2 [121, 124]. For NLOS paths, the received signal is attenuated by walls or other obstructions, which results in a high path loss exponent.

Penetration Loss

Excess penetration loss due to wall, door, or other obstacles at millimeter-wave frequencies is measured in [8, 70, 92, 121, 125, 126]. The results are presented in Table 4.10.1. For comparison purposes, measurement results at 1.3 GHz from [127], and results at 5.85 GHz from [2] are also presented.

In [8, 70, 125, 127], the penetration loss was measured directly by comparing the received signal power through the obstruction with the received signal power in free space at the same TR separation. In [2, 121], the path loss was measured over many NLOS paths, and the penetration loss

Table 5: Summary of Measured Path Loss Exponent Results

Ref.	Path	f (GHz)	n	Environments
[121]	LOS	21.6	1.2	Along corridor
	LOS	37.2	1.65	Along corridor
	NLOS	21.6	2.95	1-4 wall obstructions
	NLOS	37.2	3.3	1-4 wall obstructions
[8]	LOS	94	1.2-1.8	In a hall and a room
	LOS	94	1.2-1.8	In a corridor
	NLOS	94	3.6-4.1	In an office building floor
[123]	<25 m	40	1.5	Open concept office area
	25 - 40 m	40	4	Open concept office area

was found by optimization procedures that minimize the mean square error (MSE) between the measured and modeled path loss values.

As shown in Table 4.10.1, prominent increase in penetration loss through a dry concrete wall is observed as the carrier frequency changes from 1.3 GHz to 37.2 GHz. The lower penetration loss into exterior concrete building walls imply that microwaves have certain advantage in providing wireless access into buildings. Also, a consistent increase in penetration loss was measured as the frequency increases from 9.6 GHz to 28.8 GHz and 57.6 GHz through different material such as plywood and aluminum [125]. However, comparison of the penetration loss through plaster board walls at 5.85 GHz and 37.3 GHz does not show obvious trend.

Received Signal PDFs

At microwave frequencies, measurements have shown that the local mean power obeys a lognormal distribution [14, 128]. The lognormal distribution describes the random shadowing effects which occur over a large number of measurement locations with the same transmitter and receiver separation but different levels of clutter [14]. In [8], distribution of local mean power is studied from CW measurements at 94 GHz. Under LOS conditions, the local mean power was found approximately

Table 6: Summary of Penetration Loss Results

Reference	Obstruction	d(cm)	Loss (dB)	f (GHz)
[70]	concrete wall	75.2	43	37.2
	plasterboard wall	12.5	3.45	37.2
	wood door	4.5	0.45	37.2
	door with glass	0.4	0.56	37.2
	human body	-	35.2	37.2
[121]	double plasterboard wall	-	5.4	37.2
	double plasterboard wall	-	3.7	21.6
[8]	human body	-	15-25	94
[125]	dry plywood (1 sheet)	1.9	1	9.6
	dry plywood (1 sheet)	1.9	4	28.8
	dry plywood (1 sheet)	1.9	8	57.6
	dry plywood (2 sheet)	3.8	4	9.6
	dry plywood (2 sheet)	3.8	6	28.8
	dry plywood (2 sheet)	3.8	14	57.6
	wet plywood (1 sheet)	1.9	19	9.6
	wet plywood (1 sheet)	1.9	32	28.8
	wet plywood (1 sheet)	1.9	59	57.6
	wet plywood (2 sheet)	3.8	39	9.6
	wet plywood (2 sheet)	3.8	46	28.8
	wet plywood (2 sheet)	3.8	57	57.6
	aluminum (1 sheet)	0.32	47	9.6
	aluminum (1 sheet)	0.32	46	28.8
	aluminum (1 sheet)	0.32	53	57.6
[127]	concrete wall	-	13-20	1.3
[2]	brick wall	-	12.5-16.4	5.85
	cinderblock wall	-	22	5.85
	plasterboard wall	-	3.6-5.6	5.85

Table 6: Summary of Penetration Loss Results - Continued

Reference	Obstruction	d(cm)	Loss (dB/cm)	f (GHz)
[92, 126]	Stone wall	-	5.73	60
	Marble wall	-	1.25	60
	Concrete wall	-	6.67	60
	Aerated concrete wall	-	3.7	60
	Tiles	-	7.81	60
	Glass	-	6.05	60
	Acrylic glass	-	1.03	60
	Plasterboard wall	-	1.51	60
	wood wall	-	4.22	60
	Clipboard wall	-	5.15	60

lognormally distributed with standard deviation of 0.6 - 1.8 dB for a hall and a room, and 4-5 dB for a corridor.

As shown in Section 2.2.2, the distributions of the received signal envelope in small scale fading channels are described by PDFs. For millimeter-wave indoor channels, received signal power PDFs almost always obey Rayleigh distribution for NLOS propagation [121]. However, for LOS propagation, there are no consistent results from the literature. It is found in [129], that when there is a LOS path, the signal PDF departs from a Rayleigh distribution and tends to follow a Rician distribution. In [121, 122], received signal power PDF was found to follow a Rayleigh PDF for LOS propagation. This is explained by the existence of numerous reflected rays, which are comparable to a LOS path. The received signal consists of both these coherent waves and numerous scattered incoherent waves [4]. This situation is not mathematically described by Rician, Rayleigh, or TIP distributions. However, as the quantity of the coherent field components increases, the resulting PDF will be close to Rayleigh PDF based on the law of large number [62]. When the quantity of the coherent field components approaches two, the resulting PDF will be close to TIP. When there is only one coherent field component, the PDF is Rician. The extension of the PDF class for the

---

[4] Note that this is consistent with the measurement results of path loss exponent, where strong reflected waves increase the total received power and reduce the path loss exponent.

cases when the number of coherent waves is two or more can explain the measured PDFs that do not fit into the classical PDFs [49].

Other CW Measurements

In [8], Kajiwara studied performance of *artificial reflectors*(passive repeaters). The measurements were performed in two NLOS environments as shown in Figure 39. Measurement results show that in NLOS locations, the received signal power can be increased by 10-25 dB by using a reflector plate of 0.2 × 0.2m depending on the curvature radius and size of the convex reflector.

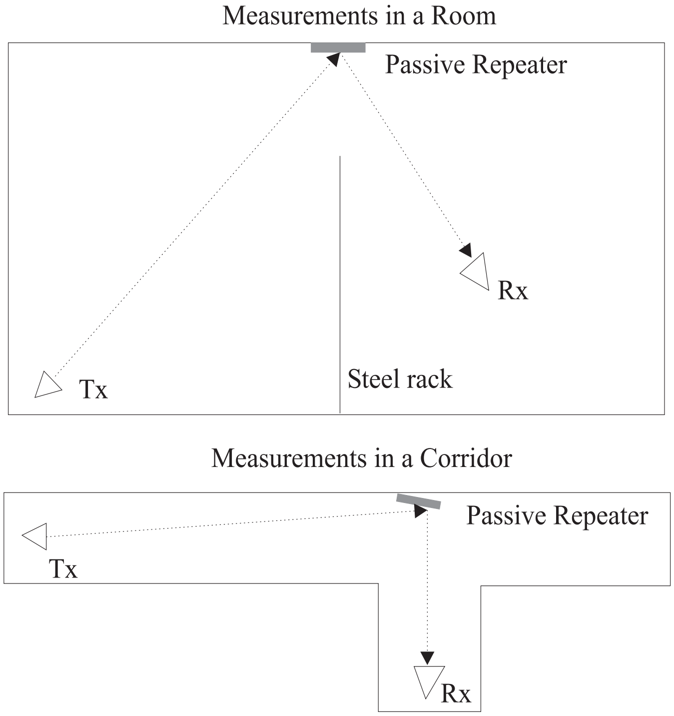

Figure 39: Passive repeater measurements [8].

In [122], Hammoudeh *et al* performed CW measurements at 60.4 GHz and 38.25 GHz in a $9 \times 10.8 \times 2.7$m empty room and a $27.5 \times 1.6 \times 2.7$m corridor using omnidirectional antennas. The transmitter was fixed at the end of the corridor or in the corner of the room. The receiver was moved along the corridor and the diagonals of the room. Measurement results were compared with ray tracing results. Ray tracing with second order specular reflection produced well matched results with the measured spatial fading signals. This indicates that for indoor millimeter-wave channels, multipath is dominated by LOS and reflections.

4.10.2 Wideband Measurement Results

Wideband measurement campaigns are reported in [11, 12, 123, 130]. Measurement results show that multipath channel dispersion is highly dependent on antenna directivity and polarization [11, 12]. In this section, the influence of antennas on multipath channel is studied in details.

Effects of Antenna Directivity

The effects of antenna diversity on multipath dispersion in indoor millimeter-wave system is studied in [11, 123]. Manabe *et al* performed wideband channel measurements at 60 GHz in a 13.51×7.81m office room using four different receiving antennas: an omnidirectional antenna, a scalar feed horn antenna with 60° beamwidth, a standard gain horn antenna with 10° beamwidth, and a scalar lens horn antenna with 5° beamwidth. The transmitting antenna was an omnidirectional monopole antenna. Only one transmitter-receiver location was measured, and the results, as shown in Table 7, indicate obvious reduction of multipath dispersion as the antenna beamwidth decreases.

Table 7: Measured Delay Spreads for Different Types of Antennas [11]

Antenna Type	omni	scalar feed horn	standard gain horn	scalar lens horn
3-dB beamwidth	-	60°	10°	5°
Delay spread (ns)	18.08	13.59	4.7	1.05

Measurements in [123], however, showed only slight reduction of delay spread when a directional antenna is used instead of an omnidirectional antenna. In [123], Bultitude *et al* performed wideband measurements at 40 GHz for two open office areas of different sizes in two different buildings. An omnidirectional and a pyramidal horn antenna with a beamwidth of 12° in both planes were used at the transmitter, and an omnidirectional antenna was used at the receiver. The transmitter antenna was fixed in the center of measurement area at a height of 2.13 m, and the receiver antenna was moved around the area at a desk level height. When the horn transmitter antenna was used, the measurement locations were all inside the area covered by main beamwidth of the horn antenna. A total of 669 receiver locations were measured. The RMS delay spread was found to be 19 ns for the small office area, and 45 ns for the large office area for 90% of the time. CDFs of RMS delay spread values for directional and omnidirectional antennas showed only slight reduction in the delay spread when the directional antenna was used. The authors conclude that there was no advantage in using a horn antenna instead of an omnidirectional antenna in this case. Furthermore, measurement results show a significant increase of multipath dispersion when the receiver was moved into the area outside the transmitter antenna main beamwidth.

In general, a directional antenna reduces multipath dispersion of the channel. However, the degree of reduction depends on the antenna beamwidth and specific propagation environments.

Effects of Antenna Polarization

Due to the different magnitude and phase of reflection coefficients for vertical, horizontal and circular polarizations, millimeter-wave channel characteristics also depend on the polarization of the antennas used. The polarization dependence of multipath propagation characteristics of an indoor millimeter-wave channel is investigated in [12]. The transmitter antenna was a scalar horn with 3-dB beamwidth of 60°, the receiver antenna was a scalar lens-horn antenna with a beamwidth of 4.6°. Both antennas were switched among vertical, horizontal, and right-hand circular polarizations. Measurements were performed in an empty office with floor area of 90 m^2 with the transmitter in a corner, and two receiver locations in the center of the office. The impulse response was measured with the receiver antenna rotating in azimuth every 5°. Measurement results, as presented in Table 8, show a slight reduction of multipath dispersion by using horizontal polarization, and a large reduction by using circular polarization as compared to vertical polarization. This relationship is expected. When a circular polarized wave is incident on a reflecting surface at a large incident angle, the direction of polarization of the reflected wave is reversed [131]. Therefore, multipath components resulting from single reflections are rejected by the receiver antenna, leading to a reduced number of multipath components. It is worth mentioning that similar results are also obtained by Kajiwara at 10 GHz, and Rappaport and Hawbaker at 1.3 GHz and 4 GHz [132, 133].

Table 8: Measured Delay Spreads for Different Polarization of Antennas [12]

	H-Polarized	V-Polarized	Right-Hand Circular Polarized
Delay Spread(location 1) (ns)	11.02	9.96	5.66
Delay Spread(location 2) (ns)	11.08	10.07	4.68

Other Wideband Measurement Results

The indoor multipath propagation channel was studied at 1.7 GHz and 60 GHz in [134]. Wideband propagation measurements were performed using a SCS with 200 MHz of RF bandwidth. For the 1.7 GHz system, omnidirectional antennas were used for both the transmitter and the receiver. For the 60 GHz system, a 20 dB horn antenna was used at the transmitter, and either a 20 dB horn or an omnidirectional antenna was used at the receiver. Measurements were performed in two laboratories ($10 \times 10m$ and $15 \times 30m$) and one corridor ($3 \times 30m$) at University of Bristol, UK. The measured RMS delay spread was always below 50 ns at 1.7 GHz, and below 40 ns at 60 GHz. These difference can be attributed to building material attenuation, frequency dependence of reflection coefficients, and different antenna types used. Results also show that the wall attenuation is on the order of 15 dB per wall. Therefore, excess path lengths of the multipath components are small, and the effect of oxygen absorption is negligible [134].

Wideband measurements were performed by Smulders and Wagemans at 58 GHz using a VNA system with a sweeping bandwidth of 2 GHz. Omnidirectional biconical antennas were used at the transmitter and the receiver. Measurements were performed in eight different indoor environments at the Eindhoven University of Technology. Due to the high attenuation of the inner walls, these environments consist of a single room, a single hall or a single corridor only. Typical RMS delay spread was between 15 to 45 ns for small rooms and 30 ns to 70 ns for large rooms. The worst case RMS delay spread was 100 ns .

4.10.3 AOA Measurements

In [12], channel impulse response was measured by rotating the receiver antenna in azimuth every 5°. The measurement set up is explained in Section 4.10.2. The main purpose was to demonstrate antenna polarization effects on multipath delay dispersion rather than to achieve AOA statistics. Therefore, AOA was measured at only two receiver locations.

In [130], Droste and Kadel performed wideband indoor measurements at 17 GHz and 60 GHz. A VNA and a mechanical positioning system were used to investigate spatial variation of channel impulse responses. The time resolution was 0.5 ns by using 2 GHz of sweep bandwidth. Measurements were performed in a room of 2.49 m × 4.87 m and in a corridor of 2 m × 17.8 m. In the room, the transmitter was located in the corner, and the receiver was moving along a 1 m track in the center of the room. In the corridor, the transmitter was at the end of the corridor, and receiver track was about 12 m from the transmitter. AOA information was reconstructed by connecting the delay time information with the information on the geometrical locations of the reflectors. Unfortunately, antenna information and other detailed measurement and modeling information were not presented in the paper.

4.10.4 Spatial Diversity

In a small scale fading situation, signals received from spatially separated antennas have essentially uncorrelated envelopes when the separation is large enough [47, 135, 136]. The probability of simultaneous fades in both signals is much lower than the probability of fade in an individual signal. In spatial diversity techniques, two or more spatially separated antennas are employed, and the received signals from these antennas are combined to produce the received information. When the diversity technique is used, the transmitted power can be reduced to achieve the same system availability as in a system without diversity. This reduction of transmitted power in dB represents *diversity gain* [121, 136].

Due to the short wavelength at millimeter-wave frequencies, the received signals become decorrelated at short separation distances on the order of several centimeters. Spatial diversity techniques at millimeter-wave frequencies were studied by Kalivas *et al* in [121]. CW measurements were performed at 21.6 and 37.2 GHz in an indoor environment at Carleton University. Received signal powers were measured from two sets of receiver antennas, which were placed several (8 to 14) wavelength apart. The sampling speed was 2000 sample/s, which corresponds to 60 and 34 samples per wave length at 21.6 GHz and 37.2 GHz, respectively. Measurements were taken at 38 locations of a $30 \times 45m^2$ office area consisting of small offices, medium-size rooms, large classrooms and corridors. A biconical antenna was used at the transmitter, and both biconical and horn antennas were used at the receiver. The beamwidths of the horn antennas were 25° at 37.2 GHz and 31° at 21.6 GHz. Results show that antenna diversity effectively reduces signal fading. The average diversity gains with selection combining and 99% availability varied between 9.6 dB and 10.1 dB. These results are close to the expected value of 10 dB, which is the theoretical diversity gain for a Rayleigh fading channel.

4.10.5 Coherent Bandwidth

In [137], Hammoudeh *et al* measured channel *coherent bandwidth* in an indoor microcell environment at 62.4 GHz. In [137], correlation bandwidth is estimated by measuring correlation coefficients of channel responses at 34 different frequency separations between 5 and 240 MHz. For each frequency separation, channel responses were taken at two frequencies at a rate of 6000 sample/s. Measurements were performed in a $1.92 \times 41 \times 2.68$ m corridor with the transmitter fixed at one end and a receiver moving towards the other end. Correlation coefficients between the measured signal envelopes as functions of distance were obtained by calculating the correlation over a window of 40λ which is moved by 10λ. Results show a decrease of the correlation coefficient with the increase of separation bandwidth. Frequency spacing of 237.8 MHz, 28.4 MHz and 2.8 MHz will ensure a correlation level below 0.5, 0.7, and 0.9, respectively, for 90% of time. According to (2.17), a corelation bandwidth of 2.8 MHz gives 7.14 ns of RMS delay spread.

4.10.6 Human Induced Variation

For indoor wireless LAN applications, one of the main sources of channel variation is the movement of people in the vicinity of the fixed terminals [138]. Human induced temporal variation of the indoor millimeter-wave channel is studied by Marinier *et al* in [138]. CW measurements were performed at 30 GHz with a *fixed* transmitter and receiver, with 0 to 4 people walking along paths parallel or perpendicular to the LOS path. Two types of transmitter antennas were used: an omnidirectional biconical antenna and a scalar horn with a 10dB beamwidth of 120°. Omnidirectional biconical antenna was used at the receiver. The transmitter antenna was located on the ceiling in the center of the room.

In a local area, received signal power level changes as the receiver moves from one position to another due to the small scale fading. In [138], the fading state of a fixed receiver is characterized by a *spatial fading level*, R, which is defined as

$$R(x_0) = \frac{P(x_0)}{\overline{P(x)}} \tag{4.116}$$

where x_0 is the specific location, $P(x_0)$ is the received signal power at this location, and $\overline{P(x)}$ is the spatial average power over the small local area around x_0.

Measurement results show that the effects of human motion on the *time average* received power depends highly on the *spatial fading state* that the receiver was in when the environment was free of movement. When the receiver is located in a spatial crest, i.e. the received signal power is higher than the local average, the movement of people (1-4) has little effect on the mean signal level. However, when the receiver is located in a deep fade, the movement of people will significantly increase the mean signal level. As the number of people increases, this dependence becomes less important. Measurement results also show that the coherent time with correlation of 50% is no greater than 3 ms for a walking speed of 0.9 m/s to 1.5 m/s.

In [73], Bultitude *et al* also studied temporal fading for a fixed transmitter and receiver in an indoor environment at 40 GHz. The temporal variation occurred when there was motion around the transmitter or receiver. Results show that fading is Rician for 50% of the time, and Rayleigh in a few instances, but does not confirm with either of these distributions the rest of time.

4.11 Research Directions

The proper design of future-generation wireless systems will require an intimate knowledge of the *wideband* millimeter-wave channel in any environment and *under any weather conditions.* Although many channel models and measurements have been produced for Cellular, PCS and microwave frequencies, broadband millimeter-wave channel modeling is in its infancy. The desired millimeter-wave channel models must fully quantify signal path loss, channel time dispersion, signal variation, and signal angular spread under any weather conditions.

One of the main difficulties associated with millimeter-wave propagation is the random nature of the propagation medium. Due to the small wavelength, most of the building or object surfaces appear as rough surfaces, and vegetation or atmospheric particles (such as rain or hail) appear as random scatterers. The literature search showed some research results in millimeter-wave propagation, including signal path loss, system coverage, multipath dispersion, rain and vegetation induced attenuation and depolarization [7, 77, 93]. However, little research has been done to characterize *weather effects on the multipath dispersion.* The time dispersion characteristic is the determining factor for the maximum data rate, time diversity or rake receiver design, and must be determined for wideband system design.

Another great challenge is the space-time channel characterization. Future broadband wireless systems explore dimensions of space, time and frequency. When highly directional antennas and wideband signals are used, spatial and temporal characteristics of the channel become extremely important. For indoor applications, the multipath channel structure may vary significantly from location to location. Ray tracing techniques have been used to model the millimeter-wave channel; however, little literature exists that carefully compares the ray tracing prediction with measured detailed multipath structure.

The following chapters focus on the above mentioned two aspects of millimeter-wave channel characterization. Chapter 5 presents an extensive measurement campaign at 38 GHz. The weather effects on the channel time dispersion and signal variation during rain and a hailstorm were investigated. The ratio of coherent power and incoherent power at various rain rates was also studied.

Based on the measurement results, a novel design technique for wideband millimeter-wave channel characterization was developed and presented in Chapter 6. Finally, Chapter 7 presents the space-time channel characterization at 60 GHz.

Chapter 5

Wideband Point-to-Point Radio Wave Propagation Study at 38 GHz

This chapter presents the results of a fixed millimeter-wave short-hop radio wave propagation study at 38 GHz . A wideband measurement campaign was performed using three cross-campus radio links from April to August 1998 at Virginia Tech. These links represent typical LMDS links in a campus environment with various levels of obstruction due to vegetation and reflections from buildings. A total of 73,963 power delay profiles (PDPs) were recorded during different weather events such as clear sky, rain, and hail.

The measurement campaign produced a variety of results including wideband power delay profiles (PDPs), short term signal variation due to rain, and attenuation due to rain, hail, glass, and vegetation. The results show that the measured rain attenuation (in excess of free space) slightly exceeds the Crane model prediction. Short term variation of received signal strength during rain follows a Rician distribution with a K factor inversely proportional to rain rate. The wideband measurements indicate that multipath can occur due to foliage and reflections from wet surfaces during rain. A theoretical study of signal variation during rain is also presented. The theory shows that the signal variations are likely due to the inhomogeneous density distributions of rain drops along the propagation path.

5.1 Introduction

Millimeter-wave frequencies are proposed to provide LMDS, NGI, and "wireless fiber" links to homes with much higher bandwidth than current systems at UHF or microwave frequencies. Time dispersion of the channel is the main limiting factor for the maximum data rates of these wideband systems. Furthermore, channel time dispersion characteristics may change during different weather events. At frequencies above 10 GHz , one must consider the interaction of EM waves with the atmosphere, and particles such as rain, snow and hail in addition to other terrain reflectors and scatterers [17, 75, 78]. Therefore, it is extremely important to characterize the *wideband* millimeter-wave channel *under different weather conditions.*

Some research results have been published for millimeter-wave channel characterization under clear weather conditions. Multipath and coverage issues for LMDS are studied in [37, 38]. Point-to-point transmissions at street level are investigated in [125]. Building scattering and propagation through vegetation are studied in [77, 93, 139]. Other works ([78, 100]) address rain attenuation and depolarization effects on the millimeter-wave channel. However, little research has investigated the multipath and time varying nature of the wideband millimeter-wave channel in different weather events.

This chapter presents one of the first studies of wideband (200 MHz RF bandwidth) propagation under different weather conditions at 38 GHz over short-haul (less than 1 km) links. The goal of the measurement campaign was to measure not only the *rain/hail attenuation*, but also the *channel time dispersion* and *signal variation under different weather conditions.*

5.2 Measurement Setup

5.2.1 Measurement System

PDPs were measured using a *sliding correlator channel measurement system* with a null-to-null radio frequency bandwidth of 200 MHz , thereby providing a multipath time resolution of 10 ns [45, 67, 140]. The system provided an effective isotropically radiated power (EIRP) of 40 dBm

, a measurement speed of 50 PDPs per second and a multipath dynamic range of 25 dB . A switch was built in the system to support two modes of operation: *spread spectrum mode* for wideband measurements, and *continuous wave (CW) mode* for system alignment and calibration. The transmitting antenna is a horn with a maximum gain of 19 dB and half power beamwidths of 45^0 and 6.5^0 in azimuth and elevation, respectively. The receiver antenna is a parabolic reflector with a maximum gain of 39 dB and half power beamwidths of 1.5^0 in both azimuth and elevation. Both antennas are vertically polarized. Details of the measurement system are presented in Chapter 3.

Weather Station

For the measurement campaign, a weather station from Davis Instruments was used to record weather data including temperature, rain precipitation, humidity, wind direction and speed. The rain gauge utilizes a tipping bucket design, and the minimum resolvable rain rate for this rain gauge is 0.01 in/min, or 15.24 mm/hour. The equipment is set up on the rooftop of the building where the transmitter or receiver is located. Figure 40 shows the rain gauge and the wind speed detector on the rooftop of the Johnson Student Center.

The weather conditions are automatically downloaded into a portable computer every minute. Both weather data files and channel responses are saved with time and date, so that the channel measurement results can be exactly matched to the weather conditions under which the measurement files are taken.

5.2.2 Measurement Sites

Measurements were conducted via three links across the Virginia Tech campus. The first link, L1, provided a 605 meter, unobstructed LOS path. The second link, L2, provided a 262 meter, obstructed path due to the dense canopy of a large oak tree. The third link, L3, provided a 262 meter, partially obstructed path due to nearby oak tree leaves that would obstruct the LOS path during windy conditions.

The geometry and picture of link L1 are presented in Figures 41, and 42. Link L1 provides an unobstructed LOS path from Slusher Hall to Whittemore Hall. For this link, the transmitter is

Figure 40: Weather monitoring system on rooftop of GBJ Student Center.

located on the thirteenth floor of Slusher Hall, the tallest building on the campus, and the receiver is placed on sixth floor of Whittemore Hall. As the figures demonstrate, LOS exists between the transmitter and receiver. The possible scattering objects are the Burruss Tower, rooftops of Burruss Hall and Hancock Hall. All the objects have at least three Fresnel zone clearances from the LOS path. The Burruss Hall roof was in the main lobe of both the transmitter and receiver antennas.

The geometry and picture of links L2 and L3 are presented in Figures 43, and 44. Links L2 and L3 provided 262 m obstructed and partially obstructed paths from McBryde Hall to the Johnson Student Center, respectively. The transmitter was located on the sixth floor of McBride Hall, and the receiver was placed on the second floor of the Johnson Student Center. The surrounding buildings provide clearance of at least three Fresnel zones, but there are some trees between the transmitter and receiver. Two offices from the sixth floor McBride building were used for transmitter locations. For link L2, the LOS path is heavily obstructed by the tree leaves. For link L3, the LOS path is not obstructed under calm weather conditions, however, it can be obstructed by the nearby tree leaves during windy conditions. Measurements via path L2 and L3 provide insight to the relationships between weather effects, scattering objects and radio wave propagation at 38 GHz .

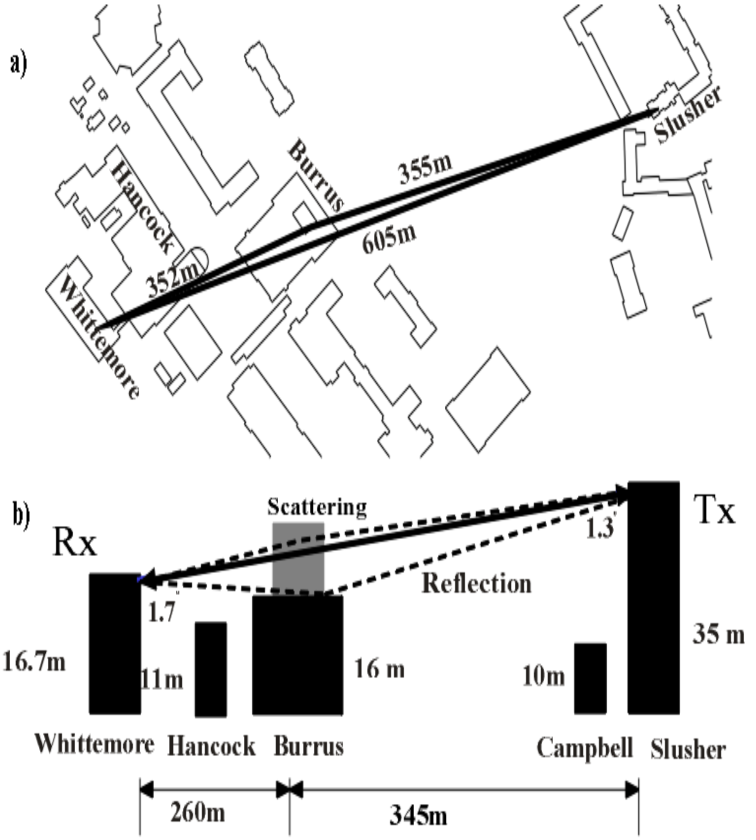

Figure 41: Geometry of the Slusher-Whittemore link: 605 m unobstructed LOS (L1). (a) top view. (b) side view.

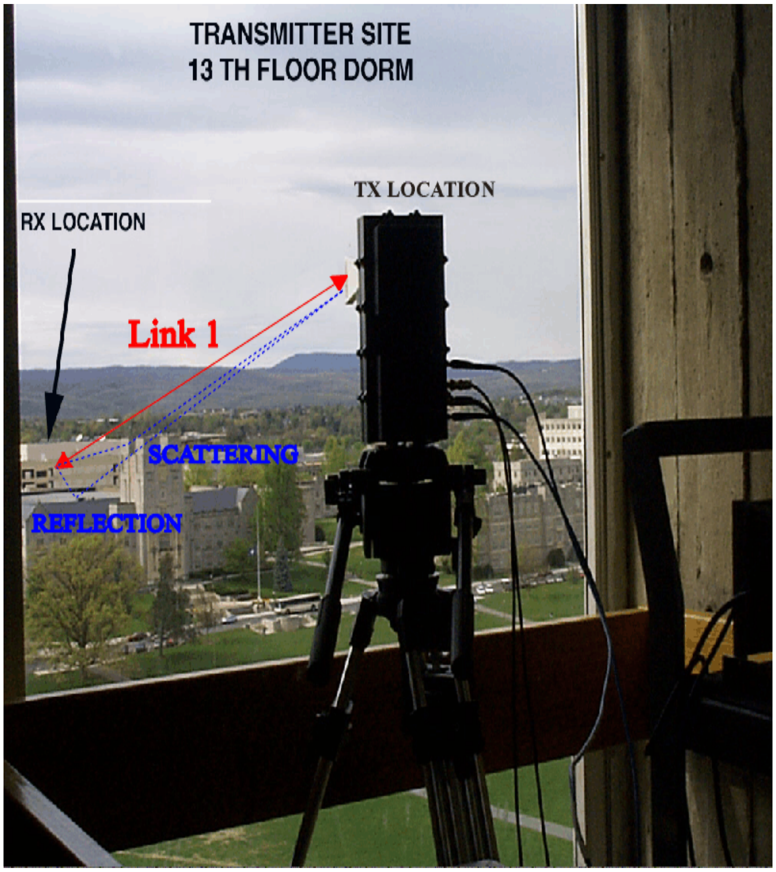

Figure 42: View from transmitter on L1.

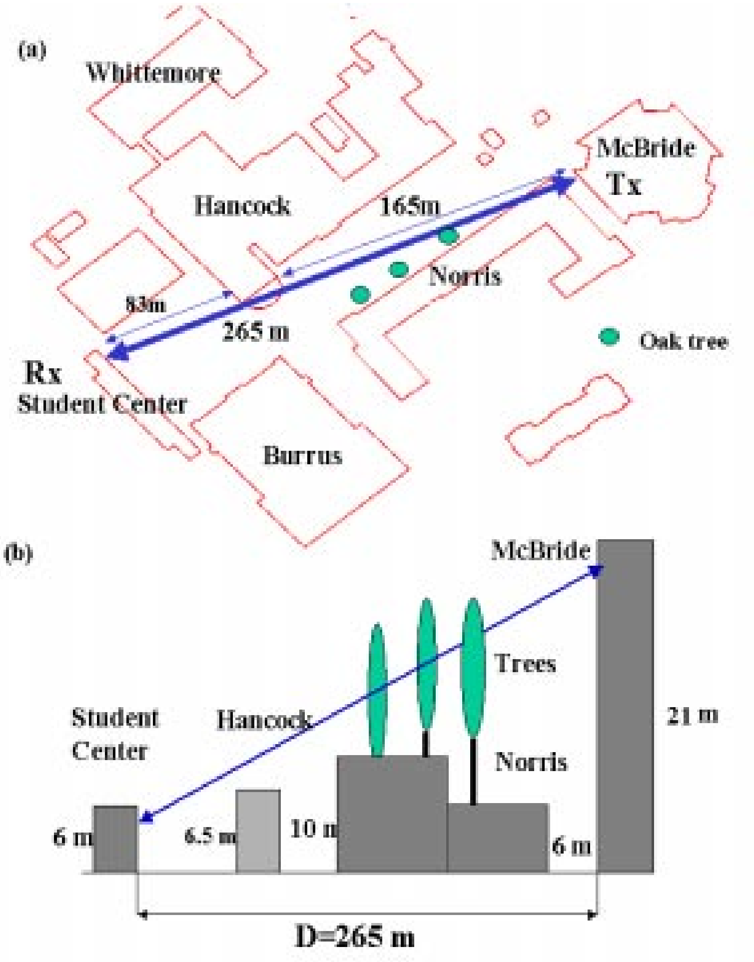

Figure 43: Geometry of the McBryde - Student Center link: 265 m obstructed link (L2,L3). (a) top view. (b) side view.

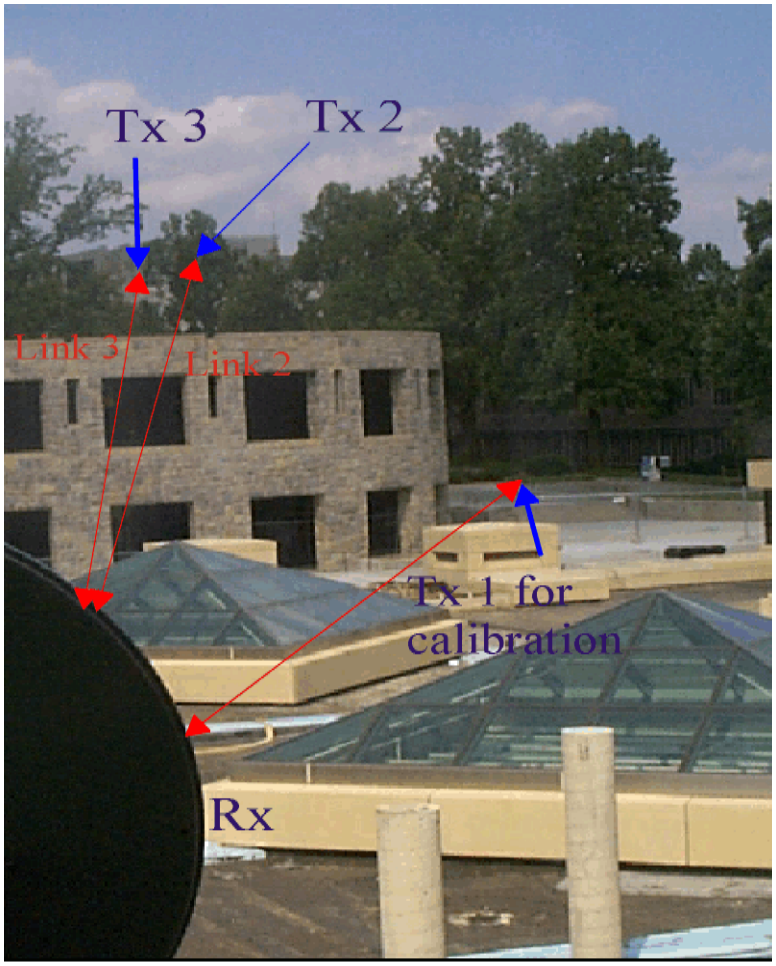

Figure 44: View from receiver on L2 and L3.

5.3 Measurement Results

A total of 73,963 PDPs were recorded for the three cross-campus links, from which 36,338 were collected during rain events and hail storms. An example of a PDP is presented in Figure 45. Each PDP was processed to determine the number of multipath components above the noise threshold, N_{MP}; the power of the LOS component, P_{LOS}; the power and excess delay time of each multipath component, P_{MP} and τ_{MP}; the mean excess delay, μ_{mean}; and RMS delay spread, σ_{τ}. Statistical results are summarized in the following sections.

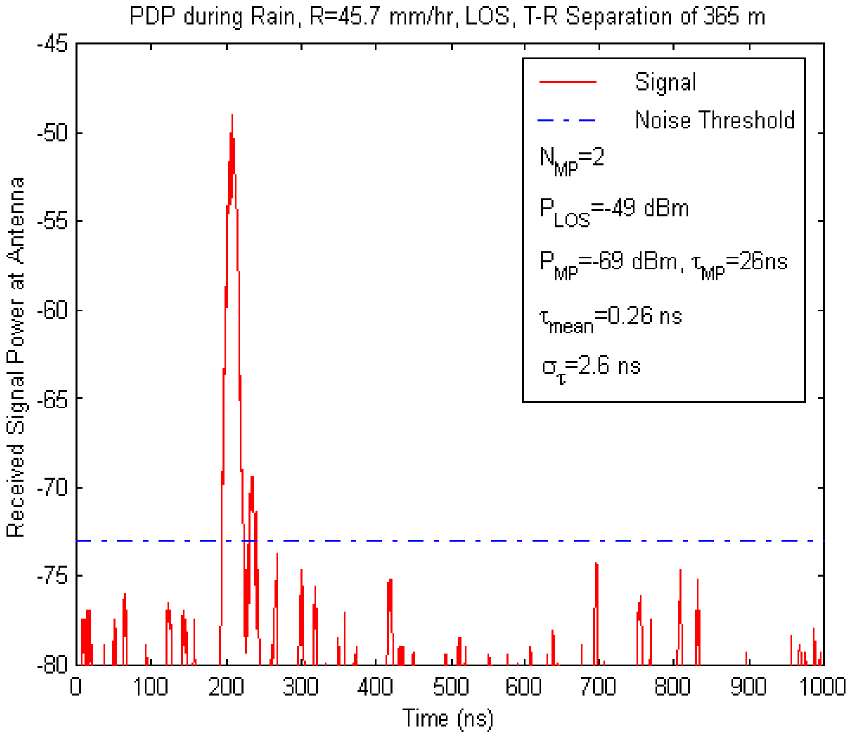

Figure 45: Typical PDP under rainy conditions: May 3, 265 m unobstructed LOS link, average rain rate of 45.72 mm/hr.

Table 9: Summary of Multipath Occurrence and Maximum Observed Multipath (MP) Level (w.r.t. LOS). The Maximum MP Signals Were Delayed by 10 to 30 ns from LOS.

	Date	R(mm/h)	# PDPs	% of PDPs with MP > ΔP					Max MP
Threshold:$\Delta P = P_{MP} - P_{LOS}$(dB)				-10	-12	-14	-16	-18	(dB)
L1	4/23	clear	190	0	0	0	0	0	<-18
		0–15.2	100	0	0	0	0	0	<-18
	5/1	0–39.6	60	1.7	53	67	67	67	-9.1
		hail	58	1.7	1.7	1.7	1.7	6.9	-5.2
	5/3	clear	10	0	0	0	0	0	<-18
		0–45.7	620	0	0	0	3.7	27	-14.2
L2	5/27	clear	4400	0.068	0.14	0.20	1	27	-9.0
		0–15.2	3000	0.83	2.4	8.6	21	28	-9.3
L3	5/30	clear	800	0.25	0.25	0.25	0.25	21.8	-4.5
		0–15.2	8350	0.08	0.12	0.74	7.7	21	-4.75
	6/2	clear	7550	0.066	0.066	0.066	0.12	0.49	-3.1
		0–213.4	16850	0.17	0.22	0.81	4.7	17.6	-2.6
	6/3	clear	2000	0.05	0.05	0.55	11	52	-6.9
		0–45.72	4300	0.047	0.047	0.12	1.8	11	-1.4

5.3.1 Multipath Statistics.

Statistics on Multipath Occurrences.

Table 9 summarizes the multipath statistics for different rain rates, R (mm/hr), and multipath threshold levels, $P_{MP} - P_{LOS}$, where P_{LOS} is the power of the received LOS component and P_{MP} is the power of any received multipath component.

Results from Table 9 show the following trends in millimeter-wave propagation:

- No strong multipath occurs on the unobstructed LOS link under clear weather conditions. This is an expected result due to the highly directional antennas (See Section 5.2.1) used in the link and the absence of scatterers near the LOS path.

- Strong multipath components may occur under severe weather conditions even on unobstructed LOS link, as shown in the May 1^{st} and 3^{rd} results. These multipath components may be caused by the inhomogeneity of the media or reflection from wet surfaces.
- On obstructed links, multipath can occur under both clear and rainy conditions. The presence of multipath on L2 and L3 was a consequence of the scattering by tree leaves.

The measured PDPs on L1 showed that changes in weather events can significantly affect the wideband behavior of millimeter-wave channels. Figure 46 compares measured PDPs during different weather events. This figure shows the presence of multipath components during light rain on May 3^{rd} and heavy rain on May 1^{st}. On May 3^{rd}, the multipath components persisted after the rain event until the surrounding buildings dried out.

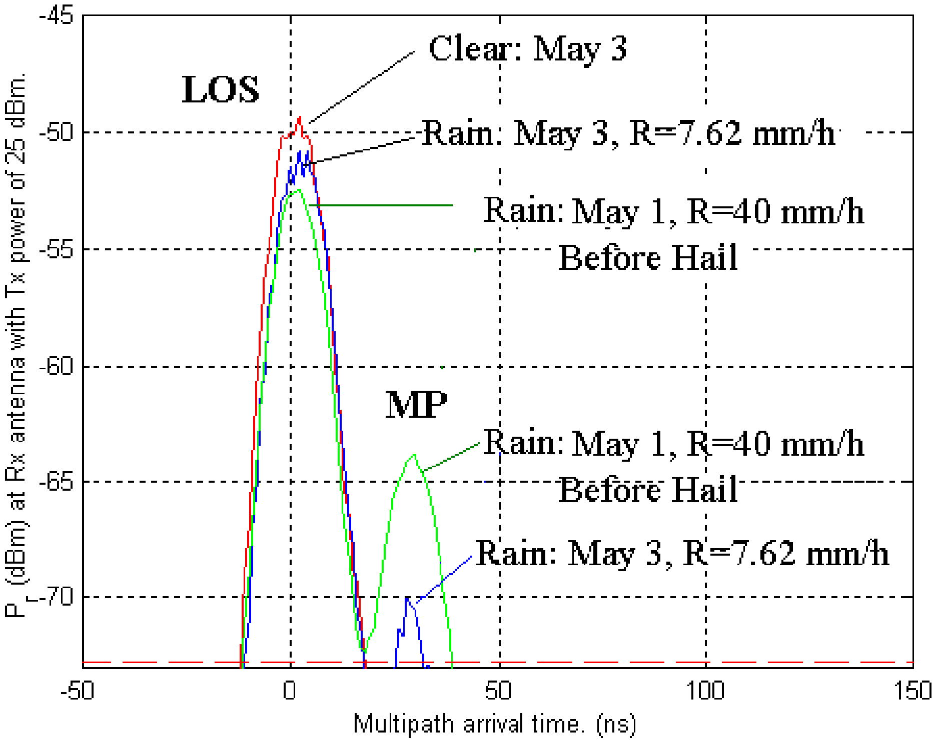

Figure 46: Comparison of PDPs: 605 m unobstructed LOS. Note: no multipath was measured under clear conditions.

Two hypotheses may explain the presence of multipath on May 1^{st}. The first one is based on inhomogeneities in the atmosphere. Multipath components that occurred right before and after the hailstorm may be caused by the sharp edge of the hailstorm cell, which was illuminated by the antenna main lobe or first side lobe. In [101], de Wolf and Ligthart showed that multipath could occur at the edges of very intense and compact rain cells. Pressure, temperature, and rain could alter the refractivity of the atmosphere, thus creating varying propagation paths.

The second hypothesis is based on the change of the electromagnetic properties of the reflecting building surfaces or the formation of standing water surfaces on the building roofs and walls during rain. The rough building surfaces would diffusively scatter the incoming wave during dry conditions. However, if the surface becomes wet or a standing water surface forms, the reflected power in the specular direction would increase. Multipath components were observed after the rain stopped, which seems to support this hypothesis. Also, measurements from [92] show that the reflected power can increase as much as 15 dB when the dry concrete is soaked with water.

Statistics on Multipath Parameters

In Table 10, statistics on mean excess delay and RMS delay spread are presented both in average and maximum for all the PDPs that contain multipath components. Also, maximum multipath level is calculated with respect to the LOS component. Results show that, during rain, the RMS delay spread can be as high as 9.7 ns on an unobstructed LOS path, and 15.9 ns on an obstructed LOS path.

5.3.2 Short-term Variation.

Short-term wideband signal power variations were analyzed at constant rain rates over a two to three minute observation time. The measured probability density functions (PDFs) of the received signal were found to fit a Rician distribution. An example of measured and theoretical PDF is shown in Figure 47(a).

The Rician PDF for received signal envelope is [50]

$$f_V(v) = \frac{v}{\sigma^2} \exp\left\{-\frac{v^2 + A^2}{2\sigma^2}\right\} I_0\left(\frac{Av}{\sigma^2}\right) \tag{5.117}$$

where v is signal envelop, $A^2/2$ is the coherent power and σ^2 is the incoherent power. The PDF

Table 10: Mean Excess Delay, RMS Delay Spread and Maximum Multipath (MP) Level (w.r.t. LOS) from PDPs Containing Multipath Components.

Link	Date	R(mm/hr)	$\overline{\tau}$ (ns)	τ_{max} (ns)	$\overline{\sigma}$ (ns)	σ_{max} (ns)	Max MP(dB)
L1	5/1	40	1.7	3.1	6.4	9.7	-9.1
		Hail	0.64	2.31	3.4	6.61	-5.2
	5/3	0–45.7	0.5	3.5	3.5	6.1	-14.2
L2	5/27	clear	0.7	5	3.9	8.1	-9.0
		< 15.2	1.43	9.9	7.5	15.4	-9.3
L3	5/30	clear	0.4	2.8	4.2	5.9	-4.5
		< 15.2	0.7	9.1	5.3	15.9	-4.75
	6/2	clear	0.4	3.4	4.1	7.8	-3.1
		0–213	0.7	5.3	5.3	10	-2.6
	6/3	clear	0.8	2.5	5.9	9.9	-6.9
		0–213	0.36	4.2	3.2	9.7	-1.4

for the received power, $P = V^2/2$, is then given by

$$f_P(p) \;=\; \frac{1}{\sigma^2}\exp\left\{-\frac{2p+A^2}{2\sigma^2}\right\} I_0\left(\frac{A\sqrt{2p}}{\sigma^2}\right) \tag{5.118}$$

where p is the random variable of received power.

The mean received power, μ_p, and standard deviation, σ_p^2, are given by

$$\mu_p = E\{p\} = \sigma^2 + A^2/2 \tag{5.119}$$

$$E\{p^2\} = 2\sigma^4 + 2A^2\sigma^2 + A^4/4 \tag{5.120}$$

$$\sigma_p^2 = E\{p^2\} - E^2\{p\} = \sigma^4 + A^2\sigma^2 \tag{5.121}$$

where E{•} denotes ensemble average or time average for ergodic systems. μ_p and σ_p^2 can be measured from averaging the received signal power over short period. Then solving (5.119) and (5.121) for A and σ, coherent power, $A^2/2$, and incoherent power, σ^2, can be estimated.

The Rician distribution can also be parameterized by total power and K factor, defined as the ratio

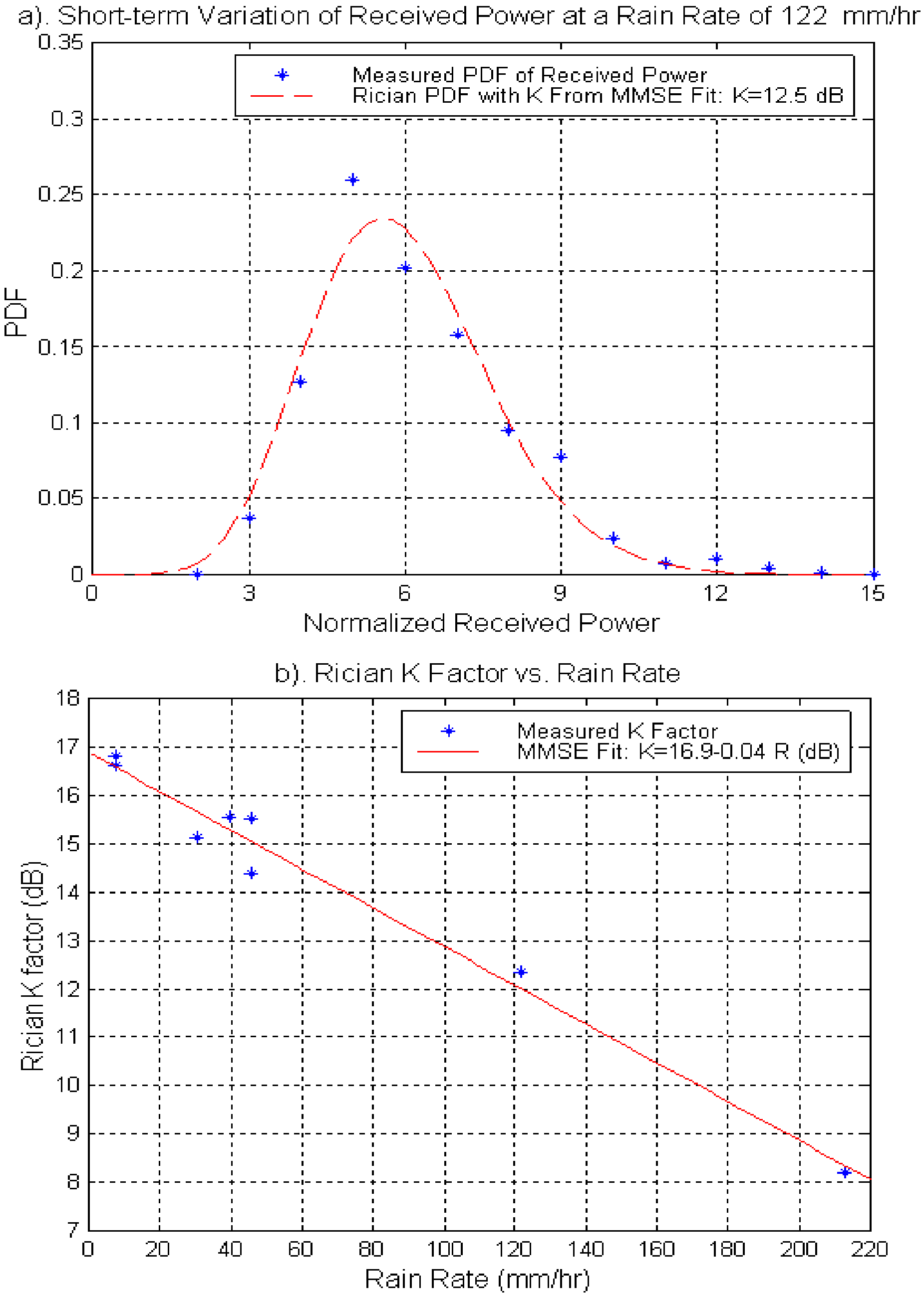

Figure 47: a) Received power PDF over 2-3 minute interval: June 2, 265 m partially obstructed link, R=122 mm/hr. b) Rician K factor vs. rain rate

of coherent to incoherent powers in dB:

$$K = 10\log\frac{A^2/2}{\sigma^2} = 10\log\left(\frac{\sqrt{\mu_p^2-\sigma_p^2}}{\mu_p-\sqrt{\mu_p^2-\sigma_p^2}}\right) \quad \text{dB} \tag{5.122}$$

As shown in (5.122), the K factor is independent from the total received power and can be estimated from measured mean and variance of the received power.

The resulting K factors for different rain rates are presented in Figure 47(b). A minimum mean square error (MMSE) linear fit leads to

$$K = 16.88 - 0.04R \quad \text{dB} \tag{5.123}$$

As expected, the K factor (dB) is proportional (with a negative sign) to rain rate R (mm/hr), which implies that incoherent power increases and the coherent power decreases with increasing rain rate. The PDPs in fact show a decrease of the LOS power as the multipath power increases during rain. A theoretical study of short-term signal variation during rain is presented in Section 5.4.

5.3.3 Rain Attenuation.

Excess rain attenuation, A(R) (dB), for a given rain rate, R, was measured as $A(R) = P(0) - P(R)$, where $P(0)$ and $P(R)$ are the measured received powers under clear condition and rain, respectively.

As shown in Figure 48, the instantaneous received signal power, $P(R)$, displays a strong correlation with rain rate. Excess rain attenuation was compared to the Crane model prediction [78]. As shown in Figure 49, measured results undergo slightly higher attenuation than the prediction by the Crane model. Using the measurement results, upper bounds were derived for rain attenuation, thereby providing a worst case estimate for system planning purposes. The upper bounds exceed the Crane model prediction by 2.7 dB and 5.2 dB for link L1 and L2, respectively. A simple expression relating distance and rain rate, or a margin of error may be applied for short-haul links as compared to the Crane model.

The measurement results give rise to upper bounds for rain attenuation. Equations (5.124) and (5.125) provide expressions of these upper bounds for an unobstructed LOS path and a partially

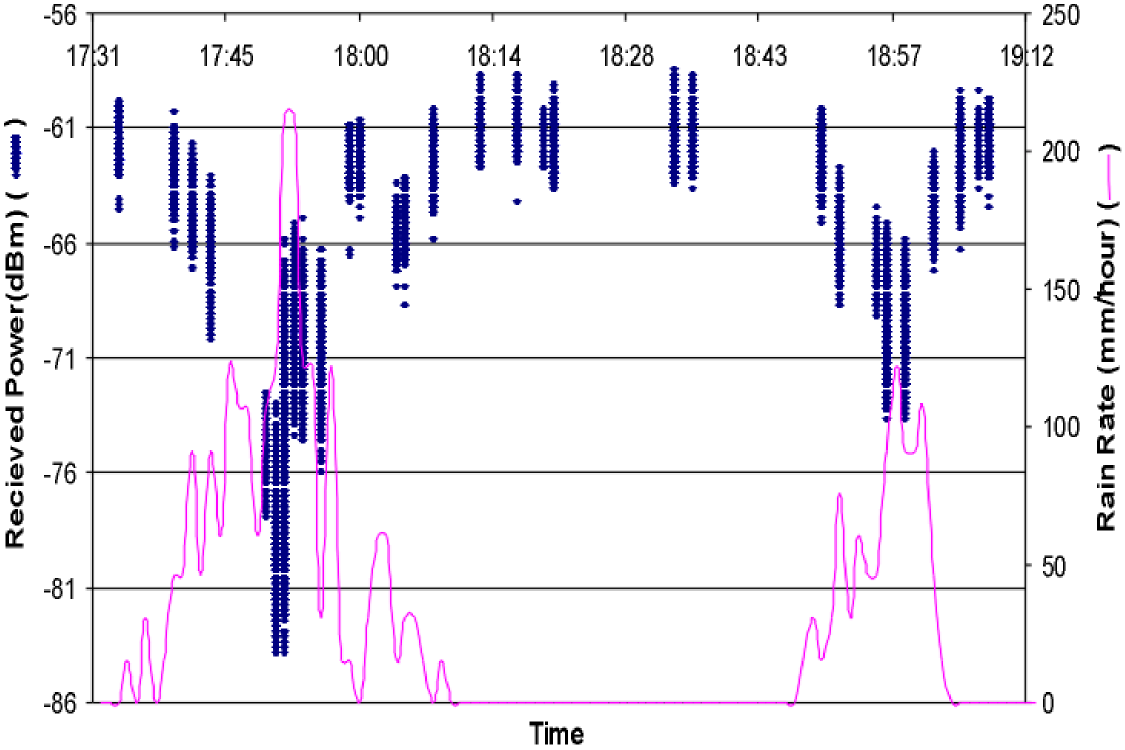

Figure 48: Received signal power during rain: June 2^{nd}, 265 m partially obstructed LOS. Each point represents a wideband power measurement taken every 0.02 s.

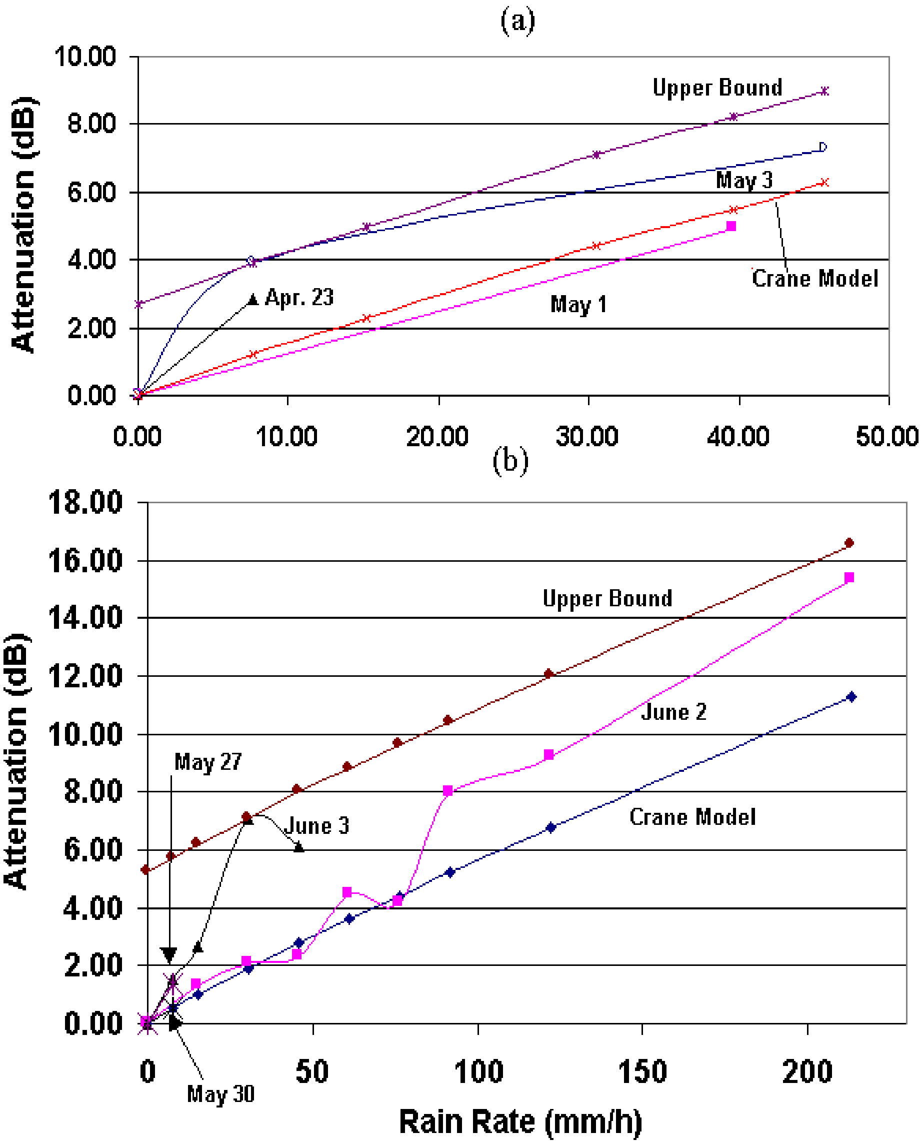

Figure 49: Measured rain attenuation in excess of free space path loss and comparison to the Crane model: a) 605 m unobstructed LOS; b) 265m partially obstructed, and obstructed links.

obstructed LOS path.

$$P^{LOS}_{upperbound}(R, D) = P_{crane}(R, D) + 2.7 \quad \text{(dB)} \tag{5.124}$$

$$P^{partialLOS}_{upperbound}(R, D) = P_{crane}(R, D) + 5.2 \quad \text{(dB)} \tag{5.125}$$

where P_{crane} is the attenuation estimate based on the Crane model, R (mm/hr) is the rain rate, and D (m) is the path length. These upper bounds provide wireless engineers with a simple relationship between excess path attenuation, rain rate and path length for short-haul links. The upper bound for partial obstructed LOS path provides a worst-case attenuation estimate that accounts for both rain and foliage.

5.3.4 Hail Attenuation.

Hail attenuation was measured during a hailstorm on link L1. The hail had a size of 0.5 to 1.5 cm in diameter, and resulted in excess attenuation as high as 25.7 dB over the 605 meter path. The attenuation varied by 7 dB about the mean during the two-minute hailstorm.

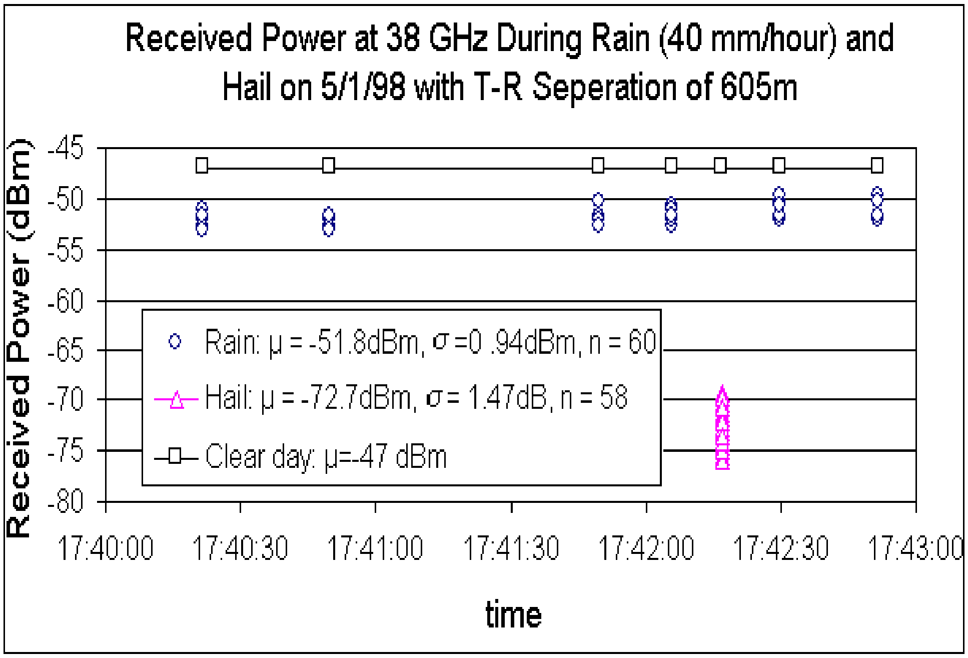

Figure 50: Hail attenuation measurements on May 1: average excess attenuation of 25.7 dB over the 605 m path, signal variation of 7 dB .

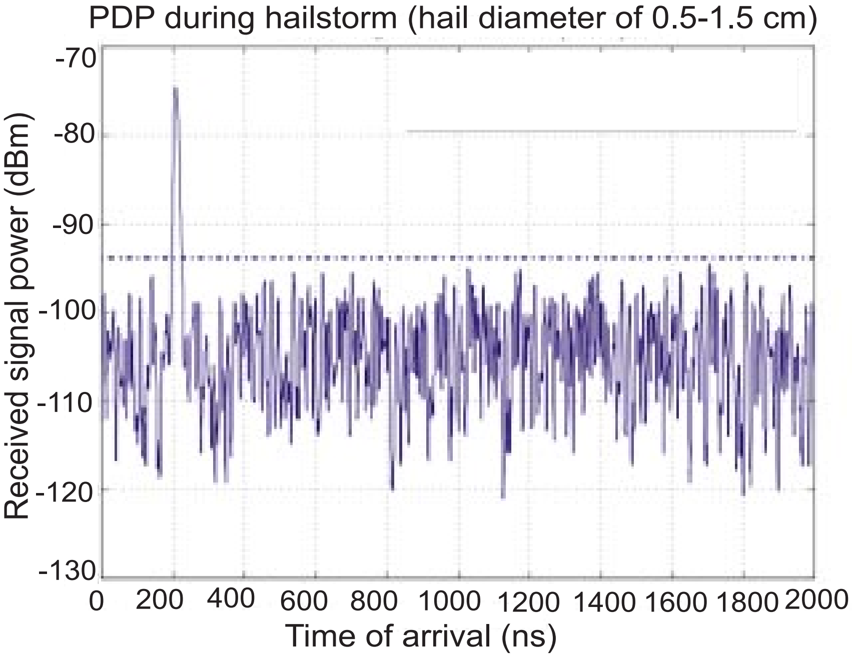

Figure 51: Typical PDP during hailstorm: average received signal power is 27.6 dB lower than the LOS power during clear weather.

The results of the rain and hail attenuation for May 1 are shown in Figure 50. The mean value of the received power, μ, and standard deviation, s, during the rainstorm and the hailstorm were calculated. The number of PDPs, n, is listed to highlight the statistical significance of the attenuation results. Comparison with the received signal power of -47 dBm under clear conditions shows that the hailstorm resulted in attenuation as high as 25.7 dB over the 605 m path. Also, the signal level varied for 7 dB around the mean received signal value during the hailstorm, while the signal variation was much less during the rain before and after the hailstorm. A typical PDP taken during the hailstorm is presented in Figure 51. The received LOS signal power in this PDP is only -74.6 dBm , which is 27.6 dB lower than the LOS power during clear weather.

5.3.5 Other Attenuation Measurements.

Excess attenuation through window glass was measured by comparing received power through free space and the window glass. The attenuation of a tempered, double-pane, tinted, store front glass, was measured to be 25.5 dB . Measurements in [70] showed that the penetration loss through a plain glass door was only 0.56 dB .

Attenuation of dense leaves on an oak tree in link L2 was measured on a calm, sunny day. The average excess attenuation was found to be 17 dB .

5.4 Theoretical Study of Short-term Signal Variation During Rain

The power observed on several point-to-point links during rain fluctuated over short intervals of two to three minutes. The measurement results are presented in Section 5.3.2. This section shows that the fluctuations are probably due to inhomogeneities in the rain rate that move across the line of sight during the sampling time.

5.4.1 Introduction

This theoretical study is aimed at explaining the observed ratio of incoherent power P_i to coherent power P_c of a 37.5 GHz signal propagated from a transmitter over a 265 m and a 605 meter one-way path to a receiver in the presence of rain. The received power was observed every 0.02 seconds during a two to three minute sampling period. Its average is P_c and the difference between the instantaneous power P and P_c is the incoherent component (with zero mean). The rain intensity (in mm/hr) was measured by gathering rain drops at one intermediate location.

The observed results for $10\log_{10}(P_{rms}/P_c)$ are gathered in Table 11. Several conclusions have been reached. The variations in power appear to be due to local variations in the rain rate over distances considerably less than the path length. These variations can drift across the line of sight well within the sampling time, and thus cause variations in power. Statistical description of rainfall in [110, 141] has shown that the rain rates are indeed inhomogeneous along the horizontal path. Research for satellite-to-ground propagation also confirms this conclusion [105, 106, 142, 143].

We have rejected other hypotheses. For example, although a multipath reflection from a nearby roof appeared to be able to yield a side-lobe component, this component would not have been incoherent. Off-axis scattering into the receiver from rain drops also has been investigated [101] and rejected because the contribution to P_i would be too small.

Table 11: $10\log_{10}(P_{rms}/P_c)$

$u_r(mm/hr)$	7.6	7.6	30.5	39.6	45.7	45.7	122	213
265 m		-16.8	-15.1			-14.4	-12.4	-8.2
605 m	-16.6			-15.6	-15.5			

5.4.2 Signal Analysis

The received signal is well represented by an electric field vector,

$$\vec{E} = \vec{E_0} e^{-\psi} \quad \text{with} \quad \psi = \gamma - j\phi \tag{5.126}$$

Here, $\vec{E_0}$ is the field that would have been received in the absence of rain, ϕ is the phase change due to the presence of rain, and γ is the attenuation due to scattering and absorption of energy out of the line of sight. Hence the received power is $P = P_0 e^{-2\gamma}$ where $P_0 = |\vec{E_0}|^2$. We will argue in the next section that the attenuation γ can be written as the sum of a steady component $\bar{\gamma}$ and a Gaussian random part $\delta\gamma$ with zero mean. Consequently we obtain,

$$P_c = P_0 \left\langle e^{-2\gamma} \right\rangle = P_0 e^{-2\bar{\gamma}} \left\langle e^{-2\delta\gamma} \right\rangle = P_0 e^{-2\bar{\gamma}} e^{2\langle \delta\gamma^2 \rangle} \tag{5.127}$$

The last step follows from a general property of a lognormal variable with zero mean. For the incoherent power $P_i = P - P_c$ we need to calculate a root mean square as lowest significant statistic.

$$P_{rms} = P_c e^{2\langle \delta\gamma^2 \rangle} \sqrt{e^{4\langle \delta\gamma^2 \rangle} - 1} \tag{5.128}$$

5.4.3 Variations in Attenuation γ

The attenuation is given [144] by the real part of

$$\psi = \frac{2\pi}{k} \int_0^L dz \int_0^\infty dD n_4(z, D) f(D, k, \epsilon) \tag{5.129}$$

Here $k = \omega\sqrt{\mu_0 \epsilon}$ is the wavenumber in the medium between $z = 0$ and $z = L$. It can be taken to be the free-space value within the accuracy of this work. The dielectric permittivity of a drop is given by ϵ. The particle drop-size distribution n_4 (given in m^{-4}) is generally a function of position z and drop diameter D. The function $f(D, k, \epsilon)$ is the forward-scattering amplitude(given in m) of a single spherical particle with effective diameter D. It may be possible to expand the analysis to non-spherical particles but that is not essential here. We shall make one other assumption to simplify the analysis: the particle drop-size distribution function is given by

$$n_4(z, D) = n_3(z)p(D) \tag{5.130}$$

where $n_3(z)$ is the particle density in m^{-3} and $p(D)$ is a probability density in m^{-1}.

Several distributions are commonly used. Among these is the Marshall-Palmer(M-P) distribution [144] with

$$p(z, D) = \Lambda e^{-\Lambda D}, \quad \Lambda = 4100 u_r^{-0.21} m^{-1} \tag{5.131}$$

given that u_r is the overall rain rate in mm/hour, and D is given in m. The M-P connection between density and parameter Λ is $\Lambda n_3(z) = 8.1 \times 10^6$ m^{-4}. It follows that $n_3(z)$ is a function of location z. As a result,

$$\gamma = \frac{2\pi}{k} F(k, \bar{D}, \epsilon) \int_0^L dz n_3(z) \qquad \text{with} \qquad F(k, \bar{D}, \epsilon) \equiv Re\left[\int_0^\infty dD p(D) f(D, k, \epsilon)\right] \tag{5.132}$$

Here, $\bar{D}$ is the mean particle diameter. If all particles have diameters $D \ll \lambda$ (λ is the wavelength), then

$$F(k, \bar{D}, \epsilon) = \frac{3\pi}{2} k Re[K] \bar{D}^3 \quad \text{with} \quad K \equiv \frac{\epsilon/\epsilon_0 - 1}{\epsilon/\epsilon_0 + 2} \tag{5.133}$$

At 37.5 GHz, the wavelength $\lambda \approx 8$ mm, and the parameter $kD/2$ is determined by the ratio of D to λ/π, i.e. by the ratio of D to 2.5 mm. The mean rain drop diameter $\bar{D}$ is described , at least for a Marshall-Palmer drop-size distribution [144] by

$$\bar{D} \approx 1/4.1 u_r^{0.21} \tag{5.134}$$

where D is in mm and u_r is in mm/hr. The Rayleigh approximation requires this ratio to be small, but this is not the case for larger values of the rain rate u_r. Equation (5.132) is the basis for our analysis. The key issue here is the appearance of a path integral over particle density.

Figure 52 illustrates the situation as we hypothesize it to be. The contours are those of the average density $\bar{n}_3$. Possibly, higher densities are inside, lower ones outside. The arrows indicate wind direction.

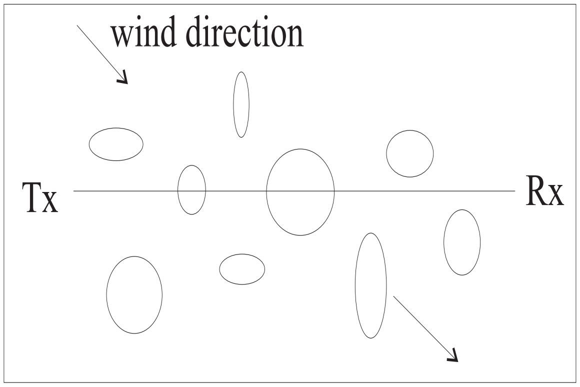

Figure 52: Patches of rain across the LOS

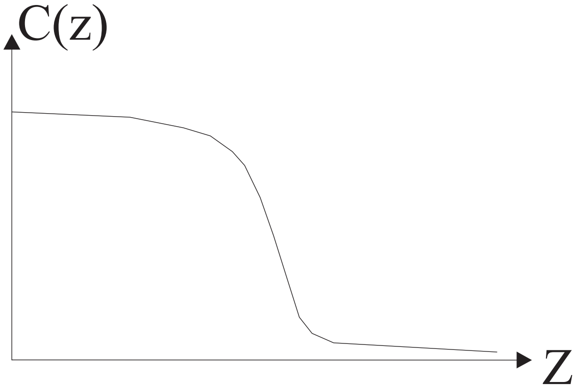

Figure 53: General form $C(z)$

Thus $n_3(z) = \bar{n}_3 + \delta n_3(z)$ which defines the fluctuation of the density around the average, $\delta n_3(z)$. Consequently,

$$\delta\gamma = F(k, \bar{D}, \epsilon) \int_0^L dz \delta n_3(z) \tag{5.135}$$

can be considered to be a Gaussian variable with zero mean, due to the central-limit theorem of statistics (if there are a sufficient number of small fluctuation cells crossing the line of sight at any time). Thus,

$$\langle \delta\gamma^2 \rangle = F^2(k, \bar{D}, \epsilon) \int_0^L dz_1 \int_0^L dz_2 \langle \delta n_3(z_1) \delta n_3(z_2) \rangle \tag{5.136}$$

Under the assumption of isotropy and of a slowly-varying variance, we may set

$$\langle \delta n_3(z_1) \delta n_3(z_2) \rangle = \langle \delta n_3^2(z) \rangle C(|z_1 - z_2|) \tag{5.137}$$

in which $C(z)$ has the general form shown in Fig. 53.

A crucial property of this normalized correlation function is $\int_0^\infty dz C(z) = l$ and we shall make the reasonable assumption that l is considerably smaller than L. In fact, l is basically a statistical measure of a diameter of a fluctuation $\delta n_3(z)$.

Under the reasonable assumption that $l \ll L$ (just how much ?smaller? is somewhat uncertain), we can write,

$$\int_0^L dz_1 \int_0^L dz_2 \langle \delta n_3(z_1) \delta n_3(z_2) \rangle \approx \int_0^L dz_1 \langle \delta n_3^2(z_1) \rangle \int_{-\infty}^{\infty} d\triangle z C(|\triangle z|) \approx 2Ll \langle \delta n_3^2 \rangle \tag{5.138}$$

Consequently we obtain,

$$\langle \delta\gamma^2 \rangle = F^2(k, \bar{D}, \epsilon) 2Ll \langle \delta n_3^2 \rangle \tag{5.139}$$

If this is compared to the average of (5.134) which yields we obtain,

$$\frac{(\delta\gamma)_{rms}}{\bar{\gamma}} = \sqrt{\frac{2l}{L}} \frac{(\delta n_3)_{rms}}{\bar{n}_3} \tag{5.140}$$

5.4.4 Signal Analysis (Contd.)

Returning to (5.128) we note that

$$10\log_{10}(P_{rms}/P_i) = 8.686\langle\delta\gamma^2\rangle + 10\log_{10}[\sqrt{e^{4\langle\delta\gamma^2\rangle - 1}}] \tag{5.141}$$

Under the assumption that $\langle\delta\gamma^2\rangle$ is a quantity sufficiently small so that the exponential in (5.141) can be expanded into only its first two terms, we obtain

$$10\log_{10}(P_{rms}/P_i) = 8.686\langle\delta\gamma^2\rangle + 3.01 + 5\log_{10}[\langle\delta\gamma^2\rangle] \tag{5.142}$$

To estimate this, we utilize (5.140) to rewrite (5.142) as

$$10\log_{10}(P_{rms}/P_i) = 8.686\langle\delta\gamma^2\rangle + 3.01 + 10\log_{10}\bar{\gamma} + 5\log_{10}\left[\sqrt{\frac{2l}{L}}\frac{(\delta n_3)_{rms}}{\bar{n}_3}\right] \tag{5.143}$$

From Olsen, et al. [99], we find $8.686\bar{\gamma} \approx 0.156u_r$ for 37.5 GHz, $L = 0.6$ km and temperature between 0° and 20° C, which, when inserted into (5.143) yields

$$10\log_{10}(P_{rms}/P_i) \approx -14.5 + 10\log_{10}[u_r] + 5\log_{10}\left[\frac{2l}{L}\frac{\langle\delta n_3^2\rangle}{\bar{n}_3}\right] + 8.686\langle\delta\gamma^2\rangle \tag{5.144}$$

Let us now estimate the magnitude of $\langle\delta\gamma^2\rangle$ from (5.140) and the Rayleigh ($\bar{D} \ll \lambda$) expression $\bar{\gamma} = \frac{3\pi}{2}k\bar{D}^3K_rL\bar{n}_3$. Some typical numbers are $k \approx 795$ m^{-1}, $L \approx 600$ m, $K_r \approx 0.9$, $\bar{n}_3 \approx 2000$ m^{-3}, $\bar{D} \leq 0.001$ m, which yields $\bar{\gamma}^2 \approx 16$. Equation (5.140) states that this value must be multiplied by the factor $(2l/L)[(\delta n_3)_{rms}/\bar{n}_3]^2$. The factor $2l/L$ is probably not very small (which renders application of the central-limit theorem in (5.135) somewhat dubious) but the factor $[(\delta n_3)_{rms}/\bar{n}_3]^2$ is very likely to be small. So it is not at all improbable that we may neglect the last term in (5.144).

Under the assumption that $\sqrt{2l/L}[(\delta n_3)_{rms}/\bar{n}_3] \approx 0.04$ we reduce (22) to

$$10\log_{10}(P_{rms}/P_i) \approx -28.5 + 10\log_{10}[u_r] \tag{5.145}$$

The last term of (5.144) would be close to 0.22, which is indeed negligible. Equation (5.145) is plotted in Fig. 54.

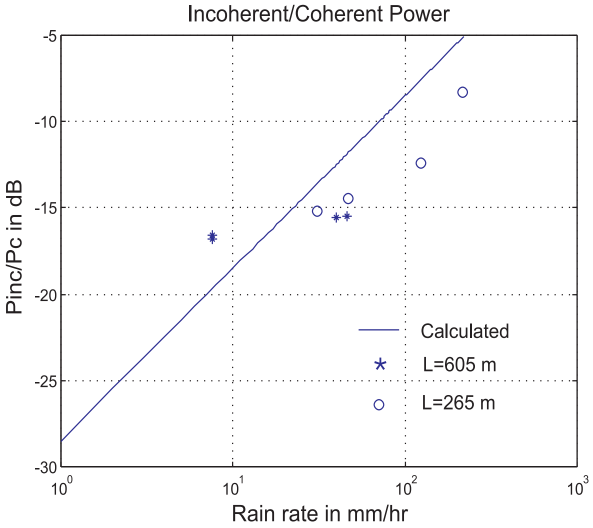

Figure 54: $10\log_{10}(P_{rms}/P_c)$ as function of rain rate

Note that the choice of a constant value for $\sqrt{2l/L}[(\delta n_3)_{rms}/\bar{n}_3]$ yields a curve with a slope that appears to fit the data if the constant is chosen correctly. The rationale for choosing $\sqrt{2l/L}[(\delta n_3)_{rms}/\bar{n}_3] \approx 0.04$ is that this choice appears to give a curve that fits the data. One can only say, in the absence of measurements of $(\delta n_3)_{rms}$ and of l that the value 0.04 is consistent with realistic possibilities. This relatively small value at least indicates that the presence even of relatively small fluctuations of δn_3 suffices to yield a P_{rms} consistent with the observations. Research for groud-to-satellite communications has shown variation of rain rate along the horizontal paths [105, 143], which supports the theory. Unfortunately, no detailed rain rate measurements were taken in this measurement campaign that might confirm this possibility quantitatively.

5.5 Summary

This chapter presents a measurement campaign that investigated weather effects on multipath dispersion and signal variation at millimeter-wave frequencies. Wideband measurement campaign was performed at 38 GHz on three point-to-point links, including a 605 m unobstructed LOS link, a 265 m obstructed link and a 265 m partially obstructed link. A total of 73,963 PDPs were recorded under clear, rain and hail conditions. These results provide quantitative channel information for millimeter-wave communication system design and system installation.

Wideband measurement results indicate that *time dispersion characteristics of the channel may change during different weather events*. Multipath statistics shows that while very few multipath components were detected in clear, dry weather, more multipath components were detected during rain. Due to the high bandwidth requirements for future LMDS and NGI systems, slight multipath delay dispersion may result in intersymbol interference. The multipath dispersion results from this measurement campaign, summarized in Tables 9 and 10, provide important statistics for the design of equalizers or rake receivers, as well as for the selection of optimum data rate and modulation techniques.

Weather effects on received signal power were analyzed in terms of *mean attenuation* and *short-term variation*. Excess rain attenuation is measured from light rain to extremely heavy rain. Upper bounds of the mean attenuation were provided based on a modified Crane model in (5.124) and (5.125) for both unobstructed and partially obstructed LOS links as functions of rain rate and path length. These upper bounds allow radio engineers to determine the additional fade margin necessary for the reliable operation of wideband communication systems at millimeter-wave frequencies.

PDPs were recorded at a rate of 50 PDPs per second, which allowed us to analyze the short-term signal variation at constant rain rate over a 1-2 minute interval. *Results show that received signal variation during rain follows a Rician distribution. The relationship between Rician K factor and rain rate as given in (5.123) shows increased scattered power at high rain rates.* At any rain rate, the short-term variation of signal power can be modeled based on the K factor, estimate from (5.123), and the average received power, estimated from the average rain attenuation models and the link budget. This signal variation model can be used for AGC design or system outage probability estimates.

Measurement results show that *rain, hail, glass and foliage may cause high attenuation to the millimeter-wave signal*. For example, averaged attenuation due to hail was as much as 25.7 dB over the 605 m path. These results must be taken into account in link budget and system coverage estimation.

A theoretical study of the signal variation during rain is also presented. The theory is based on the fundamental principles of wave propagation through random media of scatters. The results show that the ununiform distribution of rain drop density along the propagation path can result in the signal fluctuation. The estimated values of K factor agrees well with the measurement results. However, the theory finds the signal statistics to be governed by a lognormal distribution. Further measurements are required to verify the theoretical hypothesis.

The wideband measurement results provide great insight into millimeter-system design and installation. High signal attenuation can result from rain, hail, and vegetation. Foliage, smooth reflecting surfaces, and flat surfaces (on which a standing water surface may form during rain) may cause multipath, especially under severe weather conditions. *This multipath delay spread is a limiting factor for the maximum data rate in the millimeter-systems.* Based on the measurement results, a novel design technique is developed that predicts the worst-case channel multipath dispersion under any weather conditions. This model is presented in Chapter 6.

Chapter 6

A Novel Prediction Technique for Wideband Point-to-Point/Multipoint Millimeter-wave Channel

Channel time dispersion is a limiting factor to maximum data rate and reliable operation of millimeter-wave systems. As shown in Chapter 5, time dispersion in millimeter-wave point-to-point systems may be caused by objects near the LOS path, and is subject to change during different weather conditions.

This chapter presents a novel prediction technique that estimates worst-case multipath channel characteristics for fixed point-to-point systems under any weather conditions. This technique applies canonical antenna patterns and site specific information to estimate wideband channel characteristics including relative power, TOA and AOA of each multipath component. New metrics, which we call the *excess delay zone* and *relative power zone*, are defined and contour plots are developed to determine potential reflectors from an area site map. This approach greatly simplifies site planning of emerging LMDS and other millimeter-wave systems, and incorporates worst-case scattering during rain [39, 40].

6.1 Introduction

Today's microwave links typically span 1-60 km [75]. These links use very tall antenna towers and rely on free space propagation. *For microwave links, main radio wave propagation considerations are LOS path clearance, earth curvature, refraction index change of the atmosphere, and ground reflection* [24, 25]. Fresnel zone clearance is the primary criterion to avoid diffraction loss. Multipath fading caused by refraction index change in the atmosphere is modeled in [4, 74]. *However, these models were developed for clear-path long-haul links and are not appropriate or sufficient for millimeter-wave links, where buildings or foliage are nearby.*

Millimeter-wave links have shorter length (less than several kilometers) and support higher data rates than their microwave counterparts, and may be deployed in both rural and urban areas where buildings are in close proximity. For LMDS systems, highly directional antennas are used only at the receiver, and a sector antenna, with a broader antenna pattern, is used at the transmitter. Wideband measurement results from [10, 37, 39] show multipath in short millimeter-wave links. These multipath components are caused by the foliage or building surfaces near the LOS path. Furthermore, millimeter-wave links are extremely sensitive to weather events such as rain and hail [39, 75, 78]. Precipitation induces fading and additional dispersion in the channel as moisture and standing pools of water change the reflective properties of the scatterers in the environments [39].

Ray tracing is one of the most widely used techniques to provide site-specific predictions [145, 146, 147, 148]. It has been used to predict wideband channel response at millimeter frequencies [10, 117, 149]. However, accurate prediction of a millimeter-wave channel requires detailed three dimensional site information. When such detailed information is not available, millimeter-wave ray tracing provides only qualitative predictions of the channel [117, 149].

This chapter presents a new technique for wideband channel characterization that employs knowledge of the antenna directivity and millimeter-wave propagation features. Contour plots are developed to estimate received power and arrival time of potential multipath components from a site map of a millimeter-wave system. The presented design principles provide new clearance criteria for the deployment of millimeter-wave links that minimize channel dispersion and maximize network throughput.

6.2 3D Geometry of a Point-to-Point Link

A 3D geometrical model of a point-to-point millimeter-wave link is presented in Figure 55, where the line-of-sight (LOS) path length is D, and a scatterer is located at (x_0, y_0, z_0).

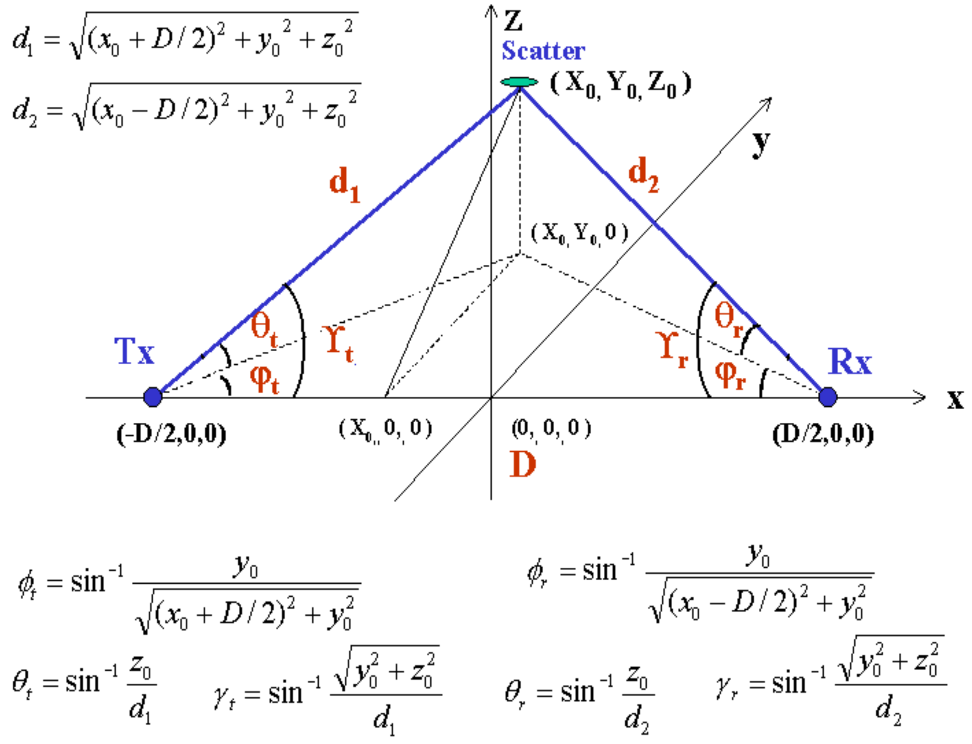

$$d_1 = \sqrt{(x_0 + D/2)^2 + y_0^{\,2} + z_0^{\,2}}$$

$$d_2 = \sqrt{(x_0 - D/2)^2 + y_0^{\,2} + z_0^{\,2}}$$

$$\phi_t = \sin^{-1}\frac{y_0}{\sqrt{(x_0 + D/2)^2 + y_0^2}} \qquad \phi_r = \sin^{-1}\frac{y_0}{\sqrt{(x_0 - D/2)^2 + y_0^2}}$$

$$\theta_t = \sin^{-1}\frac{z_0}{d_1} \qquad \gamma_t = \sin^{-1}\frac{\sqrt{y_0^2 + z_0^2}}{d_1} \qquad \theta_r = \sin^{-1}\frac{z_0}{d_2} \qquad \gamma_r = \sin^{-1}\frac{\sqrt{y_0^2 + z_0^2}}{d_2}$$

Figure 55: Geometry of a point-to-point link with an arbitrary scatter in 3D.

The scatterer may be a building wall, a rooftop, ground, or any object that has a large reflecting surface relative to the wavelength, which is on the order of millimeters for LMDS (at 38 GHz , for example, the wavelength is only 7.9 mm). Part of the incident wave from the transmitter antenna is reflected/scattered by the object to the receiver antenna. If the power of this reflected wave is significant with respect to the LOS component, this multipath component introduces dispersion into the channel. In a fixed point-to-point millimeter-wave channel, the power of the multipath component depends on the location of the object, the reflection loss, and the antenna patterns. The arrival time of the multipath component depends only on the location of the object and the link length. (Small propagation delays due to refractive index variations are negligible for typical short millimeter-wave links.)

Instead of calculating power and delay of a multipath component caused by a scatterer in a given location, a more general approach uses new concepts of the relative power zone and the excess delay zone. We define a *relative power zone* as the region where a strong reflector may cause a multipath component with a certain power level relative to the LOS signal. We define an *excess delay zone* as the region where a strong reflector may cause a multipath component with a certain delay time with respect to the LOS signal.

6.3 Relative Power Zone

When highly directional antennas are used, the power of EM waves is mainly concentrated in the direction of the antenna mainlobes. Specifically, when transmitter and receiver antennas are aligned, the transmitted power is concentrated in the region along the LOS path. Strong multipath components can be result only from the scatterers near the LOS path. Relative power zone is a metric to quantitatively describe the energy concentration of the EM waves, and identify the region where strong reflectors would result in strong multipath components.

The relative power zone takes into account antenna gains, free space path loss and reflection/scattering loss. The canonical antennas used to demonstrate the power zone and delay zone are presented in the Appendix C.

The power of the wave reflected by the scatterer is dependent on polarization, angle of incidence, dielectric properties and surface roughness [5]. When highly directional antennas are used, strong multipath components are caused only by scatterers close to the LOS path. When the angle between the incident wave and the reflecting surface is very small (i.e. at grazing angle), the effect of the surface roughness is negligible, and the reflection coefficient has an amplitude close to 1 [5, 125]. At different incident angles, as shown in Section 5.3.1, the surface appears more reflective when it becomes wet. For a worst case scenario, which is appropriate for equalizer design specification, each scatterer is assumed to be a perfect reflector with a reflection coefficient of 1. This worst-case assumption assures a design methodology that applies in a general way with little detailed information about scatterer material or surface roughness. Practical reflection coefficients can then be taken into account based on this worst-case model (see Section 6.6). A similar approach was also used in [150] to model street-level propagation at 55 GHz .

Under the assumption that the scatterer is a large perfect reflector, the relative received power, ΔP_{MP}, of each multipath component is computed as follows

$$\Delta P_{MP} = G_t(\phi_t, \theta_t) + G_r(\phi_r, \theta_r) - [PL(d_1 + d_2) - PL(D)] \text{ (dB)} \tag{6.146}$$

where d_1 and d_2 are the distances from the reflector to the transmitter and the receiver, G_t and G_r are normalized antenna power patterns for transmitter and receiver, $[PL(d_1 + d_2) - PL(D)]$ accounts for the excess free space path loss associated with the path length difference between the reflected path $(d_1 + d_2)$ and LOS path (D), and $\phi_t, \theta_t, \phi_r, \theta_r$ are shown in Figure 55. Given a link length D and the location of the reflector (x_0, y_0, z_0), all the other parameters can be determined using the geometry shown in Figure 55.

For a certain relative power level ΔP_{MP}, the relative power zone is given by (6.146). The resulting relative power zones for the canonical antennas – a horn and a dish – are presented in Figure 56, where the contours represent the power zone boundaries.

For example, -5 dB reflection zone boundary shows the region along the LOS path, where a perfect reflector would result in a multipath with -5 dB power relative to the LOS component.

6.4 Excess Delay Zone

In a multipath channel, arrival time of each multipath wave is determined by the actual path length and the speed that the wave travels (speed of light in free space). Therefore, excess delay time of the multipath component can be determined based on the geometry and site information as follows

$$\tau_{MP} = (d_1 + d_2 - D)/c \quad \text{(s)} \tag{6.147}$$

where d_1 and d_2 are the distances from the reflector to the transmitter and the receiver, D is link length, c is the speed of light.

For a specified excess delay, τ_{MP}, the boundary of the excess delay zone forms an ellipsoid. The

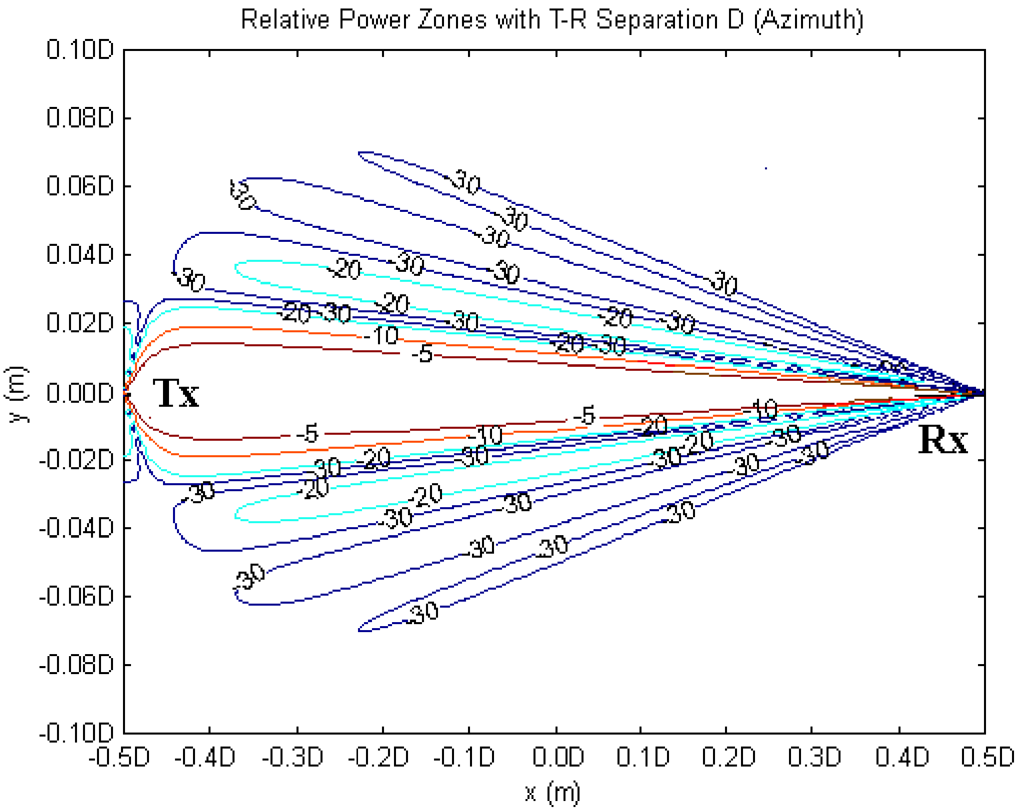

Figure 56: The relative power contour plot in azimuth for horn and parabolic antennas, for any D, (all contour units in dB relative to LOS power).

closed form equation for the ellipsoid is

$$\frac{x_0^2}{K_t^2/4}+\frac{y_0^2}{K_t^2/4-D^2/4}+\frac{z_0^2}{K_t^2/4-D^2/4}=1 \qquad (6.148)$$

where $K_t = D + c \times \tau_{MP}$ is a constant. It can be shown that the ratio of x and y axes of the ellipse changes with distance D and is given by $K_t/\sqrt{K_t^2 - D^2}$. An example of the excess delay zones is depicted in Figure 57 for a path length of 1000 m. The contours represent excess delay zone boundaries.

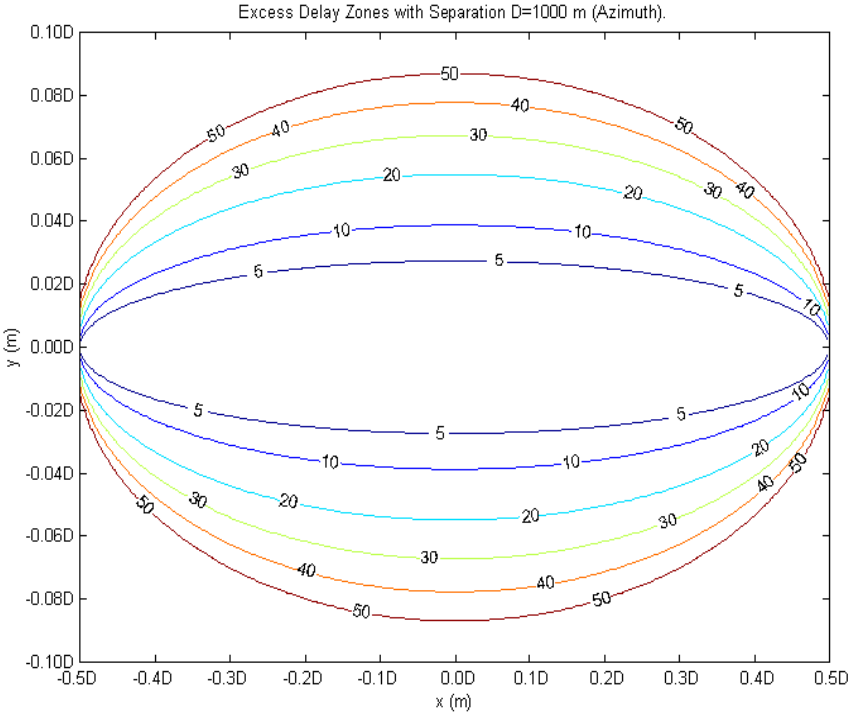

Figure 57: The excess delay contour plot in azimuth for D=1000 m (all contour units in ns).

6.5 Application Examples

6.5.1 Estimate Worst Case Multipath Based on a Site Map

The excess delay contour plot and the relative power contour plot provide a novel technique to identify worst case multipath characteristics for any millimeter-wave point-to-point/multipoint system deployment. By overlaying the plots onto a site map and identifying potential scatterers, engineers can quickly estimate the delay and power of possible multipath components.

Figure 58 presents an example site map. A building with a flat surface is located on the 10 ns contour line of the excess delay zone plot and the -20 dB contour line of the relative power zone plot, then the worst-case estimate of the multipath power and arrival time from this scatterer are -20 dB and 10 ns relative to LOS, assuming no scattering loss. If this is the only significant scatterer, the worst-case mean excess delay and RMS delay spread for this case are 0.1 ns and 0.99 ns, respectively. Angles of arrival, θ_r and ϕ_r, are calculated based on geometry from the contour plots.

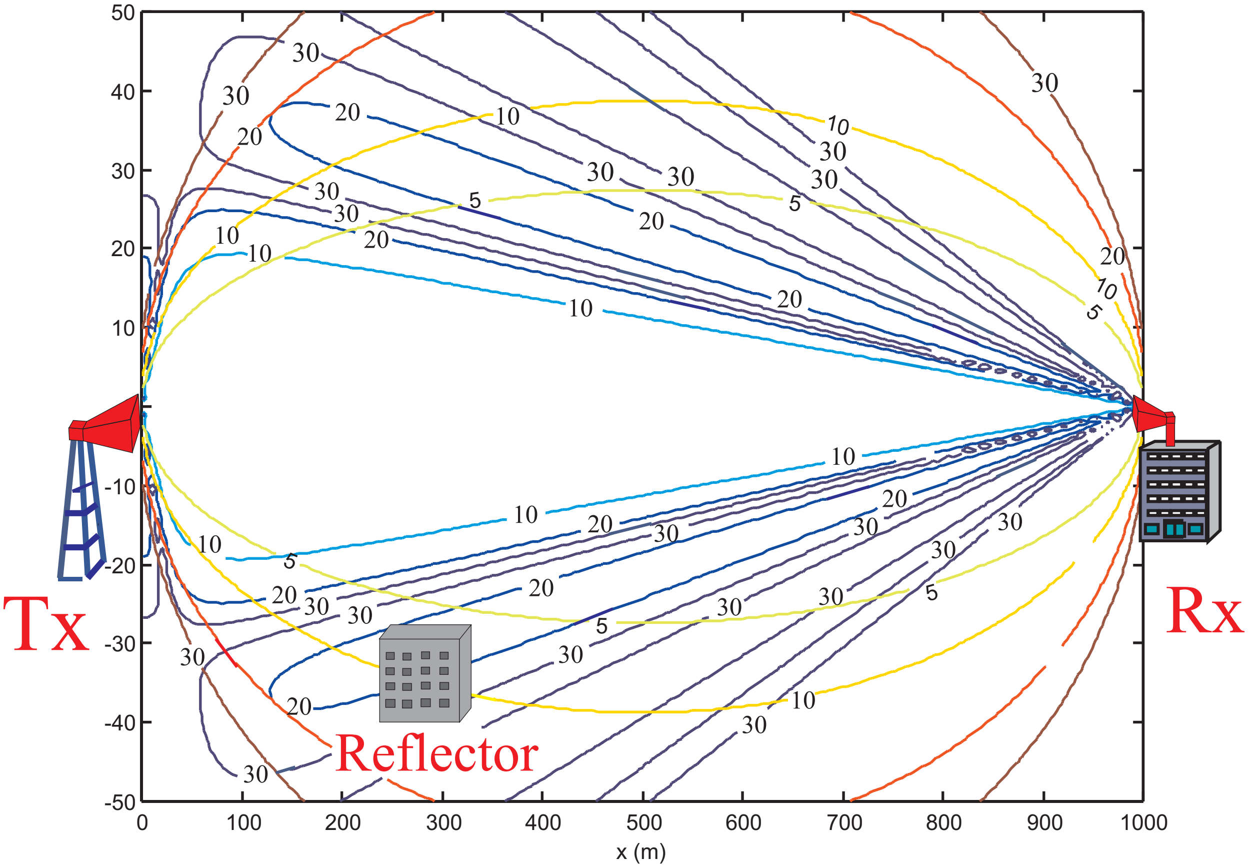

Figure 58: Example of application of power zone and delay zone on site map.

6.5.2 Clearance Criterion for Given Multipath Requirements

Identical to Fresnel zone clearance, the excess delay zone and relative power zone boundaries to the LOS path can be used as a deployment guideline. We define the maximum distance of a power (or delay) zone, y_{pz}^{max} (or y_{dz}^{max}), as the maximum distance from a power (or delay) zone boundary to the LOS path. These maximum distances are similar to the maximum Fresnel zone radii and can be determined analytically from link length, D, expected delay, τ_{MP}, and expected power, ΔP_{MP}. From (6.148), the maximum distance of an excess delay zone, y_{dz}^{max}, is given by

$$y_{dz}^{max} = \sqrt{(K_t^2 - D)/4} = \sqrt{[(D + \tau_{MP}C)^2 - D^2]/4} \quad \text{(m)} \tag{6.149}$$

where τ_{MP} is in seconds, and D is in meters. Table 12 shows maximum excess delay zone distance for typical D and τ_{MP}.

Table 12: Maximum Distances of Excess Delay Zone for Horn and Parabolic Antennas.

D	Maximum Excess Delay Zone Distances (m)				
τ_{MP}	10 ns	20 ns	30 ns	40 ns	50 ns
500 m	27.4	38.8	47.6	55.1	61.7
1 km	38.8	54.9	67.2	77.7	86.9
2 km	54.8	77.5	95.0	109.7	122.7
3 km	67.1	94.9	116.3	134.3	150.2
4 km	77.5	109.6	134.2	155.0	173.4
5 km	86.6	122.5	150.1	173.3	193.8

Table 13: Maximum Distances of Relative Power Zone for Horn and Parabolic Antennas.

D	Maximum Relative Power Zone Distances (m)				
ΔP_{MP}	5 dB	10 dB	20 dB	30 dB	35 dB
500 m	7	10	19	35	46
1 km	14.5	19.5	38.5	70	92
2km	29	39	77	140	185
5km	72	96	192	352	461

The maximum distance of a relative power zone, y_{pz}^{max}, is evaluated using (6.146). As shown in Table 13, y_{pz}^{max} is approximately proportional to D. This is expected. When directive antennas are used for short-hop links, most of the energy is concentrated near the LOS path. Therefore, in (6.146), term $(PL(d_1 + d_2) - PL(D))$ is relatively small and relative power zones are mainly determined by the antenna patterns. The exact relationship between y_{pz}^{max} and ΔP_{MP} can be expressed in terms of Bessel function and *sinc* function from (C.183) and (C.184). However, a simple relationship can be achieved by applying a polynomial fit to the exact solutions from Table 13. This results in the following

$$y_{pz}^{max} = \frac{D}{1000}(0.07\Delta P_{MP}^2 - 0.195\Delta P_{MP} + 12.6) \text{ (m)} \tag{6.150}$$

where D is in meters, and ΔP_{MP} is in dB.

Equations (6.149) and (6.150) relate the required multipath delay and power with maximum clearance distances. For instance, if a system requires no multipath within 10 ns of delay and -20 dB of power relative to LOS component, then y_{dz}^{max} is 38.8 m from (6.149), and y_{pz}^{max} is 36.7 m from (6.150). Then a clearance distance of 38.8 m (i.e. no scatterer within 38.8 m) from LOS would be desirable to achieve required system performance.

6.6 Comments Regarding the Model

A two dimensional geometrical model has been reported in [55, 151] to predict power, delay and AOA for the omnidirectional antennas. The model developed in this work is a more generalized *three dimensional* model, that takes into account *any combination of directional antenna patterns.*

Figure 56 is developed using canonical antennas for any link length and Figure 57 is generated for a link length of 1000 m for any antenna type. Using (6.146) and (6.148), one can easily develop plots for *any* link length and *any* type of antenna.

The excess delay zones and relative power zones are spatial fields in three dimensions. Due to its radial symmetry about LOS path, the excess delay zone can be applied to any point in three dimensional space. However, since the antenna patterns are generally not radially symmetric, the relative power zone in azimuth and elevation planes are different. Therefore, one should also develop relative power contour plots for the elevation plane. For any given point in the space, it is possible to find the projections onto these orthogonal planes. Then, the power of the received multipath component is approximated by the sum of powers (in dB) in each plane.

The relative power zone and excess delay zone have interesting relationships with Fresnel zones. Fresnel zones represent successive regions where a path length from the transmitter to the receiver is $n\lambda/2$ greater than the LOS path [14], where λ is the wavelength. In fact, the excess delay zone can be viewed as a macro-Fresnel zone, where the distance between two successive zone boundaries gives rise to a particular propagation delay. A 1 ns delay corresponds to 0.3 m path difference, or 38 wavelengths at 38 GHz . Therefore, the excess delay zone boundaries are much larger than the Fresnel zone boundaries. For the specified antennas and a path length of 1000 m, the maximum distances of 10 ns delay zone and -20 dB power zone are approximately the same as the 760^{th}

Fresnel zone radius. Fresnel zones are used to describe diffraction loss, while power zone and delay zone are used to estimate power and delay of potential reflected multipath components.

The model is developed for the case where the reflection coefficient is one. Realistic reflection coefficients can be measured or estimated using site-specific information. If the reflection coefficient Γ is known, then the reflection loss is given by $L_{reflect} = 10 \log_{10} |\Gamma|^2$. This loss can be added to the model by simply adjusting the power levels of the relative power zones in Figure 56 by the value of $L_{reflect}$.

Finally, the model assumes that each multipath component is the result of a single reflection. Ray tracing can be applied to account for higher orders of reflection. Based on the system requirements, the contour plots may be used to define the environment necessary for more involved ray tracing techniques [149].

6.7 Summary

This chapter presents a novel design technique to estimate wideband channel characteristics in millimeter-wave point-to-point/multipoint communications systems. Relative power zones and excess delay zones are defined to predict multipath power and arrival time. Relative power zone describes the power concentration of the EM waves due to the directional antenna patterns, and identifies the region where a perfect reflector would give rise to a strong multipath component. Excess delay zone describes the direct relationship between path length and multipath arrival time. It identifies the region where a perfect reflector would give rise to a multipath component with a certain delay.

Based on these definitions, contour plots are developed to identify the excess delay zone and relative power zone boundaries. Similar to Fresnel zone clearance, new clearance criteria are developed to achieve system requirements on power and delay of multipath components.

Since these contour plots and zone boundaries are dependent only on the antenna patterns and the link length, they may be applied to *any* site. By overlaying the contour plots on the site map, application engineers can quickly determine potential reflectors. The power and delay zones and their contour plots provide practical guidelines for millimeter-wave system design and deployment.

Chapter 7

Spatial and Temporal Characteristics of 60 GHz Indoor Channels

This chapter presents wideband measurement results and models for 60 GHz channels. Multipath components were resolved in time by using a sliding correlator with 10 ns resolution, and in space by sweeping a directional antenna with 7° half power beamwidth around the azimuth. Power delay profiles (PDPs) and power angle profiles (PAPs) were measured in various indoor and short-range outdoor environments. Detailed multipath structure was retrieved from PDPs and PAPs, and compared with site-specific environments. Results show an excellent correlation between the propagation environments and the multipath channel structures. The measurement results confirm that the majority of the multipath components can be determined from image based ray tracing techniques for LOS applications. For NLOS propagation through walls, the structure of composite walls must be considered for propagation prediction. From the recorded PDPs and PAPs, received signal power and statistical parameters of angle-of-arrival (AOA) and time-of-arrival (TOA) were also calculated. These parameters accurately describe the spatial and temporal properties of millimeter-wave channels, and can be used as practical values for broadband wireless system design over 60 GHz short-range channels.

7.1 Introduction

Advanced wireless systems explore dimensions of time, frequency and space to maximize the data rate and system capacity. Design of space-time coding, equalization, adaptive antenna, and rake receiver techniques relies on accurate characterization of the propagation channel. Classical channel models were developed for narrowband microwave systems with omnidirectional antennas [47, 48]. For millimeter-wave wireless systems with high data rates and directional antennas, small-scale fading is much more difficult to characterize than for omni-narrowband systems. Efficient design of these systems depends on detailed knowledge of the multipath structure of the channel, and narrowband channel models are no longer sufficient.

The research work presented in this chapter focuses on characterization of 60 GHz channels both in space and time delay. The 60 GHz spectrum is proposed for future-generation broadband wireless systems in indoor and short-range outdoor environments, where the radio wave channel varies significantly from location to location. In practice, site-specific prediction techniques, such as ray tracing, are used to model millimeter-wave channels [149]. However, little literature is available to carefully verify the ray-tracing model with high-resolution measurements, or to provide detailed AOA and TOA parameters for the 60 GHz channels.

The goal of this research is threefold:

- Accurately measure the channel multipath structure by separating multipath components by AOA and TOA;
- Determine the origin of multipath by relating multipath AOA and TOA to site-specific information; and
- Provide empirical values of statistical parameters of AOA and TOA for various propagation environments.

Section 7.2 presents the measurement setup. Section 7.3 relates the measured channel images to the propagation environments. Finally, Section 7.4 summarizes the measured AOA and TOA parameters.

7.2 Measurement Setup

7.2.1 Methods to Separate Multipath Components

Multipath components can be separated either by their AOA or TOA. The resulting channel characteristics can be recorded as a *power delay profile* (PDP) or a *power angle profile* (PAP). A PDP records temporal power distribution relative to multipath TOA, and a PAP records spatial power distribution relative to multipath AOA. Wideband measurement techniques, such as vector network analyzer or sliding correlator, are used to resolve multipath by their delay times. However, all measurement systems have limited time resolution. Even with the 10 ns resolution used in this measurement campaign, the received signal pulse may still contain several multipath components and fade in a small local area. One method for increasing multipath resolution is to use directional antennas at the receiver to separate multipath components, provided they arrive from different directions.

Angular separation of multipath components can be achieved by using direction-finding antenna arrays [152], synthetic aperture radar techniques [153, 154, 155], or highly directional antennas [11, 130]. In antenna array systems, multiple antennas are used at the receiver. Signals received at the array elements are weighted and combined to attenuate received signals arriving from outside the desired direction. This technique allows fast measurements of the channel, but is prone to mutual coupling among antenna elements. Synthetic aperture radar techniques eliminate mutual coupling by using only one antenna that moves into different locations of the array. It produces results similar to an antenna array, provided all measurements are taken within the channel's coherence time. Electronic beam forming techniques, such as direction-finding antenna arrays, require accurate phase measurements and elaborate processing. PAPs can also be measured by mechanically rotating a highly directional antenna. The advantage is that it does not require phase information. At low frequencies, highly directional antennas have large dimensions and present difficulty in mechanical steering. However, at millimeter wave frequencies, miniaturized directional antennas can be easily implemented.

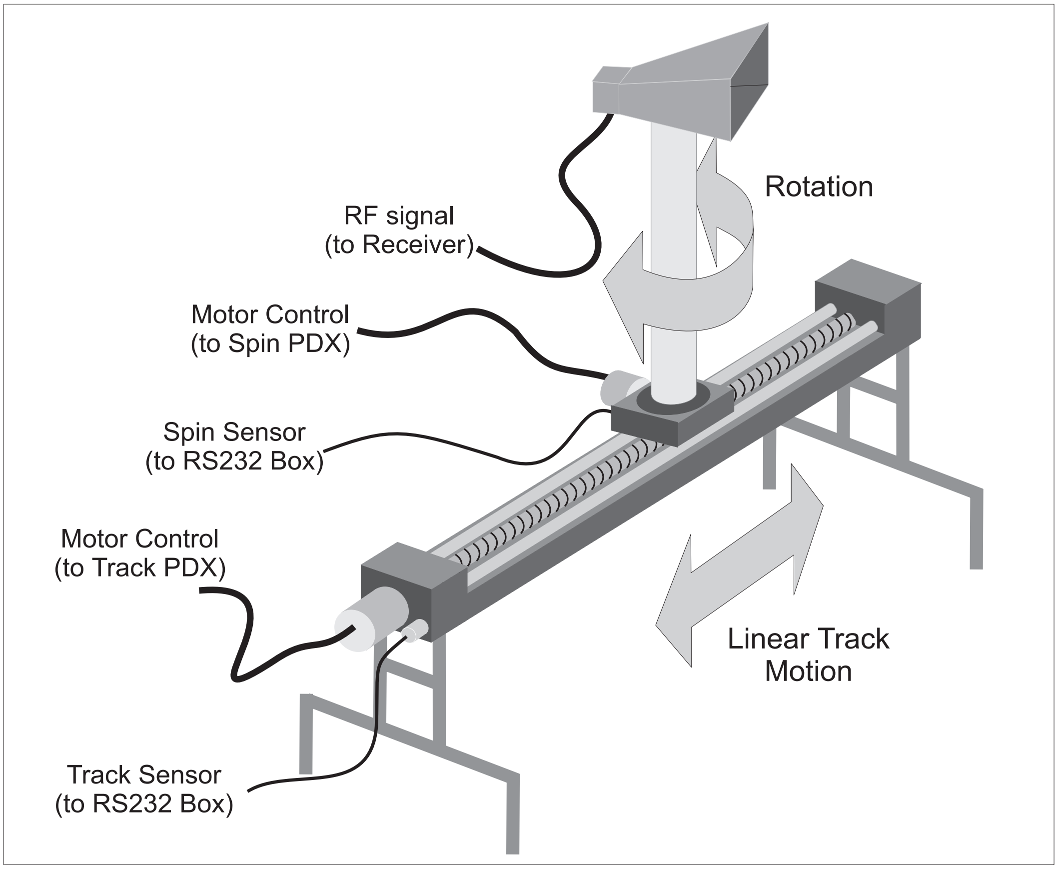

Figure 59: Automated track system [9].

7.2.2 Measurement Procedure

In this measurement campaign, a mechanically steered directional antenna was used to resolve multipath. An automated system was used to precisely position the receiver antenna along a linear track, and then rotate the antenna in the azimuthal direction. The track system is shown in Figure 59. The precisions of the track position and spin position are better than 1 mm and 1^0, respectively [9]. When a highly directional antenna is used, this system provides high spatial resolution to resolve multipath components with different AOAs. The sliding correlator technique was used to further resolve multipath components with the same AOA by their TOAs. The spread spectrum signal had a RF bandwidth of 200 MHz , which provided a time resolution of approximately 10 ns .

To represent different propagation environments, the measurements were taken in various locations

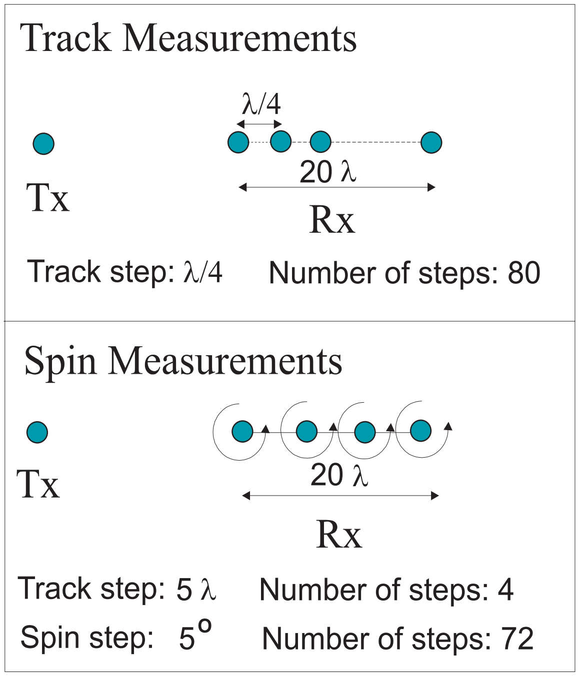

Figure 60: Track and spin measurement procedure.

(Site information is described in Section 7.2.4). At each location, both *track measurements* and *spin measurements* were performed as shown in Figure 60.

- Track measurements: During a track measurement, the transmitter and receiver antennas are aligned, and the receiver is moved along the track parallel to the LOS path. PDPs are taken at 80 positions along the track with a separation of a quarter wavelength. This allows a spatial sampling rate of 4 samples per wavelength along the track with a length of 20 wavelengths. The purpose of the track measurement is to study the range of small-scale signal variations and TOA statistics for typical indoor applications, where transmitter and receiver antennas are fixed and aligned.

- Spin measurements: During a spin measurement, the receiver is moved along the linear track to 4 different positions. The spatial separation between two successive positions is 5 wavelengths. At each position, the receiver antenna is rotated in azimuth from 0° to 360° with a step of 5°, and PDPs are recorded at each of the 72 angular steps. Then, a local average is calculated from the measurement results at 4 different positions. The local average helps to remove any residual small-scale or time-varying fading that may occur at individual positions. The averaged PDPs and PAPs are processed to obtain the AOA and TOA statistics of the channel. Definitions of the statistical parameters are presented in Section 7.4, and the measurement results are presented in Section 7.4.2. The purpose of the spin measurement is to obtain the complete spatial-temporal characteristics of the channel. The general results provide deep understanding of the wave propagation in a local area. The measured results can also be applied to verification of ray tracing channel estimation, position location algorithms, and development of fixed as well as mobile wireless applications.

7.2.3 Antenna Patterns

For this measurement campaign, an open-ended waveguide with 90° half-power-beamwidth (HPBW) and 6.7 dB gain was used as the transmitter antenna, and a horn antenna with 7° HPBW and 29 dB gain was used as the receiver antenna. These antennas were chosen to emulate typical antenna systems that are proposed for millimeter-wave indoor applications, where a sector antenna is used at the transmitter and highly directional antenna is used at the receiver. The antenna patterns were measured by performing the spin measurements in an open area in the parking lot. The antenna pattern was generated by sweeping the antenna under test and plotting the peak received power at each pointing angle. The measured antenna patterns are presented in Figure 61.

7.2.4 Site Description

A total of 33 spin and track measurements in 8 different locations were measured at the Virginia Tech campus. The site information is summarized in the maps and photos in Appendix D.

Locations 1 and 2 represent typical hallways. Location 1 was in the hallway on the fourth floor of New Engineering Building (NEB). NEB is a four-story concrete building, which was built in 1997. The hallway dimensions are 102 × 2.1 × 4.3 m (In this section, all the dimensions are given in the order of length, width and height). Location 2 was in the hallway on the second floor of Whittemore hall. The hallway dimensions are 54.7 × 2.9 × 4.3 m. For both locations, the transmitter was fixed at one end of the hallway. Several receiver positions were chosen at separations ranging from 5 m

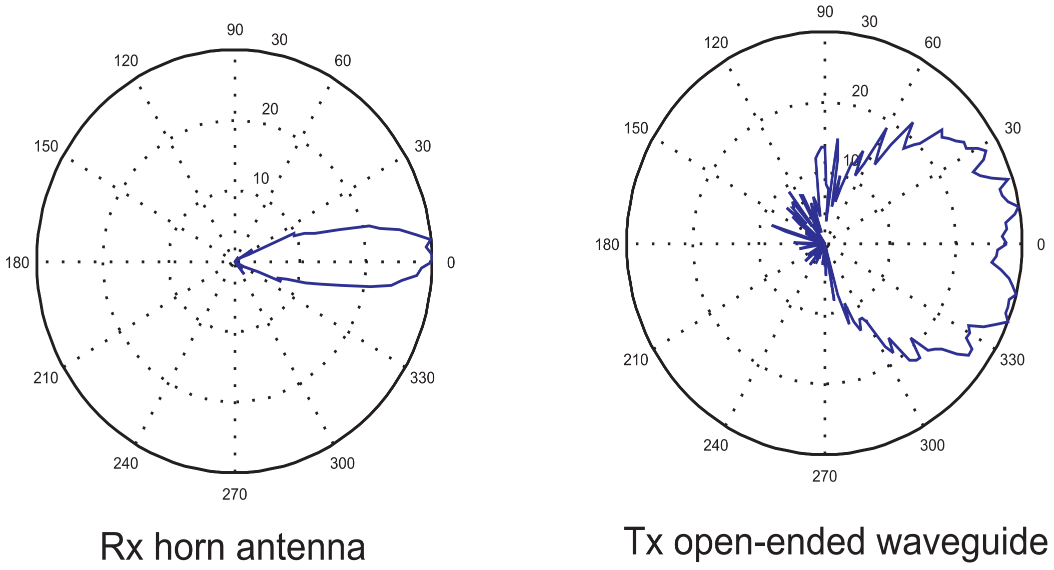

Rx horn antenna

Tx open-ended waveguide

Figure 61: Receiver and transmitter antenna patterns used in the measurement campaign.

to 60 m from the transmitter. All receiver positions had LOS to the transmitter.

Locations 3 and 4 represent small to medium-sized rooms. Location 3 was in a conference room on the fourth floor of NEB. The dimensions of the room are 6.7 × 5.9 × 4.3 m. The transmitter was fixed in one corner of the room. The receiver was placed in two different positions: in the opposite corner of the room and the center of the room. Location 4 was in a classroom in Whittemore Hall with dimensions of 8.4 × 7.1 × 4.3 m. The transmitter was fixed in one corner of the room. The receiver was placed in four different positions: the center and the other three corners of the room.

Locations 5 and 6 were chosen to study NLOS propagation from a hallway to a room, and from a room to an adjacent room, respectively. In location 5, the receiver was in a laboratory with dimensions of 11.7 × 5.1 × 4.3 m. The transmitter was placed in the hallway. Two different positions were measured. In one position, the transmitter and receiver antennas were separated by a composite wall with metallic studs inside. In the other position, the antennas were separated by the glass door. In location 6, the transmitter and receiver were placed in two adjacent rooms separated by a composite wall with metallic studs inside. The dimensions of the rooms are 11.7 × 5.1 × 4.3 m and 5.1 × 4.3 × 4.2 m. The metallic studs are separated by 40 cm (16 in).

Locations 7 and 8 were outdoor locations. Location 7 was in a parking lot with no cars. The only possible scatterers were the lamp posts. This location was selected to perform free-space calibration and antenna pattern measurements. Location 8 was near the exterior stone wall of NEB. The transmitter and receiver were placed along the wall with a separation of 2 m to 5 m between the antennas. Both antennas were 3.5 m from the wall. The simple propagation environments of locations 7 and 8 were chosen to verify the system performance.

The main rational of choosing these eight locations was to provide a variety of different propagation scenarios for the measurements, and also provide controllable environments for analysis and site-specific channel modeling.

7.3 Relating Multipath Structure to Propagation Environments

7.3.1 Power Angle Profiles

This section investigates the correlation between the propagation environments and the multipath AOA. Measured PAPs are imported into the site-map to identify the origin of each multipath component.

Examples of the PAP results are shown in Figure 62 for propagation within a room, in Figure 63 for propagation in a hallway, and in Figure 64 for propagation into rooms.

The PAPs exhibit strong correlation with the propagation environments. The following observations were made from the recorded PAPs:

- *Propagation within a room*: As shown in Figure 62, when the LOS path exists, the maximum multipath component is always from the LOS direction. The value of the maximum multipath power is given as P in dBm in the legend. Powers of the other small multipath components are given in dB in the figure relative to the maximum power. LOS and the first-order reflected waves contribute the majority of the multipath components (the order of reflection is referring to the number of reflections that a multipath component goes through before it reaches the receiver). In the center location 4.2, there are only three strong multipath components: one is the LOS component, the other two are first-order reflected waves from the sidewalls. The

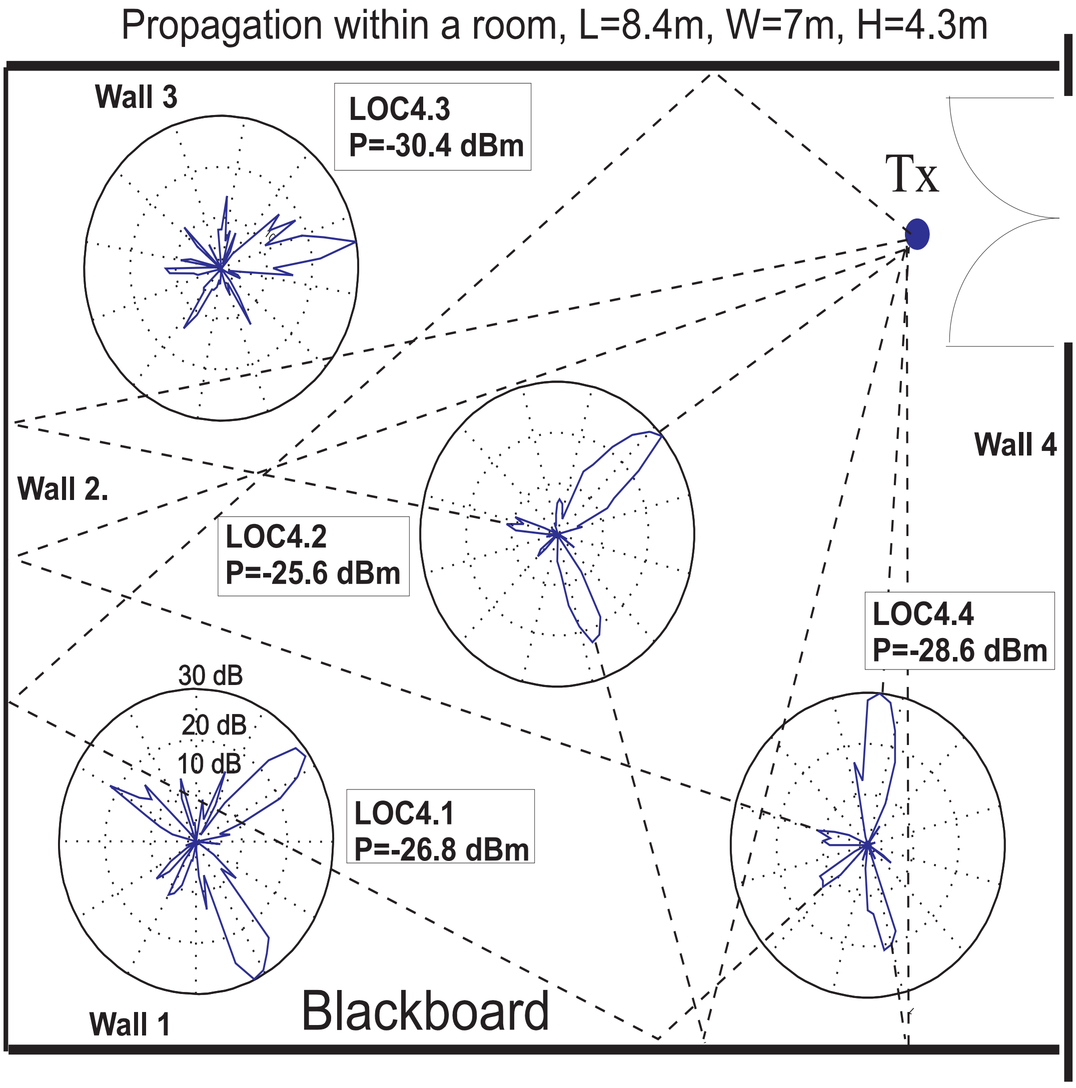

Figure 62: AOA measurements for propagation within a room (location 4), relative power levels given in polar plots and peak multipath power (P) given in text. Rays are shown only for locations 4.2 and 4.4 in the figure, similar procedure can be performed for all the locations.

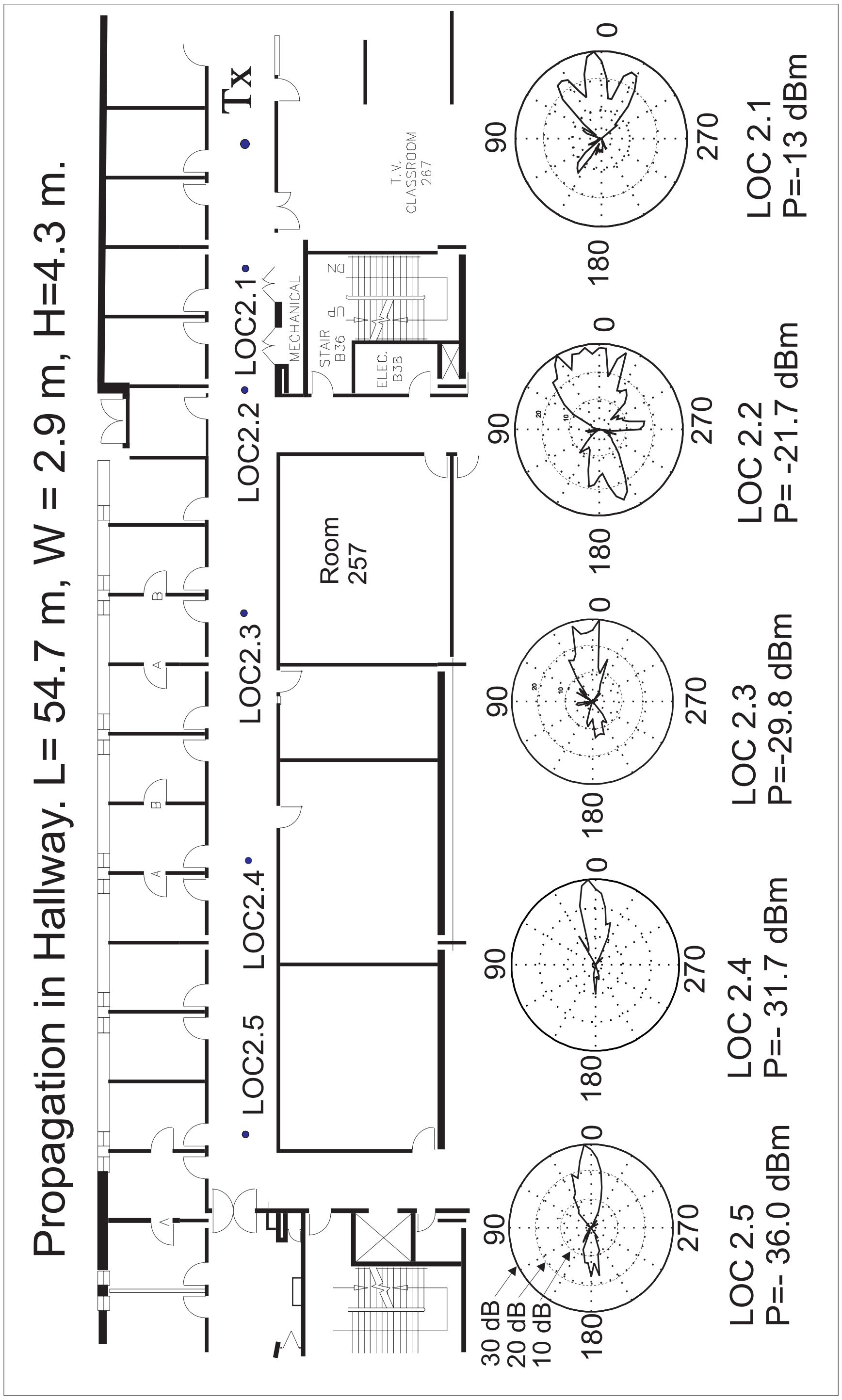

Figure 63: AOA measurements for propagation along a hallway (location 2), relative power levels given in polar plots and peak multipath power (P) given in text.

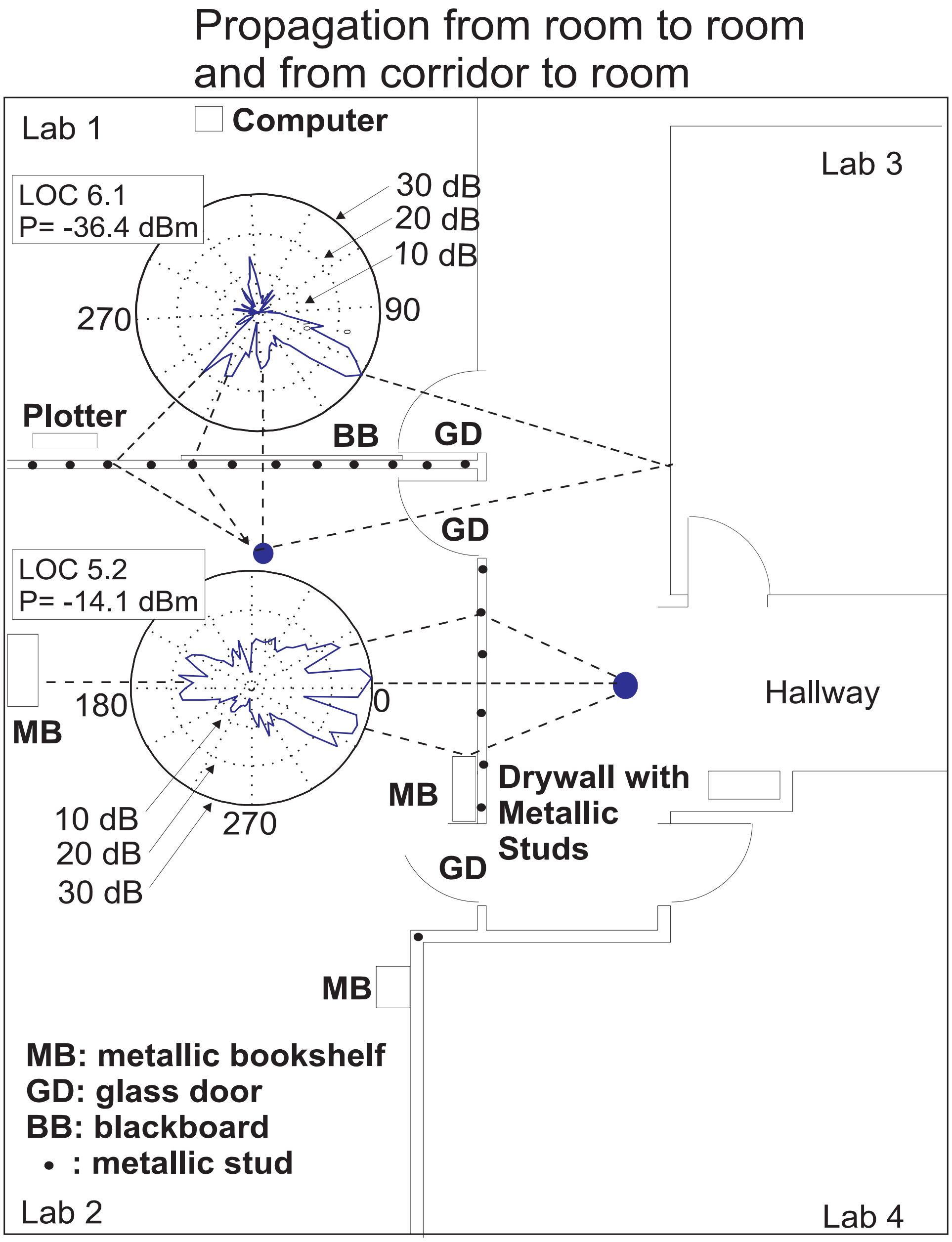

Figure 64: AOA measurements for propagation into rooms (locations 5 and 6), relative power levels given in polar plots and peak multipath power (P) given in text.

reflected wave from “wall 2” is 19 dB below the LOS component. The blackboard appears to be a strong reflector. The reflected wave from the blackboard is only 8 dB below the LOS path. There are more multipath components in the corner locations of the room. In location 4.4, the multipath components consists of LOS component, first-order reflected waves from “wall 2” and the blackboard, and the second-order reflected wave from “wall 2” and the blackboard. Similar analysis can be performed for locations 4.1 and 4.3. At location 4.1, the strong reflection of the blackboard resulted in a multipath component with comparable power with the LOS component.

- *Propagation in a hallway*: Figure 63 shows the measurement results of location 2 in the hallway. For all the measurement positions, the strongest multipath component came from the LOS direction. For location 2.1, the main multipath components are LOS and the reflected waves from the sidewalls. Location 2.2 is near the intersection of two hallways. The LOS component and reflected waves from sidewalls are still strong, but became more diffusive. A strong multipath component came from the corner of room 257. As shown in locations 2.3, 2.4 and 2.5, when the separation further increases, the reflections from the sidewalls became insignificant. The reflection from the other end of the hallway became stronger. Results from location 2.5 clearly show the LOS and the reflected wave components.

- *Propagation through walls*: Figure 64 shows the measurement results for NLOS propagation into rooms. In both locations, the radio wave propagates through a composite wall with metallic studs. Results indicate that the metallic studs have strong impact on the millimeter-wave propagation. In location 5, the metallic studs do not obstruct the LOS path. Measurement results show that the penetration loss is 9 dB through the wall between the room and the hallway. The strongest multipath component is still from the transmitter direction. Other major multipath components are reflected waves from the metallic bookshelves. The multipath energy seems to be more diffuse in their AOAs in this NLOS case as compared to the LOS propagation within a room (Figure 62). Reflections/scattering of the radio wave from the studs also contribute to the multipath components.

  In location 6, the metallic stud obstructs the LOS path, and the measurement results show that the penetration loss through the wall and the blackboard is as high as 35.5 dB. Since the LOS path was highly attenuated, the maximum multipath power came from the reflected path through two glass doors. Other strong multipath components might came from the reflection/scattering from the metallic plotter or the studs.

These measurement results clearly demonstrate a strong correlation between the propagation environments and the multipath channel structure. The following general conclusions can be made from all the measurement results:

- For LOS applications, free space propagation and reflection are the dominant propagation mechanisms. When there are no strong reflectors in the propagation environment, the reflected multipath components are at least 10 dB below the LOS component. LOS component and first-order reflected waves contribute majority of the received signal power. Strong multipath components can result from strong reflectors, such as metallic furniture. When strong reflectors are present, the reflected wave can be comparable to the LOS component. Image-based ray tracing (such as the one presented in [156]) can be used to estimate the channel multipath structure at millimeter-wave frequencies. For installation purposes or a rule-of-thumb estimation, LOS and first-order reflections can be considered based on the site geometry. For more accurate prediction, ray-tracing with second-order or third-order reflections can be used.
- For NLOS applications, the direct path can be highly attenuated and become comparable to reflected multipath components. As a result, the multipath channel structure may become more diffuse than in LOS environments. When radio waves propagate through composite walls, metallic studs within the wall must be considered. Penetration loss through the composite wall depends on the position and orientation of the studs within the wall. Results of penetration loss measurements are presented in Section 7.4.5. As shown in the measurement results from locations 5 and 6, reflection and scattering from the metallic studs may result in strong multipath components. More detailed analysis of the effects of different composite walls on short-path propagation can be found in [157] for 900 MHz , in [158] for 3.0 GHz , and in [11, 159] for 60 GHz .

It is worth noting that millimeter-wave systems are mainly proposed for LOS applications. The measurement results and analysis show that site-specific propagation models, such as ray-tracing, can be used to precisely image the space-time channel for LOS applications.

7.4 Statistical Parameters of the Channel

Site-specific prediction requires detailed knowledge of the propagation environments. When such information is not available, statistical models can be used to describe general channel properties. This section presents the statistical parameters distilled from all the measurements in different locations. The measured parameters include received signal power, TOA parameters, and AOA parameters.

7.4.1 Definition of the Statistical Parameters

TOA Parameters

TOA parameters characterize the time dispersion of a multipath channel. The recorded TOA parameters include mean excess delay, $\bar{\tau}$, RMS delay spread, σ_τ, and also their timing jitter and standard deviation in a small local area. Parameters of $\bar{\tau}$ and σ_τ are given as following [14]:

$$\bar{\tau} = \frac{\sum_{i=1}^{N} P_i \tau_i}{\sum_{i}^{N} P_i} \tag{7.151}$$

$$\sigma_\tau = \sqrt{\bar{\tau^2} - (\bar{\tau})^2} \tag{7.152}$$

$$\bar{\tau^2} = \frac{\sum_{i=1}^{N} P_i \tau_i^2}{\sum_{i}^{N} P_i} \tag{7.153}$$

where P_i and τ_i are the power and delay of the i_{th} multipath component of a PDP, respectively, and N is the total number of multipath components.

Timing jitter is calculated as the difference between the maximum and minimum measured values in a local area. Timing jitter, $\delta(x)$, and standard deviation, $\Delta(x)$, are defined as [9]

$$\delta(x) = \max_{i=1}^{M}\{x_i\} - \min_{i=1}^{M}\{x_i\} \tag{7.154}$$

$$\Delta(x) = \sqrt{\bar{x^2} - (\bar{x})^2} \tag{7.155}$$

$$\bar{x} = \sum_{i=1}^{M} x_i/M \tag{7.156}$$

$$\bar{x^2} = \sum_{i=1}^{M} x_i^2/M \tag{7.157}$$

where x_i is the measured value for parameter x ($\bar{\tau}$ or σ_τ) in the i_{th} measurement position of the spatial sampling, and M is the total number of the spatial samples in the local area. For example, for the track measurements, M was chosen to be 80.

Mean excess delay and RMS delay spread are the statistical measures of the time dispersion of the channel. Timing jitter and standard deviation of $\bar{\tau}$ and σ_τ show the variation of these parameters in the small local area.

These TOA parameters directly affect the performance of high-speed wireless systems. For instance, the mean excess delay can be used to estimate the search range of rake receivers, and the RMS delay spread can be used to determine the maximum transmission data rate in the channel without equalization. The timing jitter and standard deviation parameters can be used to determine the update rate for a rake receiver or an equalizer.

AOA Parameters

AOA parameters characterize the directional distribution of multipath power. The recorded AOA parameters include angular spread, Λ, angular constriction, γ, and maximum fading angle, θ_{max}, and maximum AOA direction. Angular parameters Λ, γ, and θ_{max} are defined based on the Fourier transform of the angular distribution of multipath power, $p(\theta)$ [160]:

$$\Lambda = \sqrt{1 - \frac{\|F_1\|^2}{\|F_2\|^2}} \tag{7.158}$$

$$\gamma = \frac{\|F_0 F_2 - F_1^2\|}{\|F_0\|^2 - \|F_1\|^2} \tag{7.159}$$

$$\theta_{max} = \frac{1}{2}\text{Phase}\{F_0 F_2 - F_1^2\} \tag{7.160}$$

where

$$F_n = \int_0^{2\pi} p(\theta)\exp(jn\theta)d\theta \tag{7.161}$$

F_n is the n_{th} Fourier transform of $p(\theta)$. As shown in [160], angular spread, angular constriction and maximum fading angle are three key parameters to characterize the small scale fading behavior of the channel. They can be used for diversity technique, fading rate estimation, and other space-time techniques. Maximum AOA provides the direction of the multipath component with the maximum power. It can be used in system installation to minimize the path loss. More detailed analysis on these parameters is presented in Section 7.4.2.

Path Loss

The free-space *path loss* at a reference distance of d_0 is given by

$$PL_{fs}(d_0) = 20 \log\left(4\pi d_0/\lambda\right) \tag{7.162}$$

where λ is the wavelength. Path loss over distance d can be described by the path loss exponent model as follows:

$$\overline{PL}(d)[\text{dB}] = PL_{fs}(d_0)[dB] + 10n \log_{10}(\frac{d}{d_0}) \tag{7.163}$$

where $\overline{PL}(d)$ is the average path loss value at a TR separation of d, and n is the *path loss exponent* that characterizes how fast is the path loss increases with the increase of TR separation. The path loss values represent the signal power loss from the transmitter antenna to the receiver antenna. These path loss values do not depend on the antenna gains or the transmitted power levels. For any given transmitted power, the received signal power can be calculated as

$$P_r[\text{dBm}] = P_t[\text{dBm}] + G_t[\text{dB}] + G_r[\text{dB}] - PL(d)[\text{dB}] \tag{7.164}$$

where G_t and G_r are transmitter and receiver gains, respectively. The path loss exponent model and partition based path loss models are explained in detail in Section 2.1.2. In this measurement campaign, the transmitted power level was 25 dBm , the transmitter antenna gain was 29 dB and the receiver antenna gain was 6.7 dB .

7.4.2 Results of Measured Statistical Parameters

A total of 8,848 wideband PDPs and 94 PAPs were recorded, from which 2,080 PDPs were recorded through linear track measurements and 6,768 PDPs through spin measurements.

Summary of the measurement results is presented in Table 14 for spin measurements and in Table 15 for linear track measurements. The presented parameters are averaged results from individual PDPs taken in a small local area. They represent the statistical temporal and spatial characteristics for the measured 60 GHz channels. Sections 7.4.3 to 7.4.5 analyze AOA parameters, TOA parameters, and the received signal power in detail.

7.4.3 AOA Statistics

- *Angular distribution of multipath power*: Angular spread characterizes the angular distribution of the multipath power. It ranges from 0 to 1, with 0 indicating multipath coming from a single direction, and 1 indicating no clear bias in the multipath AOA [160]. Measurement results show that the angular spread ranges from 0.36 to 0.78 for hallway measurements, 0.62 to 0.84 for room measurements, from 0.63 to 0.81 for indoor NLOS propagation, and 0.12 to 0.49 for outdoor measurements with few nearby obstructions. These measurement results show a clear increase of the angular spread from the least cluttered outdoor environments to obstructed NLOS indoor environments. In the hallway where multipath components are mainly constrained along the LOS path, the angular spread is smaller than that in rooms. Also, with the increase of distance along the hallway, the angular spread increases, indicating more multipath coming from different directions which have powers comparable to the LOS component. These angular spread values accurately reflect the correlation between the propagation environments and the multipath angle of arrival distributions.

- *Angular constriction*: Angular constriction indicates how multipath components are distributed along two directions. It ranges from 0 to 1, with 1 indicating multipath energy equally distributed in two directions. High angular constriction results were observed in close distances in the hallway measurements and in the outdoor measurements near NEB. This is the result of distribution of multipath energy between LOS and strong reflected wave components.

- *Maximum fading angle*: Maximum fading angle shows the direction of the receiver motion to achieve maximum fading rate. In the far side of the corridor (locations 1.6 and 1.7, for example), the received signal consists of the LOS component along the corridor and the

Table 14: Spin Measurements: Transmitter-Receiver Separations (TR) in m, Time Dispersion Parameters ($\bar{\tau}$ and $\sigma_\mathcal{T}$) in ns, Angular Dispersion Parameters (Λ and γ) are dimensionless, Maximum Fading Angle(θ_{max}) and AOA of Maximum Multipath ($maxAOA$) in Degree, Ratio of Maximum Multipath Power to Average Power ($\frac{Peak}{Avg}$) in dB, and Maximum Multipath Power (P_{max}) in dBm.

Site Info	#	TR	$\bar{\tau}$	$\sigma_\mathcal{T}$	Λ	γ	θ_{max}	max AOA	$\frac{Peak}{Avg}$	P_{max}	Comments
LOS,hallway NEB	1.1	5	80.0	14.7	0.46	0.83	-80.7	-4	12.3	-14.9	
	1.2	10	52.0	18.8	0.44	0.74	-86.6	4	12.0	-18.2	
	1.3	20	85.9	40.1	0.56	0.28	-61.9	8	14.5	-28.8	
	1.4	30	116.6	38.7	0.42	0.22	-66.4	5	14.7	-28.3	open area
	1.5	40	84.9	60.0	0.69	0.25	4.3	5	13.9	-38.2	
	1.6	50	52.1	26.1	0.66	0.26	8.2	10	13.3	-38.2	
	1.7	60	53.2	30.3	0.78	0.36	4.0	2	13.2	-40.8	
LOS,hallway Whittemore	2.1	5	51.0	20.7	0.48	0.88	-73.5	5	12.5	-13	
	2.2	10	62.1	29.4	0.66	0.79	-72.3	21	11.4	-21.7	intersection
	2.3	20	90.7	14.6	0.36	0.43	-73.8	4	12.9	-29.8	
	2.4	30	41.2	12.3	0.41	0.15	-64.8	10	13.8	-31.7	
	2.5	40	83.7	53.8	0.72	0.19	5.0	1	13.2	-36.0	
LOS, room NEB	3.1	4.2	42.6	16.2	0.86	0.64	-79.2	0	12.5	-11.8	corner
	3.2	3.3	47.7	17.5	0.81	0.70	-79.1	5	13.1	-12.1	center
LOS, room Whittemore	4.1	7.1	46.6	13.0	0.84	0.55	-88.0	-60	12.3	-26.8	corner
	4.2	3.8	64.3	13.3	0.62	0.74	-89.6	-1	13.1	-25.6	center
	4.3	5.2	66.3	17.7	0.73	0.84	-35.2	49	14.0	-30.4	corner,$\perp$ to Tx
	4.4	4.2	77.8	13.3	0.78	0.72	-38.2	-49	14.2	-28.6	corner,$\perp$ to Tx
Hallway to room	5.1	2.4	49.1	21.4	0.81	0.13	-76.3	0	12.0	-6.0	LOS
	5.2	2.4	41.6	18.1	0.74	0.44	-89.6	5	10.3	-14.1	through wall
	5.3	2.4	95.8	14.6	0.63	0.40	-88.1	0	12.1	-5.6	LOS
	5.4	2.4	80.3	16.0	0.68	0.27	72.3	5	11.9	-8.9	through glass
Room to room	6.1	3	42.7	16.6	0.80	0.40	-25.3	52	11.5	-36.4	through wall
LOS, outdoor parking lot	7.1	1.9	41.3	17.4	0.12	0.97	-81.2	2	13.9	-15.0	Tx pattern
	7.2	1.9	56.6	16.1	0.49	0.94	-66.7	20	8.5	-29.9	Rx pattern
LOS, outdoor	8.1	2	24.4	7.7	0.26	0.76	-66.3	3	13.9	-10.1	near NEB

Table 15: Track Measurement Results: TR Separations (TR) in m, Time Dispersion Parameters ($\bar{\tau}$ and σ_τ) in ns, Variations of Time Dispersion Parameters ($\delta\bar{\tau}$, $\triangle\bar{\tau}$, $\delta\sigma_\tau$ and $\triangle\sigma_\tau$) in ns, and Average Received Power (P_r) in dBm.

Site Info	LOC #	TR	$\bar{\tau}$	σ_τ	$\delta\bar{\tau}$	$\triangle\bar{\tau}$	$\delta\sigma_\tau$	$\triangle\sigma_\tau$	P_r	Comments
LOS,hallway NEB	1.1	5	1.20	6.95	6.33	1.91	1.20	0.29	-13.7	
	1.2	10	6.16	5.88	5.06	1.20	6.16	1.73	-20.3	
	1.3	20	32.61	47.25	32.89	8.43	32.61	9.02	-36.6	
	1.4	30	15.50	31.15	10.16	3.43	15.50	5.69	-31.2	open area
	1.5	40	27.60	37.04	25.89	8.81	27.60	9.76	-40.5	
	1.6	50	46.42	28.17	36.70	8.10	46.42	10.73	-42.8	
	1.7	60	6.38	22.57	5.99	1.82	6.38	1.57	-41.5	
LOS,hallway Whittemore	2.1	5	2.22	6.24	7.52	2.38	2.22	0.73	-16.7	
	2.2	10	2.78	6.48	8.24	2.61	2.78	0.82	-24.4	intersection
	2.3	20	2.3	4.56	7.81	2.55	2.30	0.55	-32.86	
	2.4	30	22.02	33.87	13.17	4.60	22.02	6.30	-34.7	
	2.5	40	77.3	45.07	105.04	34.41	77.30	25.86	-36.3	
LOS, room NEB	3.1	4.2	0.74	4.85	6.20	1.88	0.74	0.20	-12.1	corner
	3.2	3.3	0.92	4.95	5.97	1.87	0.92	0.23	-12.9	center
LOS, room Whittemore	4.1	7.1	2.74	4.72	11.16	3.08	2.47	0.36	-29.7	corner
	4.2	3.8	2.4	4.98	11.11	3.17	2.40	0.47	-24.2	center
	4.3	5.2	12.88	31.10	26.36	6.86	12.88	2.95	-56.2	corner,$\perp$ to Tx
	4.4	4.2	21.3	33.94	31.5	7.4	21.3	5.43	-57.9	corner,$\perp$ to Tx
Hallway to room	5.1	2.4	0.83	5.50	2.41	0.69	0.83	0.32	-5.5	LOS
	5.2	2.4	2.46	7.41	2.61	0.84	2.46	0.94	-14.3	through wall
	5.3	2.4	0.71	5.36	1.30	0.41	0.71	0.25	-6.7	LOS
	5.4	2.4	1.16	5.19	1.85	0.61	1.16	0.36	-9.1	through glass
Room to room	6.1	3	10.67	14.72	23.07	6.62	10.67	1.30	-12.8	LOS
	6.2	3	14.82	21.78	34.30	8.57	14.82	3.37	-48.3	through wall
LOS,outdoor	8.1	2	7.63	24.59	10.24	2.66	7.63	1.75	-2.4	near NEB

reflected component from the end of corridor. These two components have opposite directions, and the maximum fading angle is along the LOS path. In the near side of the corridor (such as locations 1.1 and 1.2), the main multipath components are from LOS path and two reflected paths from the sidewalls. The maximum fading angle is in the direction perpendicular to the LOS path. The measurement results show maximum fading angles of $-80°$ and $-86°$ for locations 1.1 and 1.2, and $8.2°$ and $4.0°$ for locations 1.6 and 1.7, respectively. These results agree well with the expected values.

- *Direction of maximum multipath power*: Maximum AOA shows the direction of the strongest multipath component. Measurement results show strong dependence of the maximum AOA on the propagation environments. For all LOS locations, almost all maximum AOAs are close to the LOS path within ± 5 degrees. In location 6.3 and location 6.4, the spin measurements were taken with the track orthogonal to the transmitter direction. The maximum AOAs are at 49 and -49 degrees, which are the exact directions of the LOS paths. For NLOS locations, the maximum AOA is dependent on the specific propagation environments as discussed in Section 7.3.

- *Peak to average power ratio*: Peak to average power ratio characterizes the power of strongest multipath as compared to the average received power from all directions. This ratio gauges the increase of the received signal power by pointing the directional antenna in the maximum AOA direction.

- *Peak multipath power*: Peak multipath power is the power level of the strongest multipath component from all the pointing angles of the receiver antenna. Received signal power level depends on the transmitter power level and the receiver attenuator settings. Therefore, the power level may change from location to location. We shall be concerned only with the relative power for the same location. For hallway measurements at location 1, for example, the peak multipath power level decreases significantly with the increase of the separation at short distances. At large separation, such as at locations 1.5, 1.6 and 1.7, the peak multipath power remains almost constant. The same trends were observed for the total received power. This indicates the waveguide effects of the long hallway. Detailed analysis on the received signal level is presented in Section 7.4.5.

7.4.4 TOA Statistics

Channel measurement results are highly dependent on the propagation environments and the measurement system setup. Results from Tables 14 and 15 show a significant decrease of TOA delay statistics obtained from the track measurements compared to the spin measurements. For example, the mean excess delay from the track measurements in location 1.1 is only 1.2 ns , while it is 80.0 ns from the spin measurements. When transmitter and receiver antennas are aligned, such as track measurement at location 1.1, the main multipath component is the LOS component. Other multipath components are largely attenuated by the directional antenna, forcing the excess delay to be close to zero. However, if the antennas are not aligned and pointing into different directions, such as in spin measurements, the LOS path is attenuated and becomes comparable to the reflected multipath components, resulting in a significant increase of time delay parameters.

Therefore, for propagation research and system deployment, it is important to use channel propagation characteristics with consideration of the system setups. Table 15 provides channel parameters for systems with aligned antennas, while Table 14 presents results for systems with antennas pointing in arbitrary directions such as in a mobile environment.

Next, we summarize the measurement results from TOA measurements.

- RMS delay spread: When the receiver antenna was pointed to different directions, the delay spread was in the range of 7.5 ns to 76.5 ns for hallways, and 10.9 ns to 41.0 ns for rooms. The measured delay spreads are in agreement with the measurement results in [161], where typical measured delay spreads for indoor 60 GHz channels range from 15 ns to 70 ns . When the receiver antenna was fixed, the delay spread was significantly smaller. Typical ranges are from 4.6 ns to 47.3 ns in the hallways, and from 4.7 ns to 33.9 ns in the rooms.

- Mean excess delay: When the receiver antenna was rotating, the measured $\bar{\tau}$ was in the range of 41.2 ns to 116.6 ns for hallways, 42.6 ns to 77.8 ns for rooms, 41.6 ns to 91.8 ns for propagation from room to hallway and from room to room, and 24.4 ns to 56.3 ns for short distance outdoor measurements. In the hallway measurements, $\bar{\tau}$ increased significantly in the open area near the elevator, such as in location 1.4. Significant reduction of delay was also observed when the antennas were aligned and fixed.

- Timing jitter and standard deviation: Due to the small wavelength of 5 mm at 60 GHz, the radio channel may vary significantly within a small area (on the order of 20 wavelengths). Measurement results show high timing jitter and standard deviation for the measured excess delay and RMS delay spread values of all locations. These results present a quantitative measure of the channel variations in a small local area.

7.4.5 Received Signal Power

Due to the high diffraction and penetration losses, the LOS path and the reflected paths dominate the millimeter wave channel. The received signal power largely depends on the antenna pattern, antenna alignment, and propagation environments. The maximum multipath power from the spin measurements shows the power level of the strongest multipath in all AOA directions. The average power presented in the track measurements shows the spatially averaged power with both antennas aligned. For the majority of the locations, the maximum multipath component has a power level that is higher than the averaged power. The trends of signal level changes are the same for both the maximum multipath power and the average received power. These trends are summarized as follows:

- *Waveguide effects*: For hallway measurements, the received signal power decreased rapidly when the transmitter and receiver separation was increased from 2 m to 20 m. After 20 m, the received signal power did not decrease appreciably with the increase of the distance. This trend was observed from both location 1 and location 2 hallway measurements. For instance, the received powers at locations 1.5, 1.6, and 1.7 were almost the same, although transmitter-receiver distance changed from 40 to 50 and 60 m, respectively. This is due to the waveguide effects of the radio wave propagation along the corridor at further separations. At small distances, the reflected wave components are rejected by the directional receiver antenna, and the waveguide effect is not dominant. However, at long distances, reflected wave components are close to the LOS path and are received by the receiver antenna. The total received field is stronger than it should be from free space propagation, and the transmitted wave propagates in a guided fashion. The interplay of the antenna pattern, site geometry and reflected wave components can be explained using the power zone theory [40].

- *Antenna effects and power zone theory*: When directional antennas are used, the majority of the radiated energy is concentrated along the LOS path. Power zone plots are developed to characterize the power concentration. When transmitter-receiver separation is relatively small, no obstacles intersect the power zones. And, therefore, the received signal power is mainly from the LOS path. As a result, with an increase in distance, the received signal power decreases with a path loss exponent close to 2. However, when transmitter and receiver separation is large, the sidewalls of the hallway and the floor are close to the main power zone, and reflected power contributes to the total received power. The received signal consists of both LOS component and reflected components along the corridor (similar to a waveguide). Therefore, the total received power does not decrease appreciably for larger distances.

- *Effects of antenna alignments*: Due to the highly directional receiver antenna, the received signal power can vary significantly depending on the antenna alignment. This is clearly demonstrated in location 4.3, where the receiver antenna is not aligned to the transmitter antenna. The received signal power dropped from -29.7 dBm (location 4.1 with antenna aligned) to -56.2 dBm .

- *Penetration losses*: Measurements through glass door and interior walls in locations 5 and 6 showed power losses of 8.8 dB and 35.5 dB through two composite walls, and a loss of 2.5 dB through a glass door. These results indicate that the quantity and position of the metallic studs within the composite wall are important factors to determine the penetration loss. When the studs were not blocking the transmission path, the penetration loss was 8.8 dB , comparable to the loss through a plasterboard wall [159]. When the stud was blocking the transmission path, the penetration loss was 35.5 dB , comparable to the loss through a concrete wall [11, 92]. Rule-of-thumb penetration loss values are presented in Table 16.

- Scatter plot of path loss values: The total path loss from the transmitter to the receiver was calculated from the measurement results. The scatter plot is presented in Figure 65. As shown in Figure 65, for LOS propagation, the path loss values are close to the free space path loss values. For NLOS propagation, high penetration loss values can result in high path loss values. For example, in location 6, the path loss value is as high as 108 dB for the NLOS receiver location. This is caused by the 35.5 dB penetration loss through the composite wall.

Table 16: Measured Penetration Losses and Results from Literature.

Material	**Penetration loss**	**Ref.**
Composite wall with studs not in the path	8.8 dB	
Composite wall with studs in the path	35.5 dB	
Glass door	2.5 dB	
Concrete wall 1 week after concreting	73.6 dB	[11]
Concrete wall 2 weeks after concreting	68.4 dB	[11]
Concrete wall 5 weeks after concreting	46.5 dB	[11]
Concrete wall 14 months after concreting	28.1 dB	[11]
Plasterboard wall	5.4 to 8.1 dB	[159]
Partition of glass wool with plywood surfaces	9.2 to 10.1 dB	[159]
Partition of cloth-covered plywood	3.9 to 8.7 dB	[159]
Granite with width of 3 cm	>30 dB	[92]
Glass	1.7 to 4.5 dB	[92]
Metalized glass	> 30 dB	[92]
Wooden panels	6.2 to 8.6 dB	[92]
Brick with width of 11 cm	17 dB	[92]
Limestone with width of 3 cm	> 30 dB	[92]
Concrete	> 30 dB	[92]

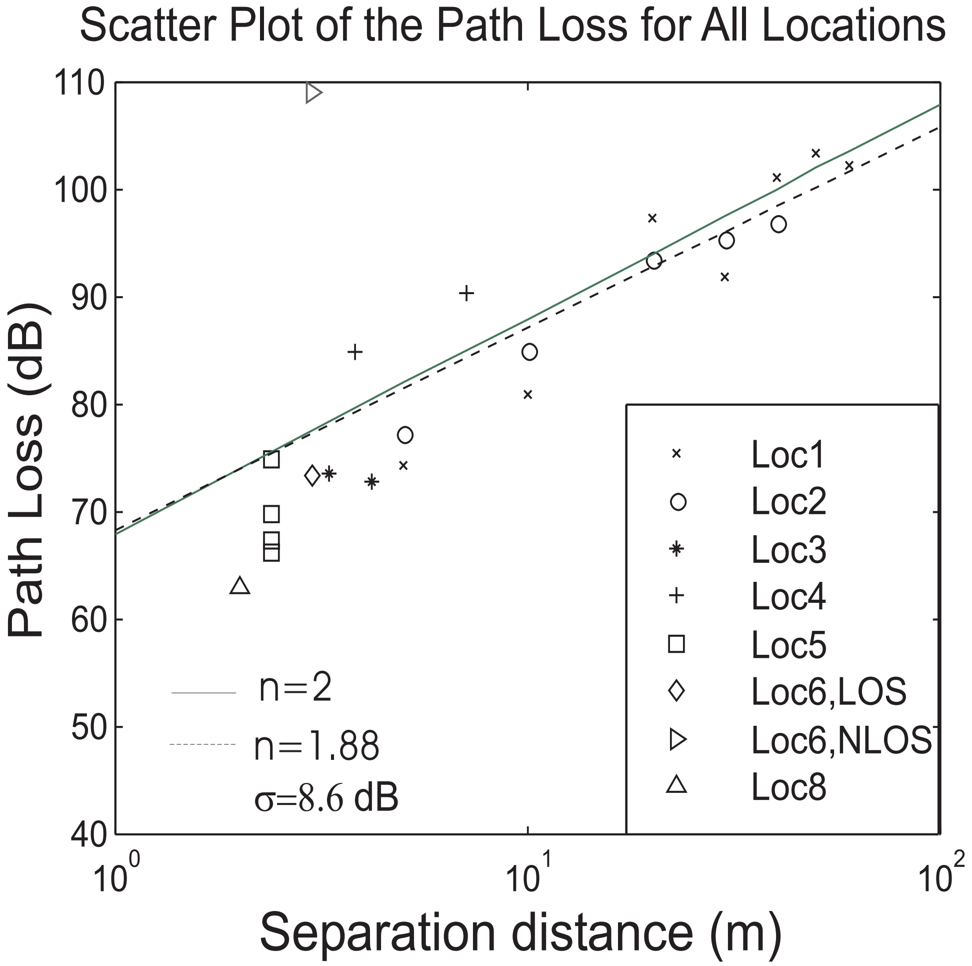

Figure 65: Scatter plot of the measured path loss values

7.5 Summary

This chapter presents an extensive measurement campaign and a detailed analysis of 60 GHz space-time channels. Multipath components were resolved in space by sweeping a directional antenna, and in time by using a spread spectrum sliding correlator system. Measurement results include PDPs, PAPs, received signal power, AOA parameters, and TOA parameters. The PAPs are analyzed in context with site-specific information. Results show strong correlation between the multipath distribution and the propagation environments. Ray tracing of first-order and second-order reflections seems to be sufficient to predict the multipath AOA structure for LOS applications. Metallic furniture and objects must be considered in the ray tracing model. Measurements through composite walls show that the wall structure can be a crucial factor in determining signal power level as well as multipath structure. Statistical parameters, such as angular spread, peak AOA, and maximum fading rate angle were measured and related to the multipath models. The measured power, AOA and TOA parameters agree well with the theoretical expectations. These measurement results not only present important empirical values for 60 GHz system design and a fundamental basis for ray tracing development and verification, but also provide a better understanding of the radio wave propagation.

Chapter 8

Summary and Future Research Directions

8.1 Summary of Results

This dissertation focuses on radio wave propagation research at millimeter-wave frequencies. Comprehensive analysis and extensive measurement campaigns were performed at 38 GHz for Local Multipoint Distribution Service (LMDS) applications, and 60 GHz for Next Generation Internet (NGI) applications. Channel models were developed based on the measurement results and are also presented.

As shown in Chapter 1, millimeter-wave bands are the best candidates for future broadband wireless systems. The most important applications are LMDS at 28 GHz and 38 GHz , and (NGI) systems at 60 GHz . However, terrestrial millimeter-wave propagation channels are still largely unknown.

In Chapter 2, fundamentals of radio wave propagation were reviewed. Important concepts, such as path loss, system coverage, multipath propagation, and space-time channel modeling were covered. Effects of receiver bandwidth and antenna beamwidth were also analyzed.

A technical review of different measurement techniques was provided in Chapter 3. First, continuous wave (CW) measurement techniques were studied. A CW measurement system was designed, and a measurement campaign was performed at 5.85 GHz to study penetration losses through buildings and trees. Secondly, two wideband measurement techniques were analyzed. Both SCS and VNA systems were implemented, and a measurement campaign was conducted to carefully compare the performance of these two systems. Thirdly, analytic estimation of the time measurement accuracy for the SCS technique was provided and verified experimentally. Finally, a SCS was built to operate at 38 GHz and 60 GHz . This system was instrumental for the millimeter-wave propagation research presented in this dissertation.

Chapter 4 presented a comprehensive overview of terrestrial millimeter-wave propagation fundamentals. Emphasis is placed on the rough surface scattering and random media scattering due to vegetation and rain. Results of a literature search on outdoor and indoor propagation measurements at millimeter-wave frequencies are presented. The literature search provided vital information for choosing the research directions of this dissertation.

Chapter 5 provided important measurement results and models for LMDS applications. One of the most important applications of the millimeter-wave spectrum is LMDS. However, little has been reported in the literature on the effects of weather on the wideband channel properties at millimeter-wave frequencies. Chapter 5 presented measurement results in the areas of channel multipath propagation, short-term signal variation, interplay of coherent power and incoherent power, and channel path loss under different weather conditions (clear sky, rain, and hailstorm). The measurement results show that millimeter-wave channels can become dispersive due to the weather effects on the building surfaces. When standing water surfaces are formed during rain, rough building surfaces can become strong reflectors and produce strong reflected multipath components. Furthermore, the measured signal variation during 2-3 minutes of constant rain rate appeared to be Rician distributed. A Rician K factor was used to describe the ratio of coherent power to incoherent power during rain. Empirical results of K factors at different rain rates were proportional to the rain rates (with a negative sign). Theoretical study revealed that the signal variations were due to the nonuniform distribution of the rain patches along the propagation path. Finally, signal attenuation during various rain storms and a hailstorm was measured. Measurement based models were developed for the signal attenuation and short-term signal variation during rain. A theoretical study of the short-term signal variation during rain was presented. The theory was developed based on the fundamental principles of wave propagation through random media of scatters. The results show that the nonuniform distribution of rain drop density along the propagation path can result in signal fluctuation. The estimated values of the K factor agrees well with the measurement results. However, the theory finds the signal statistics to be governed by a lognormal distribution. Further measurements are required to verify the theoretical hypothesis.

In Chapter 6, a novel design technique was developed to predict worst-case multipath power, AOA and TOA based on antenna patterns and site-specific information. This approach implements a single bounced reflection model. Relative power zone contour plots and excess delay zone contour plots were developed to determine multipath channel structure. These contour plots can be easily implemented for millimeter-wave system design and installation.

Finally, in Chapter 7, 60 GHz short-range channels were investigated. Future-generation wireless systems explore dimensions of space, time and frequency. However, little literature is available to characterize the space-time channels at 60 GHz . The focus of our propagation research was on the space-time channel structure at 60 GHz . The multipath components were resolved in time by the sliding correlator technique, and in angle by sweeping a directional antenna in azimuth. The measured channel multipath structures were carefully analyzed at each location in order to determine the origins of the multipath components from the propagation environments. Results show strong correlation between the channel structures and the propagation environments. Measurements in LOS environments clearly demonstrated that image-based ray tracing techniques can be used to predict detailed channel structure. Measurements in NLOS environments revealed important effects of the metallic studs of composite walls on the received signal power and multipath structure. For all the measurement results, time dispersion parameters and angle dispersion parameters were calculated from spatially averaged PDPs and PAPs. The measurements and analysis provide not only important results for 60 GHz space-time channel characterization, but also a basis for ray-tracing development and validation.

8.2 Related Publications by the Author

Several publications related to the millimeter-wave propagation research have been written by the author. These publications include three journal papers, four conference papers, two technical reports and a contribution to IEEE802.16 standard group. Two journal papers on the LMDS research were published in *IEEE Journal on Selected Area of Communications* and *IEEE Communications Letters* [40, 162]. One journal paper on the 60 GHz channel characterization is in the process of preparation. Four conference papers were written: 1) measurement results at 38 GHz were presented in IEEE VTC'99 [39]; 2) rain scattering models were presented in AP2000 [163]; 3) a coauthored paper with James Schaffner *et al* on LMDS system design issues was presented in $3rd$ International Wireless Communications Conference [26]; 4) a paper on the 60 GHz measurement results was submitted to IEEE VTC'2000 [164]. A technical report was written to carefully document the 38 GHz measurement campaign [140]. Finally, a contribution to the IEEE 802.16 standard group was submitted based on the LMDS research.

Additional papers were published by the author in the areas of measurement system design and narrowband building penetration measurements at 5.8 GHz . A paper on the measurement campaign to compare different measurement techniques was published in *Advancing Microelectronics* [61]. Several papers on the building penetration measurements at 5.85 GHz , which were coauthored with G. Durgin and T. S. Rappaport, were published in [2, 3, 57, 58, 59].

8.3 Future Research Directions

There are several areas of this dissertation that can be extended through future research. These research directions are outlined below.

- An interesting research area is to extend the measurement and models for different polarizations. This dissertation presented measurement results and models for LMDS applications. The presented results are for systems with vertical polarized antennas. Effects of vegetation on the cross polarization was studied in [98], however, there is little literature on the weather effects on the signal depolarization through LMDS links. The research on polarization will provide crucial information for systems with polarization diversity.

- It is useful to obtain realistic reflection coefficients of different surfaces. The delay zone and power zone models were developed for the worst-case estimation of the multipath delay and power. With the automated measurement system, it is possible to perform a measurement campaign to study the dependence of reflection coefficient on the surface roughness, incident angle, polarization, surface material, and surface condition (such as dry or wet). The results could also serve as a verification of the hypothesis that the surface becomes more reflective when it is wet.

- There are many possibilities for further investigation of the signal variation during rain both theoretically and experimentally. The theoretical prediction of the signal short-term variation matches well with the measurement results. The theory predicts that the short-term signal variation is due to the nonuniform distribution of the rain drop densities along the propagation path. One possible experimental verification of the theory is to perform a rain attenuation measurement campaign with several rain gauges along the propagation path. The average rain attenuation can be related to the average rain rate, and the signal variation can be studied considering different rain rates along the path.

- There is great potential to develop a ray-tracing tool based on the propagation study at 60 GHz . The measurements provided detailed information on the signal power and multipath structure in various controlled environments. The initial analysis shows excellent agreements of the measurement results and the ray tracing predictions. The measurement results could be used for ray-tracing validation and development. More measurements can be taken to support such a tool.

- In the area of channel measurement system design, there are several research directions that could be taken. These directions include coherent detection of the received signal to acquire phase information of the multipath components, miniaturization of the channel measurement system, and development of a measurement system with high temporal and spatial resolutions.

8.4 Conclusions

This research has studied radio wave propagation at millimeter-wave frequencies. Measurement systems were designed, and two extensive measurement campaigns were performed for LMDS applications at 38 GHz and NGI applications at 60 GHz .

For outdoor LOS applications, the research of this dissertation shows that weather effects have a significant impact on millimeter-wave propagation. The results presented in this research provide important guidelines for LMDS system development. Measurements and models were presented to estimate received signal level, signal variation, and channel time dispersion under different weather conditions. A simple model was developed to predict the multipath power and time delay based on the antenna patterns and the site information.

For indoor applications, the propagation environments directly affect multipath channel structure. The research results show that for LOS environments, the multipath structure can be predicted using ray-tracing techniques. However, metallic structures and furniture must be considered in the prediction techniques. For NLOS propagation through walls, metallic studs within the wall may play an important role in determining the penetration loss and multipath characteristics. These metallic structure may result in high penetration loss and high signal variability for NLOS applications. As a result, millimeter-wave systems are mainly proposed for LOS applications.

The enormous amount of free spectrum at millimeter-wave frequencies provides tremendous potential for high data rate multimedia applications. This dissertation has provided some fundamental results for the future millimeter-wave applications.

Appendix A

Measurement Results from VNA and SCS Comparison

A.1 Measurement Site Information

The measurement locations on the lawn are presented in Figure 66. The lawn was located on top of a hill near Malibu beach. To one side of the lawn is the two-story office building, and to the other side of the lawn the ground sloped down towards a road about 100 m away. There were several trees at the edge of the lawn before the downward slope, and there was one tree approximately 5 m high in the middle of the lawn. The transmitter was located in the left-bottom corner of the lawn, and three receiver sites were chosen for the measurements. The first one, Rx1, was located one meter from the transmitter, and this site was used for a one meter free space calibration measurement. The other two locations were chosen near and far from the office building. The receivers at all locations had line-of-site (LOS) propagation paths to the transmitter. At 5.85 GHz the wavelength is only about 5 cm, so the multipath delay profile can change rapidly in a small local area. At each measurement site, five measurements are taken in the local area with a separation of one full wave length.

A conference room and a hallway were chosen as the indoor measurement sites. The measurement locations are presented in Figures 67 and 68. The conference room had a long wooden table in

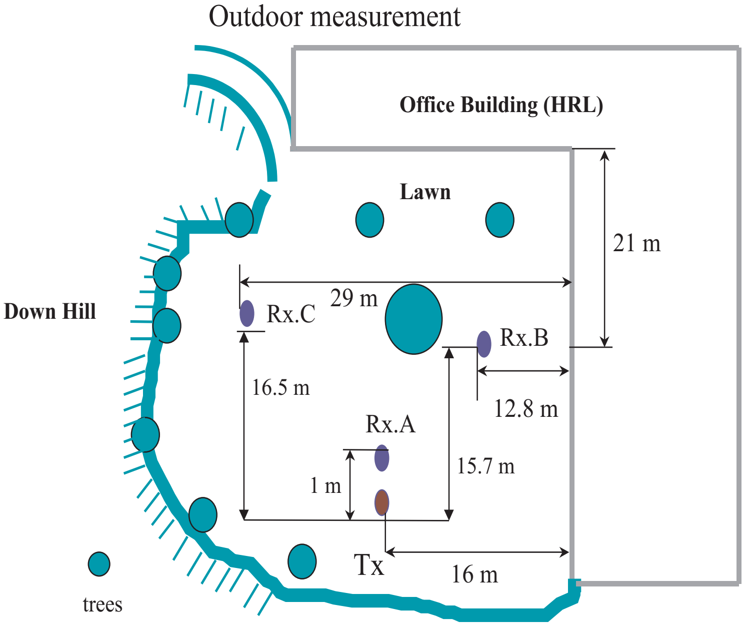

Figure 66: Measurement locations in the lawn.

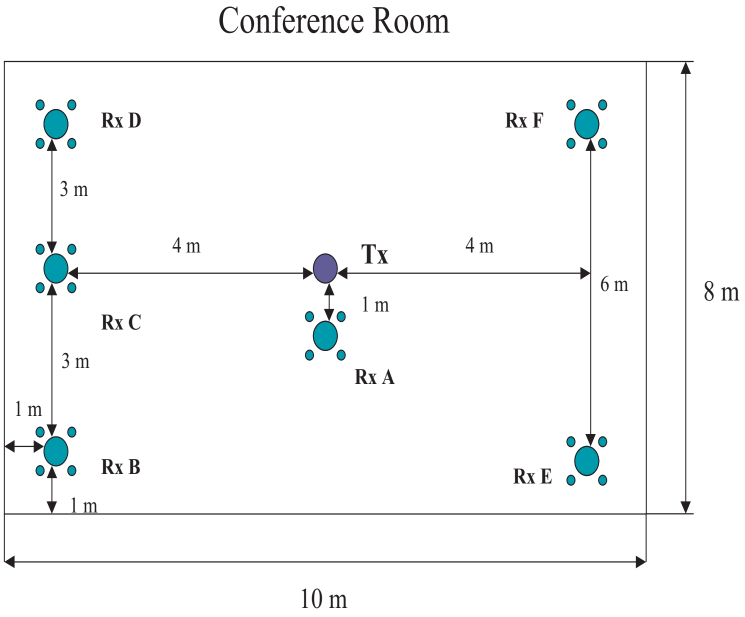

Figure 67: Measurement locations in the conference room.

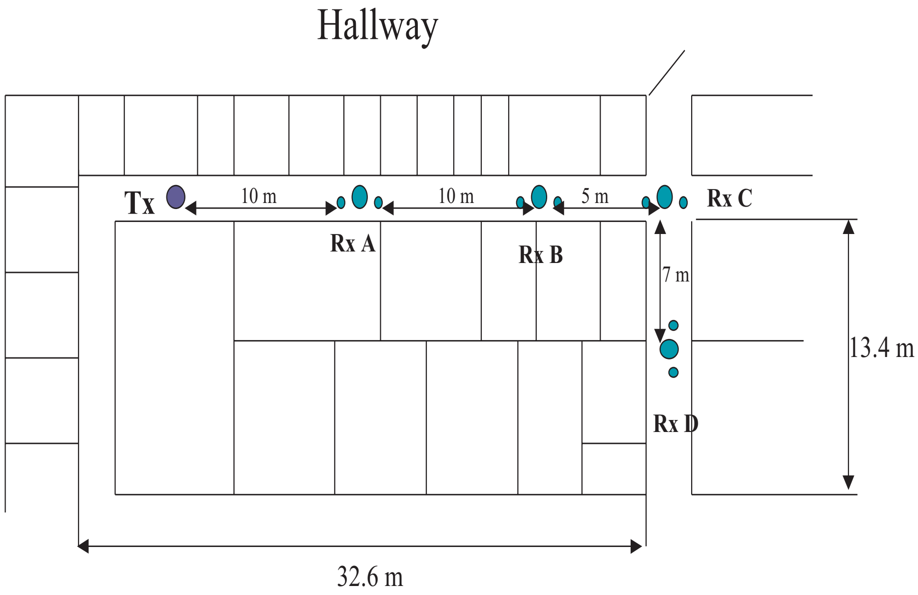

Figure 68: Measurement locations in the hallway.

the middle with chairs surrounding it. The transmitter was located in the center of the room, and several receiver locations were chosen on all sides of the room. In the hallway, the transmitter was located at one end, and receiver locations were separated down the hallway, with one measurement taken around a corner. This was the only non-LOS measurement.

A.2 Measurement Results

Measurement results for the lawn, conference room, and the hallway are summarized in Tables 17, 18 and 19.

Both measurement methods provided results that showed the influence of the surrounding scatters on the PDP. For example, for the outdoor measurement data, receiver position B had more multipath components than receiver position C, and subsequently higher values of τ and σ. This is predictable, since at location B the receiver was placed near the office building, so there were more reflections from the office building. At location C there were only few scatters near the receiver (see Figure 66).

Table 17: Results for the Lawn.

Location		# of MP		$\tau(ns)$		$\sigma_\tau(ns)$		P_{rec}(dBm)	
Garden	# pos.	SCS	VNAS	SCS	VNAS	SCS	VNAS	SCS	VNAS
Rx B	1	15	18	27.4	29.4	53.4	54.4	-77.6	-77.7
	2	15	16	27.1	26.6	53.9	51.5	-75.8	-76.8
	3	18	18	28.7	35.2	56.0	59.6	-76.7	-78.7
	4	15	20	39.5	48.9	67.1	71.8	-77.2	-78.7
	5	13	19	21.2	29.3	49.4	57.5	-74.7	-77.2
	Average	15.2	18.2	28.8	33.9	56.0	59.0	-76.4	-77.8
Rx C	1	8	11	7.96	9.98	31.7	35.6	-75.1	-76.2
	2	12	12	6.00	8.33	27.2	30.6	-74.3	-76.0
	3	12	12	5.90	7.48	26.3	29.9	-75.2	-76.9
	4	12	11	14.4	12.5	44.2	39.4	-74.8	-76.2
	5	13	12	9.66	10.3	34.5	35.3	-75.4	-76.4
	Average	11.4	11.6	8.8	9.7	32.8	34.1	-75.0	-76.3

Location C in the hallway measurement (see Figure 68) was the cross section between two hallways, and had a higher number of the multipath components than all the other hallway locations. At location D of Figure 68, which was around the corner from the transmitter and thus no LOS between the transmitter and receiver, the received power decreased by about 20 dB compared with location C, which had almost the same transmitter-receiver separation but with LOS. Also, at this location, the mean excess delay and delay spread were much higher than in the other locations.

In the conference room as many as 21 multipath components were detected in the PDP and the value of τ was as high as 100 ns. This trend was observed for all the measurement locations in the room. This was caused by the good reflection off the metallic walls, which were made from 16 gauge steel.

Table 18: Results for Conference Room.

Location		# of MP		$\tau(ns)$		$\sigma_\tau(ns)$		P_{rec}(dBm)	
Conf. Rm	# pos.	SCS	VNAS	SCS	VNAS	SCS	VNAS	SCS	VNAS
Rx A	1	14	11	14.8	15.0	39.4	35.7	-43.6	-45.6
	2	12	11	12.8	13.1	42.6	37.3	-44.6	-46.1
	3	17	15	15.3	17.7	41.1	38.8	-44.6	-46.0
	4	10	11	12.3	10.2	32.9	29.0	-44.5	-45.7
	5	18	13	11.6	11.3	43.6	33.9	-44.1	-45.6
	Aver.	14.2	12.2	13.4	13.5	39.9	34.9	-44.3	-45.8
Rx B	1	21	25	100	103	75.9	77.7	-51.9	-53.8
	2	25	24	93.6	80.5	92.3	79.6	-51.3	-53.4
	3	23	24	82.1	73.1	91.3	78.2	-49.7	-51.2
	4	20	23	67	77.3	73.5	69.6	-50.2	-51.5
	5	24	24	90.9	90.4	95.6	75.2	-50.6	-52.5
	Aver.	22.6	24	86.7	84.9	85.7	76.1	-50.7	-52.5
Rx C	1	25	22	68.5	68.6	83.3	74.1	-50.8	-52.4
	2	27	24	89.0	77.9	89.7	70.2	-51.3	-52.3
	3	26	24	86.4	85.8	75.1	71.3	-49.5	-51.6
	4	25	24	83.7	69.9	90.6	78.6	-52.3	-54.0
	5	26	27	73.7	85.2	81.6	86.2	-50.5	-52.7
	Aver.	25.8	24.2	80.3	77.5	84.1	76.1	-50.9	-52.6

Table 18: Results for Conference Room (cont.).

Location		# of MP		$\tau(ns)$		$\sigma_\tau(ns)$		P_{rec}(dBm)	
Conf. Rm	# pos.	SCS	VNAS	SCS	VNAS	SCS	VNAS	SCS	VNAS
Rx D	1	34	37	85.3	94.3	93.0	92.9	-51.8	-53.7
	2	25	26	78.2	72.5	72.2	65.1	-50.7	-51.6
	3	31	25	107	89.1	89.1	63.5	-46.7	-53.1
	4	28	34	60.2	59.7	89.3	74.7	-52.0	-52.4
	5	28	29	82.1	68.1	96.9	81.7	-51.6	-52.4
	Aver.	29.2	30.2	82.6	76.7	88.1	75.6	-50.6	-52.6
Rx E	1	27	35	110	100	100	99.2	-52.3	-52.7
	2	37	36	93.4	80.0	101	93.6	-50.2	-51.7
	3	21	31	66.8	70.9	79.7	87.3	-56.0	-51.7
	4	27	27	78.5	77.5	88.4	83.1	-50.4	-52.5
	5	26	27	76.6	73.0	96.9	87.2	-50.8	-52.2
	Aver.	27.6	31.2	85.1	80.3	93.2	90.1	-51.9	-52.2
Rx F	1	27	19	108	68.4	108	79.4	-48.5	-52.0
	2	20	13	61.9	47.3	69.3	57.5	-48.1	-52.3
	3	19	35	29.2	47.0	61.5	80.3	-54.9	-50.6
	4	24	29	61.8	55.4	90.0	84.2	-54.8	-50.4
	5	18	28	25.9	43.4	60.7	78.8	-54.1	-50.9
	Aver.	21.6	24.8	57.4	52.3	77.9	76.0	-52.1	-51.2

Table 19: Results for Hallway.

Location		# of MP		$\tau(ns)$		$\sigma_\tau(ns)$		P_{rec}(dBm)	
Hallway	# pos.	SCS	VNAS	SCS	VNAS	SCS	VNAS	SCS	VNAS
Rx A	1	8	12	4.16	8.76	13.6	28.7	-61.7	-63.8
	2	12	14	40.3	23.7	43.5	27.6	-66.4	-65.1
	3	11	13	24.3	10.9	26.0	21.5	-64.1	-64.6
	4	10	15	3.18	5.07	11.5	18.4	-58.0	-59.8
	Aver.	10.3	13.5	18.0	12.1	23.65	24.0	-62.6	-63.3
Rx B	1	9	8	3.23	2.88	12.6	12.5	-64.8	-62.6
	2	6	10	8.58	12.5	23.6	26.8	-68.6	-67.2
	3	5	11	1.63	2.29	12.2	12.2	-62.9	-61.5
	4	8	7	3.08	3.25	12.9	13.6	-63.5	-62.7
	5	10	12	4.07	3.89	16.6	18.5	-64.7	-62.9
	Aver.	7.6	9.6	4.1	5.0	15.6	16.7	-64.9	-63.4
Rx C	1	9	17	8.4	12.1	27.6	34.9	-68.4	-69.2
	2	12	17	19.4	35.6	43.7	52.5	-71.9	-74.1
	3	10	15	9	12.5	29	31.9	-68.2	-68.5
	4	8	17	3.34	4.21	16.6	20.3	-61.9	-62.6
	5	15	17	15.3	13.0	32.7	29.9	-70.7	-69.3
	Aver.	10.8	16.6	11.1	15.5	29.9	33.9	-68.2	-68.7
Rx D	1	8	9	38.4	36.7	40.6	33.8	-91.0	-91.2
	2	11	13	38.3	41.2	36.7	38.6	-87.6	-89.7
	3	13	16	45.1	42.1	45.7	44	-90.4	-91.9
	4	10	14	36.4	38	40.7	39.7	-88.3	-89.3
	Aver.	10.5	13	39.6	39.5	40.9	39.0	-89.3	-90.5

Appendix B

Analysis on Time Measurement Accuracy for the SCS

In order to improve the accuracy of the measurement and enable the transmitter and the receiver of the SCS to operate separately without a synchronization cable, rubidium frequency standard is used in the system. The accuracy of the rubidium oscillators will directly effect on the time measurement accuracy of the system. This appendix provides an error analysis resulting from the frequency offset of the rubidium oscillators. The analysis results were verified in the measurement campaign presented in Section 3.5. Based on the analysis, improvement techniques were suggested and implemented in the measurement campaign [61].

B.1 Introduction

In the SCS developed at MPRG, three PN sequences are generated: transmitter PN sequence, receiver PN sequence, and a duplicated transmitter PN sequence at the receiver for synchronization purpose. The correlation of the receiver PN and the duplicated transmitter PN generator provides a signal pulse with no propagation delay, which serves as a reference for absolute propagation delay measurements. The duplicated transmitter PN enables the transmitter and receiver to operate separately without a synchronization cable.

Rubidium oscillators (RO) running at 10 MHz are used to provide frequency references for the frequency generators at both transmitter and receiver. Since both ROs at the transmitter and receiver are free-running, they will independently drift, which will result in a small frequency offset, Δf. This offset will cause the PN sequences to drift and influence the measurement result.

The goal of the analysis is to quantitatively evaluate the effects of a given frequency offset (Δf) of the RO on the time measurements including absolute propagation time and excess delay. As shown in this analysis, a small frequency offset of the RO may result in a large time measurement error in a long measurement campaign.

We denote the transmitter PN frequency as f_T, the receiver PN frequency as f_R, and duplicated transmitter PN frequency as f_T^D. The calculation is carried out for a typical setting of the frequencies:

$$f_T = f_T^D = 100 \text{ MHz} \tag{B.165}$$

$$f_R = 99.99 \text{ MHz} \tag{B.166}$$

The general formulas, derived below, are valid for any value of Δf, or any PN frequency setting.

The reference output of an ideal RO is 10 MHz. Suppose ROs have offsets of Δf_T^{RO} and Δf_R^{RO} for transmitter and receiver, respectively. Then, the actual clock frequencies are

$$f_T^{RO} = 10 \text{ MHz} \pm \Delta f_T^{RO} \tag{B.167}$$

$$f_R^{RO} = 10 \text{ MHz} \pm \Delta f_R^{RO} \tag{B.168}$$

The PN sequences based on these references are then biased in frequencies.

$$f_T = (10 \text{ MHz} \pm \Delta f_T^{RO}) * 10 = 100 \text{ MHz} \pm 10\Delta f_T^{RO} \tag{B.169}$$

$$f_T^D = (10 \text{ MHz} \pm \Delta f_R^{RO}) * 10 = 100 \text{ MHz} \pm 10\Delta f_R^{RO} \tag{B.170}$$

$$f_R = (10 \text{ MHz} \pm \Delta f_R^{RO}) * 9.999 = 99.99 \text{ MHz} \pm 9.999\Delta f_R^{RO} \tag{B.171}$$

B.2 Influence on the Synchronization Pulses

Synchronization pulse is generated by mixing the duplicated transmitter PN sequence and the receiver sliding PN sequence. The synchronization pulse occurs when these two PN sequences align.

The duration between two synchronization pulses is the time duration between two successive alignments of the receiver and the duplicated transmitter PN sequences. Therefore, it is independent on the transmitter PN and the transmitter RO. The synchronization time is evaluated in [66] and [67] for the ideal RO frequencies. In this work, the system parameters are evaluated taken into account the frequency offset.

$$T_{sync} = \gamma_R N T_T^D \tag{B.172}$$

where N is PN sequence length, T_T^D is the chip duration of the duplicated transmitter PN sequence, and γ_R is sliding factor according to the receiver PN sequences which is defined as

$$\gamma_R = \frac{f_T^D}{f_T^D - f_R} \tag{B.173}$$

Substituting (B.173) into (B.172), we will have

$$T_{sync} = \frac{f_T^D}{f_T^D - f_R}\, N T_T^D = \frac{N}{f_T^D - f_R} = \frac{N}{0.01\ \text{MHz} \pm 0.0001 \Delta f_R^{RO}} \approx \frac{N}{0.01\ \text{MHz}} \tag{B.174}$$

The value of $0.001 \Delta f_R^{RO}$ is on the order of 10^{-7} Hz [165], which is much less than 0.01 MHz, so the interval between the synchronization pulses is dependent only on the PN length. For example, when the PN sequence length is N=2047 and the chip rates are 100 MHz and 99.99 MHz, the time duration between two synchronization pulses will be $T_{sync} = 0.2047$ sec.

B.3 Influence on Excess Delay Measurements

The excess delay is the arrival time difference between the i_{th} multipath component, t_i, and the first arrived multipath, t_1. We denote the recorded time difference (scope time) between these multipaths as $\tau_{observe} = t_i - t_1$, then the actual excess delay time, τ_{actual}, is given by

$$\tau_{actual} = \frac{\tau_{observe}}{\gamma_T} \tag{B.175}$$

where sliding factor,γ_T, is defined as

$$\gamma_T = \frac{f_T}{f_T - f_R} \tag{B.176}$$

. When the ROs do not have frequency offsets, γ_T is 10,000 for the given frequencies f_t and f_r in (B.165) and (B.166).

When the ROs have frequency offsets, the frequency values are given by (B.169) and (B.171). For these frequency values , the value of γ_T is

$$\gamma_T = \frac{100 \text{ MHz} \pm 10\Delta f_T^{RO}}{0.01 \text{ MHz} \pm 10\Delta f_T^{RO} \mp 9.999\Delta f_R^{RO}} \approx 10000 \tag{B.177}$$

The values of $10\Delta f_R^{RO}$ and $9.999\Delta f_R^{RO}$ are in the order of $2 * 10^{-3}$ Hz which is much less than 0.01 MHz [165]. The influence of the frequency offsets is negligible.

Notice that in this work we introduced the new definitions of sliding factors γ_R and γ_T, taking into account the different frequencies between f_T and f_T^D due the RO frequency offset. For cases where frequency offsets Δf_T^{RO} and Δf_R^{RO} are 0, the new defined sliding factors (γ_T and γ_R) will degenerate to the sliding factor (γ) defined in [14, 66].

B.4 Influence on the Absolute Propagation Time Measurements

Let's suppose we start the three PN sequences at the same time. The synchronization pulse is generated from receiver PN and duplicated transmitter PN. The actual alignment time depends on the transmitter PN and receiver PN. Therefore, if there is a difference between the transmitter PN and its duplicate, the synchronization pulse will occur not at exactly the same time as the transmitter PN and the receiver PN align. As depicted in Figure 69, this error accumulates with each successive synchronization pulse and cause recorded PDPs drifting from the synchronization pulse with time.

As calculated in Section B.2, the synchronization pulse, T_{sync}, occurs every 0.2047 seconds. The actual alignment occurs every

$$T_{align} = \gamma_T \; N \; T_T = \frac{f_T \; N \; T^T}{f_T - f_R} = \frac{2047}{0.01 \text{ MHz} \pm 10\Delta f_T^{RO} \mp 9.999\Delta f_R^{RO}} = T_{sync} + \Delta T \tag{B.178}$$

So after every acquisition, i.e. 0.2047 second, the first multipath will shift by ΔT from the synchronization pulse providing the channel is stationary. This error accumulates by $N\Delta T$ over N code sequences. The following calculation estimates this error for the practical frequency offset values.

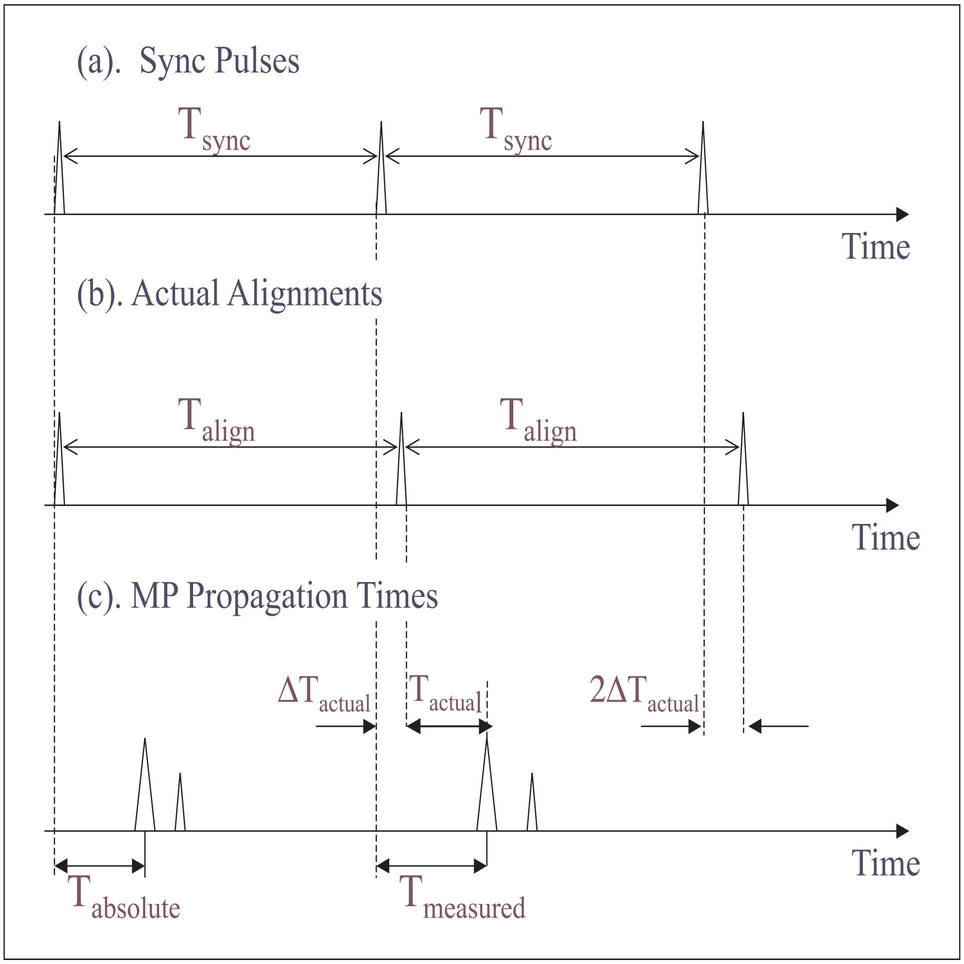

Figure 69: Influence of the frequency offset on (a) time between sync pulses, (b) time between actual alignments of PNs, and (c) absolute propagation time.

From the Electrical Specifications of [165], the Daily Aging Rate (the error after first 24 hours on) is $2 * 10^{-11} * f$. As we have the output frequency of RO at 10 MHz, the frequency offset will be $\Delta f = 2 * 10^{-11} * 10 * 10^{6} = 2 * 10^{-4}$ Hz. For these values,

$$T_{align} = \frac{2047}{0.01 \text{ MHz} \pm 10 * 2 * 10^{-4} \mp 9.999 * 2 * 10^{-4}}$$

$$Max\{T_{align}\} = \frac{2047}{0.01 \text{ MHz} - 10 * 2 * 10^{-4} - 9.999 * 2 * 10^{-4}} = 0.204700081 \text{ s} \tag{B.179}$$

$$Min\{T_{align}\} = \frac{2047}{0.01 \text{ MHz} + 10 * 2 * 10^{-4} + 9.999 * 2 * 10^{-4}} = 0.204699918 \text{ s} \tag{B.180}$$

$$Max\{\Delta T_{observe}\} = T_{align} - T_{sync} = \pm 82 \text{ ns} \tag{B.181}$$

$\Delta T_{observe}$ is the observed time shift of the measured multipath at the oscilloscope assuming the display resolution of the oscilloscope can discern less than 82 ns.

In order to evaluate the time shift of the multipath in the real propagation time after every synchronization cycle (0.2047 second),we will need to divide this time by γ, i.e.

$$\Delta T_{actual} = \pm\frac{82 \text{ ns}}{\gamma} = \pm\frac{82 \text{ ns}}{10000} = \pm 8.2 \text{ ps/cycle} \tag{B.182}$$

This equation provides the maximum error in the absolute propagation time measurement of 8.2 ps per every 0.2047 seconds. This gives a maximum shifting rate of 40.06 ps/s , or 2.4 ns/min , or **144.2 ns/hour**.

Notice that after several hours' operation, the error becomes as big as hundreds of ns. This causes the display to slowly slide across the oscilloscope screen. The observed drift of PDPs on the oscilloscope also depends on the time resolution. For example, if the time scale of the oscilloscope is 1 ms per division. For Tektronix 2432A, there are 50 sample bins per division, so the time resolution is $20\mu s/bin$ of scope time or 2 ns/bin of real time. This means that a real time shift of 2 ns will result in a bin shift on the oscilloscope. Based on the above 40.06 ps/s shifting rate, we will observe one bin shift on the oscilloscope only every 49.9 s and we will observe one division shift every 41.6 min.

In order to achieve the required accuracy, we need to connect the transmitter and receiver with a synchronization cable and get their PN sequence generators synchronized again, then separate them for long distance operation. Or we can compensate for the error by tracking the linear accumulation of ΔT over time. In fact, practical use of the system shows the shifting of the multipath is well estimated by this calculation. A summary of the time measurement accuracy analysis results is given in Table 20. This analysis was verified in the measurement campaign presented in Section 3.5. As shown in Figure 18, the time shift of the PDPs are indeed linearly dependent on the measurement time.

Table 20: Time Measurement Error due to Specified RO Frequency Offsets and PN Frequency Settings.

	1 min	1 hr	5 hr	1 day
Sync Pulse Repetition	0	0	0	0
Excess Delay Time	0	0	0	0
Absolute Prop. Time	2.4 ns	144.2 ns	721 ns	3.461 μs
Drifting on Scope	1 bin	1 div	7.2 div	34.6 div

Appendix C

Canonical Antenna Patterns for Relative Power Zone Derivation

The power and delay zone approach is demonstrated for following canonical antenna system: the uniformly illuminated rectangular aperture antenna as the transmitting antenna and the uniformly illuminated circular aperture antenna as the receiving antenna. These antennas were selected to represent antenna systems proposed for emerging millimeter-wave point-to-multipoint links. The transmitting (hub) antenna has half power beamwidths of 45° and 6.5° in azimuth and elevation, respectively. The receiver (subscriber) antenna has half power beamwidths of 1.5° in both azimuth and elevation.

The normalized far-field radiation power patterns, $G_t(\phi_t, \theta_t)$ and $G_r(\phi_r, \theta_r)$, for these antennas are given in [95] as follows

$$G_t(\phi_t, \theta_t) = \left| \frac{sin[\pi(a/\lambda)sin(\phi)]sin[\pi(b/\lambda)sin(\theta)]}{\pi^2(ab/\lambda^2)sin(\phi)sin(\theta)} \right|^2 \tag{C.183}$$

where λ is the wavelength, and a and b are dimensions of the rectangular aperture.

$$G_r(\gamma_r) = |\pi r^2 2J_1(\xi)/\xi|^2 \tag{C.184}$$

where $\xi = 2\pi(r_0/\lambda)sin(\gamma_r)$, J_1 is the first-order Bessel function, and γ_r is the angle in spherical coordinate system as shown in Figure 55. The resulting antenna patterns are presented in Figure 70.

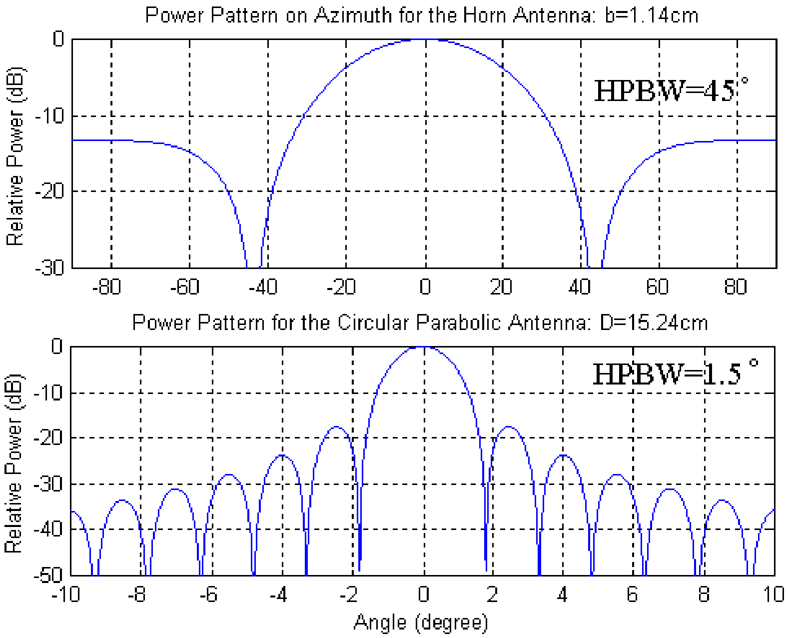

Figure 70: Theoretical power patterns for horn and dish antennas: azimuth.

Appendix D

Site Photos and Maps for 60 GHz Measurement Campaign

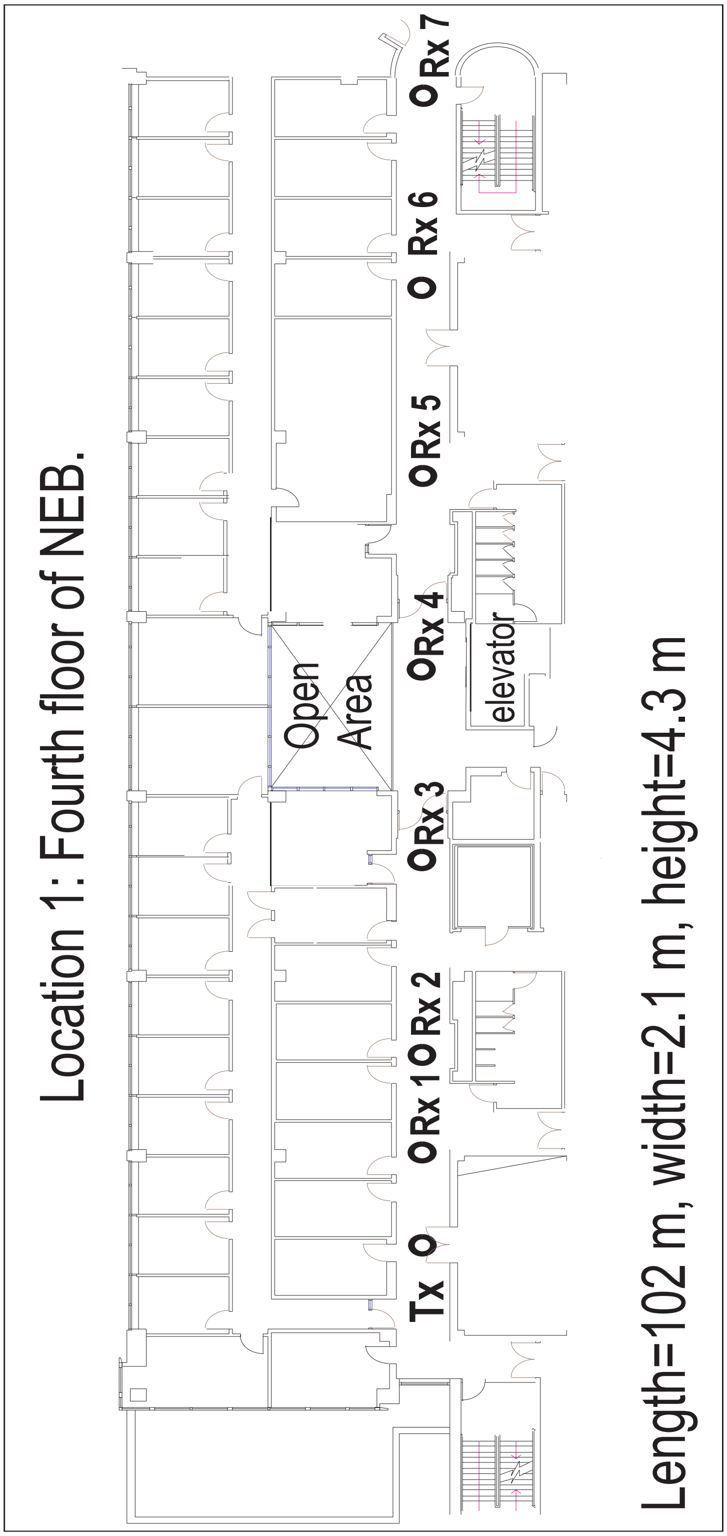

Figure 71: Location 1 – hallway on the third floor of NEB building.

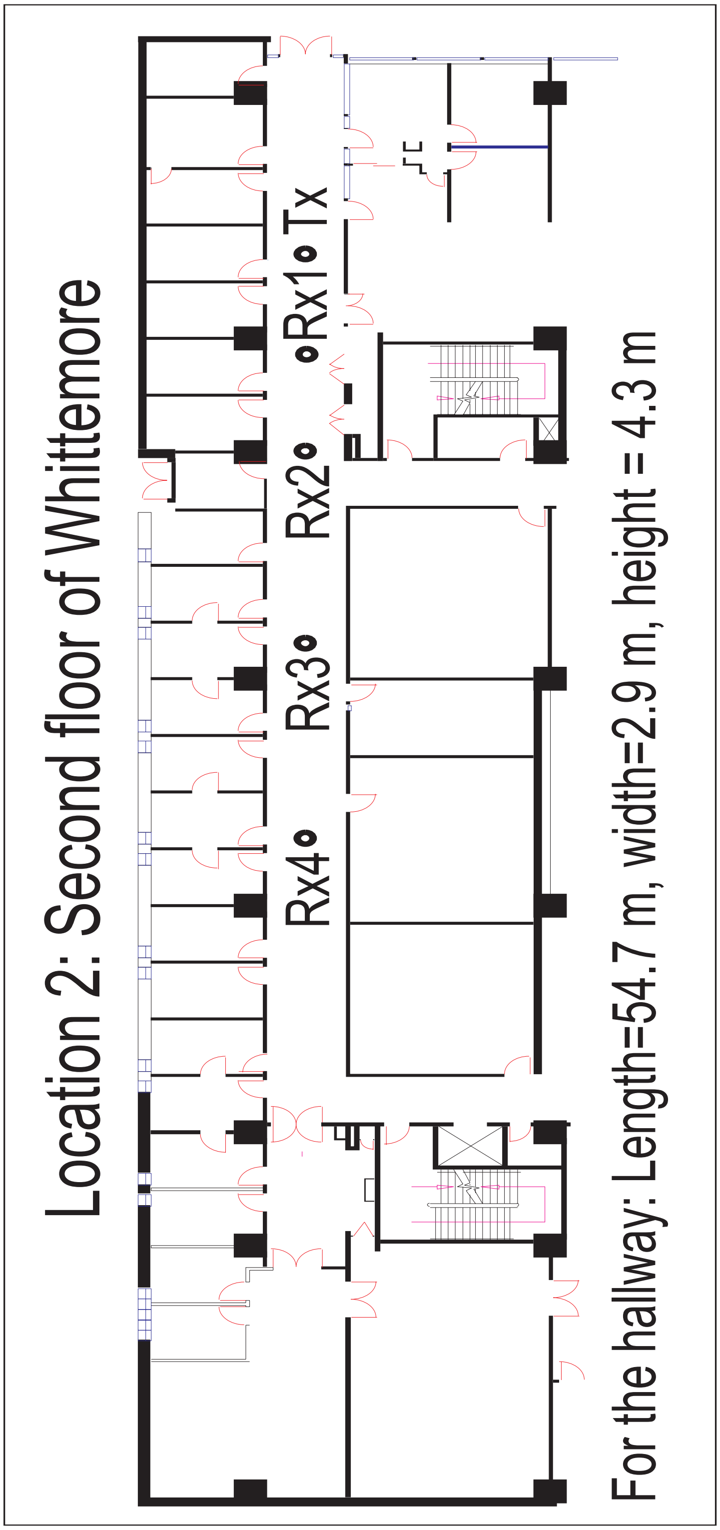

Figure 72: Location 2 – hallway on the second floor of Whittemore building.

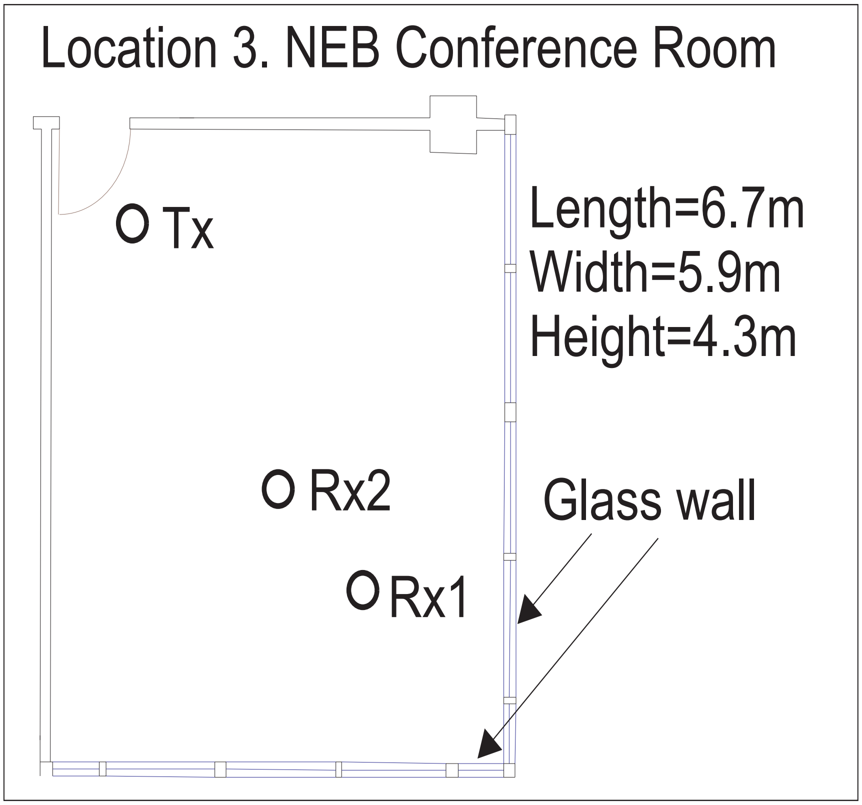

Figure 73: Location 3 – conference room in NEB.

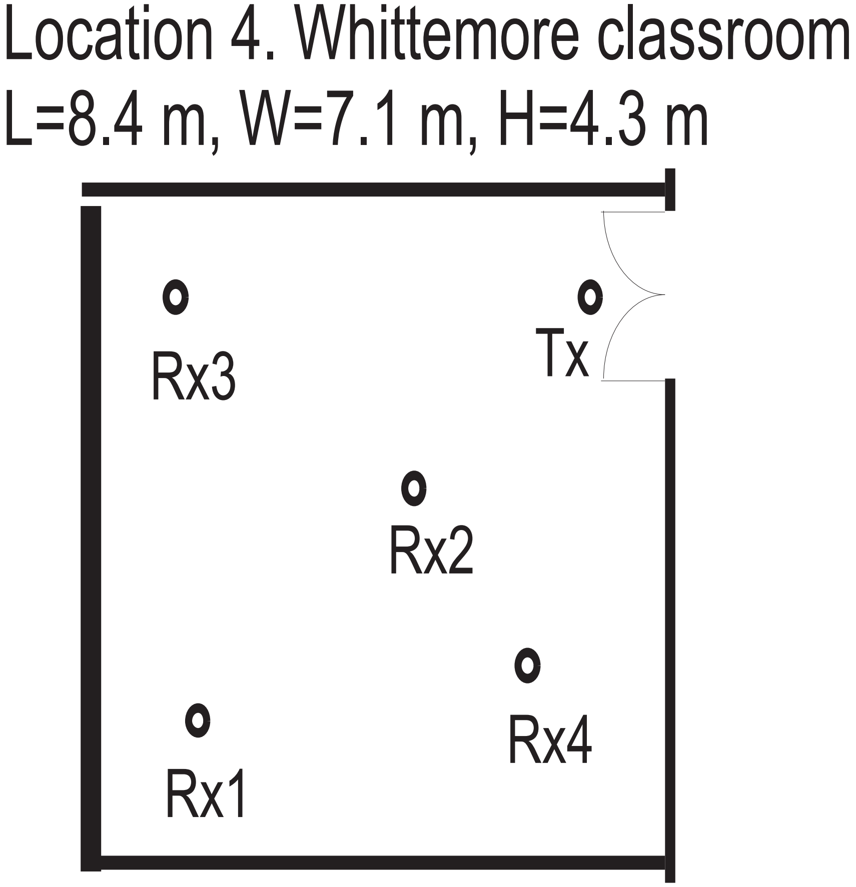

Figure 74: Location 4 – classroom in Whittemore.

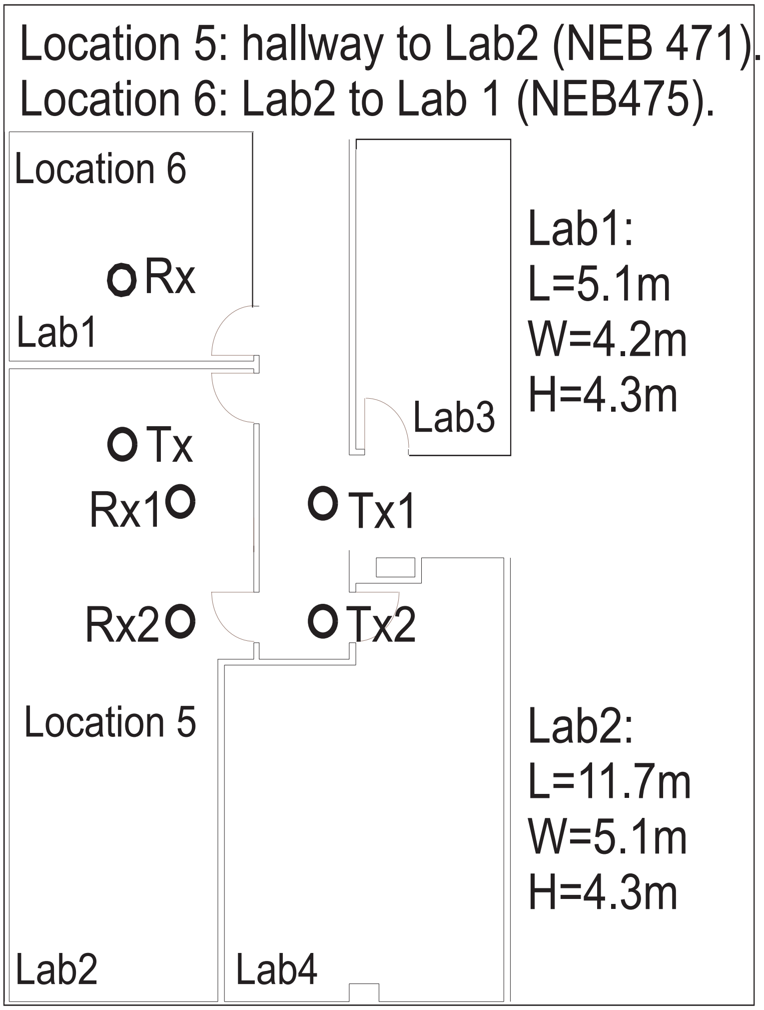

Figure 75: Location 5 – from hallway into Lab 2 in NEB, and location 6 – from Lab 2 to Lab 3 in NEB.

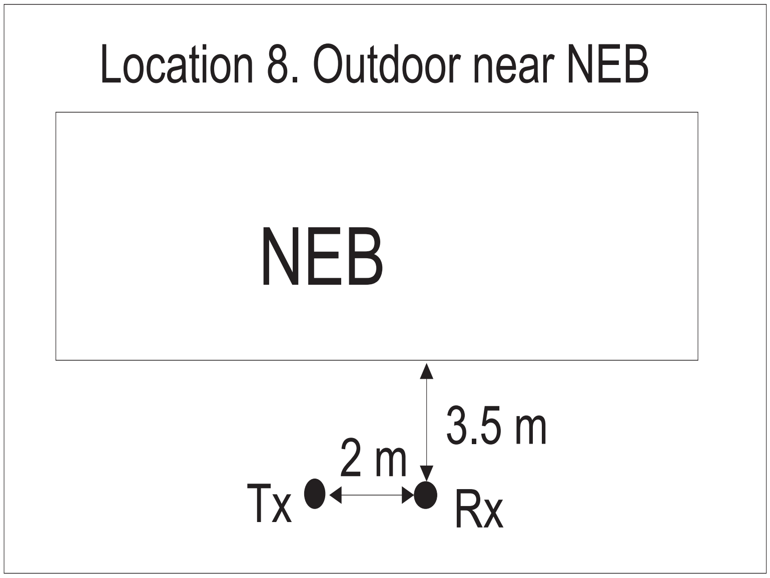

Figure 76: Location 8 – outdoor near NEB building.

Figure 77: Location 1.2 – hallway on the third floor of NEB building, near the transmitter.

Figure 78: Location 1.4 – hallway on the third floor of NEB building, open area near elevator.

Figure 79: Location 1.7 – hallway on the third floor of NEB building, far from transmitter.

Figure 80: Location 2 – hallway on second floor of Whittemore Hall.

Figure 81: Location 3.1 – conference room 460 in NEB building.

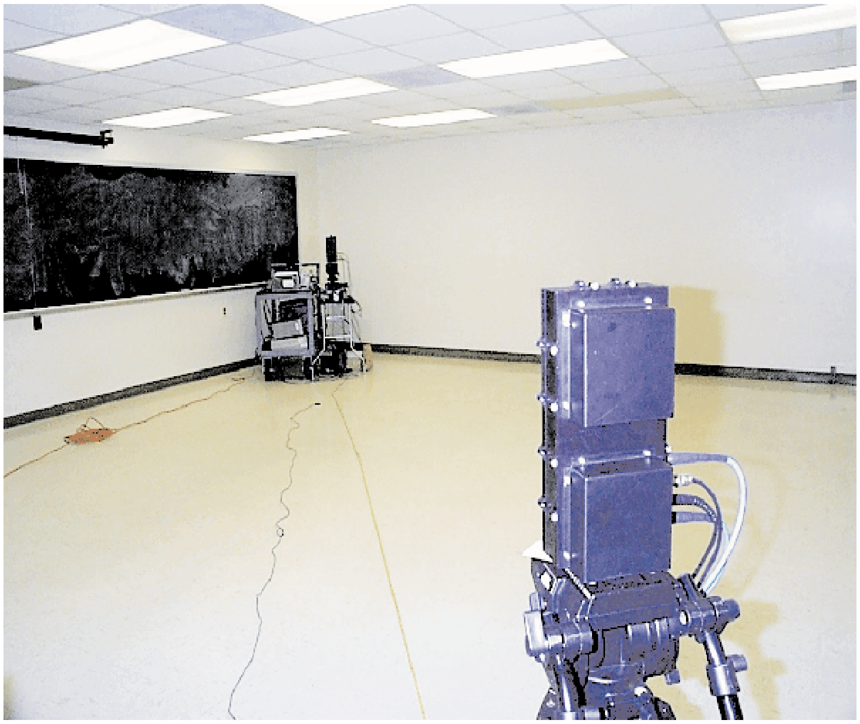

Figure 82: Location 4 – measurements in classroom 277 in Whittemore Hall.

Figure 83: Location 5.1 – measurements within the lab.

Figure 84: Location 5.3 – hallway to room measurements through a glass door.

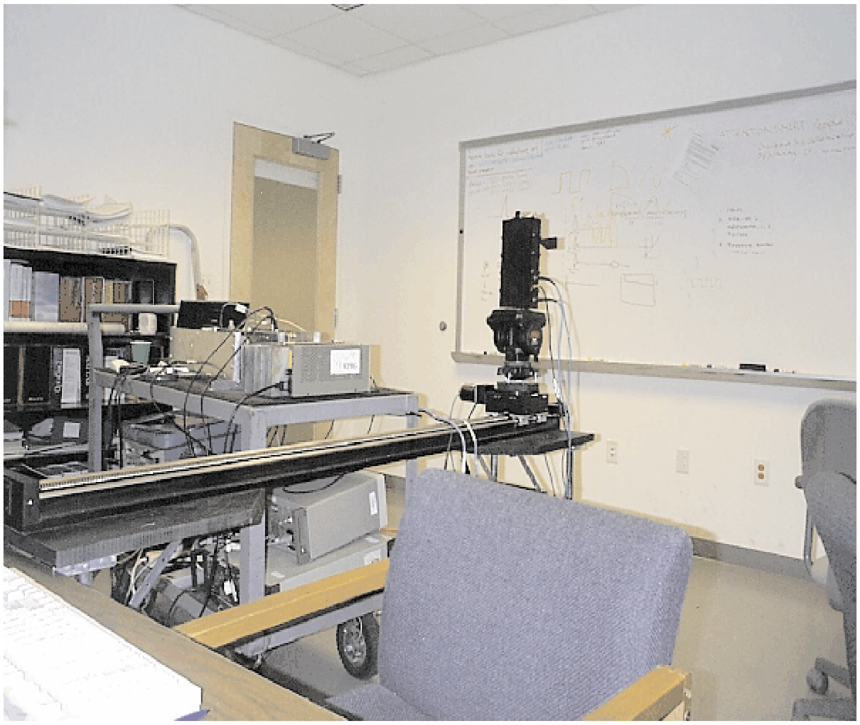

Figure 85: Location 6: measurements from room to room through a wall .

Figure 86: Location 7 – outdoor measurments in a parking lot.

Figure 87: Location 8: outdoor measurements near a stone wall of NEB building.

Appendix E

Abbreviations and Acronyms

AMPS: Advanced Mobile Phone Systems
AOA: Angle of Arrival
ART: Advanced Radio Telecom Corporation
ATM: Asynchronous Transfer Mode
B-ISDN: Broadband Integrated Services Digital Network
BER: Bit Error Rate
CW: Continuous Wave
DSP: Digital Signal Processing
EIRP: Effective Isotropic Radiated Power
EM: Electro-Magnetic
ETSI: European Telecommunications Standard Institute
FCC: Federal Communications Commission
GSM: Global System for Mobile
HIPERLAN: High-Performance Radio Local Area Network
HDTV: High Definition Television
IC: Integrated Circuits
IF: Intermediate Frequency
ISI: Intersymbol Interference
ISM: Industrial, Scientific, and Medical band

ITS: Intelligent Transport Systems

LMDS: Local Multipoint Distribution Services

LMCS: Local Multipoint Communications Services

LO: Local Oscillator

LOS: Line of Sight

MBS: Mobile Broadband Systems

MMIC: Microwave and Millimeter-wave Monolithic IC

NGI: Next Generation Internet

NII: National Information Infrastructure

NLOS: Non Line of Sight

PAP: Power Angle Profile

PBX: Private-Branch Exchange

PCN: Personal Communication Network

PCS: Personal Communications Services

PDF: Probability Density Function

PDP: Power Delay Profile

PN: Pseudo-Noise

RF: Radio Frequency

SCS: Sliding Correlator System

SNR: Signal to Noise Ratio

TIP: Two-Wave with Incoherent Power

TOA: Time of Arrival

UHF: Ultrahigh Frequency

VHSIC: Very High Speed Integrated Circuit

VNA: Vector Network Analyzer

XPD: Cross-Polarization Discrimination

WLAN: Wireless Local Area Network

WLL: Wireless Local Loop Telephony

References

[1] O. Andrisano, V. Tralli, and R. Verdone, "Millimeter Waves for Short-Range Multimedia Communication Systems," *Proc. IEEE*, vol. 86, pp. 1383–1401, July 1998.

[2] G. D. Durgin, T. S. Rappaport, and H. Xu, "Measurements and Models for Radio Path Loss and Penetration Loss In and Around Homes and Trees at 5.85 GHz," *IEEE Transactions on Communications*, vol. 46, Nov 1998.

[3] G. D. Durgin, H. Xu, and T. S. Rappaport, "Path Loss and Penetration Loss Measurements in and around Homes and Trees at 5.85 GHz," tech. rep., MPRG TR-97-10,Virginia Tech, June 1997.

[4] C. Ruthroff, "Multiple-Path Fading on Line-of-Sight Microwave Radio Systems as a Function of Path Length and Frequency," in *Bell Syst. Tech. J.*, vol. 50, pp. 2375–2398, September 1971.

[5] J. A. Ogilvy, *Theory of Wave Scattering from Random Rough Surfaces.* New York: Adam Hilger, 1991.

[6] P. Beckmann and A. Spizzichino, *The Scattering of Electromagnetic Waves from Rough Surfaces.* New York: Pergamon Press Inc., 1963.

[7] G. M. Whitman, F. Schwering, A. A. Triolo, and N. Y. Cho, "A Transport Theory of Pulse Propagation in a Strongly Forward Scattering Random Medium," *IEEE Transactions on Antennas and Propagation*, vol. 44, pp. 118–127, Jan 1996.

[8] A. Kajiwara, "Millimeter-Wave Indoor Radio Channel Artificial Reflector," *IEEE Transactions on Vehicular Technology*, vol. 46, pp. 486–493, May 1997.

[9] G. D. Durgin, V. Kukshya, E. Lau, and T. S. Rappaport, "Measurement-Based Spatial-Temporal Channel Modeling for Handheld Multi-media Terminals.," tech. rep., MPRG,Virginia Tech, Dec 1999.

[10] E. J. Violette, R. H. Espeland, R. O. DeBolt, and F. Schwering, "Millimeter-Wave Propagation at Street Level in an Urban Environment," *IEEE Trans. Geosci. Remote Sensing*, vol. 26, pp. 368–380, May 1988.

[11] K. Sato, T. Manabe, J. Polivka, T. Ihara, Y. Kasashima, and K. Yamaki, "Measurement of the Complex Refractive Index of Concrete at 57.5 GHz," *IEEE Transactions on Antennas and Propagation*, vol. 44, pp. 35–39, Jan 1997.

[12] T. Manabe, K. Sato, H. Masuzawa, K. Taira, T. Ihara, Y. Kasashima, and K. Yamaki, "Polarization Dependence of Multipath Propagation and High-Speed Transmission Characteristics of Indoor Millimeter-Wave Channel at 60 GHz," *IEEE Trans. Veh. Tech.*, vol. 44, pp. 268–274, May 1995.

[13] A. D. Kucar, "Mobile Radio: An Overview," *IEEE Comm. Magazine*, pp. 72–85, Nov. 1991.

[14] T. S. Rappaport, *Wireless Communications: Principles and Practice.* New Jersey: Prentice-Hall Inc., 1996.

[15] W. Stallings, *ISDN and Broadband ISDN with Frame Relay and ATM.* New Jersey: Prentice-Hall, 3 ed., 1995.

[16] Federal Communications Commission, "General Auction Data," http://www.fcc.gov/wtb/auctions/.

[17] J. D. Parsons, *The Mobile Radio Propagation Channel.* New York: John Wiley & Sons, 1994.

[18] P. Smulders, *Broadband Wireless LANs: A Feasibility Study.* PhD thesis, Eindhoven Univ. of Tech., The Netherlands, Dec. 1995.

[19] L. E. Larson(Ed), *RF and Microwave Circuit Design for Wireless Communications.* Boston: Artech House, 1997.

[20] Industry Canada, "Wireless Broadband - Canada Paving the Way," http://info.ic.gc.ca/.

[21] European Telecommunications Standards Institute, "Broadband Radio Access Networks," http://www.etsi.org/.

[22] L. M. Correia and R. P. Prasad, "An Overview of Wireless Broadband Communications," *IEEE Commun. Magazine*, pp. 28–33, Jan. 1997.

[23] K. H. Craig and J. R. Norbury, "Interference Mechanisms Which Affect Frequency Reuse on Short Line-of-Sight Millimetric Links," in *Proc. ICAP, IEE Conf Pub 370*, pp. 2.999–2.1002, 1993.

[24] W. Rummler, "Multipath Fading Channel Models for Microwave Digital Radio," *IEEE Commun. Magazine*, vol. 24, pp. 30–42, Nov. 1986.

[25] W. Rummler, "A New Selective Fading Model: Application to Propagation Data," in *Bell Syst. Tech. J.*, vol. 58, pp. 1037–1071, May-June 1979.

[26] J. H. Schaffner, H. Izadpanah, D. Gregorie, H. P. Hsu, H. Xu, R. J. Boyle, and T. S. Rappaport, "Millimeter Wave Wireless Technology and Testbed Development for Wideband Infrastructure Access," in *Session WCC-98TA7, 3rd International Wireless Commun. Conf.*, pp. 175–179, Nov. 1998.

[27] G. Heftman, "LMDS Set to Challenge for Last-Mile Supremacy," *Microwave and RF*, pp. 30–38, April 1999.

[28] National Institute of Standards and Technology, "National Information Infrastructure (NII)," http://nii.nist.gov/nii/niiinfo.html.

[29] W. C. Jakes(Ed), *Microwave Mobile Communications.* New York: IEEE Press, 1974.

[30] W. C. Y. Lee, *Mobile Cellular Telecommunications Systems.* New York: McGraw-Hill, 1989.

[31] L. W. Couch II, *Digital and Analog Communication Systems.* New York: Macmillan, Inc, 4th ed., 1993.

[32] B. Razavi, *RF Microelectronics.* Upper Saddle River, NJ: Prentice Hall PTR, 1998.

[33] J. C.-I. Chuang, "The Effects of Time Delay Spread on Portable Communications Channels with Digital Modulation," *IEEE Journal on Selected Areas in Communications*, vol. SAC-5, pp. 879–889, June 1987.

[34] W. L. Stutzman and G. A. Thiele, *Antenna Theory and Design.* New York: Wiley, 1981.

[35] M. A. Panjwani, A. L. Abbot, and T. S. Rappaport, "Interactive Computation of Coverage Regions for Wireless Communication in Multifloored Indoor Environments," *IEEE Journal on Selected Area of Communications*, vol. 14, pp. 420–430, April 1996.

[36] R. D. Murch, J. H. M. Sau, and K. W. Cheung, "Improved Empirical Modeling for Indoor Propagation Prediction," in *IEEE 45th Vehicular Technology Conference*, (Chicago, IL), pp. 439–443, July 1995.

[37] P. B. Papazian, M. Roadifer, and G. A. Hufford, "Initial Study of the Local Multipoint Distribution System Radio Channel," tech. rep., NTIA Report 94-315, Aug. 1994.

[38] S. Y. Seidel and H. Arnold, "Propagation Measurements at 28 GHz to Investigate the Performance of Local Multipoint Distribution Service (LMDS)," in *Proc. IEEE GLOBECOM '95*, pp. 754–757, 1995.

[39] H. Xu, T. S. Rappaport, R. J. Boyle, and J. Schaffner, "Radio Wave Propagation Study at 38 GHz," in *Proc. IEEE VTC'99*, pp. 1575–1579, May 1999.

[40] H. Xu, T. S. Rappaport, R. J. Boyle, and J. Schaffner, "Measurements and Modeling for Radio Wave Propagation at 38 GHz," *IEEE Journal on Selected Areas on Communications*, April 2000.

[41] G. Turin, F. Clapp, T. Johnston, S. Fine, and D. Lavry, "A Statistical Model of Urban Multipath Propagation," *IEEE Transactions on Vehicular Technology*, vol. 21, no. 1, 1972.

[42] H. Hashemi, "The Indoor Radio Propagation Channel," in *Proc. IEEE*, vol. 81, pp. 943–968, July 1993.

[43] H. Hashemi, "Impulse Response Modeling of Indoor Radio Propagation Channels," *IEEE Journal on Selected Areas in Communications*, vol. 11, pp. 967–978, September 1993.

[44] P. Bello, "Characterization of Randomly Time-Variant Linear Channels," *IEEE Transaction on Communications Systems*, pp. 360–393, December 1963.

[45] D. C. Cox, "Delay Doppler Characteristics of Multipath Delay Spread and Average Excess Delay for 910 MHz Urban Mobile Radio Paths," *IEEE Transactions on Antennas and Propagation*, vol. AP-20, pp. 625–635, September 1972.

[46] D. C. Cox and R. P. Leck, "Distributions of Multipath Delay Spread and Average Excess Delay for 910 MHz Urban Mobile Radio Paths," *IEEE Transactions on Antennas and Propagation*, vol. AP-23, pp. 206–213, March 1975.

[47] R. H. Clark, "A Statistical Theory of Mobile-Radio Reception," *Bell System Tech. J.*, vol. 47, pp. 957–1000, 1968.

[48] M. J. Gans, "A Power-Spectral Theory of Propagation in the Mobile Radio Environment," *IEEE Transaction on Vehicular Technology*, vol. VT-20, pp. 27–38, Feb 1972.

[49] G. D. Durgin and T. S. Rappaport and D. A. de Wolf, "More Complete Probability Density Functions for Fading in Mobile Communications," in *IEEE VTC'99*, (Houston, TX), May 1999.

[50] S. O. Rice, "Statistical Properties of a Sine Wave Plus Random Noise," *Bell System Technical Journal*, vol. 27, pp. 109–157, Jan 1948.

[51] L. Rayleigh, *The Theory of Sound.* London: MacMillan, 3rd ed., 1896.

[52] S. O. Rice, "Mathematical Analysis of Random Noise," *Bell System Technical Journal*, vol. 23, pp. 282–332, July 1944.

[53] S. O. Rice, "Mathematical Analysis of Random Noise (continued)," *Bell System Technical Journal*, vol. 24, pp. 46–156, Jan 1945.

[54] D. Reudink, "Properties of Mobile Radio Propagation Above 400 MHz," *IEEE Transactions on Vehicular Technology*, Nov 1974.

[55] J. C. Liberti and T. S. Rappaport, *Smart Antennas for Wireless Communications: IS-95 and Third Generation CDMA Applications.* New Jersey: Prentice Hall, Inc, 1999.

[56] G. D. Durgin and T. S. Rappaport, “A Basic Relationship Between Multipath Angular Spread and Narrowband Fading in a Wireless Channel,” *IEE Electronic Letters*, 1998.

[57] G. D. Durgin, T. S. Rappaport, and H. Xu, “5.85 GHz Radio Path Loss and Penetration Loss Measurements In and Around Homes and Trees,” *IEEE Communications Letters*, vol. 40, Mar 1998.

[58] G. D. Durgin, T. S. Rappaport, and H. Xu, “Radio Path Loss and Penetration Loss Measurements In and Around Homes and Trees at 5.85 GHz,” in *IEEE GLOBECOM 98*, Nov 1998.

[59] G. D. Durgin, T. S. Rappaport, and H. Xu, “Partition-Based Path Loss Analysis for In-Home and Residential Areas at 5.85 GHz,” in *IEEE APS Conference*, June 1998.

[60] D. C. Cox, “Time and Frequency Domain Characterizations of Multipath Propagation at 910 MHz in a Suburban Mobile Radio Environment,” *Radio Science*, pp. 1069–1077, December 1972.

[61] H. Xu, T. S. Rappaport, J. Schaffner, and H. P. Hsu, “The Sliding Correlator and Network Analyzer Channel Sounding Methods for Wideband Multipath Propagation Measurements at 5.85 GHz,” *Advancing Microelectronics: 1998 Special Wireless Issue*, vol. 25, no. 3, pp. 40–54, 1998.

[62] A. Papoulis, *Probability, Random Variables, and Stochastic Processes.* New York: McGraw-Hill, 1984.

[63] J. G. Proakis and D. G. Manolakis, *Digital Signal Processing: Principles, Algorithms, and Applications.* New Jersey: Prentice Hall, 3rd ed., 1996.

[64] N. Patwari, “Measured and Modeled Time and Angle Dispersion Characteristics of the 1.8 GHz Peer-to-Peer Radio Channel,” Master’s thesis, Virginia Polytechnic Institute and State University, Blacksburg, VA, May 1999.

[65] N. Benvenuto, “Distortion Analysis on Measuring the Impulse Response of a System Using a Crosscorrelation Method,” *Bell Laboratory Technical Journal*, vol. 63, pp. 2171–2191, December 1984.

[66] W. G. Newhall, K. Saldanha, and T. S. Rappaport, "Using RF Channel Sounding Measurements to Determine Delay Spread and Path Loss," *RF Design*, pp. 82–88, Jan 1996.

[67] W. G. Newhall, T. S. Rappaport, and D. G. Sweeney, "A Spread Spectrum Sliding Correlator System for Propagation Measurements," *RF Design*, pp. 40–54, April 1996.

[68] T. S. Rappaport and C. D. McGillem, "UHF Fading in Factories," *IEEE Journal on Selected Areas in Communications*, vol. 7, pp. 40–48, January 1989.

[69] T. S. Rappaport, S. Y. Seidel, and R. Singh, "900 MHz Multipath Propagation Measurements for U.S. Digital Cellular Radiotelephone," *IEEE Transactions on Vehicular Technology*, pp. 132–139, May 1990.

[70] L. Talbi and G. Delisle, "Experimental Characterization of EHF Multipath Indoor Radio Channels," *IEEE J. Select. Areas Commun.*, vol. 14, pp. 431–440, Apr. 1996.

[71] S. Y. Seidel, T. S. Rappaport, S. Jain, M. Lord, and R. Singh, "Path Loss, Scattering, and Multipath Delay Statistics in Four European Cities for Digital Cellular and Microcellular Radiotelephone," *IEEE Transactions on Vehicular Technology*, vol. 40, pp. 721–730, November 1991.

[72] D. M. Devasirvatham, "Time Delay Spread and Signal Level Measurements of 850 MHz Radio Waves in Building Environments," *IEEE Transactions on Antennas and Propagation*, vol. AP-34, November 1986.

[73] R. Bultitude, S. A. Mahmoud, and W. A. Sullivan, "A Comparison of Indoor Radio Propagation Characteristics at 910 MHz and 1.75 GHz," *IEEE Journal on Selected Areas in Communications*, vol. 7, January 1989.

[74] A. Crawford and W.C. Jakes, JR, "Selective Fading of Microwaves," *Bell Syst. Tech. J.*, vol. 31, pp. 68–90, Jan. 1952.

[75] R. L. Freeman, *Radio System Design for Telecommunications (1-100 GHz).* New York: John Wiley & Sons, 1987.

[76] ITU, "Propagation Data and Prediction Methods Required for the Design of Terrestrial Line-of-Sight Systems," tech. rep., Recommendation ITU-R P.530-6.

[77] F. K. Schwering, E. J. Violette, and R. H. Espeland, “Millimeter-Wave Propagation in Vegetaion: Experiments and Theory,” *IEEE Trans. Geosci. Remote Sensing*, vol. 26, pp. 355–367, May 1988.

[78] R. K. Crane, *Electromagnetic Wave Propagation Through Rain.* New York: John Wiley & Sons, 1996.

[79] M. Born and E. Wolf, *Principles of Optics: Electromagnetic Theory of Propagation, Interference and Diffraction of Light.* January 1998.

[80] T. A. Russell, C. W. Bostian, and T. S. Rappaport, “A Deterministic Approach to Predicting Microwave Diffraction by Buildings for Microcellular Systems,” *IEEE Transactions on Antennas and Propagations*, vol. 41, pp. 1640–1649, December 1993.

[81] D. E. Kerr, *Propagation of Short Radio Waves.* New York: McGraw-Hill, 1951.

[82] C. A. Balanis, *Advanced Engineering Electromagnetics.* New York: John Wiley & Sons, 1989.

[83] W. S. Ament, “Toward a theory of reflection by a rough surface,” in *IRE*, vol. 41, pp. 142–146, Jan. 1953.

[84] L. Boithias, *Radio Wave Propagation.* New York: McGraw-Hill, 1987.

[85] O. Landron, M. J. Feuerstein, and T. S. Rappaport, “A Comparison of Theoretical and Empirical Reflection Coefficients for Typical Exterior Wall Surfaces in a Mobile Radio Environment,” *IEEE Transactions on Antennas and Propagation*, vol. 44, pp. 341–351, March 1996.

[86] D. A. Kapp and G. S. Brown, “A New Numerical Method for Rough Surface Scattering Calculations,” *IEEE Transactions on Antennas and Propagation*, vol. 44, pp. 711–721, May 1996.

[87] C. Macaskill and B. J. Kachoyan, “Iterative Approach for the Numerical Simulation of Scattering from One- and Two-Dimensional Rough Surfaces,” *Applied Optics*, vol. 32, pp. 2839–2847, May 1993.

[88] S. O. Rice, "Reflection of Electromagnetic Waves from Slightly Rough Surfaces," *Communications on Pure and Applied Mathematics*, vol. 4, pp. 351–378, 1951.

[89] G. S. Brown, "Application of the Integral Equation Method of Smoothing to Random Surface Scattering," *IEEE Transactions on Antennas and Propagation*, vol. AP-32, pp. 1308–1312, Dec. 1984.

[90] G. S. Brown, "A New Approach to the Analysis of Rough Surface Scattering," *IEEE Transactions on Antennas and Propagation*, vol. 39, pp. 943–948, July 1991.

[91] D. A. Kapp and G. S. Brown, "Effect of Correlation Between Shadowing and Shadowed Points in Rough Surface Scattering," *IEEE Transactions on Antennas and Propagation*, vol. 42, pp. 1154–1160, Aug. 1994.

[92] B. Langen, G. Lober, and W. Herzig, "Reflection and Transmission Behaviour of Building Materials at 60 GHz," in *Proc. IEEE PIMRC'94*, (Hague, Netherlands), pp. 505–509, Sep. 1994.

[93] A. Seville, U. Yilmaz, P. Charriere, N. Powell, and K. H. Craig, "Building Scatter and Vegetation Attenuation Measurements at 38 GHz," in *Proc. ICAP, IEE Conf Pub 407*, pp. 46–50, Apr. 1995.

[94] S. Y. Seidel, *Site-Specific Propagation Prediction for Wireless In-Building Personal Communication System Design.* PhD thesis, Blacksburg, VA, February 1993.

[95] M. L. Skolnik, *Introduction to Radar Systems.* New York: McGraw-Hill, 2nd ed., 1980.

[96] J. V. Rees, "Measurements of the Wideband Radio Channel Characteristics for Rural, Residential and Suburban Areas," *IEEE Transactions on Vehicular Technology*, vol. VT-36, pp. 1–6, February 1987.

[97] F. K. Schwering and R. A. Johnson, "A Transport Theory of Millimeter-Wave Propagation in Woods and Forests," *Journal of Wave-Material Interaction*, vol. 1, pp. 205–235, April 1986.

[98] P. B. Papazian, G. A. Hufford, R. J. Achatz, and R. Hoffman, "Study of the Local Multipoint Distribution Service Radio Channel," *IEEE Tran. Broadcasting*, vol. 43, June 1997.

[99] R. L. Olsen, D. V. Rogers, and D. B. Hodge, "The aR^b Relation in the Calculation of Rain Attenuation," *IEEE Trans. Antennas Propagat.*, vol. AP-26, pp. 318–329, March 1978.

[100] S. Lin, "Statistical Behavior of Rain Attenuation," *Bell Syst. Tech. J.*, vol. 52, pp. 557–581, Apr. 1973.

[101] D. de Wolf and L. Ligthart, "Multipath Effects Due to Rain at 30-50 GHz Frequency Communication Links," *IEEE Trans. Antennas Propagat.*, pp. 1132–1138, Aug. 1993.

[102] M. A. Morgan, "Finite Element Computation of Microwave Scattering by Raindrops," *Radio Science*, no. 6, pp. 1109–1119, 1980.

[103] M. A. Morgan and K. K. Mie, "Finite Element Computation of Scattering by Inhomogeneous Penetrable Bodies of Revolution," *IEEE Trans. Antennas Propagat.*, pp. 202–208, 1979.

[104] S. O. Ajose, M. N. Sadiku, and U. Goni, "Computation of Attenuation, Phase Rotation, and Cross-Polarization of Radio Waves Due to Rainfall in Tropical Regions," *IEEE Trans. Antennas Propagat.*, pp. 1–5, Jan. 1995.

[105] J. E. Allnutt, *Satellite-to-ground radiowave propagation.* London,UK: Peter Peregrinus Ltd., 1989.

[106] T. Pratt and C. W. Bostian, *Satellite Communications.* John Wiley & Sons, 1986.

[107] W. L. Stutzman, T. Pratt, A. Safaai-Jazi, P. W. Remaklus, J. Laster, B. Nelson and H. Ajaz, "Results from the Virginia Tech propagation experiment using the Olympus satellite 12, 20 and 30 GHz beacons," *IEEE Transactions on Antennas and Propagation*, vol. 43, pp. 54–62, Jan. 1995.

[108] R. B. Penndorf, "Scattering and Extinction Coefficients for Small Absorbing and Nonabsorbing Aerosols," *Journal of Optical Society of America*, vol. 52, pp. 896–904, 1962.

[109] D. M. A. Jones and A. L. Sims, "Climatology of Instantaneous Rain Retes," *Journal of Applied Meteorology*, vol. 17, pp. 1135–1140, 1978.

[110] A. E. Freeny and J. D. Gabby, "A Statistical Description of Intense Rainfall," *Bell System Technical Journal*, vol. 48, pp. 1789–1856, 1969.

[111] R. Valentin, “Statistiken der regendampfung fur rundfunkverbindungen uber 10 ghz,” Tech. Rep. 455-TBr-62, Technischer Bericht, Research Center, Deutsche Bundespost Telekom, Darmstadt, Germany, 1977.

[112] R. K. Crane, “Prediction of Attenuation by Rain,” *IEEE Transactions on Communications*, pp. 1717–1733, Sept. 1980.

[113] R. Dalke, G. Hufford, and R. Ketchum, “Radio Propagation Considerations for Local Multipoint Distribution Sysrtems,” tech. rep., NTIA Report 96-331, Aug. 1996.

[114] CCIR, “Propagation Data and Prediction Methods Required for Earth-Space Telecommunications Systems,” tech. rep., Recommendations and Reports of the $XVII_{th}$ Plenary Assembly, Report 564, 1990.

[115] G. Gilder, “The New Rule of the Wireless,” *Telecosm Archive*, http://www.forbes.com/asap/gilder/index.htm.

[116] Microflect Corporation, “Passive Repeater Engineering Manual 161A,” 1984.

[117] L. M. Correia and J. R. Reis, “Wideband Characterisation of the Propagation Channel at 60 GHz,” in *Proc. PIMRC’96*, (Taipei,Taiwan), Oct. 15-18 1996.

[118] L. M. Correia, J. J. Reis, and P. O. Frances, “Analysis of the Average Power to Distance Decay Rate at the 60 GHz Band,” in *Proc. PIMRC’97*, (Phoenix,Arizona), May 1997.

[119] L. M. Correia and P. O. Frances, “A Propagation Model for the Estimation of the Average Received Power in an Outdoor Environment in the Millimeter Waveband,” in *Proc. IEEE VTC’94*, (Stockholm, Sweden), June 1994.

[120] P. Vasconcelos and L. M. Correia, “Fading Characterization of the Mobile Radio Channel at the Millimeter Waveband,” in *Proc. PIMRC’97*, (Phoenix,Arizona), May 1997.

[121] G. Kalivas, M. El-Tanany, and S. Mahmoud, “Millimeter-Wave Channel Measurements with Space Diversity for Indoor Wireless Communications,” *IEEE Transactions on Vehicular Technology*, vol. 44, pp. 494–505, Aug. 1995.

[122] A. M. Hammoudeh and G. Allen, “Millimetric Wavelengths Radiowave Propagation for Line-of-Sight Indoor Microcellular Mobile Communications,” *IEEE Transactions on Vehicular Technology*, vol. 44, pp. 449–460, Aug. 1995.

[123] R. J. C. Bultitude, R. F. Hahn, and R. J. Davies, “Propagation Considerations for the Design of an Indoor Broad-Band Communications System at EHF,” *IEEE Trans. Vehicular Technology*, vol. 47, pp. 235–245, February 1998.

[124] A. G. Emslie, R. L. Lagace, and P. F. Strong, “Theory of the Propagation of UHF Radio Waves in Coal Mine Tunnels,” *IEEE Transactions on Antennas and Propagation*, vol. AP-23(2), pp. 192–205, March 1975.

[125] E. Violette, R. Espeland, and K. Allen, “Millimeter-Wave Propagation Characteristics and Channel Performance for Urban-Suburban Environments,” tech. rep., NTIA Report 88-239, Dec. 1988.

[126] L. M. Correia and P. O. Frances, “Estimation of Materials Characteristics from Power Measurements at 60 GHz,” in *Proc. IEEE PIMRC’94*, (Hague, Netherlands), Sep. 19-23 1994.

[127] T. S. Rappaport, “The Wireless Revolution,” *IEEE Communications Magazine*, pp. 52–71, Nov 1991.

[128] D. C. Cox, R. R. Murray, and A. W. Norris, “800 MHz Attenuation Measured in and around Suburban Houses ,” *Bell Laboratory Technical Journal*, vol. 673, July-August 1984.

[129] A. R. Tharek and J. P. McGeehan, “Indoor Propagation and Bit Error Rate Measurements at 60 GHz using Phase-Locked Oscillators,” in *Proc. 38th IEEE Veh. Technol. Conf.*, pp. 127–133, May 1988.

[130] H. Droste and G. Kadel, “Measurement and Analysis of Wideband Indoor Propagation Characteristics at 17 GHz and 60 GHz,” in *IEE Antennas and Propagation, Conference Publication No. 407*, pp. 288–291, April 1995.

[131] W. L. Stutzman, *Polarization in Electromagnetic Systems.* Artech House, 1993.

[132] A. Kajiwara, “Line-of-Sight Radio Communication Using Circular Polarized Waves,” *IEEE Transactions on Vehicular Technology*, vol. 44, pp. 487–493, August 1995.

[133] T. S. Rappaport and D. A. Hawbaker, "Wide-band Microwave Propagation Parameters Using Circular and Linear Polarized Antennas for Indoor Wireless Channels," *IEEE Transactions on Communications*, vol. 40, pp. 240–245, Feb 1992.

[134] R. Davies, M. Bensebti, M. Beach, and J. McGeehan, "Wireless Propagation Measurements in Indoor Multipath Environments at 1.7 GHz and 60 GHz for Small Cell Systems," in *Proc.* 41^{st} *IEEE Veh. Tech. Conf.*, (St. Louis), pp. 589–593, 1991.

[135] W. C. Jakes, "A Comparison of Specific Space Diversity Techniques for Reduction of Fast Fading in UHF Mobile Radio Systems," *IEEE Transactions on Vehicular Technology*, vol. VT-20, pp. 81–91, November 1971.

[136] A. Turkmani, A. Arowojolu, P. Jefford, and C. Kellett, "An Experimental Evaluation of the Performance of Two-Branch Space and Polarization Diversity Schemes at 1800 MHz," *IEEE Transactions on Vehicular Technology*, vol. 44, pp. 318–326, May 1995.

[137] A. M. Hammoudeh, J. P. Kermoal, and M. G. Sanchez, "Coherence Bandwidth Measurements in an Indoor Microcell at 62.4 GHz," *IEE Electronics Letters*, vol. 34, pp. 429–431, March 1998.

[138] P. Marinier, G. Delisle, and C. Despins, "Temporal Variations of the Indoor Wireless Millimeter-Wave Channel," *IEEE Trans. Antennas Propagat.*, vol. 46, pp. 928–934, June 1998.

[139] D. Jones, R. Espeland, and E. Violette, "Vegetation Loss Measurements at 9.6, 28.8, 57.6 and 96.1 GHz Through a Conifer Orchard in Washington State," tech. rep., NTIA Report 89-251, Oct 1989.

[140] H. Xu, R. B. Boyle, T. S. Rappaport, J. Schaffner, and R. Lovestead, "Radio Wave Propagation Study at 38 GHz," tech. rep., MPRG TR-98-5, Virginia Tech, Sept 1998.

[141] A. Mawira, J. Neesen, and F. Zelders, "Estimation of the effective spatial extent of rain showers from measurements by a radiometer and a raingauge network," in *IEE Conf. Publ. 195: International Conference on Antennas and Propagation (ICAP81)*, pp. 133–137, 1981.

[142] D. J. Fang, "A new way of estimating microwave attenuation over a slant propagation path based on raingauge data," *IEEE Transactions on Antennas and Propagation*, vol. AP-24, pp. 381–384, 1976.

[143] M. Yamada, A. Ogawa, and H. Yokoi, "Precipitation attenuation in the low elevated earth-satellite path," in *IECE Tech. Group Antennas and Propagation*, vol. AP 75-66, (Japan), 1975.

[144] R. Doviak and D. Zrnic, *Doppler Radar and Weather Observations.* San Diego: Academic Press, Harcourt Brace Jovanovich, 2 ed., 1993.

[145] T. S. Rappaport and S. Sandhu, "Radio-Wave Propagation for Emerging Wireless Personal-Communication Systems," *IEEE Antennas and Propagation Magazine*, vol. 36, pp. 14–24, Oct 1994.

[146] H. Bertoni, W. Honcharenko, L. Maciel, and H. Xia, "UHF Propagation Prediction for Wireless Personal Communications," in *Proc. IEEE*, pp. 1333–1359, Sept. 1994.

[147] S. Tan and H. Tan, "A Microcellular Communications Propagation Model Based on the Uniform Theory of Diffraction and Multiple Image Theory," *IEEE Transactions on Antennas and Propagation*, vol. 44, pp. 1317–1326, Oct 1996.

[148] S. Y. Seidel and T. S. Rappaport, "Site-Specific Propagation Prediction for Wireless In-Building Personal Communication System Design," *IEEE Transactions on Vehicular Technology*, vol. 43, pp. 879–891, Nov 1994.

[149] P. Charriere, K. H. Craig, and A. Seville, "A Ray-Based, Millimeter Wave Urban Propagation Tool," in *Proc. ICAP, IEE Conf Pub 407*, pp. 258–261, Apr. 1995.

[150] H. J. Thomas, R. S. Cole, and G. L. Siqueira, "An Experimental Study of the Propagation of 55 GHz Millimeter Waves in an Urban Mobile Radio Environment," *IEEE Transactions on Vehicular Technology*, vol. 43, pp. 140–146, Feb. 1994.

[151] P. Petrus, J. H. Reed, and T. S. Rappaport, "Geometrically Based Statistical Channel Model for Macrocellular Mobile Environments," in *Proc. IEEE VTC '96*, pp. 1197–1201, 1996.

[152] J. Litva, A. Ghaforian, and V. Kezys, “High-Resolution Measurements of AOA and Time-Delay for Characterizing Indoor Propagation Environments,” vol. 2, (Calgary, Cananda), pp. 514–518, July 1996.

[153] J. Fuhl, J. P. Rossi and E. Bonek, “High-resolution 3-d direction-of-arrival determination for urban mobile radio,” *IEEE Transactions on Antennas and Propagation*, vol. 45, April 1997.

[154] J.P. Rossi, J.P. Barbot and A.J. Levy, “Theory and measurement of the angle of arrival and time delay of uhf radiowave using a ring array,” *IEEE Transactions on Antennas and Propagation*, vol. 45, May 1997.

[155] Y.L.C. de Jong and M.H.A.J. Herben, “High-Resolution Angle-of-Arrival Measurement of the Mobile Radio Channel,” *IEEE Transactions on Antennas and Propagation*, vol. 47, Nov. 1999.

[156] C.M.P. Ho and T. S. Rappaport and M. P. Koushik, “Antenna Effects on Indoor Obstructed Wireless Channels and a Deterministic Image-Based Wide-Band Propagation Model for In-Building Personal Communication Systems,” *International Journal of Wireless Information Networks*, vol. 1, no. 1, 1994.

[157] C. L. Holloway, P. L. Perini, R. R. Delyser and K. C. Allen, “Analysis of Composite Walls and Their Effects on Short-Path Propagation Modeling,” *IEEE Transactions on Vehicular Technology*, vol. 46, pp. 730–738, August 1997.

[158] W. Honcharenko and H. Bertoni, “Transmission and Reflection Characteristics at Concrete Block Walls in the UHF Bands Proposed for Future PCS,” *IEEE Transactions on Antennas and Propagation*, vol. 42, pp. 232–239, February 1994.

[159] K. Sato, T. Manabe, et.al., “Measurements of Reflection and Transmission Characteristics of Interior Structures of Office Building in the 60-GHz Band,” *IEEE Transactions on Antennas and Propagation*, vol. 45, pp. 1783–1792, Dec 1997.

[160] G. D. Durgin and T. S. Rappaport, “Three Parameters for Relating Small-Scale Temporal Fading Statistics to Multipath Angles-of-Arrival,” in *PIMRC’99*, (Osaka, Japan), pp. 1077–1081, Sept 1999.

[161] P. Smulders and L. Correia, "Characterisation of propagation in 60 ghz radio channels," *Electronics & Communication Engineering Journal*, pp. 73–80, Apr. 1997.

[162] H. Xu, T. S. Rappaport, R. J. Boyle, and J. Schaffner, "38 GHz Wideband Point-to-Point Measurements under Different Weather Conditions.," *IEEE Communications Letters*, vol. 4, pp. 7–8, January 1999.

[163] H. Xu, D.A. de Wolf and T. S. Rappaport, "Experimental and Theoretical Study of Short Term Signal Variation during Rain," in *AP2000*, (Davos, Swizerland), April 2000.

[164] H. Xu, V. Kukshya and T. S. Rappaport, "Spatial and Temporal Characterization of 60 GHz Channels," in *Submitted to IEEE VTC'2000*, (Boston, MA), 2000.

[165] EFRATOM Time & Frequency Products, Inc., *Low Cost Rubidium Oscillator: Installation, Operation and Calibration Manual.* Efratom Division, 1994.

Vita

Hao Xu was born in Wuhan, P.R. China on February 28, 1971. He received his B.S.E.E. and M.S.E.E in Moscow Power Engineering Institute and State University, Moscow, Russia in 1994 and 1996, respectively. In 1989, as a result of his third place finish in the national entrance examination to universities in China, he received Zhang Zhongzhi Price Award from the University of Science and Technology of China, and was selected to study in Moscow. Since Fall 1996, he has been a research assistant at MPRG, Virginia Tech, working towards his Ph.D. degree. His research focuses on radio wave propagation and RF channel modeling, including the design and development of channel sounding systems. Current research includes millimeter-wave propagation at 38 GHz and 60 GHz.

Hao Xu received his B.S.E.E and M.S.E.E with the highest honors with a GPA of 4.0. In 1998, he has received Communications Society Stephen O. Rice Prize Paper Award. He is a member of Eta Kappa Nu, Sigma Si and the IEEE.